JAEA-Review
2009-036

JAEA-Review

JAEA-Tokai Tandem Annual Report 2008
April 1, 2008 - March 31, 2009

Department of Research Reactor and Tandem Accelerator

Nuclear Science Research Institute
Tokai Research and Development Center

November 2009

Japan Atomic Energy Agency

日本原子力研究開発機構

本レポートは独立行政法人日本原子力研究開発機構が不定期に発行する成果報告書です。
本レポートの入手並びに著作権利用に関するお問い合わせは、下記あてにお問い合わせ下さい。
なお、本レポートの全文は日本原子力研究開発機構ホームページ（http://www.jaea.go.jp）
より発信されています。

独立行政法人日本原子力研究開発機構　研究技術情報部　研究技術情報課
〒319-1195　茨城県那珂郡東海村白方白根 2 番地 4
電話 029-282-6387, Fax 029-282-5920, E-mail:ird-support@jaea.go.jp

This report is issued irregularly by Japan Atomic Energy Agency
Inquiries about availability and/or copyright of this report should be addressed to
Intellectual Resources Section, Intellectual Resources Department,
Japan Atomic Energy Agency
2-4 Shirakata Shirane, Tokai-mura, Naka-gun, Ibaraki-ken 319-1195 Japan
Tel +81-29-282-6387, Fax +81-29-282-5920, E-mail:ird-support@jaea.go.jp

JAEA-Review 2009-036

JAEA-Tokai Tandem Annual Report 2008
April 1, 2008 – March 31, 2009

Department of Research Reactor and Tandem Accelerator

Nuclear Science Research Institute
Tokai Research and Development Center
Japan Atomic Energy Agency
Tokai-mura, Naka-gun, Ibaraki-ken

(Received September 15, 2009)

The JAEA-Tokai tandem accelerator complex has been used in various research fields such as nuclear science and material science by researchers not only of JAEA but also from universities, research institutes and industrial companies. This annual report covers developments of accelerators and research activities carried out using the tandem accelerator, superconducting booster, and radioactive nuclear beam accelerator, from April 1, 2008 to March 31, 2009. Fifty-five summary reports were categorized into seven research/development fields:

(1) accelerator operation and development
(2) nuclear structure
(3) nuclear reaction
(4) nuclear chemistry
(5) nuclear theory
(6) atomic physics and solid state physics
(7) radiation effects in materials

This report also lists publications, meetings, personnel, committee members, cooperative researches and common use programs.

Keywords : JAEA-Tokai Tandem Accelerator, Operation Results, Nuclear Structure, Nuclear Reaction, Nuclear Chemistry, Nuclear Theory, Atomic Physics, Solid State Physics, Radiation Effects in Materials, Progress Report.

Editors : Yuichiro NAGAME, Satoshi CHIBA, Norito ISHIKAWA, Shin-ichi MITSUOKA, Mitsuo KOIZUMI, Makoto MATSUDA , and Suehiro TAKEUCHI

JAEA-Review 2009-036

原子力機構東海タンデム加速器2008年度年次報告

日本原子力研究開発機構
東海研究開発センター原子力科学研究所
研究炉加速器管理部

(2009年9月15日受理)

原子力機構東海タンデム加速器施設は、原子核科学や物質科学などの様々な分野において、原子力機構を初めとして、大学や公立研究機関、民間企業に利用されている。本年次報告書は、タンデム加速器、ブースター加速器、放射性核種加速装置を利用し、2008年4月1日から2009年3月31日までの期間に実施された研究活動の英文要約をまとめたものである。総数55件の要約を下記の7部門に分類した。

（1）加速器の運転状況と開発
（2）原子核構造
（3）原子核反応
（4）核化学
（5）原子核理論
（6）原子物理及び固体物理
（7）材料の照射効果

また、発表論文と会議での口頭発表、タンデム加速器に関与した職員、タンデム加速器専門部会委員、大学等との共同研究課題、及び施設共用課題のリストを掲載した。

原子力科学研究所：〒319-1195　茨城県那珂郡東海村白方白根2-4
編集者：永目　諭一郎、千葉　敏、石川　法人、光岡　真一、小泉　光生、松田　誠、
竹内　末広

Foreword

This report covers research and development activities with the tandem accelerator, its superconducting booster and TRIAC radioactive ion accelerator at JAEA Tokai, for the period of FY 2008 (April 1, 2008 to March 31, 2009). During this period, the tandem accelerator was operated over a total of 210 days and delivered 25 different ions to the experiments in the fields of nuclear physics, nuclear chemistry, atomic physics, solid state physics and radiation effects in materials. Fifty-four research programs were carried out in collaboration with a total of about 250 researchers from universities and research institutes. The TRIAC was operated for 25 days. We held a meeting in celebration of a-hundred-thousand hours of accelerator operation for experiments on January 6 and 7 in 2009, inviting Dr. Akira Tonomura as a lecturer and having 26 oral presentations and 48 posters, with about 120 participants. The following are some of the highlights in FY 2008.

In the development of the tandem accelerator and the booster, the in-terminal 14.5-GHz ECR ion source, installed last fiscal year, has been operated in good condition. We delivered high-intensity and high-energy heavy-ion beams from this ion-source. We have accelerated multiply charged xenon beams up to 30+. This charge state enabled us to accelerate xenon ions to the beam energy of 480 MeV, which was the highest for single-end electrostatic accelerators.

As research highlights facilitating TRIAC, a test experiment searching for unbound resonance states in ^{10}Be via ^{8}Li + d reaction, diffusion study of ionic conductors, an R&D experiment searching for the time reversal symmetry break by using spin-polarized ^{8}Li beams were conducted. As development of TRIAC, we injected ^{140}Xe ions into the charge breeding ECR ion source and measured the residual activities in order to understand the elementary process of charge breeding.

In research of nuclear structure, in-beam γ-ray spectroscopy experiments of ^{40}Ar and ^{189}Pt and Coulomb excitation experiments of ^{84}Sr and ^{124}Xe have been made by utilizing the multiple γ-ray detectors, GEMINI-II; a new super-deformed band was found in ^{40}Ar. High-spin states in ^{248,250,252}Cf were identified up to 12^{+} states by using heavy-ion transfer reactions with a high-radioactive Cf target. Excited states in ^{255}No were established for the first time through α-γ spectroscopy of ^{259}Rf produced in the ^{251}Cf(^{12}C,4n)^{259}Rf reaction. The ground-state configuration of ^{259}Rf was also identified.

In research of nuclear reactions, fission fragment mass distribution in ^{30}Si + ^{238}U was measured around the Coulomb barrier. The variation of the mass distribution with bombarding energy shows the nuclear orientation effects of the well-deformed ^{238}U. Fusion-fission cross sections in ^{19}F + ^{209}Bi at sub-barrier energies were determined by a radiochemical method to study sub-barrier fusion hindrance in heavy-mass systems.

In research of nuclear chemistry, the anion-exchange experiment with element 105, dubnium (Db) together with its homologues Nb and Ta has been conducted in HF/HNO_3 solution with the newly developed apparatus AIDA-II. The characteristic anion-exchange behavior of Db at the fluoride ion

concentration [F^-] = 0.003 M was observed. The result clearly demonstrates that the fluoro complex formation of Db is significantly different from that of the group-5 homologue Ta in the 6th period of the periodic table while it is close to that of the lighter homologue Nb in the 5th period.

In research of nuclear theory, a new shell-model interaction was constructed to cover the full sd-pf shell space. Based on it, the non-monotonic change of the shell gap beyond N=28 was interpreted by an interplay between central and tensor forces. A new formulation was carried out for the incomplete and complete fusion cross sections with the CDCC method, and it was applied to ^{7}Li(d,n) and (d,p) reactions. Single-particle structures in the super-heavy region and equation of state of low-density nuclear matter at finite temperature were also investigated.

In research of atomic physics and solid state physics, Coster-Kronig electrons from high-Rydberg states produced in high-energy collisions of Nq+(q=1-3) with He were measured for the first time.

In research of radiation effects in materials, ion-track formation of UO_2 irradiated with high-energy heavy ions was extensively investigated in order to evaluate damage of high-burnup nuclear fuels. Nanometer-size ion-tracks were observed in UO_2 irradiated with 210 MeV Xe, indicating that high-energy fission fragments can form severe damages via formation of ion-tracks.

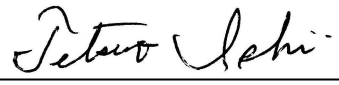

Tetsuro ISHII, Deputy Director, Department of Research Reactor and Tandem Accelerator

Contents

This is a blank page.

目　　次

This is a blank page.

CHAPTER 1

Accelerator Operation and Development

This is a blank page.

1.1 Operation and usage of tandem accelerator and booster

T. Ishii[1], Y. Tsukihashi[1], S. Hanashima[1], S. Abe[1], N. Ishizaki[1], A. Osa[1], H. Tayama[1], M. Matsuda[1], T. Nakanoya[1], H. Kabumoto[1], M. Nakamura[1], K. Kutsukake[1], Y. Otokawa[1] and T. Asozu[1]

The tandem accelerator and booster were operated for experiments from July 14, 2008 to November 12, 2008, and from January 16, 2009 to May 6, 2009. The total operation time of the tandem accelerator for FY2008 (from April 1, 2008 to March 31, 2009) was 210 days and 25 different beams were delivered for experiments. The experimental proposals and the usage of the beam times for FY2008 are summarized in Table 1 and Table 2, respectively.

In FY2008, the in-terminal 14.5-GHz ECR ion source, SUPERNANOGUN, was operated in good condition. We have obtained high-intensity and high-energy heavy-ion beams from this ion source. We accelerated a 0.5 pμA Kr beam of 12+ charge state. We confirmed the acceleration of multiply charged Xe beams up to 30+ , attaining the beam energy of 480 MeV.

Table 1. Experimental Proposals.

Research proposals accepted by the program advisory committee:	
In-house staff proposals	10
Collaboration proposals	44
Number of experiment proposed	54
Total number of scientists participating in research	
from out side	251
in-house	258
Number of institutions presented	35

Table 2. Usage of beam-times in different research fields.

Research field	Beam time (days)	(%)
Nuclear physics	96	45.7
Nuclear chemistry	22	10.5
Atomic and material sciences	66	31.4
Industrial use	7	3.3
Accelerator development	19	9.0
total	210	

Distributions of the terminal voltage and ion species for experiments are shown in Fig. 1 and Fig. 2, respectively. Most of the beams were extracted from three negative ion sources, SNICS-2. The hydrogen beam and multiply charged ion beams of nitrogen, oxygen and rare gases were accelerated from the in-terminal ECR ion source. The ECR ion source was used as much as 31 % of all the beam time.

The super-conducting booster was operated for a total of 17 days to boost the energies of 6 different beams from the tandem accelerator, as is summarized in Table 3. These beams were used for experiments of nuclear physics. Eight resonators out of 40 resonators was treated by a high-pressure water jet spray rinse (HPWR).

[1]Japan Atomic Energy Agency (JAEA)

The ^{7}Li and proton beams were supplied to the TRIAC (Tokai Radioactive Ion Accelerator Complex) experiments for 25 days. The radioactivities of ^{8}Li and ^{142}Ba were ionized and separated by ISOL and injected into the TRIAC.

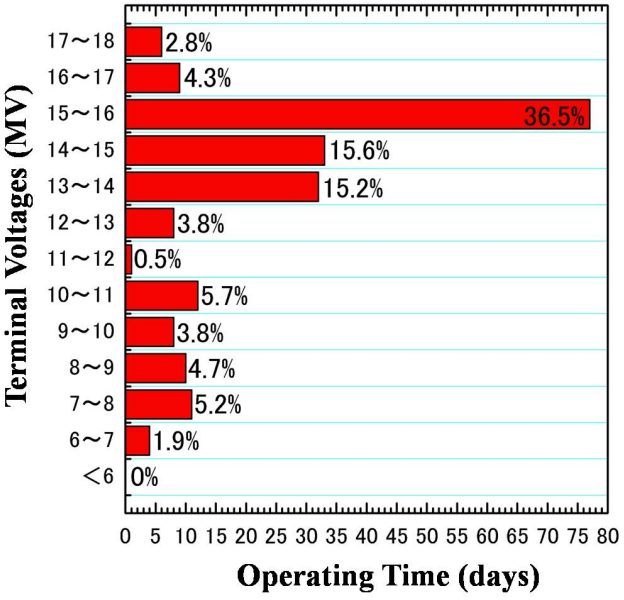

Fig. 1 Distribution of terminal voltages.

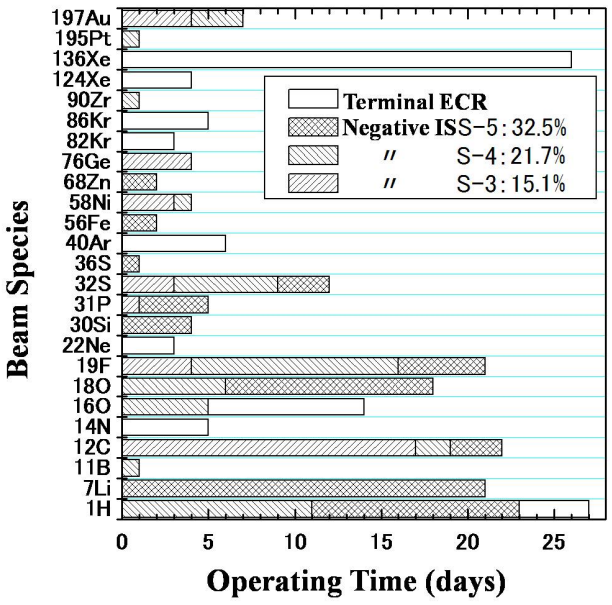

Fig. 2 Distribution of beam species accelerated for experiments.

Table 3. Boosted ion beams for experiments.

Beam species	Boosted energies (MeV)	Beam times (days)
^{58}Ni	360	1
^{68}Zn	374	2
^{82}Kr	380	2
^{86}Kr	383-434 (12 energy points)	3
	392,429,438	1
^{76}Ge	339-383 (30 energy points)	4
^{124}Xe	560	4

1.2 KEK-JAEA joint RNB project

S.C. Jeong on behalf of TRIAC Collaboration[1]

The Tokai Radioactive Ion Accelerator Complex (TRIAC) is operating for nuclear physics and materials science experiments at JAEA-Tokai tandem accelerator facility under collaboration between KEK and JAEA (TRIAC collaboration). Produced by the proton-induced fission reactions of ^{nat}UC, the radioactive ions (RIs) were extracted and mass-separated as singly charged ions by the isotope separator on-line (ISOL) of JAEA. They were charge-bred to higher charge states with a charge-to-mass ratios of about 1/7 using charge breeding electron cyclotron resonance ion source (CB-ECRIS) called as KEKCB. And then, the charge-bred RIs were accelerated by using a series of heavy ion linacs, the split-coaxial radiofrequency quadrupole (SCRFQ) and the inter-digital H (IH) linacs. In FY 2008, radioactive isotope of ^{142}Ba of 1.1 MeV/*A* has been developed for a future experiment. The intensity at the secondary target was several 10^3 particles/sec. Duty factors of the linac complex were increased to 75% from 50% by tuning the cooling water temperature of linacs. The operation with 100% duty factor is under development.

One of the key issues for ISOL-based RI beam facility is development of CB-ECRIS. In particular, we are trying to reduce the background ions produced by the ECR plasma, and to increase the charge breeding efficiencies. For the reduction of the background, we changed all materials which faced to the ECR plasma to a 99% pure aluminum called A1050. However, we could not supply higher voltage than several kV to the plasma chamber as a result of changing the material. It may be attributed to the welding point of the deceleration electrode. Now, we has made a seamless electrode without the welding. The test of the new electrode and plasma chamber will be carried out early in FY2009.

As reported in the last year, we obtained the smaller charge breeding efficiencies for the non-gaseous elements. The charge breeding efficiencies can be regarded as the product of two efficiencies; the capture efficiency by the ECR plasma and the ionization efficiency for step-by-step charge breeding. In general, for the ECRIS the latter efficiency is almost independent from the element. And thus, the difference of charge breeding efficiencies may attribute to the inadequate capture by the ECR plasma. In order to study the capture process, we injected ^{111}In into the ECR plasma, which has a half-life as long as 2.8 days to breed the charge of the ions as usual, and measured the residual activities which have not been extracted as multi-charged ions. We observed three components in azimuthal distribution, 120-degrees periodic distribution, isotropic one, and the anisotropic one as presented in Fig. 1. The latter anisotropy well demonstrated the not-straight injection of the beam. We expect to increase the efficiency by further tuning beam injection. In addition, we observed two peaks along the beam axis for the components with symmetric distribution in azimuthal angle. They were located around the minimum confinement magnetic field and around the extraction anode plate. The latter peak may be reduced by changing the position of the extraction anode. The R&D of the electrode will be performed in FY2009

[1] Corresponding author, N. Imai : High Energy Accelerator Research Organization (KEK)

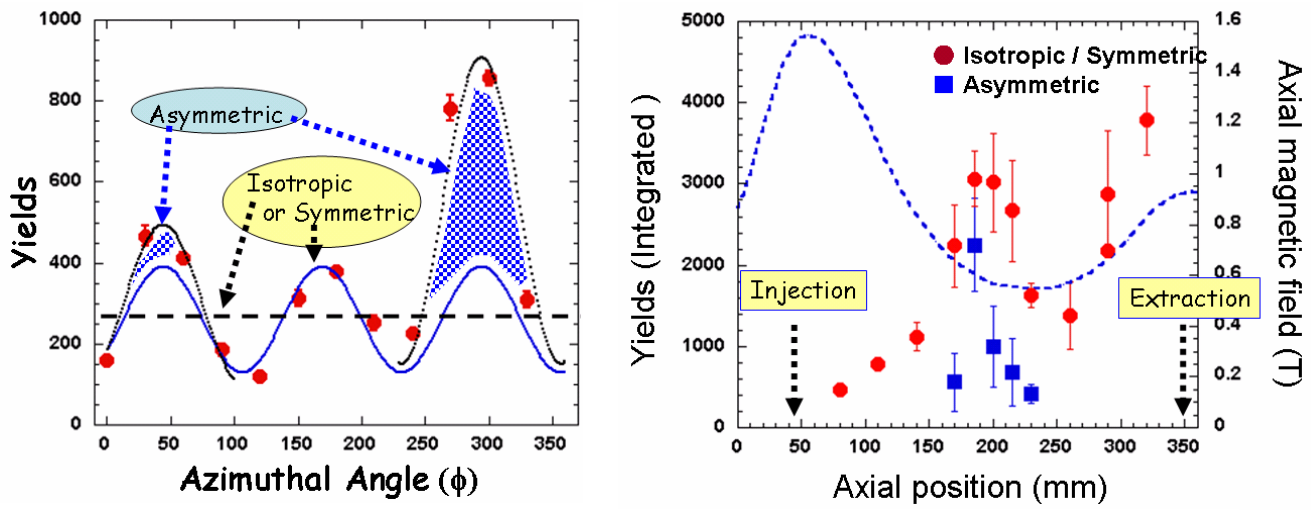

Fig.1 (Left) Azimuthal distribution of residual activities of ^{111}In in the plasma chamber around the minimum magnetic field. Three components, 120 degrees periodic, isotropic, and asymmetric distributions were observed. (Right) Axial distribution of the activities. In the cases of the isotropic and symmetric components, they were centered at the minimum magnetic field and the extraction anode.

Increasing the acceleration energy is highly desired both for the experiments of nuclear reactions and for the further acceleration using the JAEA superconducting linac. Theoretical simulations provided parameter sets to increase the beam energy by changing the amplitude and phases of the respective acceleration tanks of IH linac from the designed values. We attempted to verify the calculation by accelerating the $^{16}O^{4+}$ beam provided from KEKCB. By analyzing the momentum of the beam, we made sure the acceleration up to 1.37 MeV/*A*.

The following experiments were carried out in FY2008 using the RI beams of ^{8}Li from TRIAC: (1) Test experiment searching for the highly excited state in ^{10}Be via ^{8}Li + d reaction (RNB08-J01). (2) Diffusion study of ionic conductors using the short-lived isotopes (RNB08-J03). (3) Search for the time reversal symmetry break by using spin-polarized RI beams (RNB08-K10). Some details of the experiments can be found in this report.

1.3 Development of target-ion source system for the separation of ^{9}Li

A. Osa[1], Y. Otokawa[1] and S. C. Jeong[2]

A short-lived isotope beam, ^{9}Li ($T_{1/2}$=178 ms), is required with intensity of more than 5 x 10^{3} ions/s on the target at the end of TRIAC to the study of highly-excited state of ^{11}Be. In our previous work, we have chosen ^{13}C (^{7}Li, ^{8}Li) neutron transfer reaction by ^{7}Li primary beam and a 99% enriched ^{13}C sintered disk target for the production of ^{8}Li ($T_{1/2}$=838 ms). The 99% enriched ^{13}C thick graphite disk was mounted to the catcher position of the surface ionization type ion source with 3-μm thick tungsten-window. The target was bombarded with a 67-MeV $^{7}Li^{3+}$ beam with intensity of about 100 pnA. In this condition, the separation yield of ^{8}Li was evaluated to be 1 x 10^{6} ions/s. However, the separation yield of ^{9}Li ($T_{1/2}$=178 ms) was observed as few as 10^{2} ions/s.

A release profile of Li from the target/catcher/ion-source system was measured using the heavy ion implantation technique [1]. As shown in Figure 1, the fast component of release time of Li ions from the ^{13}C sintered target was 3.2 s. Decay loss of ^{8}Li and ^{9}Li is calculated by $\exp(-\ln(2)/T_{1/2} \times \tau)$, where $T_{1/2}$ is the half-life of nuclei and τ is the release time. The values are 7.1×10^{-2} for ^{8}Li and 3.9×10^{-6} for ^{9}Li. So, we thought that the long release time caused a significant loss of the ^{9}Li beam intensity.
In a search for high-temperature-resistant target material for the production of ^{9}Li, we found out that boron nitride (BN) has a short release time of Li; as shown in Figure 1, the fast component release time from the 0.25mm^{t} hot pressed BN sheet was 120 ms. The values calculated by above function are improved to 9.1×10^{-1} for ^{8}Li and 6.3×10^{-1} for ^{9}Li.With a hot pressed BN sheet target, we obtained a ^{9}Li beam with an intensity of 10^{4} ions/s after separation by JAEA-ISOL.

We found a thickness dependence of the release time: the values of τ_{fast} are 1.9 s for 0.6 mm^{t} BN and 120 ms for 0.25 mm^{t} BN. If the enhancement of the yield of ^{9}Li depends only on the release time, we should find a thickness dependence in the ratio of ^{9}Li yield to ^{8}Li one . However, the ratio of the yield ^{9}Li/^{8}Li is almost 1/10 for both thicknesses. In this setup, one neutron transfer from ^{11}B to ^{7}Li is a major reaction to produce ^{8}Li. On the other hand, there is some possible channels to produce ^{9}Li; two neutron transfer from ^{11}B to ^{7}Li, two neutron transfer from the tungsten-window to ^{7}Li, two proton removal from ^{11}B, etc. We carry on the development and the search to clarify the mechanism of this target-ion source system.

[1] Japan Atomic Energy Agency (JAEA)
[2] High Energy Accelerator Research Organization

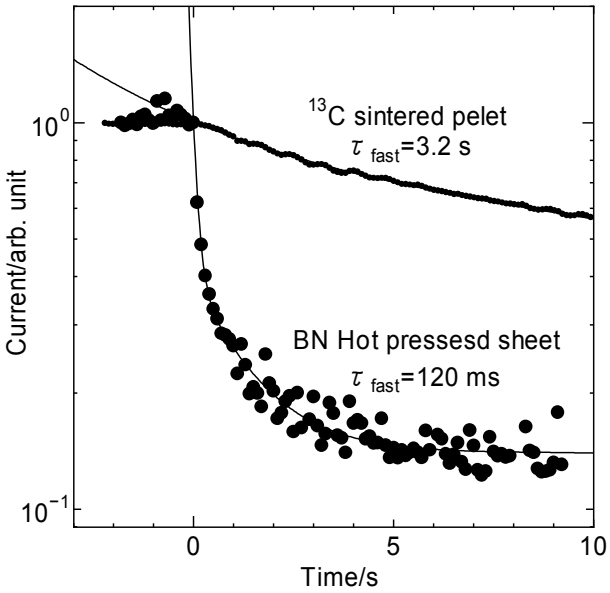

Figure 1. Release profile of Li

References

[1] R. Kirchner, Nucl. Instrum. Methods. B**70** (1992) 186.

1.4 Development of radioactive ion beam production systems for TRIAC

Y. Otokawa[1], A. Osa[1], T. K. Sato[1], M. Matsuda[1], S. Ichikawa[1] and S.C.Jeong[2],

For acceleration of medium-heavy neutron-rich radioactive ion beam (RIB) with Tokai Radioactive Ion Accelerator Complex (TRIAC) [1], two types of ion sources have been installed in an isotope separation on-line at the JAEA (JAEA-ISOL) [2]; a forced electron beam induced arc discharge version-B2 (FEBIAD-B2) type ion source with a target container and a surface ionization type one. With the both ion sources, about 100 isotopes produced in proton-induced fission of ^{238}U have been ionized and mass-separated with separation efficiencies of 0.1%-30%. In addition, radioactive ion beams of ^{123}In ($T_{1/2}$=5.9s), ^{143}Ba ($T_{1/2}$=14.3s) were successfully accelerated to the energy of 0.178MeV/u with TRIAC [2].

For mass separation of short-lived isotopes, it is important that the time interval between production and collection after mass-separation of radioisotopes is kept as short as possible. Unfortunately, the FEBIAD-B2 ion source has relatively long release time for Xe, Kr, In, Sn isotopes and so on. So, we have never mass-separated short-lived Sn isotopes that have half-lives shorter than ~ 1s, due to the nuclear decay losses in the target-ion source.

The release time of isotopes produced inside the target-ion source is governed by diffusion, adsorption-desorption (sticking) and effusion processes. The diffusion time in the target as well as the sticking time on the ion source wall strongly depends on the operation temperature. Thus, to make the release time much shorter, the operation temperature is needed as high as possible. But, the operation temperature of the FEBIAD-B2 ion source is 1550℃. To lessen the nuclear decay losses for short-lived isotopes, we have developed a new target-ion source.

The new target-ion source was modeled after the FEBIAD version-E type ion source which was operated at a temperature between 2000 K and 2300 K [3]. Since in the original design of the ion source it was not capable of loading a several gram uranium-carbide target, we made a few modifications. Schematic view of new ion source system is show in Fig. 1. An external target container with a volume of 0.56cm^3 (ϕ=6mm, L=20mm) to hold uranium carbide inside is connected with a plasma chamber. The target container is heated by electron bombardment from a couple of surrounding tungsten filaments. The temperature at the target was calibrated against the input power by using an optical pyrometer. It turned out that the target was heated to 2000^{o}C at the total input power of 1200W (the target input power of 900W and the anode input power of 300W). Under this condition, ionization efficiency of stable Xe fed by the test leak measured 15%. Also, short-lived isotopes of ^{129}In ($T_{1/2}$=0.61s) and ^{133}Sn ($T_{1/2}$=1.20s) were successfully mass-separated with the strength of 1×10^3 ion/s.

[1] Japan Atomic Energy Agency (JAEA)
[2] High Energy Accelerator Research Organization (KEK)

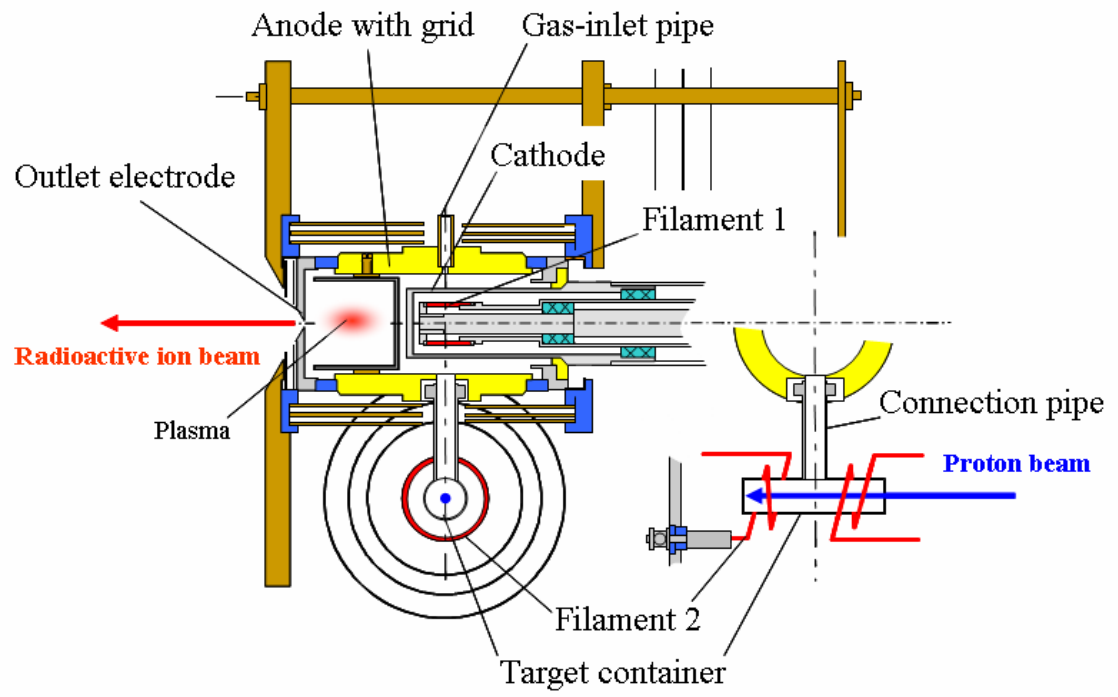

Fig1. Schematic view of new ion source system

References:

[1]. H. Miyatake et al., Nucl. Instr. and Meth.B **204** (2003) 746.

[2] A.Osa et al., Nucl. Instr. and Meth. B **266** (2008) 4394 and B **261** (2007) 1048.

[3] R. Kirchner, K.H. Burkard, W. Hüller, O. Klepper, Nucl. Instr. and Meth. **186** (1981) 295.

1.5 Beam performance of in-terminal ECR ion source injector

M. Matsuda[1], T. Asozu[1] and K. Kutsukake[1]

All permanent magnet type ECR ion source powered with 14.5 GHz RF was installed in the terminal of the tandem accelerator at JAEA-Tokai in order to increase beam intensity, beam energy and beam species. A layout of in-terminal ECR ion source (TECRIS) injector is illustrated in fig. 1. After exchanging a broken circulator at the outlet of RF amplifier, the maximum RF power became 200 W. By the increase of RF power, highly charged intense ion beams could be supplied, which were as intense as the original performance of the ECRIS. The beam intensities of ions from TECRIS are shown in fig. 2. The terminal voltage was 15 or 16 MV and the extracted voltage was 20 or 25 kV. Ions of Ne^{8+}, Ar^{12+}, Kr^{17+} and Xe^{22+} were obtained with beam intensity of 100 pnA or more, the intensities of highly charged heavy ions were increased by a factor of 10 ~ 100 compared with the past. xenon ion energy reached 480MeV which is the world record as a single-end electrostatic accelerator. The intensities of xenon ion beams accelerated at 16MV for their charge state from 5+ to 30+ are shown in fig. 3. These ion beams were accelerated over a wide energy range of 80 ~ 480 MeV. For ions whose charge states were higher than 14+, the extracted voltage was set to 25 kV. For ions with the charge states lower than 13+, the extracted voltage was set to 5 or 10 kV, because the maximum field strength of the 90° injection magnet was not high enough to bend these ions.

A turbo molecular pump (TMP) system has been installed in the high voltage terminal in order to evacuate noble gas when noble gas ions are used. However, in continuous operation for several days, the ion pumps were sometimes instable with noble gas because the terminal TMP was not enough to completely evacuate noble gas. So, it was caused with the remaining noble gas. Two additional pumping stations were installed near the entrance and the exit of the main acceleration tube at outside the SF_6 pressure tank in order to decrease the concentration of noble gas in the beam line. To make the pumping system oil-free, a

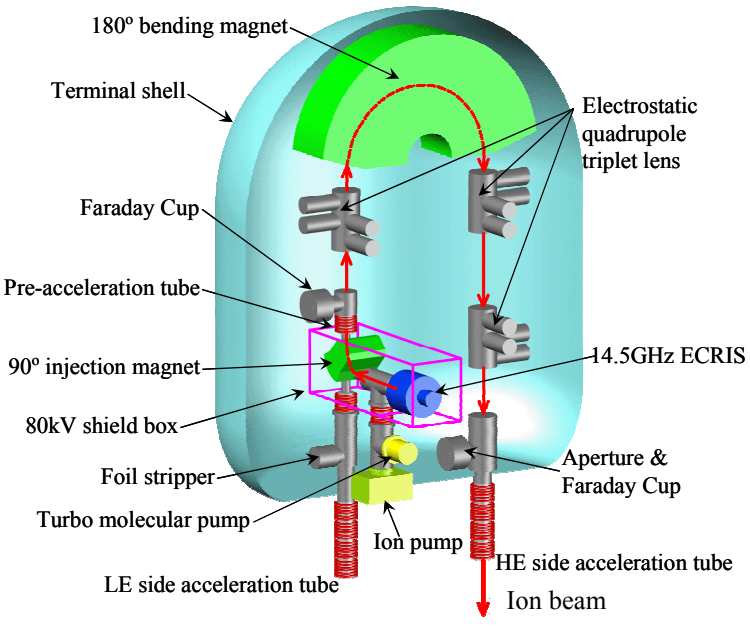

Fig. 1 14.5 GHz TECRIS injector developed for the tandem accelerator. The ion beam generated by the ECRIS is bent with 90° injection magnet and 180° bending magnet, and then accelerated through the main 20 MV acceleration tube toward the earth potential.

[1] Japan Atomic Energy Agency (JAEA)

diaphragm pump was employed for a fore-line pump, and two TMP of 350 L/s and 250 L/s were connected in series in order to obtain the ultra high vaccum. After the installation of these pumping systems, the ion pump instability has hardly occured.

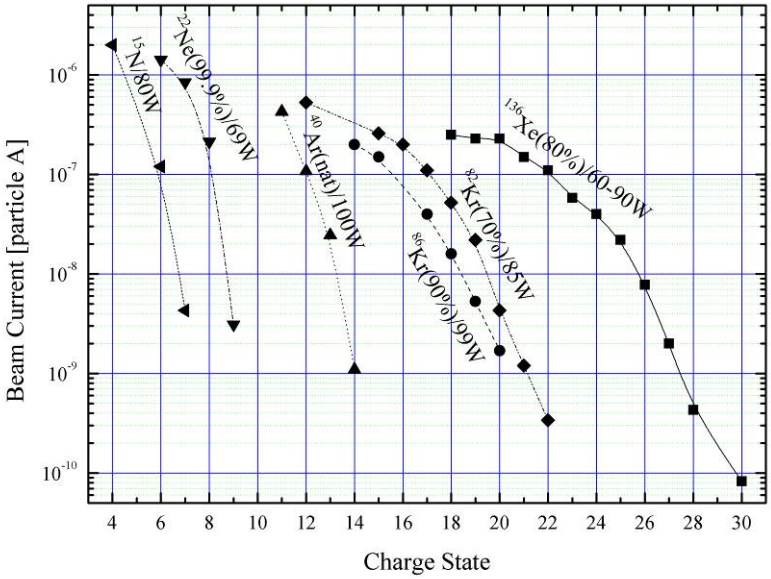

Fig. 2 Charge state distributions of noble gases and nitrogen ions from 14.5 GHz TECRIS injector. Beam intensities were measured at the exit of tandem accelerator.

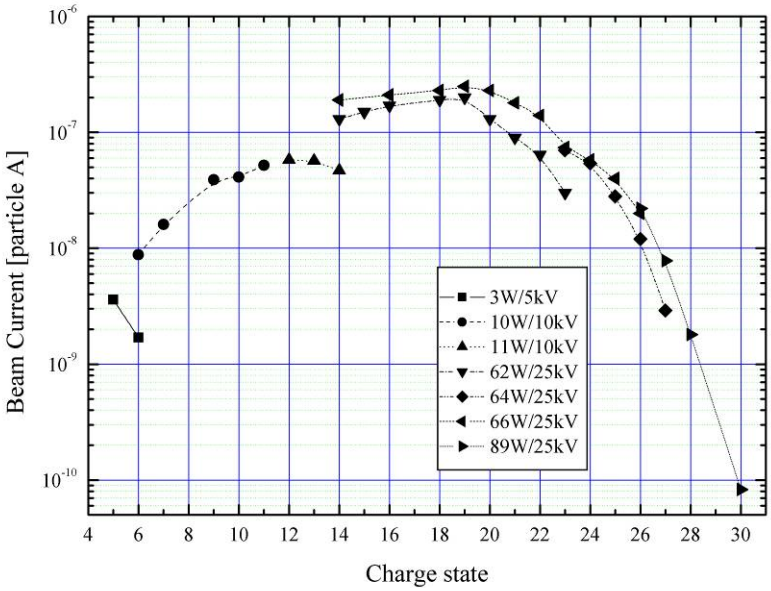

Fig. 3 The intensities of xenon ion beams of the charge state from 5+ to 30+ after the acceleration at 16 MV. The symbols represent different RF power / extraction voltage, shown in the inset.

References

[1] M. Matsuda et al., JAEA-Tokai Tandem Annu. Rep. 2007, JAEA-Review 2008-054 (2008)10-11.

1.6 Improvement of acceleration field gradients of superconducting resonators by high pressure water jet rinsing and anodizing

H. Kabumoto[1], N. Ishizaki[1], T. Yoshida[2], T. Ishiguro[2] and K. Yamaguchi[2]

We have been carrying out a high pressure water jet rinsing (HPWR) to re-condition the superconducting booster since 2006, and have finished 12 resonators of 3 cryostats by 2007 [1, 2]. The HPWR is a technology of removing small contaminations on resonator surfaces, and very effective for the improvement of acceleration field gradients. We applied such a HPWR to two cryostats (No.3 & 5) in 2008. Figure 1 shows the changes of acceleration field gradients (E_{acc}) at an RF power input of 4 W and quality factors (Q_0) at low electric fields before and after the HPWR. In the case of four superconducting resonators (17-20) in cryostat No.5, the acceleration field gradients were improved from 4.6 MV/m to 6.1 MV/m on their average. On the other hand, the acceleration field gradients of the resonators (9-12) in cryostat No.3 did not change very much around 3.5 MV/m on their average.

The difference was caused due to 'hydrogen Q disease' [3]. The quality factors of the cryostat No.3 resonators were around 2.0×10^8 which were very low compared with that of 1.0×10^9 of the cryostat No.5 resonators. Twenty resonators of the first four cryostats of the superconducting booster (cryostat No.1, 2, 3, 4) were fabricated at the early days. At that time, the treatment of niobium surfaces had not been established well, and niobium had absorbed a lot of hydrogen during electro-polishing. Such hydrogen pollution resulted in heavy degradation in the resonator Q-values. It depends not only on the quantity of absorbed hydrogen but also on the time for the resonator temperature to pass through 120 K to 80 K before going down to 4.2 K. Generally, it is thought that niobium hydrate, which is a poor superconductor, will be formed around that temperature.

We examined anodizing with a spare resonator for the purpose of reducing the effect of hydrogen Q disease. Figure 2 shows the result of off-line performance tests before and after the anodizing. Before the oxidation treatment, the resonator Q_0 at a low electric field was 4.4×10^8 at 4.2 K after the fast cooling down process that it took only 1-2 hours to pass the 120-80 K region. On the other hand, the resonator Q_0 was 4.9×10^7 at 4.2 K after the resonator temperature was held at 100 K for 20 hours (simulated as a slow cooling down). This result showed that the resonator had been polluted by hydrogen. We carried out a 40V anodizing treatment using 2 % ammonia solution. The thickness of the oxide surface was estimated about 80 nm. After the oxidation treatment, the resonator Q_0 at a low electric field was improved to 7.7×10^8 in the fast cooling down case, and 1.6×10^8 in the slow cooling down case. We think that oxygen on the niobium surface may bond with hydrogen, and it would be effective against the hydrogen Q disease. We tried mild baking at 120 ℃ for this resonator after the oxidation treatment. But, it resulted in lower resonator Q-values at high fields in the fast cooling down case.

[1] Japan Atomic Energy Agency (JAEA)
[2] ATOX co.,ltd.

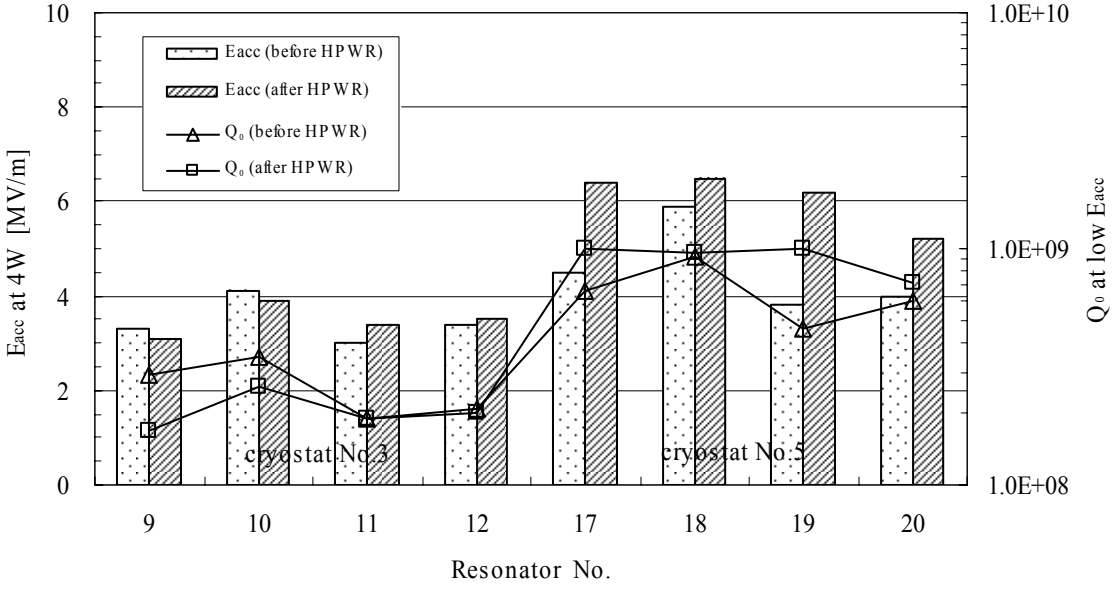

Fig. 1 Acceleration field gradients (E_{acc}) and quality factors (Q_0) before and after the HPWR.

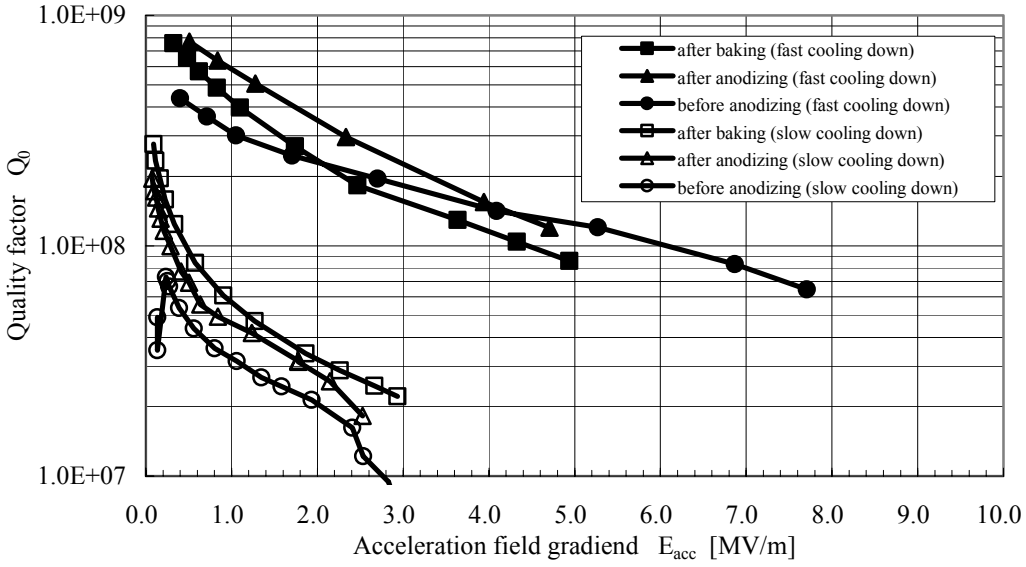

Fig. 2 Q_0-E_{acc} curves before and after the anodizing.

References

[1] H. Kabumoto et al., JAEA-Tokai TANDEM Ann. Rep. 2007, JAEA-Review 2008-054 (2008) 16.

[2] H. Kabumoto et al., JAEA-Tokai TANDEM Ann. Rep. 2006, JAEA-Review 2007-046 (2008) 15-16.

[3] K. Saito and P. Kneisel, Proc. of the 3rd EPAC, Berlin, Germany, (1992) 1231.

1.7 Development of the column voltage measurement system using load cell sensors

K. Kutsukake[1], M. Matsuda[1] and S. Hanashima[1]

The tandem accelerator has the column composed of twenty 1 MV modules. We started to develop a module voltage measurement system for the tandem accelerator column. A trouble that the voltage of the accelerator does not rise as expected is a serious matter to the electrostatic accelerator. It is important to trace the module voltages in case of such a trouble. To solve this problem, we considered to build a measurement system using load cell sensors. The system will make it easy to find the cause of unexpected column trouble, and it is useful for shortening repair time. We are planning to install load cell sensors in every column casting as sketched in Fig. 1. Holes of about 10 cm diameter are open in the column casting. A load cell sensor can be installed in one of the holes of the column casting. A parallel electric field is excited between the column castings. The electrode on the load cell sensor receives the electrostatic force. The distortion of the load cell sensor is converted into an electronic signal, so that every column module voltage can be measured. A calculation model is shown in Fig. 2. The electrostatic force between the electrodes becomes the following,

$$F = \frac{\varepsilon S V^2}{2d^2} \approx 96.58 \times 10^{-15} \cdot V^2 \ \ [N].$$

When the applied voltage of the electrode is 1MV, we obtain

$$F \approx 9.85 \ [gf] \ \ (\because 1 kgf \approx 9.807 \, N).$$

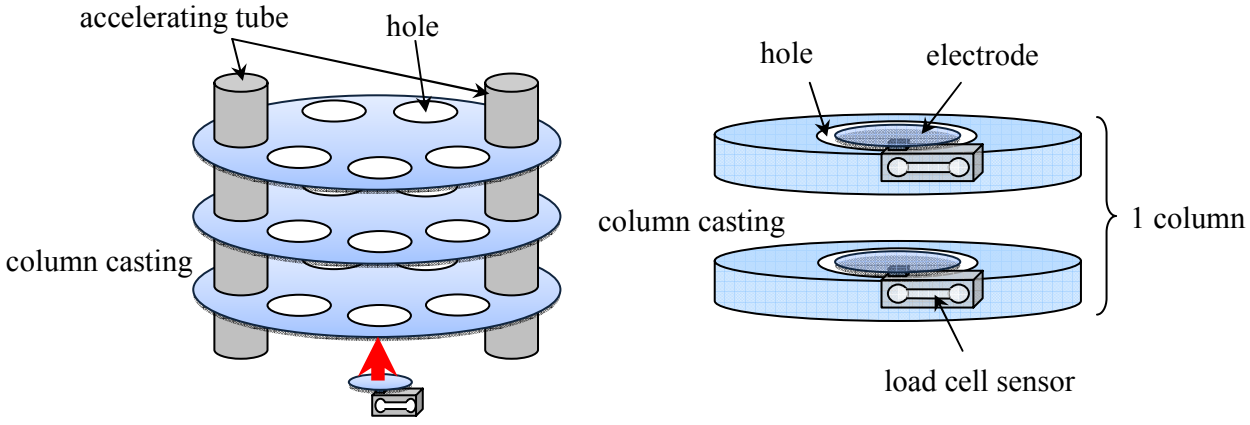

Fig. 1 Installation features of load cell sensors inside tandem accelerator column castings.

[1] Japan Atomic Energy Agency (JAEA)

The result means that the electrostatic force of about 9.85gf pulls each electrode set on the load cell sensor. We tested the road cell sensor by using dummy electrodes. The gap distance d between the dummy electrodes was changed to 0.6, 1.1, 1.9 and 2.5 cm to vary the electric field strength. A load cell sensor of the rated load 300g and a 24kV high-voltage power supply were used in this experiment. The result is shown in Fig. 3. For the actual voltage applied to each column of the tandem accelerator is about 1MV, the electric field gradient of each column is about 1.64MV/m. From the Fig. 3, the column voltage of the tandem accelerator could be measured by using the load cell sensor. The load cell sensor which used for this experiment has enough sensitivity to measure the tandem accelerator column voltage. We are going to install such sensors on all twenty column modules in the near future.

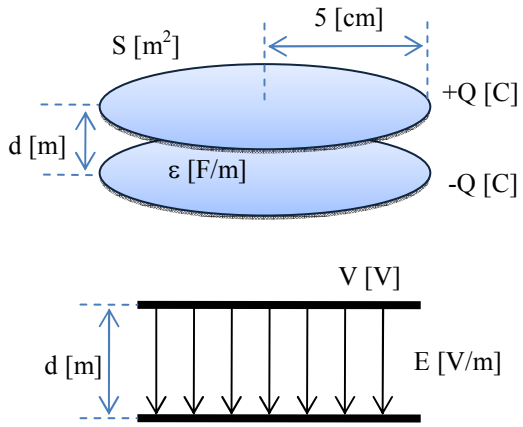

Fig. 2 Calculation model of the sensor electrode set on the tandem accelerator column modules.

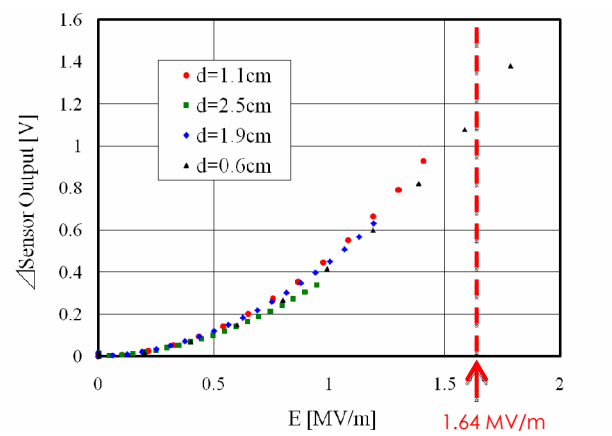

Fig. 3 Output voltage of the road cell sensor as a function of electric field gradient.

1.8 Influence of the median potential in electrostatic steerers on beam optics

T. Asozu[1], M. Matsuda[1]and K. Kutsukake[1]

We use high voltage electrostatic steerers (ES), which have been used for high energy ions in the high voltage terminal, also for low energy ions from the in-terminal injector. Those have been equipped with unipolar DC power supplies to feed high voltages to their electrodes. The voltages of the electrodes, Y_1 and Y_2, are changed keeping the sum of the voltages, $Y_1 + Y_2$, constant as shown in Fig.1. The potential Y_m on the median plane between the electrodes is a half of the sum. So that, an ion beam passing on the plane always feels the potential of V_m. This median potential in the ES affects the beam trajectory as an einzel lens does. Therefore we simulated the beam trajectory with SIMION™.

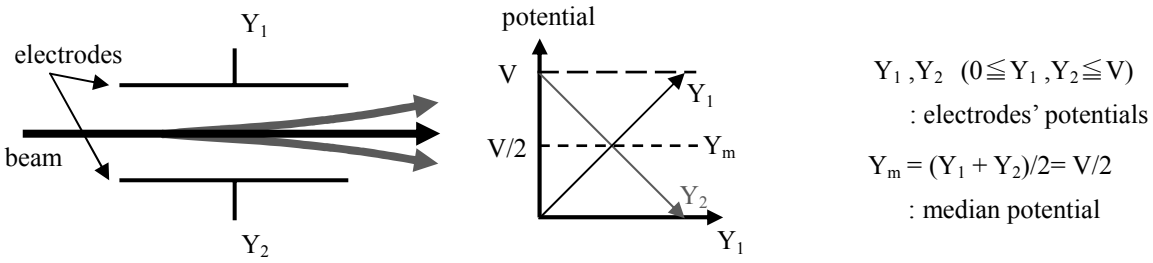

Fig.1 The mechanism of the ES in the terminal.

Figure 2 shows proton beam trajectories by a pair of electrodes at a voltage of 16kV. The incident beam is a 20mm wide beam which contains parallel rays aligned every 1mm on X and Y axis. The rays are 100keV protons for the simulation of a proton beam injected from the terminal ion source. The electrodes are 128mm(Z)×108mm(X) rectangular. The distance between the electrodes is 34 mm.

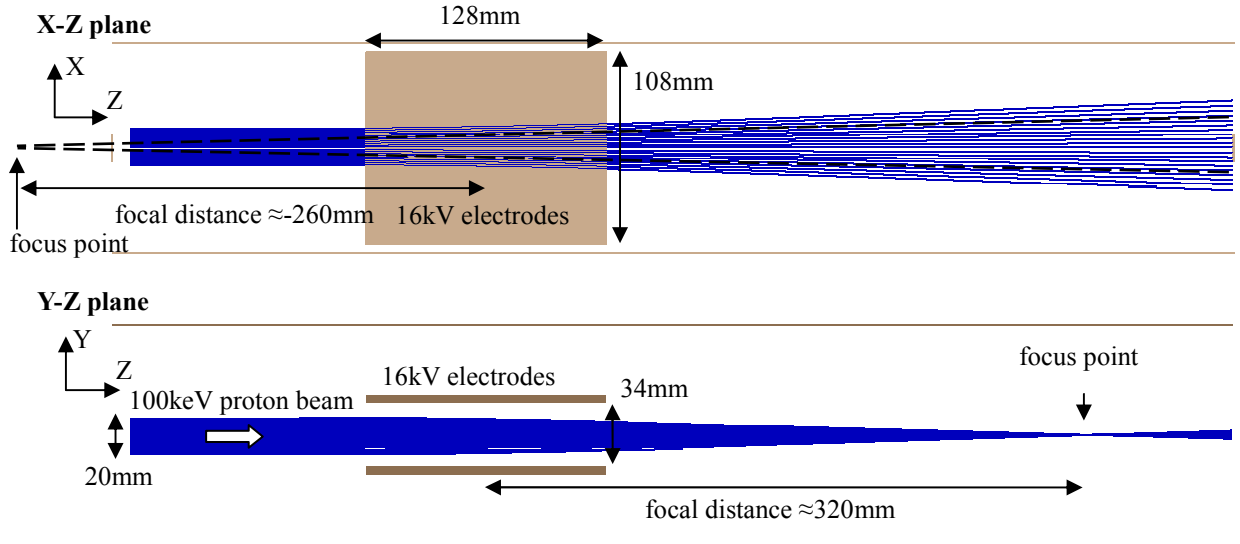

Fig.2 Trajectories of 100keV proton beam for 16kV ES.

[1]Japan Atomic Energy Agency (JAEA)

The beam spreads in the X-Z plane and focuses in the Y-Z plane as shown in Fig.2. The electric field in the ES acts not only as the focusing lens but also as the divergent lens. The X-Z plane shows a diverging effect with focal distance of -260mm and the Y-Z plane shows a focusing effect with focal distance of 320mm. These unnecessary lens effects are as strong as those of the electrostatic quadrupole triplet lenses (EQ) in the terminal. In fact, we have to retune the EQ to keep the most effective transfer for the proton beam.

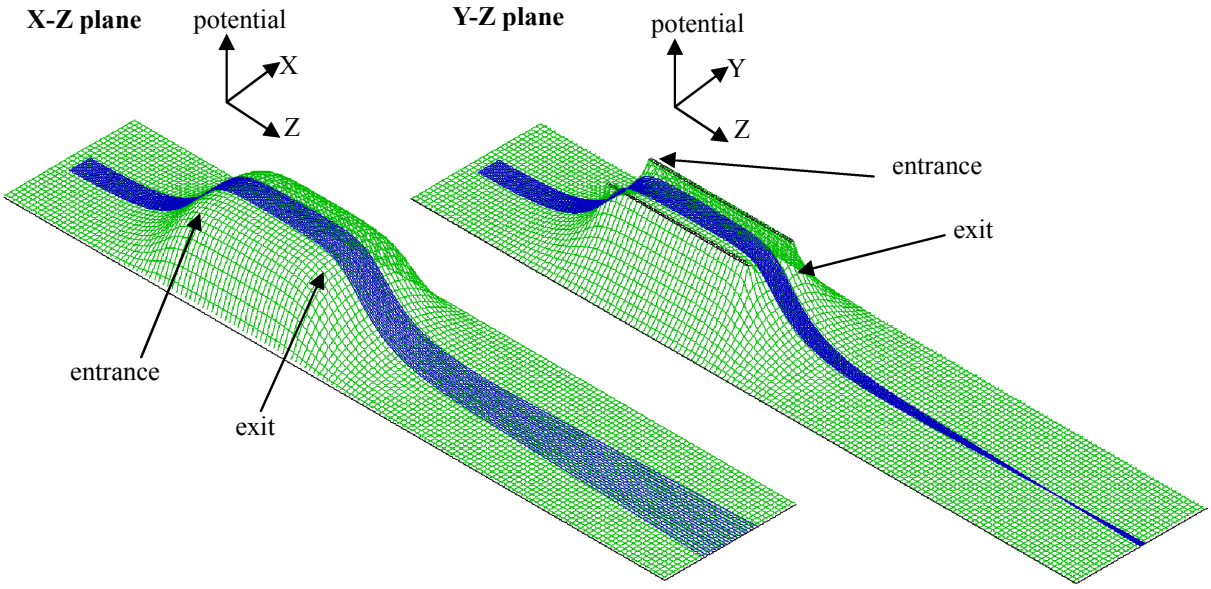

Fig.3 Electrical potentials and beam trajectories.

Figure 3 shows the electrical potentials and beam trajectories of the X-Z plane and the Y-Z plane. In the X-Z plane, the potential shape in X direction is convexly curved at the entrance and exit of the ES. Protons are subjected to outward forces from such potential surface. On the other hand, in the Y-Z plane, the potential shape in Y direction is concavely curved. Protons are subjected to inward forces. Thus, the lens effects of beam trajectories are strong at the entrance and exit of the ES. To reduce the lens effects, we should lower the median potential. We are introducing a multiplying factor circuit to the unipolar DC power supply for the variable tuning of the median potential (see another report by K. Kutsukake *et al.*). Furthermore, a compact bipolar high voltage DC supply is currently under development to install in the terminal.

1.9 Remodeling of electronics for electrostatic steerers

K. Kutsukake[1], M. Matsuda[1], T. Asozu[1] and S. Hanashima[1]

We remodeled the control form of the electrostatic steerer (ES TL-1) power supply. Output characteristics as a function of voltage control (VC) and control form of the electrostatic steerer before remodeling are shown in Fig. 1. Control signal (ES TL-1 Y) is divided into two signals (ES TL-1 Y+ and ES TL-1 Y-) by the mixer, and inputted to high voltage power supplies to give the output voltages as shown in the upper part of Fig. 1. When ion beam pass through the electrostatic steerer without steering, the high voltages applied to the electrostatic steerer electrodes are equal. So, there exists a lens effect on the ion beam. Minimizing the lens effect improves ion-beam transmission. A variable voltage control function, Multiplying Factor (MF), was added after the mixer, and the output became possible to vary as shown in Fig. 2. MF is changed in the range of 0 V to 10 V, and lens effect can be minimized by lowering the applied voltages on the steerer electrodes. Signals (Y+ and Y-) are respectively calculated with the MF signals by multipliers. The control signal voltages of the electrostatic steerer power supply is as follows, (ES TL-1 Y+) = (Y+) (MF) /10, (ES TL-1 Y-) = (Y-) (MF) /10. The multipliers made it possible to vary the high voltage outputs from 0 to the maximum of the high voltage power supply. As a result, the transmission of the ion-beam was improved. Similar remodeling of the control form of electrostatic steerer will be done for other electrostatic steerers.

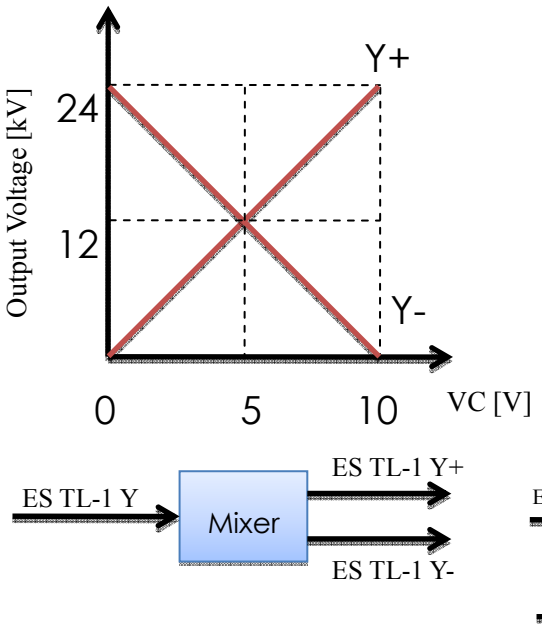

Fig. 1 Output of the control system of ES TL-1 without MF signal.

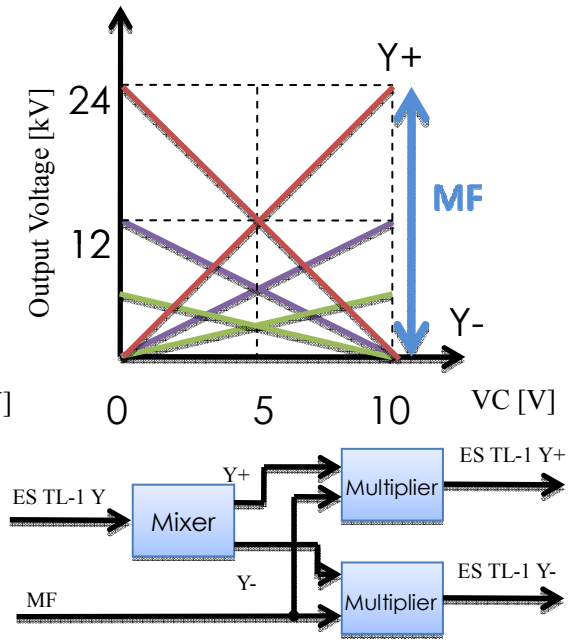

Fig. 2 Output of the control system of ES TL-1 with MF signal.

[1] Japan Atomic Energy Agency (JAEA)

1.10 Replacement of old PCs in the accelerator control system

S. Hanashima[1]

It is difficult to use the same computer for a long time, because of rapid revolution of the hardware and the software. Figure 1 shows a block diagram of the control system used for daily operation of the tandem accelerator. In our system (named as Accell), we use micro processors called Transputers. Until the fiscal year 2007, the oldest PCs and last ones of ours had been used since 1995 and 2000, respectively. Considering about their typical lifetime, it was desired to renew the PCs. In Accell, a core of real time control is a network of the Transputers and some PCs must take communications to Transputers. Those Transputers and its development tools were so old that the manufacturers had discontinued their support long before. For such tools, there were no new replacements that assured their compatibility to

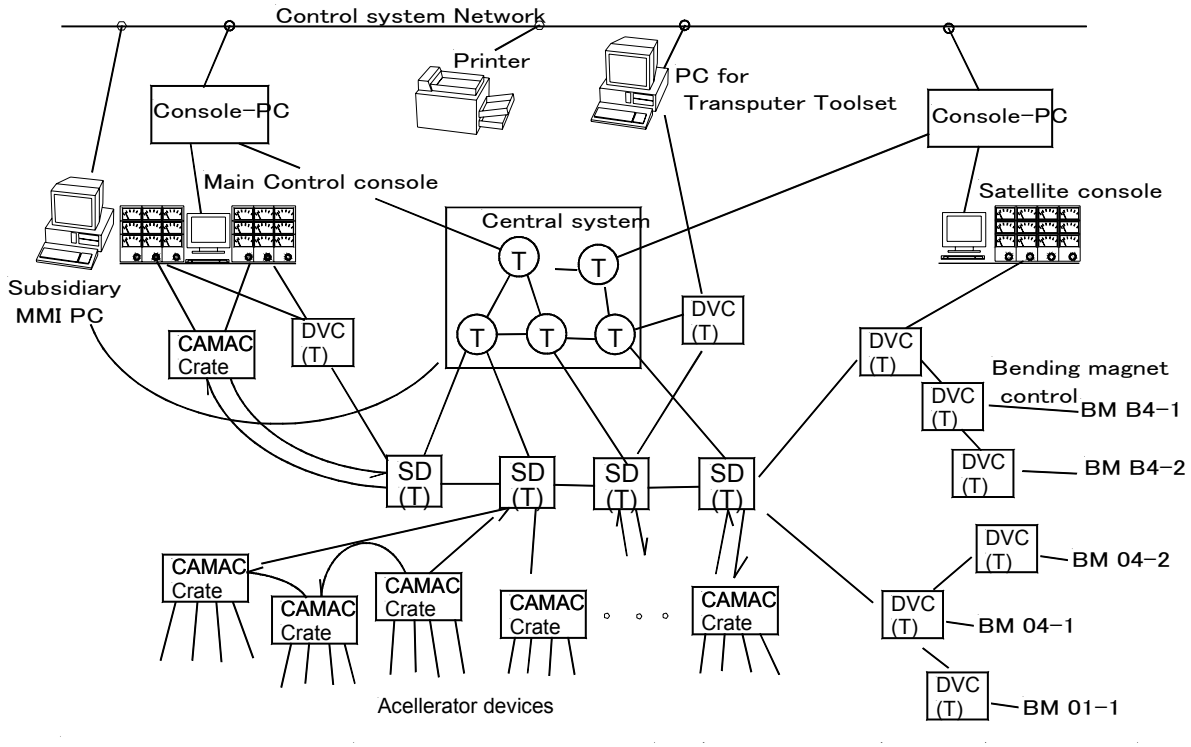

state-of-the-art computers.

Fig. 1 Sub system for daily control of the tandem accelerator

T: Transputer, SD: Serial Highway Driver, DVC: Device controller. There are 4 PCs linked to Transputers.

In Accell, PCs which must have linked to Transputers are divided into two categories. The one is for a development system of the Transputers and the other is for PCs working as man-machine-interface (MMI).

---

[1] Japan Atomic Energy Agency (JAEA)

In 2007, the former was a Windows 95 machine and the later one's operating system was a Windows/NT 4.0. ISA bus is required for both PCs to communicate with Transputers: one could say that it is an outdated PC technology. There is no ISA bus in many commercially available PCs today. Generations of Windows OS have changed also. We thought that it was too expensive to make a new communication method compatible to the Transputers and to their tools on a last operating system. So we searched some newer Windows OS for upward compatibility to the previous tools and/or the previous drivers. And we found that Windows98/SE is still available for the development transputer system and Windows XP professional for MMI PC.

There is a specification called as PICMG 1.0 standard in the field of process control. In the standard, a computer has both ISA bus and PCI bus. A single board computer (SBC) and a passive back plane are used instead of a mother board in the case of usual PC. We selected 2U height passive back plane and single board computer made by Advantech. Seven PICMG computers with Pentium 4 processor, 1 G Byte memory and 160 G Byte HDD were constructed.

For the MMI PC, installation of the OS and applications had gone straight forward. On the other hand, about the computer for the Transputer development system, we needed special configurations instead of default setting. The settings needed were limit values of virtual memory cache size and disk partitioning size. The new computers have been engaging well with the old control system of the tandem accelerator since the end of 2008.

1.11 Improvement of a bending magnet control program in the accelerator control system

S. Hanashima[1]

In our control system, there are 5 bending magnets with function of field feedback control. It has been pointed out here that the feedback action was too slow to efficient use for the beam course switching magnet. One reason of the slowness was a filter parameter used for feedback control. From the point of installation of the power supply of the magnet, it seemed to have an awkward character, by which a fault trip was caused when changing speed of the current was faster than some level. To avoid this phenomenon, the feedback filter had been set at a very slow response. The other reason was poor accuracy of the approximate function of field value vs. current value of the magnet.

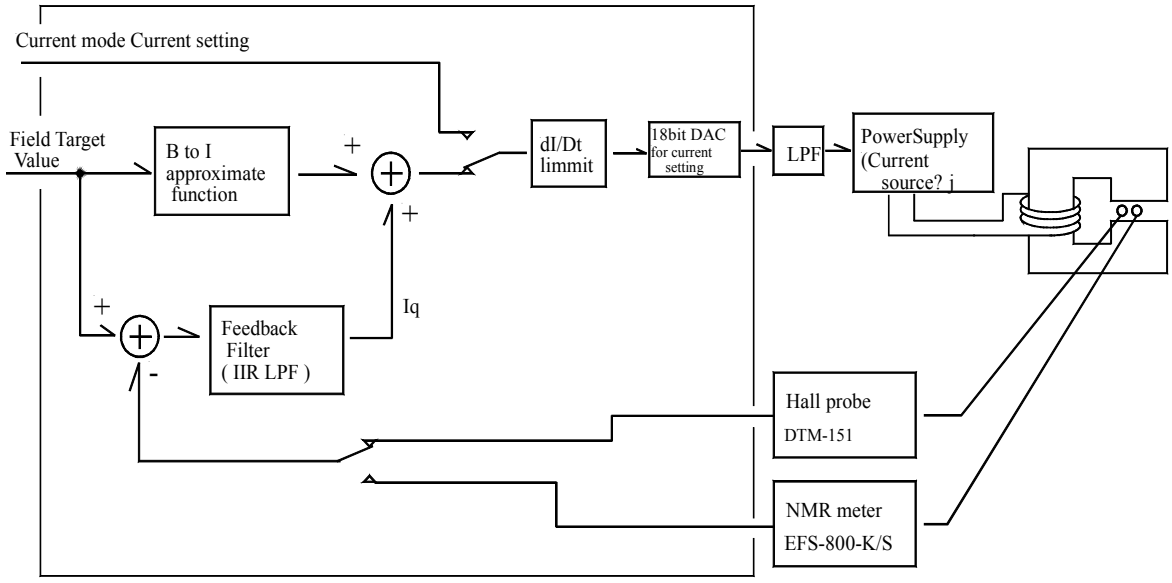

Fig. 1 Diagram of the feedback control for a bending magnet.
The large box shows boundaries of a device controller.

For the problem caused by a fast current change, we found out that a trip signal was generated at a flow sensor of cooling water of the magnet, and the fringing field of the magnet induced the false signal. We put a plate of soft steel at the side of the flow sensor to bypass the fringing field. Since then, we have been able to change the current with varying speed of full scale per 10 seconds without such a trip.

In our method of the feedback control, major part of current setting is calculated by an approximate function from the field target value. Fig. 1 shows a block diagram of the magnet control. The feedback is

[1] Japan Atomic Energy Agency (JAEA)

made on the residual error using measured field value. If the approximation is good, the amount of the feedback is small and fast response of the control is expected. For the approximate function, we had used a function in the form of $I = C1*(1 + C2*B^2)*B$, where I, B, C1 and C2 were the magnet current, the field value and two parameters, respectively. We searched for better formula, where formula is simple and load of calculation is small. After some trials, a function in the form of $I = C1*(1 + (C2*B)^8)*B$ was found to be good for our magnets. In the new form, we can set the parameters that the error is less than about ±0.5% of full scale.

The control program for the magnets was modified to accept the above research results. The filter parameter was also changed to allow faster response. A limiter of current changing rate was set in addition. This combination has enabled both of fast response for a small change of the target value and safety for a large change of the target value.

1.12 Activity of reducing SF_6 gas leakage at the tandem accelerator

T.Nakanoya[1], H.Tayama[1], H.Kabumoto[1], M.Matsuda[1] and Y.Tsukihashi[1]

Tandem accelerator facility uses a large amount of SF_6 gas for electrical insulation. Since SF_6 is regarded as a kind of green house gases that causes global worming, it is strongly required to reduce such gas emission into the atmosphere in recent years. But every year we had to add about 1 to 2 ton of new SF_6 gas. From this fact, a lot of SF_6 gas in the accelerator tank clearly seems to have been leaking into the atmosphere through the gas handling system shown in Fig.1 Reducing such gas leakage is also very important for saving the running cost as well as for environmental consideration. Therefore we estimated the amount of leakage and investigated the sources.

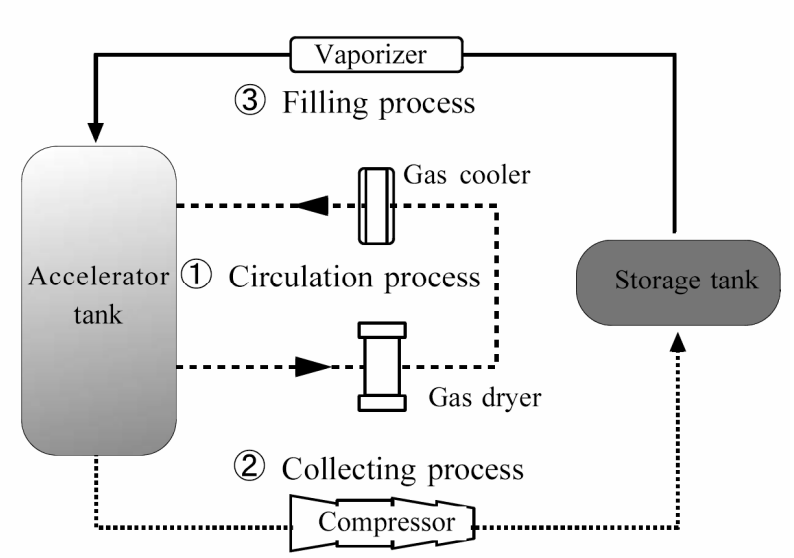

Fig. 1. SF_6 gas handling cycle at the tandem accelerator
The broken line ① shows SF_6 gas circulation during operation periods. Before maintenance periods of accelerator, SF_6 gas is transferred from the accelerator tank to the storage tank by a compressor as shown in ②. After a maintenance period, the accelerator tank is refilled with SF_6 gas through a vaporizer in the line of ③.

We calculated the amount of SF_6 gas lost in FY2008 using the ideal gas equation and day to day maintenance log, and found that about 1700 kg of SF_6 gas had been lost. Figure 2 shows the amounts of estimated lost gas as a function of operation periods in the recent 5 years. About 300 kg of SF_6 gas was wasted regardless of operation periods. It is considered as a loss of residual gas in the collecting process to the storage tank. And, the amounts of lost SF_6 gas mostly increased with increasing accelerator operation

[1] Japan Atomic Energy Agency (JAEA)

period. During the operation periods, SF_6 gas was circulated between accelerator tank and circulation system that consisted of a gas dryer and cooler. There must be leaks from somewhere in the accelerator tank or circulation system. Therefore, we carried out a leak search using a mobile SF_6 gas detector. For improving the leak detection sensitivity, we completely covered flanges with plastic bag and waited several hours to measure as shown in Figure 3. Using this method, we could detect small leaks which had not been found by in situ measurement. As a result, we detected some leak spots at two view port flanges, two of gondola wire flanges, center rod of corona probe components and Capacitor Pick Off (CPO) flange. We did not find any other leak part in the circulation system.

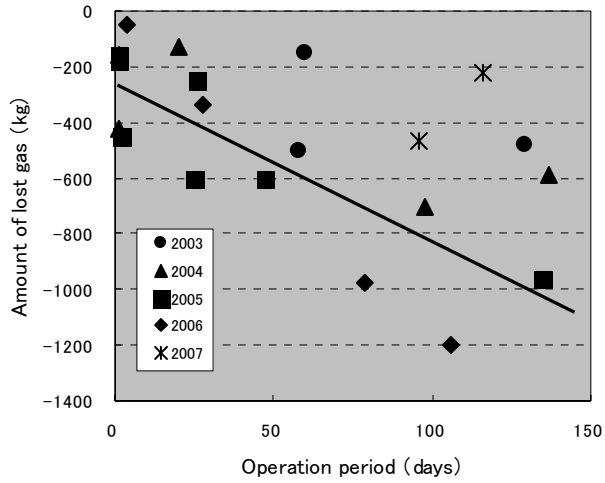

Fig. 2. The amount of lost SF_6 gas as a function of operation periods
The line is an eye-guide.

Fig. 3. Collecting leaking SF_6 gas in a plastic bag for searching leak spots.

In a maintenance period, these leaking parts were taken apart and checked up. Flat plastic gaskets had been used for view port flanges. Loss of their elasticity and shortage of sealing pressure were considered as the causes of the leak. We replaced them with new O-ring gasket to improve air-tightness. The gondola wire flanges were sealed by O-ring gaskets, but flange surfaces had rusted and been stained by wire grease. We cleaned up the surface and scraped the rust off. With the corona probe, an O-ring pressing screw used for sealing the movable center rod was loose. We re-tightened the screw and cleaned up the sealing surface of movable rod. With the CPO electrode, a current read out feed-though had a screw part which was wound with seal tape and screwed into a flange. The tape had been thinned by repetition of loosening and tightening the screw. We re-bandaged the screw thick enough with seal tape. We examined those repaired parts by pressurizing them with SF_6. Any leak of SF_6 was not detected. We will continue the leak search and reduce the SF_6 gas leakage.

This is a blank page.

CHAPTER 2

Nuclear Structure

This is a blank page.

2.1 Spectroscopy of ^{108}Ag via neutron transfer reactions

J. J. Carroll[1], T. Shizuma[2], T. Ishii[2], G. P. Trees[1], N. Caldwell[1], I. Mills[1], T. Harle[1],
H. Makii[2], R. Takahashi[2], D. Nagae[2], T. Hayakawa[2], E. Ideguchi[3],
P. M. Walker[4], S. A. Karamian[5] and R. S. Chakrawarthy[1]

The odd-odd nucleus ^{108}Ag has been suggested to provide tests of different physical processes. Doublet bands have been recently identified in ^{105}Ag [1] whose properties suggest a chiral origin. It was proposed in that work that ^{108,109}Ag nuclei might evidence similar chiral doublets or, by their absence, indicate that silver lies on the border for this behavior. In contrast, a different mechanism has been proposed to explain the appearance of $\Delta I = 1$ doublet bands in odd-odd nuclei with A ~ 130 due to coupling of $\nu h_{11/2} \times \pi h_{11/2}$ orbitals. This mechanism has been referred to as the "chopsticks" mode based on a pictorial description of the coupling of angular momenta that may provide doublet bands [2]. The prediction is that the B(M1;I→I-1)/B(E2;I→I-2) ratio for interband transitions between doublet bands will allow a resolution of which model (chiral or "chopsticks" mode) is responsible for those bands. A doublet band structure has already been identified for ^{108}Ag [3] based on coupling between $\nu h_{11/2} \times \pi g_{9/2}$ orbitals, but those data did not support evaluation of this question.

A long-lived isomeric state exists in ^{108}Ag, having an excitation energy of 110 keV and a half-life of 418 years. It has been suggested [4] that such isomers might find practical applications in high-energy-density batteries if a means could be found by which to artificially induce their depletion. For ^{108}Ag, the available nuclear data [3] suggest that a level at 366 keV provides decay branches to the isomer and toward the ground state, as shown in Fig. 1. Thus, this higher-lying state may serve as a "depletion level" and its excitation from the isomer could initiate an energy-releasing process. The branching ratios from the 364 keV state are unknown from previous work.

An experiment was performed at the tandem accelerator facility, JAEA, Tokai during August 2008. A beam of ^{18}O ions with an energy of 135 MeV was incident on a self-supporting target of enriched ^{107}Ag in which a variety of reactions were induced. Among those were one neutron transfer reactions that produced ^{108}Ag in an excited state and corresponding to scattered projectiles of ^{17}O. The identification of scattered projectiles was accomplished by four surface-barrier Si ΔE-E detectors. Seven HPGe

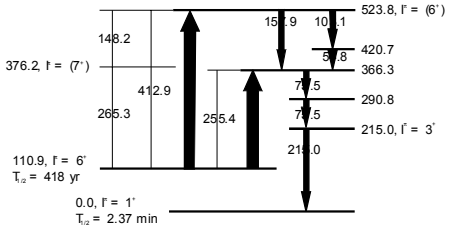

Fig. 1 Partial level scheme adapted from [3], showing potential depletion transitions for ^{108m}Ag.

[1] Youngstown State University, USA
[2] Japan Atomic Energy Agency (JAEA)
[3] University of Tokyo
[4] University of Surry, UK
[5] Joint Institute for Nuclear Research, Russia

detectors were arranged to detect gamma rays emitted in coincidence with particles registering in the Si detectors. Thus, selection of the events within to the “banana” gate filtered the entire body of data obtained during ~ 70 hours of irradiation to focus on the ^{107}Ag(^{18}O, ^{17}O)^{108}Ag reaction.

Detailed data analysis is underway, but already some new information appears in preliminary analysis of the gamma rays emitted during decay of excited states of ^{108}Ag. The incident beam axis and the direction of the scattered projectile define the reaction plane, and a comparison of the numbers of gamma rays emitted to HPGe detectors within (I_γ^{in}) and perpendicular (I_γ^{out}) to the reaction plane provide useful information. Specifically, a value of the ratio $I_\gamma^{in}/I_\gamma^{out} < 1$ identifies that gamma ray with a dipole transition, while a value $I_\gamma^{in}/I_\gamma^{out} > 1$ corresponds to a quadrupole transition. Evaluation of these ratios indicates that the 215 keV transition in Fig. 1 is of quadrupole character, confirming that the 215 keV state has an angular momentum of 3. Likewise, the two transitions with energies near 75 keV in Fig. 1 are identified as being of dipole character, leading to a first identification of their angular momenta. These results already provide new insight into the question of induced depletion of the ^{108}Ag isomer, while detailed analysis of the entire data continues. Of course, other reactions, including Coulomb excitation of ^{107}Ag, are contained within the total data set.

References

[1] J. Timár, N. Pietralla, G. Rainovski, et al., Phys Rev. C **76**, 024307 (2007).
[2] K. Higashiyama, N. Yoshinaga, and K. Tanabe, Phys. Rev. C **72**, 024315 (2005).
[3] F. R. Espinoza-Quiñones, E. W. Cybulska, G. R. Emediato, et al., Phys Rev. C **52**, 104 (1995).
[4] J. J. Carroll, S. A. Karamian, L. A. Rivlin, et al., Hyperfine Int. **135**, 3 (2001).

2.2 Shape coexistence in ^{189}Pt

X.H. Zhou[1], W. Hua[1], Y.H. Zhang[1], M. Oshima[2], Y. Toh[2], M. Koizumi[2], H. Harada[2], K. Furutaka[2], F. Kitatani[2], S. Nakamura[2], Y. Hatsukawa[2], M. Ohta[2], K. Hara[2], T. Kin[2] and M. Sugawara[3]

The neutron-deficient Pt-Hg nuclei are well known to exhibit shape coexistence phenomenon, and this has provided the motivation for extensive studies both experimentally and theoretically [1]. Different structures associated with prolate, oblate, and tri−axial shapes within the same nucleus have been identified experimentally [1]. Due to the pronounced transitional character, the nucleus ^{189}Pt would be rather soft with respect to β and γ deformations, and the shape-polarizing effects arising from valence nucleons might be significant. It is our primary aim to extend the level scheme of ^{189}Pt to high-spin states, and to study the shape coexistence phenomenon.

High-spin states in ^{189}Pt have been investigated using the ^{176}Yb(^{18}O, 5n) reaction at beam energies of 88 MeV and 95 MeV. The ^{18}O beam was provided by the tandem accelerator at JAEA. The target was an isotopically enriched ^{176}Yb metallic foil of 2.1 mg/cm^2 thickness with a 7.6 mg/cm^2 Pb backing. The GEMINI-II [2] γ-ray detector array was employed to detect the in-beam γ rays. A total of 220×10^6 γ-γ coincidence events were recorded. A complicated level scheme was established for ^{189}Pt and presented in Fig. 1. The level scheme of ^{189}Pt known in the previous work [3,4] was extended greatly to high spin states. Positions of the observed transitions in the level scheme were determined by the γ-γ coincidence relationships, γ–ray relative intensities, and γ–ray energy sums.

A revised particle-rotor model (PRM), which can treat rotational band based on multi-quasiparticle configuration, was developed recently [5]. This model was used to interpret the band structure in ^{189}Pt. Rotational band built on the $\nu i_{13/2}^{-1}$ configuration has been observed systematically in the neighboring odd-A Pt-Hg nuclei, and we propose band 1 is associated with the $\nu i_{13/2}^{-1}$ configuration. Supposing a $\gamma\sim30^o$ rotational core, the level energy and signature splitting of band 1 can be well reproduced by PRM calculations. By analyzing the main components of wave function, it is suggested that band 1 is mainly associated with the 11/2[615] configuration. Considering the possible Nilsson orbits near the Fermi surface, the $\nu f_{5/2}(p_{3/2})$ and $\nu i_{13/2}^{-2}\nu f_{5/2}(p_{3/2})$ configurations may be assigned to band 2 and structure 1, respectively. The configuration assignments are supported by PRM calculations when they are prolate and oblate deformed, respectively. The two cascades in structure 1 have similar level spacing and they might be associated with the $\nu i_{13/2}^{-2}\nu f_{5/2}(p_{3/2})$ configurations. The calculations indicate that the low-j components in the configurations are either 5/2[503] or 3/2[501], whose quantum numbers satisfy the characteristic of pseudo-Nilsson orbits [6]. Therefore, we suggest the two rotational bands in structure 1 to be a pair of pseudo-spin partner.

[1] Institute of Modern Physics, Chinese Academy of Sciences
[2] Japan Atomic Energy Agency (JAEA)
[3] Chiba Institute of Technology

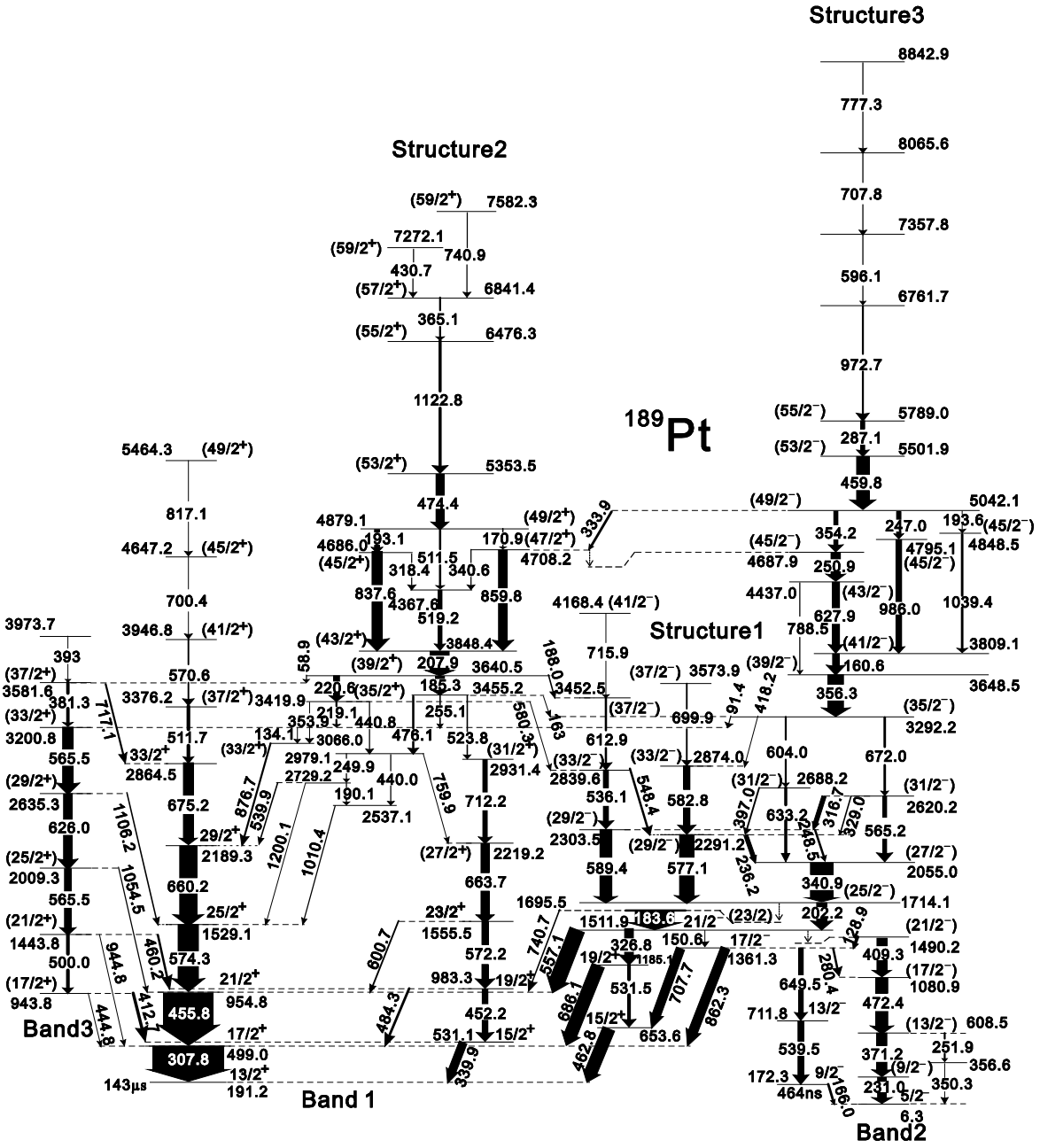

Fig. 1 Level scheme of ^{189}Pt established in the present work.

Acknowledgement: This work was performed under the Common-Use Facility Program of JAEA.

References

[1] X. H. Zhou et al., Phys. Rev. C75 (2007) 034314.

[2] M. Oshima et al., J. Radioanal. Nucl. Chem., 278 (2008) 257-262.

[3] S. C. Wu et al., Nuclear Data Sheets 100 (2003) 1-140.

[4] M. Piiparinen et al., Phys. Rev. Lett. 34 (1975) 1110-1113.

[5] S. Q. Zhang et al., Phys. Rev. C75 (2007) 044307.

[6] A. E. Stuchbery et al., J. Phys. G: Nucl. Part. Phys. 25 (1999) 611-616.

2.3 Decay study on fission products with on-line isotope separator

M. Shibata[1], M. Asai[2], A. Osa[2], M. Oshima[2], A. Kimura[2], M. Koizumi[2] and T. K. Sato[2]

Beta-decay energy (Q_β) measurement is one of the precise methods to determine atomic masses and it is also important for evaluation of the decay heat of the nuclear power plants in nuclear engineering. Based on the previous studies with the total absorption detectors [1-3], another total absorption detector which is composed of a clover detector and BGO Compton suppressors have been developed [4]. In this year, in order to determine the energy loss of the detector to higher energy region, the Q_β to 10 MeV were measured, and successively, those of neutron-rich Eu isotopes, which were recently identified, were measured.

Uranium carbide (UC_2) target containing 670 mg/cm^2 of ^{238}U was bombarded with 32 MeV proton beams generated by the TANDEM accelerator at JAEA with the intensity of about 100-600 nA. The radioactive ion beams were implanted into thin Mylar tape controlled by a computer. With the clover detector, singles spectrum and coincidence spectrum with the BGO detectors were measured simultaneously for each nucleus [4]. At the beginning, the $^{91\text{-}94}$Rb and $^{140\text{-}142}$Cs isotopes were measured after separating from other fission products by using an on-line isotope separator (Tokai-ISOL). The Q_βs and half-lives for the nuclei are between 5.2 and 10.2 MeV, and between 2 and 60 s, respectively. Next, the Q_βs of two Europium isotopes: ^{162,164}Eu were measured. The measurements were continued to obtain sufficient statistics for every nucleus, over 15 hours for each Eu isotope. The counting rate was always kept lower than 2 kcps to reduce pulse pile-up. The total absorption event were extracted by subtracting the coincidence spectra by multiplied a factor of 1.25 from the singles one. The analytical procedure was described in the last report [4].

As shown in Fig.1, the effective energy loss of the detector was determined to 200(20) keV to 8.2 MeV. The energy loss value slightly depends on the analysis using the response function, nevertheless, the uncertainty of the energy loss was almost 20 keV. However, it was found the energy loss for ^{94}Rb (Q_β=10.3MeV) was larger than the others, and much precise analysis including the response function is needed. Next, Figure 2 shows the measured spectra of $^{162,\ 164}$Eu, and the preliminary result of folding analysis. The adopted regions for the analysis were shown as the regions of interest (ROI). The folded spectra fit well to the experimental spectra in the ROIs, those are 4200-5200 keV and 5000-6000 keV for ^{162}Eu and ^{164}Eu, respectively. To check the analysis, deduced Q_β with folding analysis were changed ±50keV that are shown in dotted and broken curves in downside of Fig.2. These differences do not have influence on the final results. Preliminary results of 5571(20) for ^{162}Eu and 6382(75) keV for ^{164}Eu, ^{164}Eu is recently identified as a new isotope [2], are in agreement with the previously measured values with another detector within the uncertainties (5575(60) and 6430(70) keV, respectively)[2]. The result in ^{164}Eu still has larger uncertainty owing to less statistics, nevertheless, it is probably expected to have much statistics with much intense proton beam. In conclusion, the newly developed total absorption detector can measure

[1] Nagoya University
[2] Japan Atomic Energy Agency(JAEA)

Q_β up to 8 MeV with systematic uncertainty of 20 keV. For much higher Q_β, additional considerations are needed. In addition, as shown the spectrum for ^{162}Eu in Fig.2, γ-rays are observed in higher energy than 3 MeV. It means the detector is also expected to identify the level structure up to high energy region. The level schemes of the Eu isotopes are also under construction.

Present study is the result of "Study on nuclear data by using a high intensity pulsed neutron source for advanced nuclear system" entrusted to Hokkaido University by the Ministry of Education, Culture, Sports, Science and Technology of Japan (MEXT).

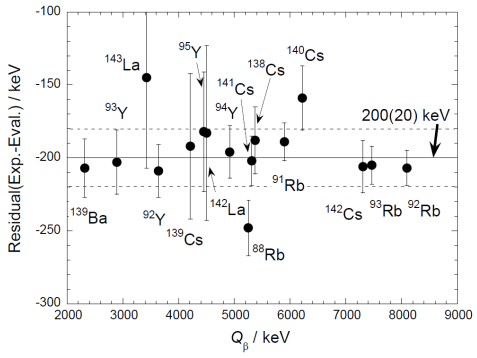

Fig.1 Effective energy loss of the total absorption detector. The results of $^{91\text{-}93}$Rb and $^{140\text{-}142}$Cs were deduced in this experiments. The ^{94}Rb are excluded.(see the text) The others were previously reported in ref .4.

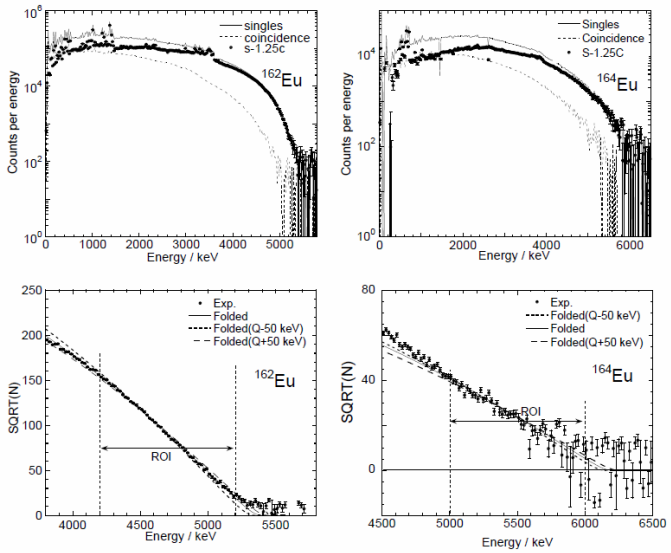

Fig.2 Measured spectra of neutron-rich ^{162,164}Eu isotopes (upside) and the results of folding analysis (downside).

References

[1] M. Shibata et al., J. Phys. Soc. Japan. 71 (2002) 1401-1402.

[2] H. Hayashi et al., Euro. Phys. J. A 34 (2007) 363-370.

[3] H. Hayashi et al., Nucl. Inst. and Methods in Phys. Res. A 606(2009) 484-489.

[4] M. Shibata, et al., JAEA-Tokai Tandem Ann. Rep. 2007, JAEA-Review 2008-054(2008)42-43.

[5] G. Audi et al., Nucl. Phys. A 729 (2003) 337-676.

2.4 Coulomb excitation experiments of ^{124}Xe

M. Koizumi[1], Y. Toh[1], M. Oshima[1], A. Kimura[1], Y. Hatsukawa[1], K. Furutaka[1],
H. Harada[1], F. Kitatani[1], S. Nakamura[1] and M. Sugawara[2]

Being located in a transitional region, Xe isotopes gradually change their properties from a γ-unstable rotational character (A ~ 124) to a vibrational (A = 134). In terms of dynamic symmetry of IBM, the change is considered as a shape phase transition from O(6) to U(5) symmetry. Theoretical calculations suggested that the E(5) critical point of the shape phase transition would appear at around A = 130 in Xe isotopes [1,2]. To understand the characters of those nuclei, information on electromagnetic properties such as B(E2)s and quadrupole moments is required.

Coulomb excitation is a useful method for measurements of electromagnetic properties near ground states of nuclei [3,4]. Our systematic study revealed nuclear properties and evolutions of structures of stable nuclei with A ~ 70 [5-12]. To obtain electromagnetic properties of Xe isotopes, we have started systematic study with a Coulomb excitation technique.

Coulomb excitation experiments with ^{124}Xe beams were carried out. The energies of ^{124}Xe beams were 385 MeV and 560 MeV; the beam currents were about 0.5 pnA in both experiments. Coulomb excitation of ^{12}C(^{124}Xe, γ) was investigated with the 385-MeV beam, and that of ^{208}Pb(^{124}Xe, γ) was investigated with the 560-MeV beam; the both beam energies do not exceed the Coulomb barrier. The target thicknesses of carbon and ^{208}Pb were 500 μm and 0.9 μm (1 mg/cm^2), respectively. The γ-ray detector array, GEMINI-II

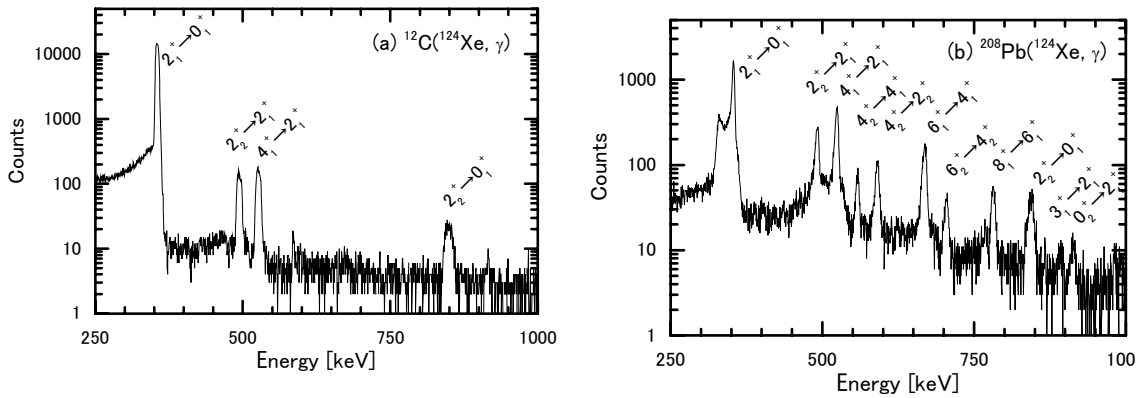

Fig. 1. Doppler-corrected particle-γ coincidence spectra measured with a Ge detector placed at 105^o to the beam direction. (a) A spectrum obtained in a ^{12}C(^{124}Xe, γ) reaction. (b) A spectrum obtained in a ^{208}Pb(^{124}Xe, γ) reaction; the peak at the left shoulder of the $2_1^+ \rightarrow 0_1^+$ transition is a background peak, which will be suppressed in further analysis.

[1] Japan Atomic Energy Agency (JAEA)
[2] Chiba Institute of Technology

[13], was used to detect de-excitation γ-rays, and the particle detector array, LUNA [14], was used to detect recoiled or scattered particles. Particle-γ coincidence events were recorded event by event. Totally, about 2×10^7 events and about 9×10^7 events were obtained in the $^{12}C(^{124}Xe, \gamma)$ experiment and in the $^{208}Pb(^{124}Xe, \gamma)$ experiment, respectively.

Figure 1 shows Doppler-corrected γ spectra. Since in the $^{12}C(^{124}Xe, \gamma)$ reaction the scattering angles of ^{124}Xe are limited to less than 10 degrees, positions of recoiled carbon particles were used for Doppler correction. In the $^{208}Pb(^{124}Xe, \gamma)$ experiment, positions of scattered ^{124}Xe particles were used for Doppler correction. Four and eleven de-excitation γ-rays were observed in the $^{12}C(^{124}Xe, \gamma)$ experiment and in the $^{208}Pb(^{124}Xe, \gamma)$ experiment, respectively. Identifications of the observed peaks are shown in Fig. 1. In the $^{12}C(^{124}Xe, \gamma)$ Coulomb excitation experiment, ^{124}Xe was excited up to the 4_1^+ and 2_2^+ states. In the $^{208}Pb(^{124}Xe, \gamma)$ experiment, ^{124}Xe was excited up to the 10_1^+ and 6_2^+ states; the excitation energy of the 10_1^+ and 6_2^+ states are 2331 keV and 2143 keV, respectively. In addition, $3_1^+ \rightarrow 2_1^+$ and $0_2^+ \rightarrow 2_1^+$ γ-rays were also observed in the $^{208}Pb(^{124}Xe, \gamma)$ spectra. Analysis of the experimental data is in progress. B(E2) values and quadrupole moments will be deduced with the χ^2 minimum search code GOSIA.

References

[1] D.L. Zhang and Y.X. Liu, Chin. Phys. Lett. 20 (2003) 1028-1030.
[2] R. Fossin, Dennis Bonatsos, and G.A. Lalazissis, Phys. Rev. C73 (2006) 044310.
[3] K. Alder and A. Winther, Coulomb Excitation (Academic, New York, 1966).
[4] K. Alder and A. Winther, Electromagnetic Excitation (North Holland, Amsterdam, 1975).
[5] Y. Toh et al., J. Phys. G 27 (2001) 1475-1480.
[6] Y. Toh et al., Eur. Phys. J. A 9 (2000) 353-356.
[7] A. Osa et al., Phys. Lett. B 546 (2002) 48-54.
[8] M. Zielinska et al., Nucl. Phys. A 712 (2002) 3-13.
[9] M. Koizumi et al., Eur. Phys. J. A 18 (2003) 87-92.
[10] M. Sugawara et al., Eur. Phys. J. A 16 (2003) 409-414.
[11] M. Koizumi et al., Nucl. Phys. A 736 (2003) 46-58.
[12] T. Hayakawa et al., Phys. Rev. C 67 (2003) 064310.
[13] K. Furuno et al., Nucl. Instrum. Methods Phys. Res. A 421 (1999) 211; M. Oshima et al., J. Radioanal. Nucl. Chem. 278 (2008) 257-262.
[14] Y. Toh et al., Rev. Sci. Inst. 73 (2002) 47-50.

2.5 Alpha-gamma spectroscopy of ^{259}Rf produced by using a mixed Cf target

M. Asai[1], K. Tsukada[1], Y. Kasamatsu[1,], T. K. Sato[1], A. Toyoshima[1], Y. Ishii[1], R. Takahashi[1,3], Y. Nagame[1], T. Ishii[1], I. Nishinaka[1], D. Kaji[2], K. Morimoto[2] and Y. Kojima[4]

Gamma rays following the α decay of ^{259}Rf have been observed for the first time by means of α-γ coincidence spectroscopy. Excited states in the daughter nucleus ^{255}No have been established, and their spin-parities, configurations, and the ground-state configuration of ^{259}Rf have been evaluated. These experimental data allow us to extract energy spacing and order of single-particle orbits, which give us valuable information on the shell structure and the evolution of nuclear deformation in superheavy nuclei.

The nucleus ^{259}Rf was produced with the ^{251}Cf(^{12}C,4n)^{259}Rf reaction using a mixed Cf target. The target consisting of 63% ^{249}Cf, 12% ^{250}Cf, and 25% ^{251}Cf with a 1.4-mm diameter and 420-μg/cm^2 thickness was prepared by electrodeposition onto 2.16-mg/cm^2 thick Be backing foil. The ^{12}C beam with an average intensity of 540 pnA was focused on the target so as not to hit the aperture with a 3.0-mm inner diameter placed just in front of the target. The total beam dose was 3.6×10^{18} particles accumulated for a total of 14-day beam time. The beam energy was 71.4 MeV on target, at which the cross section of the ^{251}Cf(^{12}C,4n)^{259}Rf reaction was estimated to be 100 nb by the HIVAP-code calculation. Reaction products recoiling out of the target were continuously transported through a 25-m long capillary with a He/KCl aerosol jet into a rotating wheel α-γ detection system [1], and were deposited on thin foil forty of which were set on the wheel. The wheel periodically rotated at 6.0-s intervals to move the deposited sources to two consecutive detector stations each of which was equipped with two Si detectors and two Ge detectors. Alpha-singles and α-γ coincidence events were recorded event by event together with time information.

Figure 1(a) shows a γ-ray spectrum in coincidence with 8510–8810 keV α particles. Two prominent γ lines are observed at 97.3 and 146.7 keV in addition to intense No L X rays. Alpha events in coincidence with these γ rays are mostly concentrated on around 8770 keV which is in good accordance with the α energy of ^{259}Rf; the literature values of α energies and intensities of ^{259}Rf are 8770keV (60%) and 8870 keV (40%) [2]. Alpha particles with energies of >8800 keV are not coincident with any γ rays except for weak No L X rays. In the α-singles spectrum, 8620, 8770, 8880, and 9010 keV α groups are observed in this energy region. The most intense α group of 8880 keV is attributed to the α decay of ^{211m}Po (8883 keV) produced in the reaction with ^{208}Pb, an impurity the target includes. The weak α groups of 8620 and 9010 keV are attributable to the α decay of ^{257}Rf [3,4] produced via the ^{249}Cf(^{12}C,4n)^{257}Rf reaction. The α decay of ^{257}Rf also emits the intense 8770 keV α group whose energy is the same as that of the α transition of ^{259}Rf. However, this α group is known to populate the isomeric state in ^{253}No with a half-life of 24.6 μs [5], and thus, to emit no prompt γ ray. On the other hand, the 8620 keV α group is expected to be followed by emissions of high-energy γ rays or K X rays. The weakly observed No $K_{\alpha 1}$ and $K_{\alpha 2}$ X rays in Fig. 1(a)

[1] Japan Atomic Energy Agency
[2] RIKEN
[3] Tokyo University of Science
[4] Hiroshima University

probably originate from the α decay of ^{257}Rf. The No L X rays observed in the spectrum should also originate in part from ^{257}Rf. In addition, there should be weak 8800 keV (19%) and 8860 keV (81%) α lines associated with the α decay of ^{257}Lr produced via the EC decay of ^{257}Rf [4], although no γ ray is observed in coincidence with these high-energy α particles. On the basis of the above considerations, it is concluded that the observed 97.3 and 146.7 keV γ rays should originate from the α decay of ^{259}Rf.

Figure 1(b) shows a proposed decay scheme of ^{259}Rf, established in analogy with that of ^{257}No [1], the lighter N = 155 isotone. A partial decay scheme of ^{257}No is shown in Fig. 1(c). The ground-state configurations of the daughter nuclei ^{255}No and ^{253}Fm are both 1/2$^+$[620]. Energy difference and intensity ratio of the 97.3 and 146.7 keV γ transitions are very similar to those of the 77.0 and 124.1 keV ones in the α decay of ^{257}No, which are the transitions from the 3/2$^+$[622] state to the 5/2$^+$ and 1/2$^+$ states in the 1/2$^+$[620] rotational band. The transition to the 3/2$^+$ state in the 1/2$^+$[620] band should also be observed in the α decay of ^{259}Rf, which corresponds to the 101.8 keV transition in the α decay of ^{257}No. A few γ-ray events around 125 keV are a candidate for this transition. These results strongly suggest that the ground-state configuration of ^{259}Rf should be 3/2$^+$[622], which is the same as that of ^{257}No but is different from those of the lighter isotones ^{255}Fm and ^{253}Cf. This indicates that the order of the Nilsson orbits is inverted between ^{255}Fm and ^{257}No.

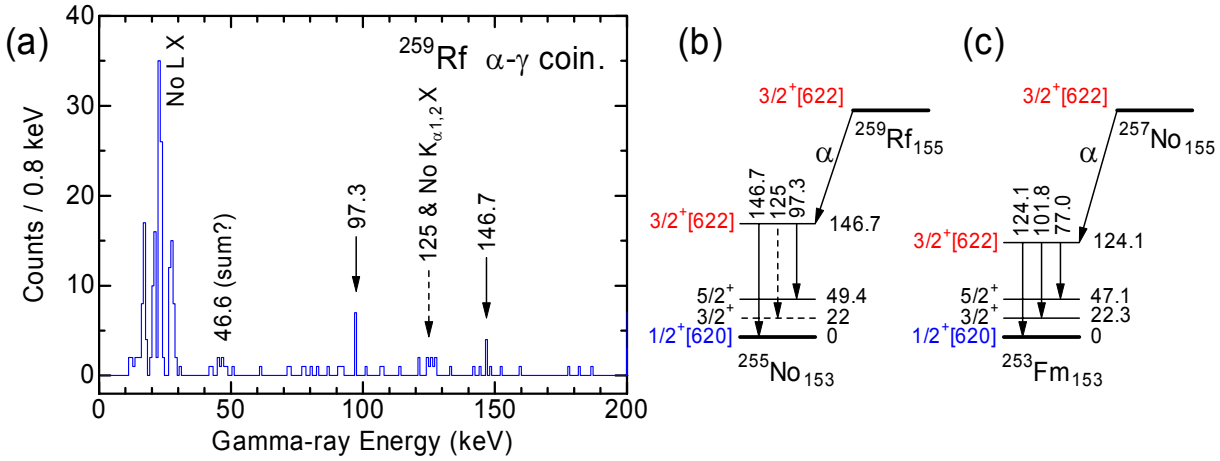

Fig. 1 (a) Gamma-ray spectrum observed in coincidence with 8510–8810 keV α particles. (b) Proposed decay scheme of ^{259}Rf. (c) Partial decay scheme of ^{257}No [1].

References

[1] M. Asai et al., Phys. Rev. Lett., 95 (2005) 102502-1-4.
[2] C. E. Bemis, Jr. et al., Phys. Rev. C, 23 (1981) 555-558.
[3] C. E. Bemis, Jr. et al., ORNL-4976 (1074) 37-39.
[4] F. P. Heßberger et al., Z. Phys. A, 359 (1997) 415-425.
[5] B. Štreicher et al., Acta Phys. Pol. B, 38 (2007) 1561-1564.

2.6 Superdeformed band in ^{40}Ar

E. Ideguchi[1], S. Ota[1], T. Morikawa[2], M. Oshima[3], M. Koizumi[3], Y. Toh[3], A. Kimura[3], H. Harada[3], K. Furutaka[3], S. Nakamura[3], F. Kitatani[3], Y. Hatsukawa[3], T. Shizuma[3], M. Sugawara[4], H. Miyatake[5], Y. Watanabe[5], Y. Hirayama[5] and M. Oi[6]

After systematic investigations of the super deformation (SD) in various mass regions [1], a new 'island' of SD nuclei was found in the nuclear chart around A～40 (i.e., ^{36}Ar [2], ^{40}Ca [3,4], and ^{44}Ti [5]). These N=Z nuclei are magic and near magic systems whose ground states have a spherical shape. In order to produce the collective degrees of freedom necessary for the formation of SD states, cross-shell excitations involving both the *sd* and *pf* shells are necessary. SD shell structure in this mass region plays an important role in forming such large deformed structures. The gap at β_2～0.6 at N=Z=20 is associated with the SD band of ^{40}Ca with 8 particle 8 hole (8p-8h) configuration built on the third 0^+ state. Another gap at β_2～0.5 at N=Z=18 is associated with the observed SD band in ^{36}Ar [2] which is built on the second 0^+ state with 4p-4h configuration. The presence of many deformed gaps in this region may imply large deformed structures at high-spin states in A～40 nuclei. Woods-Saxon single-particle diagram [3] shows the large deformation gaps at β_2～0.5 for Z=18 and N=22. As a consequence, a SD band structure is expected in ^{40}Ar to be built on the second 0^+ state with 6p-4h configuration, which is similar to those observed in ^{38}Ar [6] and ^{42}Ca [7]. In order to investigate the SD band in ^{40}Ar, we have performed in-beam γ-ray spectroscopy using a ^{18}O+^{26}Mg reaction.

The experiment was performed at the tandem accelerator facility of the Japan Atomic Energy Agency. The ^{18}O beam of 70 MeV was used to irradiate the two stacked ^{26}Mg target foils of 0.47 and 0.43 mg/cm^2 thickness. High-spin states in ^{40}Ar were populated via the ^{26}Mg(^{18}O,2p2n)^{40}Ar reaction. Gamma rays were detected by the GEMINI-II array [8] comprising 16 HPGe detectors with BGO anti-Compton suppressor shields, in coincidence with charged particles detected by the Si-Ball [9], a 4π array consisting of 11 ΔE Si detectors of 170 μm thickness. The HPGe detectors were placed at 6 different angles, namely 47º (4 Ge's), 72º (2 Ge's), 90º (2 Ge's), 105º (4 Ge's), 144º (1 Ge) and 147º (1 Ge) with respect to the beam direction, which enables us to perform angular distribution and DCO analyses. The most forward Si detector was segmented to 5 and other detectors were segmented to 2 each, and in total 25 channels were used, which enhances the selectivity of multi-charged-particle events. With a trigger condition of more than 2 Compton suppressed Ge detectors firing in coincidence with charged particles, a total of 6.6×10^8 events were collected.

The γ-γ coincidence relations were examined by gating on the low-lying known γ-ray transitions, and the previously reported level scheme of ^{40}Ar [10] was confirmed up to the 6.8 MeV level. In addition, 2 γ-ray

[1] CNS, University of Tokyo
[2] Kyushu University
[3] Japan Atomic Energy Agency (JAEA)
[4] Chiba Institute of Technology
[5] KEK
[6] Senshu University

cascade transitions of 2269 and 2699 keV were newly identified in coincidence with the 992, 1441 and 1841 keV transitions. Accordingly, these 5 γ-ray transitions form a rotational band ranging from 2^+ to 12^+ states as shown in Fig. 1. The result of the DCO analysis is consistent with the E2 character of the in-band transitions. The large moment of inertia of the band in ^{40}Ar comparable to those of SD bands in ^{36}Ar and ^{40}Ca (Fig. 2), and the measured transition quadrupole moment (～1.45 eb) indicates the super-deformed shape of the band with the deformation parameter β_2～0.53.

In order to understand the super-deformed shape and the high-spin behavior of the band in ^{40}Ar theoretically, self-consistent cranked Hartree-Fock-Bogoliubov calculations based on the P+QQ two-body interaction [11] were performed. The calculation shows that the 6p-4h structure with deformation parameter β_2～0.57 appears in ^{40}Ar, which is in good agreement with the experimental results.

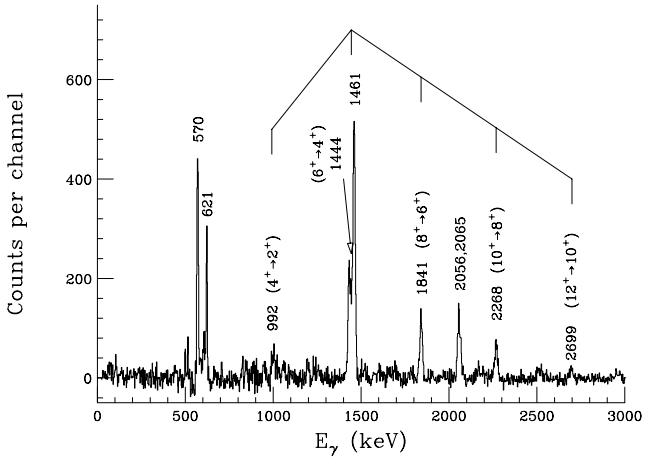

Fig. 1 γ-ray spectrum created by gating on the in-band transitions of SD band in ^{40}Ar.

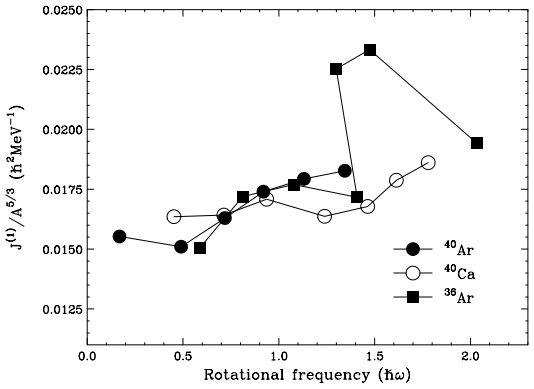

Fig. 2 Kinematical moment of inertia $J^{(1)}$ of the SD bands in ^{40}Ar, ^{36}Ar [2] and ^{40}Ca [3], scaled by $A^{5/3}$.

References

[1] B. Singh, R. Zywina, R.B. Firestone, Nucl. Data Sheets 97 (2002) 241-592.
[2] C.E. Svensson *et al.*, Phys. Rev. Lett. 85 (2000) 2693-2696.
[3] E. Ideguchi *et al.*, Phys. Rev. Lett. 87 (2001) 222501/1-4.
[4] C.J. Chiara *et al.*, Phys. Rev. C 67 (2003) 041303(R)/1-5.
[5] C.D. O'Leary *et al.*, Phys. Rev. C 61 (2000) 064314/1-7.
[6] D. Rudolph *et al.*, Phys. Rev. C 65 (2002) 034305/1-8.
[7] M. Lach *et al.*, Eur. Phys. J. A 16 (2003) 309-311.
[8] M. Oshima *et al.*, J. Radioanal. Nucl. Chem. 278 (2008) 257-262.
[9] T. Kuroyanagi *et al.*, Nucl. Instrum. Methods Phys. Res. A316 (1992) 289-296.
[10] E. Bitterwolf *et al.*, Z. Phys. A 313 (1983) 123-132.
[11] M. Oi, Phys. Rev. C 76 (2007) 044308/1-15.

2.7 Coulomb excitation measurement of ^{84}Sr

Y. Toh[1], M. Koizumi[1], M. Oshima[1], A. Toyoshima[1], H. Harada[1], K. Furutaka[1], F. Kitatani[1], S. Nakamura[1], A. Kimura[1], Y. Hatsukawa[1], A. Osa[1], M. Sugawara[2] and T. Morikawa[3]

Sr isotopes (Z=38) belong to the family of elements close to the Z=40 subshell closure which exhibit a change from almost spherical (at N=50) to strongly deformed nuclei at both ends (N=40, 62) of the series [1-3]. H. Zhang et al. have performed calculations in the RMF(DDDI), RMF(CPI) and RMF theory for both the prolate and oblate configurations [4]. The deformations of nuclei have been obtained from the relativistic Hartree minimization with pairing. It is seen that the RMF(DDDI) theory gives a well-deformed prolate shape for lighter isotopes. Further, the addition of a few neutrons below the closed neutron shell leads to an oblate shape and turns into a spherical one at the magic number N=50. For nuclei above N=50, the RMF theory predicts the prolate deformation again. The nuclear deformation can be determined in measurements of quadrupole moments. Coulomb excitation is a useful method to deduce quadrupole moments without taking into account the effects of nuclear interaction [5, 6].

A ^{84}Sr target with approximately 1 mg/cm^2 thickness was excited by a 19 MeV ^{12}C beam. The Sr target was obtained by an electrodeposition on a gold-foil surface from $SrCO_3$ solution. A γ-ray detector array, GEMINI-II (upgraded version of GEMINI [7]), consisting of 16 Ge detectors with BGO Compton suppression shields, was used to detect de-excitation γ rays. Ge detectors were placed at θ = 47˚, 72˚, 90˚, 105˚, 147˚, and 144˚ relative to the incident beam. Scattered particles are detected with a position-sensitive particle detector system [8] with four plastic scintillators each of which is coupled to a position-sensitive

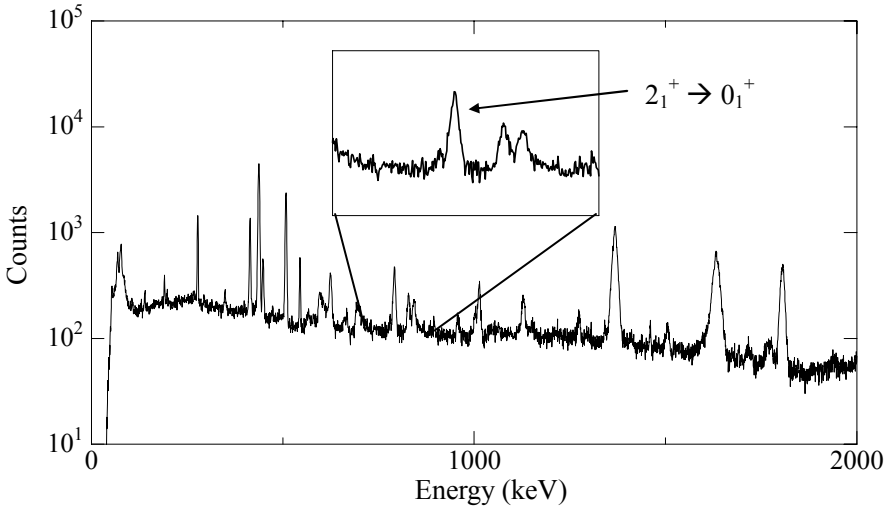

Fig. 1 An example of spectra of Coulomb excitation experiment. A transition from the first 2^+ state to the ground state of ^{84}Sr was observed.

[1] Japan Atomic Energy Agency (JAEA)
[2] Chiba Institute of Technology
[3] Kyushu University

photomultiplier tube. It covers approximately 30% of the total solid angle, ranging from 20° to 67° and from 113° to 160° to the incident beam direction. The angular resolution was 3.1° in FWHM near the edge of the detector and 1.9° at the center. The information on the location of particles was used for Doppler-shift corrections of the γ ray from ^{84}Sr, simultaneously providing the impact-parameter dependence of the γ-transition intensity. The experimental data were recorded event by event on a hard disk when one Ge detector and one particle detector gave coincident signals. Fig. 1 gives an example of spectra of γ rays in coincidence with scattered particles.

The transition from the first 2^+ state to the ground state (793.3keV) of ^{84}Sr was clearly observed. Gamma rays from fusion reactions (^{12}C + ^{12}C, ^{12}C + ^{16}O) and Coulomb excitation of ^{197}Au were also observed because the target contained oxygen and carbon and was supported by the gold backing foil. The γ ray from the $4_1^+ \rightarrow 2_1^+$ transition (974.6 keV) of ^{84}Sr was not found in the present experiment, to normalize the γ-ray yield from the target particle de-excitation. E2 matrix elements may be determined by using the transition of ^{197}Au as a reference, for which the B(E2) values are well known [9, 10]. The experimental data will be analyzed in detail by using a least-squares search code GOSIA [11, 12], which will reveal the B(E2) transition probability and the quadrupole moments. This will help us to understand the ground state properties of Sr isotopes.

References

[1] F. Buchinger et al., Phys. Rev. C41 (1990) 2883-2897.
[2] P. Bonche et al., Nucl. Phys. A530 (1990) 149-170
[3] D. Hirata et al. Phys. Lett. B314 (1993) 168-172
[4] H. Zhang et al. Eur. Phys. J., A30 (2006) 519-529
[5] K. Alder and A. Winther, Coulomb Excitation, Academic, NewYork, (1966).
[6] K. Alder and A. Winther, Electromagnetic Excitation, North Holland, Amsterdam, (1975).
[7] K. Furuno et al., Nucl. Instrum. Methods Phys. Res., A421 (1999) 211-226.
[8] Y. Toh et al., Rev. Sci. Instrum., 73 (2002) 47-50.
[9] M. A. Schumaker et al., Phys Rev. C78 (2008) 044321.
[10] X. Huang and C. Zhou, Nucl. Data Sheet, 104 (2005) 283-426.
[11] T. Czosnyka et al., Nucl. Phys., A 458 (1986) 123-136.
[12] T. Czosnyka, C.Y. Wu and D. Cline, Bull. Am. Phys. Soc., 28 (1983) 745-746.

2.8 Charge radii in macroscopic-microscopic mass models

H. Iimura[1] and F. Buchinger[2]

We are conducting laser spectroscopy to determine the charge radii of unstable nuclei produced by the JAEA tandem accelerator. In order to compare the experimental results with theoretical predictions, we calculated the charge radii in the flame of the finite-range droplet model (FRDM). The FRDM is presently the most sophisticated and successful macroscopic-microscopic approaches to mass models [1]. Even though charge radii can be calculated from this model, they were not included as input data when the optimum model parameters were determined. Thus, comparing between predicted and experimental radii serves as cross check of the reliability of the model. For further examination of the model, we expanded the radii calculation over the full nuclear chart rather than in the mass region we are investigating experimentally. The calculated charge radii were compared with the experimental data taken from recent extensive compilation [2].

The charge radii were calculated by using the prescriptions outlined in the paper of Myers and Schmidt (MS) [3]. In the FRDM, the mean-square charge radius (R^2) is written as

$$R^2 = \left\langle r^2 \right\rangle_u + \left\langle r^2 \right\rangle_r + 3b^2 + s_p^2 , \tag{1}$$

where $\left\langle r^2 \right\rangle_u$ is the contribution from the size of the uniform distribution, $\left\langle r^2 \right\rangle_r$ the contribution from the Coulomb redistribution, b the surface-diffuseness parameter, and s_p = 0.8 fm is the rms charge radius of the finite proton. Being different from MS, we included triaxiality (γ) and octupole deformation (β_3) into the radius calculation by giving the uniform-distribution part as

$$\left\langle r^2 \right\rangle_u = \frac{3}{5} R_Z^2 \left(1 + \alpha_2^2 + \frac{10}{21}\alpha_2^3 \cos 3\gamma + \frac{5}{7}\alpha_3^2 - \frac{27}{35}\alpha_2^4 + \frac{10}{7}\alpha_2^2\alpha_4 + \frac{5}{9}\alpha_4^2 + \frac{20}{21}\alpha_2\alpha_3^2 \right), \tag{2}$$

with

$$\alpha_l = \sqrt{\frac{2l+1}{4\pi}}\beta_l . \tag{3}$$

Here R_Z is the sharp radius for the proton distribution. For γ= 0° and γ= 60°, the nuclear shape is axially symmetric. If the shape is axially symmetric and simultaneously reflection-symmetric (β_3 = 0), the uniform distribution part reduces to the same expression as that of MS. As for the redistribution part, we do not change the expression of MS. The values of tri-axiality, octupole and hexadecapole (β_4) deformation parameters were taken from the table of Möller and co-workers [1,4], which were calculated by the finite-range liquid-drop model (FRLDM). It should be noted that the FRDM and FRLDM calculations contain only static deformations, although the zero-point fluctuation about the minimum of the potential well contributes to mean-square charge radii. There has been no calculation of shape fluctuation across the nuclear chart, but it can be estimated from nuclear transition rates. In order to empirically include the shape

[1] Japan Atomic Energy Agency (JAEA)
[2] McGill University

fluctuation into our radius calculation, we use the β_2 parameters deduced from the experimental $B(E2; 0_1^+ \rightarrow 2_1^+)$ values instead of using those determined within the FRLDM. The experimental $B(E2; 0_1^+ \rightarrow 2_1^+)$ were taken from the recent comprehensive compilation [5].

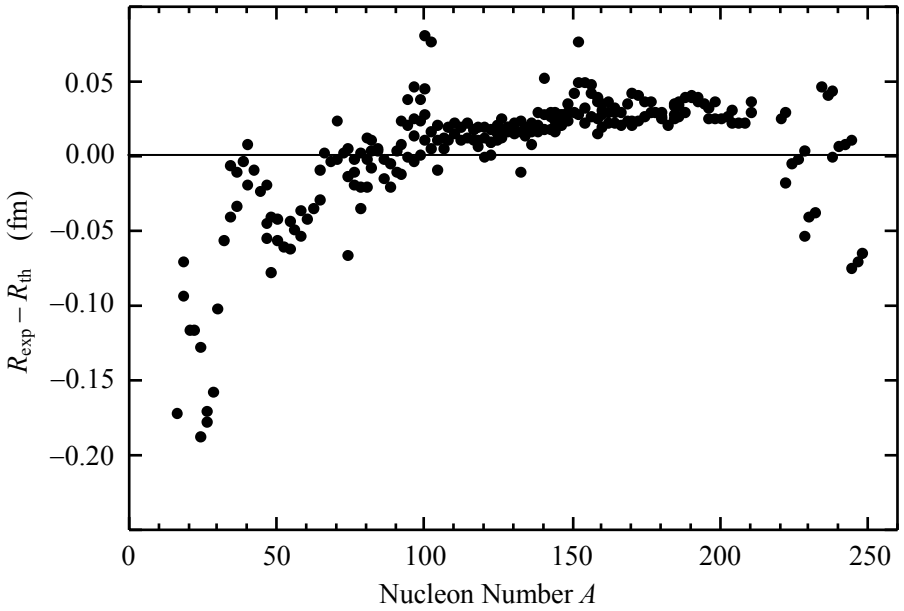

Fig. 1 Difference between experimental (R_{exp}) and calculated (R_{th}) rms charge radii *versus* A.

Fig.1 shows our results for the difference between the experimental and calculated charge radii of the 242 nuclei, for which both the experimental charge radii and $B(E2; 0_1^+ \rightarrow 2_1^+)$ are available. In this calculation, we used the surface-diffuseness parameter b = 0.893 fm, which was obtained by fitting to these 242 nuclei. As seen in this figure, the difference $R_{exp} - R_{th}$ considerably scatters in the mass regions $A < 110$ and $A > 210$. In $A < 110$ the difference is largely negative, which means R_{th} is too big. In the mass region $110 < A < 210$ the difference fluctuates less. If we adjust the surface-diffuseness parameter b to 0.93 fm, the difference $R_{exp} - R_{th}$ shifts downward, giving a better fit in the mass region $110 < A < 210$. This value of b parameter is reasonable from the stand point of electron-scattering data. The reason for the bad agreement for $A < 110$ and $A > 210$ deserves further investigation. On the low mass side, one would expect the breakdown of a "liquid-drop-like" model at some point, but probably not as early as in the A =110 region.

References

[1] P. Möller *et al*., At. Data Nucl. Data Tables, 59 (1995) 185-381.
[2] I. Angeli, At. Data Nucl. Data Tables, 87 (2004) 185-206.
[3] W. D. Myers and K. –H. Schmidt, Nucl. Phys. A410 (1983) 61-73.
[4] P. Möller *et al*., At. Data Nucl. Data Tables, 94 (2008) 758-780.
[5] S. Raman, C. W. Nestor jr. and P. Tikkanen, At. Data Nucl. Data Tables, 78 (2001) 1-128.

2.9 In-beam γ-ray spectroscopy of ^{248,250,252}Cf using neutron-transfer reactions

R. Takahashi[1,2], T. Ishii[2], D. Nagae[2], M. Asai[2], H. Makii[2], K. Tsukada[2], A. Toyoshima[2], Y. Ishii[2], M. Matsuda[2], A. Makishima[3], T. Shizuma[2], T. Kohno[4] and M. Ogawa[5]

We have studied high-spin states of neutron-rich trans-uranium nuclei of ^{236}Th (z=90), ^{240,242}U (z=92), ^{245,246}Pu (z=94), and ^{249,250}Cm (z=96) [1-5]. In Cf (z=98) nuclei, no in-beam γ-ray spectroscopy has been performed. The ground-state bands in ^{248,250,252}Cf were only known up to 6^+, 8^+, and 6^+, respectively. In the present work, high-spin states in ^{248,250,252}Cf have been extended.

We have measured de-excitation γ rays in ^{248,250,252}Cf populated by neutron-transfer reactions with a ^{249,250,251}Cf target and a 153 MeV ^{18}O beam. The target electrodeposited on a 0.9 mg/cm^2 aluminum foil consists of 63% ^{249}Cf, 13% ^{250}Cf, and 24% ^{251}Cf with a thickness of 0.45mg/cm^2 and a diameter of 0.8mm. The activity of the target was 1.4 MBq.

Outgoing particles were detected by four sets of Si Δ E-E detectors and were separated by mass number. γ rays emitted from residual nuclei were measured by six Ge detectors, in coincidence with outgoing particles. In order to obtain spectra of ^{250,252}Cf from ^{249,251}Cf(^{18}O,^{17}O)^{250,252}Cf reactions, we set the gates on ^{17}O particles with the measured kinetic energies corresponding to the excitation energies of ^{250,252}Cf nuclei

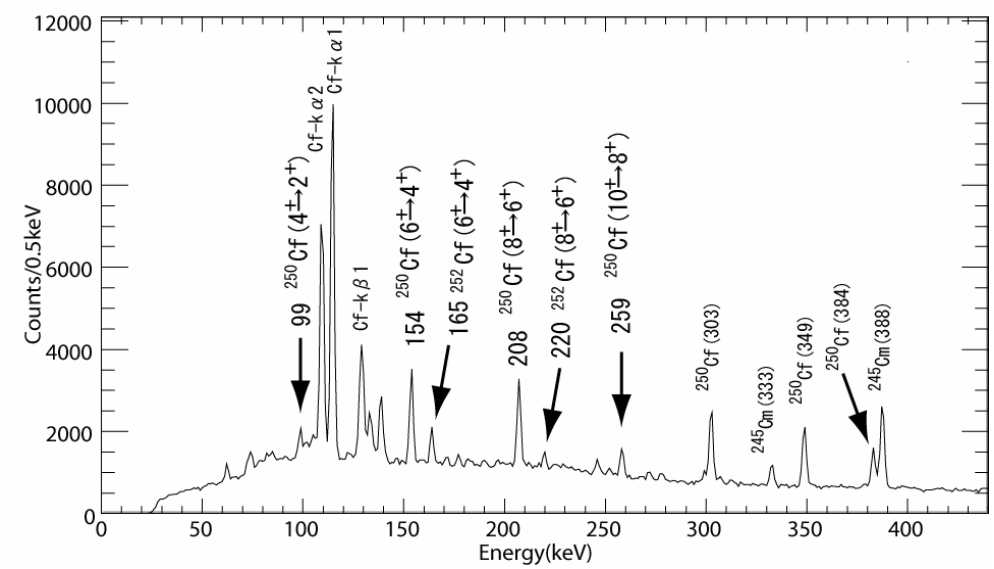

Fig. 1 A spectrum of γ-rays in coincidence with ^{17}O particles with kinetic energies corresponding to the excitation energies of ^{250}Cf between 0 and 6 MeV.

[1] Tokyo University of Science
[2] Japan Atomic Energy Agency (JAEA)
[3] National Defense Medical College
[4] Tokyo Institute of Technology
[5] Komazawa University

below the neutron separation energies, between 0 and 6 MeV. For the ^{248}Cf spectrum from ^{249}Cf(^{18}O,^{19}O)^{248}Cf reactions, we set the gates on ^{19}O particles with the measured kinetic energies corresponding to the excitation energies of ^{248}Cf nuclei below the neutron separation energy. The γ rays in the ground-state bands of ^{250,252}Cf were clearly observed as shown in fig. 1. These γ rays were coincident with each other. The in-plane to out-of-plane intensity ratios of these γ rays, I_γ(in-plane)/ I_γ(out-of-plane) > 1, explained that these transitions are stretched *E*2 types. The ground-state bands in ^{248,250,252}Cf were extended up to 10^+, 12^+, and 10^+ states, respectively. The results are summarized in fig. 2.

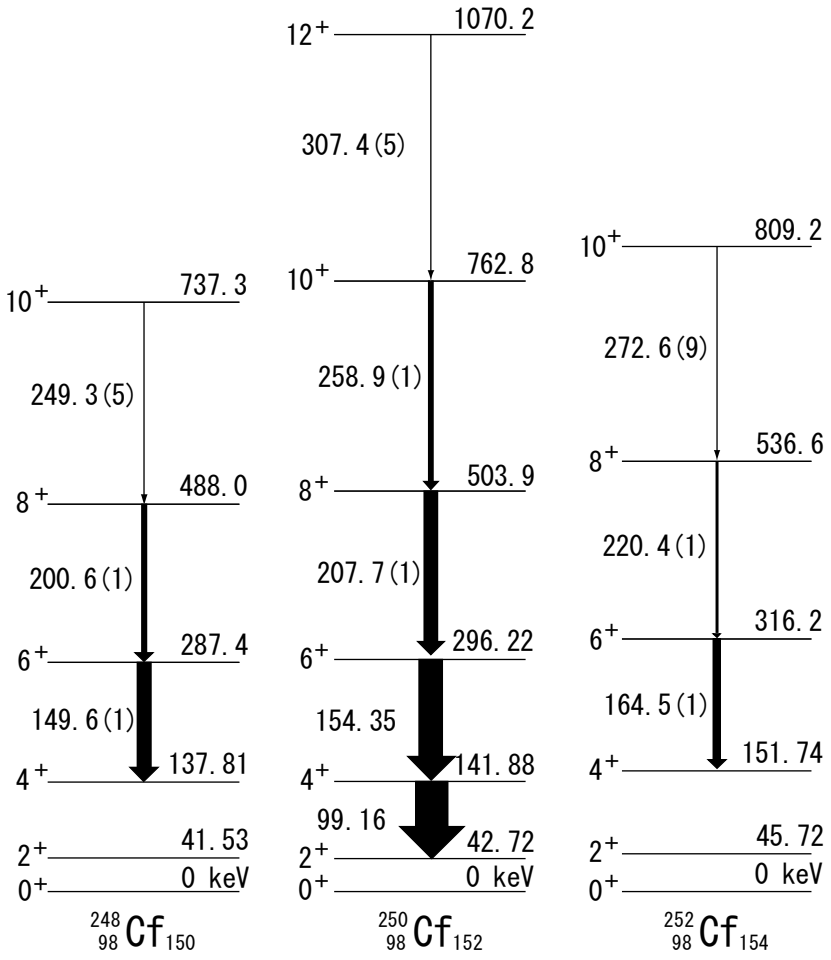

Fig. 2 Level schemes of the ground-state bands of ^{248,250,252}Cf.

References

[1] T. Ishii et al., Phys. Rev., C72 (2005) 021301(R) (1-5).
[2] T. Ishii et al., J. Phys. Soc. Japan, 75 (2006) 043201 (1-4).
[3] T. Ishii et al., Phys. Rev., C76 (2007) 011303(R) (1-5).
[4] H. Makii et al., Phys. Rev., C76 (2007) 061301(R) (1-5).
[5] T. Ishii et al., Phys. Rev., C78 (2008) 054309 (1-11)

2.10 Development of RI ion trap system

D. Nagae[1], T. Ishii[1], H. Makii[2], R. Takahashi[3], T.K. Sato[1], A. Osa[1] and S. Ichikawa[1]

Low-energy (~ 3 keV) and low-emittance (~ 2 π mm mrad) pulsed radioactive nuclear beam (RNB) is useful for measurement of fundamental properties of nucleus such as binding energy, charge radius, and magnetization distribution with high accuracy. In order to produce such RNBs, a trap system has been developed at the central beam line of the isotope separator on-line (ISOL) [1,2]. There are four fundamental processes in producing the pulsed RNB: (i) injecting ions into a gas-filled RF linear ion trap on a potential slightly below the beam energy, (ii) confining the ions with RF + DC electric field, (iii) extracting the ions as bunches, (iv) modifying the potential energy of the ions using a pulse cavity. The details are described elsewhere [3].

On-line test of the trap system has been carried out using $^{21}Na^{+}$ produced in the $^{12}C + ^{12}C$ fusion reaction. The Na beam energy from the ISOL was 21 keV. The extracted ions were stopped on a multi-anode type micro-channel plate (MCP) detector placed on the exit of the trap system to measure the time and spatial distributions of the ions. Figure 1 shows the time-of-flight spectrum of ions ejected out of the trap system. By adjusting the DC electric field at the extraction side of the trap, the time width of extracted ions was obtained to be FWHM ~ 2 μs. This result will allow producing low-energy RNBs using pulse cavity since a flight time in the pulse cavity is estimated to be about 6 μs with the kinetic energy of extracted ions is about 3 keV. The beam width of the trapped ions was measured as FWHM ~ 13 mm using the MCP. To produce low-energy heavy RNBs up to A ~ 200, modifying an RF + DC electric circuit is now in progress.

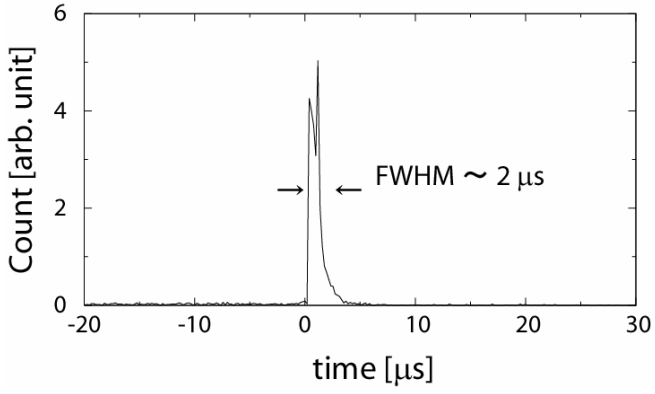

Fig. 1 Time-of-flight spectrum of $^{21}Na^{+}$ ions extracted from the trap system.

References

[1] H. Makii et al., JAEA Tandem Annu. Rep. 2005, JAEA-Revew 2006-029 (2006) 37-38.
[2] H. Makii et al., JAEA Tandem Annu. Rep. 2007, JAEA-Revew 2008-054 (2008) 46-47.
[3] F. Herfuth et al., Nucl. Instrum. Methods Phys. Res., A469 (2001) 254-275.

[1] Japan Atomic Energy Agency (JAEA)
[2] High Energy Accelerator Research Organization (KEK)
[3] Tokyo University of Science (TUS)

2.11 Lifetime measurement for the first 2^+ state in ^{162}Gd

D. Nagae[1], T. Ishii[1], R. Takahashi[2], M. Asai[1], H. Makii[3], A. Osa[1], T.K. Sato[1] and S. Ichikawa[1]

New neutron-rich europium isotopes $^{163, 164, 165, 166}$Eu were identified in previous experiments and measured the excitation energies for $_{64}$Gd isotopes [1, 2]. It has been revealed that the excitation energies of the first 2^+ state, $E(2^+)$, in even-even $_{64}$Gd isotopes show local minimum at neutron number $N = 98$ as shown in Fig. 1. The same tendency was also found in $_{66}$Dy isotopes [3]. On the other hand, the values of $E(2^+)$ for $_{68}$Er, $_{70}$Yb, and $_{72}$Hf isotopes decrease as neutron number increase toward at $N = 104$ midshell. These results suggest the sudden deformation of nuclear shape at $N = 98$. In order to clarify the mechanism of the local minimum at $N = 98$, the lifetime of the first 2^+ state at 71.5 keV in ^{162}Gd have been measured to deduce the reduced transition probability, B(E2), by means of $\beta - \gamma$ delayed coincidence technique for ^{162}Eu since the B(E2) is sensitive to nuclear deformation.

The experiment was performed using the isotope separator on-line. The ^{162}Eu was produced in proton-induced fission with UC_x target. The target was bombarded by a 32 MeV proton beam with intensity about 1 μA. Fission products were diffused-out from the target, and then ionized with surface ionization type ion source [1]. The mass-separated ^{162}Eu was implanted into Mylar tape in a tape transport system and periodically transported to a detection position. The detection position was equipped with a Pilot-U 60 mm × 63 mm × 1-mm thick plastic scintillator and a 38 mm diameter × 5 mm thick BaF_2 scintillator to detect β and γ- rays, respectively. Typical energy spectra of γ- rays for ^{162}Gd are shown in Fig. 2. A γ- ray of 71.5 keV corresponding to the $2^+ \rightarrow 0^+$ transition has been observed. Analysis of the lifetime of the first 2^+ state is now in progress.

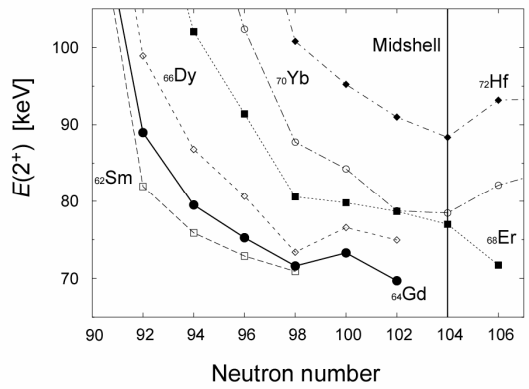

Fig. 1 Excitation energies of the first 2^+ states

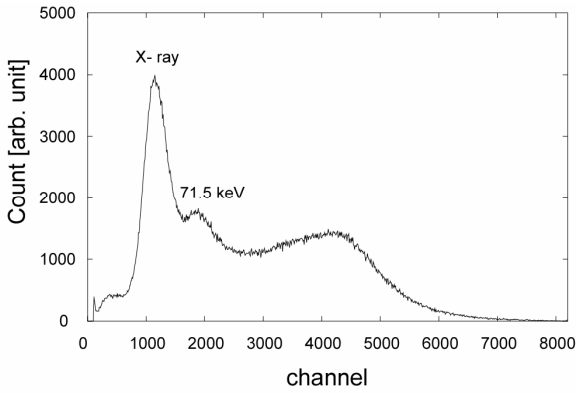

Fig. 2 Energy spectra of γ-rays for ^{162}Gd

References

[1] A. Osa et al., Nucl. Instrum. Methods Phys. Res., B 266 (2008) 4394-4397.

[2] T.K. Sato et al., JAEA Tandem Annu. Rep. 2006, JAEA-Revew 2007-046 (2006) 32-33.

[3] M. Asai et al., Phys. Rev. C 59 (1999) 3060-3065.

[1] Japan Atomic Energy Agency (JAEA)
[2] Tokyo University of Science (TUS)
[3] High Energy Accelerator Research Organization (KEK)

2.12 A new technique to measure half-lives of long-lived isomers using a total absorption detector

M. Asai[1], H. Hayashi[2], A. Osa[1], T. K. Sato[1], Y. Otokawa[1], D. Nagae[1], K. Tsukada[1], Y. Miyashita[3], H. Ouchi[3], S. Izumi[3], T. Shinozuka[3] and M. Shibata[2]

It is extremely difficult to measure half-lives of isomeric states in the range of 10 μs < $t_{1/2}$ < 10 ms populated by the β decay. In usual βγ spectroscopy, the half-life is determined by measuring time intervals between β and γ detections. For isomers with $t_{1/2}$ < 10 μs, correlations between β and γ can easily be measured with a coincidence technique, which allows us to observe isomeric transitions very sensitively as well as to determine their half-lives. On the other hand, for isomers with $t_{1/2}$ > 10 μs, the longer the half-life is, the more difficult to extract the true correlation events from increasing number of random correlation events. To decrease the random correlation events, it is essential to decrease counting rates of β and γ detections. However, this also results in a lack of statistics of true correlation events, which makes it impossible to observe isomeric γ transitions as well as to determine their half-lives. To overcome this dilemma, we have developed a new technique to measure half-lives of long-lived isomers in the range of 10 μs < $t_{1/2}$ < 10 ms using a total absorption detector.

The total absorption detector consists of two large-volume BGO scintillators each of which has a 120 mm diameter and a 100 mm thickness. Two scintillators are placed with a 4 mm apart and sandwich radioactive sources between them. This detector has almost 100% full-energy deposition efficiencies for <500 keV γ rays and <2 MeV electrons, and over 90% for <1 MeV γ rays and <7 MeV electrons. The sources are prepared by the implantation onto a thin aluminized Mylar tape with an on-line isotope separator, and periodically transported to the position between the scintillators. Energy signals from the two scintillators are summed with a sum amplifier, and registered event-by-event with time stamps of a 5 ns resolution. This detector was originally developed for Q_β measurements by Shibata et al. [1,2] Since all β, γ, conversion electrons, and characteristic X rays emitted in cascade by a β decay deposit their energies on the detector simultaneously, their signals are summed up in energy and registered as a single event. Thus, no discrete γ-ray peak is observed in the energy spectrum because it is summed with β rays which have a continuous energy distribution. Figure 1(a) shows a typical total absorption spectrum observed by this detector for the β decay of ^{141}Cs. On the other hand, if an excited state in the daughter nucleus has a half-life longer than a few μs, γ rays depopulating that state are observed as an event different in time from that of β ray. Thus, a line peak whose energy corresponds to that of the isomer appears in the total absorption spectrum. Figure 1(b) shows a total absorption spectrum for the β decay of ^{162}Eu, in which a prominent 1449 keV peak does appear in addition to a continuous energy component. This peak corresponds to the 1449 keV isomeric state in the daughter nucleus ^{162}Gd, which was first discovered in our previous γ-γ coincidence experiment for the β decay of ^{162}Eu [3]. This energy spectrum demonstrates that the total absorption detector is very

[1] Japan Atomic Energy Agency
[2] Nagoya University
[3] Tohoku University

sensitive to detecting isomeric states with a half-life longer than a few μs populated by the β decay, and searching for unknown isomers.

In order to determine the half-life of the 1449 keV isomer, time intervals between β and γ detections were extracted from the event-by-event data. Here, events with energies of 1910–4430 keV are considered as those of the β transitions populating the isomer, and events with 1310–1480 keV are as γ transitions depopulating the isomer. Figure 2 shows the extracted time interval spectrum. An exponential decay with a half-life of 86.4(11) μs is clearly observed, which corresponds to the half-life of the 1449 keV isomer in ^{162}Gd. A longer decay component with a half-life of 7.7 ms corresponds to the time intervals between randomly correlated events with an average count rate of 90 cps. It is obvious that the isomeric component with a half-life longer than that of random component cannot be observed with this technique. The total absorption detector has a sensitivity to observe β decay with an intensity down to a few Bq, which implies that the longest half-life to be determined should be ~100 ms with this technique. Physics discussions on the 1449 keV isomer in ^{162}Gd will be given in a forthcoming paper.

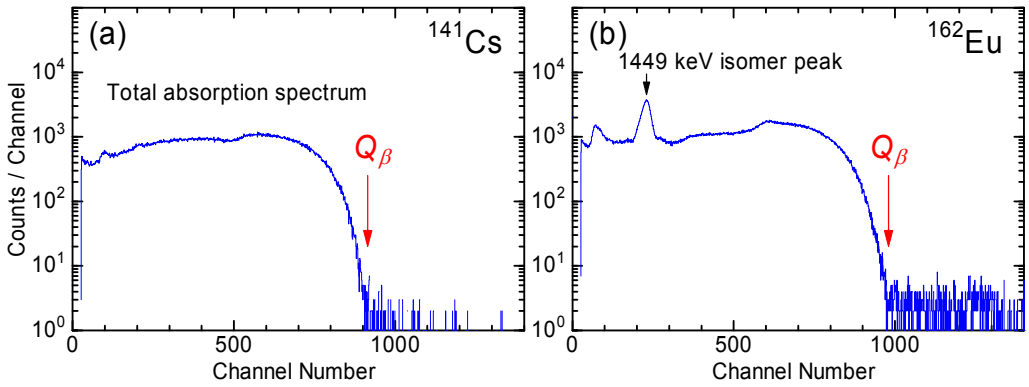

Fig. 1 (a) Total absorption spectrum for the β decay of ^{141}Cs. (b) Total absorption spectrum for the β decay of ^{162}Eu. The 1449 keV isomer peak is observed.

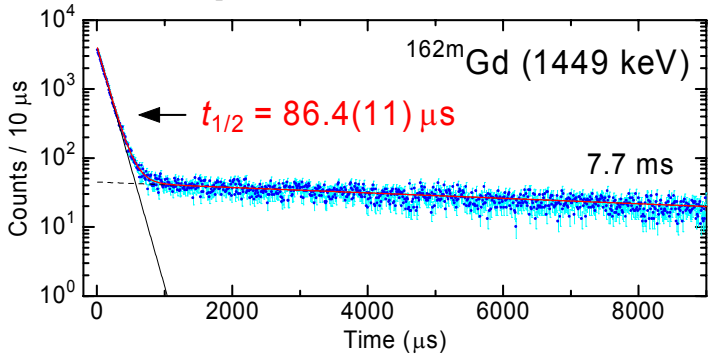

Fig. 2 Decay curve of the 1449 keV isomer in ^{162}Gd. Time intervals between β and γ detections which populate and depopulate the 1449 keV isomer, respectively, are plotted.

References

[1] M. Shibata et al., Nucl. Instrum. Methods A, 459 (2001) 581-585.

[2] H. Hayashi et al., Eur. Phys. J. A, 34 (2007) 363-370.

[3] M. Asai, to be published.

2.13 Search for highly excited states in ^{10}Be using deuteron elastic reaction to ^{8}Li

H. Miyatake[1,2], H. Ishiyama[1], S.C. Jeong[1], X.Y. Watanabe[1], N. Imai[1], Y. Hirayama[1], H. Makii[1], S. Mitsuoka[2], K. Nishio[2], T. Sato[2], T. Teranishi[3], T. Fukuda[4], Y. Mizoi[4], H. Sato[5, 2], K. Yamaguchi[6, 1], A. Takashima[7] and M. Suga[7]

In the previous experiment (RNB-K01), we observed a resonant-like structure at E = 1.0 MeV in the center-of-mass system of ^{8}Li(d, t) reaction. This energy corresponds 22.4 MeV state in ^{10}Be, as shown in Fig. 1, reported also as a proton/triton decaying state both in the neutron capture experiment of ^{9}Be and in the resonant particle decay spectroscopy of ^{7}Li + ^{7}Li. It indicates a possibility of this state as a coexisting state of α + t + t and $\alpha + \alpha$ + n + n cluster configurations [1]. The aim of this experiment is to determine spin and parity for further discussion of this state using resonance elastic scattering of deuteron to ^{8}Li.

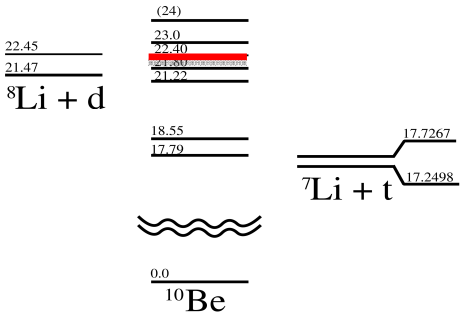

Fig. 1 Level schemes relevant to the ^{8}Li

According to the PAC recommendation, we have performed a feasibility test for this measurement during 3 days machine time. Irradiating the ^{8}Li RNB of 0.94 MeV/u with 4.5 kpps to the CD_2 target of 2.6 mg/cm^2 thick, we successfully obtained scattered deuteron in correlation spectrum of the energy and the time-of-flight by utilizing the simple detector set-up as shown in Fig. 2.

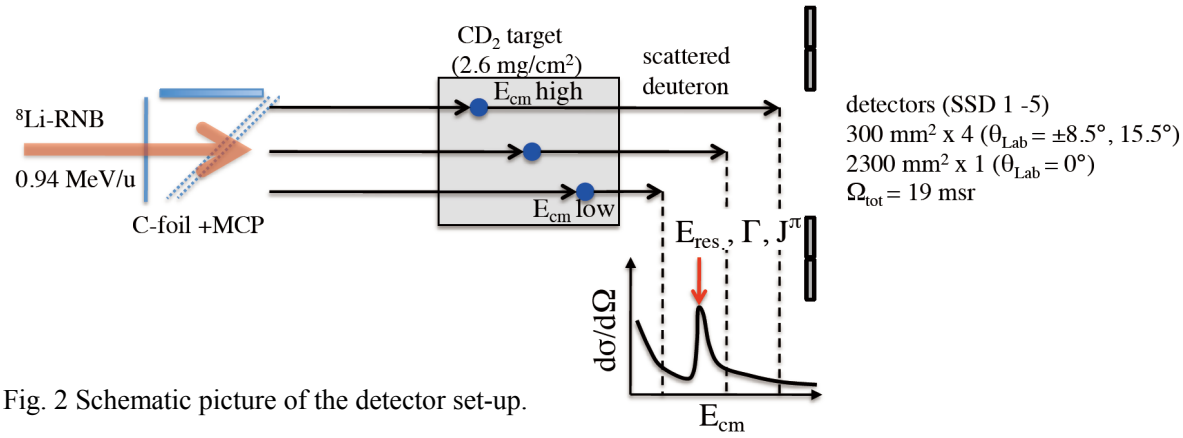

Fig. 2 Schematic picture of the detector set-up.

[1] High Energy Accelerator Research Organization
[2] Japan Atomic Energy Agency (JAEA)
[3] Kyushu University
[4] Osaka Electro-Communication University
[5] Ibaraki University
[6] Tsukuba University
[7] Osaka University

In the measured energy-time correlation spectrum, tritons, ^{8}Li particles passing through pin-holes of the target, and α particles decaying from ^{8}Li were observed in the same time as shown in Fig. 3. These particles were well resolved. Based on the result, it becomes clear that the resonance elastic scattering spectroscopy is feasible with usual ^{8}Li beam intensity (~50 kpps) and modified detector set-up covering the solid angle of 100 msr being 10 times larger than the present one.

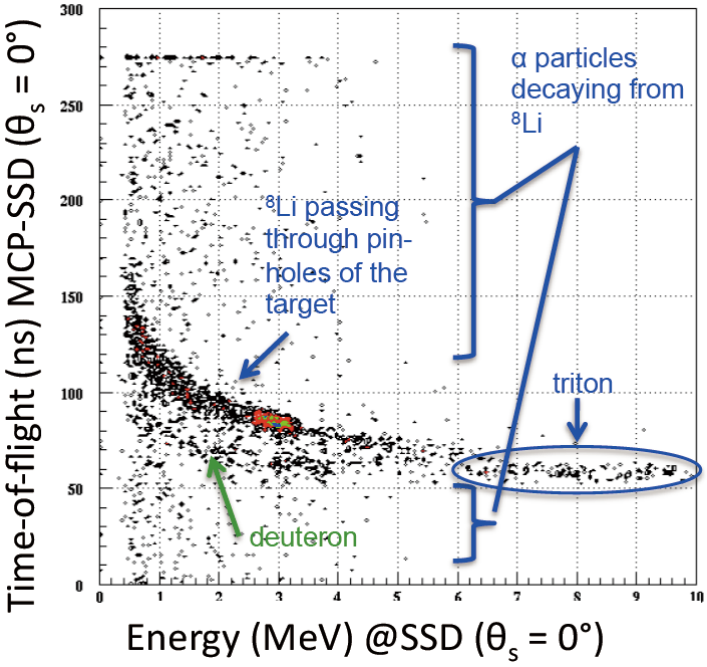

Fig. 3 Energy and time correlation spectrum.

[1] N. Itagaki et al., Phys. Rev. C77 (2008) 067301.

CHAPTER 3

Nuclear Reaction

This is a blank page.

3.1 Indirect determination of neutron radiative capture reaction cross section of medium heavy nuclei

N. Imai[1], H. Ishiyama[1], H. Sato[2], S.C. Jeong[1], D. Nagae[3], K. Nishio[3], Y. Hirayama[1], H. Makii[3], S. Mitsuoka[3], H. Miyatake[1], K. Yamaguchi[4] and Y.X. Watanabe[1]

The properties of unstable nuclei have been extensively studied for nuclear physics and nuclear-astrophysics. Under this trend, the facilities to generate low-energy radioactive isotope beams have been constructed and planned in the world. One of the physics programs to pursue is to reveal the single particle structure of the neutron-rich nuclei [1]. It is not only because the structure directly relates to the shell evolution, but also because the single particle wave function can give the direct radiative capture (DRC) reaction cross section. In the case of the DRC reaction, the cross sections can be obtained with the E1 transition operator and the neutron bound state wave function [2].

One of ways to study the single particle structure of unstable nuclei is to measure the neutron transfer reaction under the inverse kinematics condition. For example, the radioactive isotope beam is irradiated on the CD_2 target, and the recoiled protons will be measured. The scattering angles sensitive to the final state wave functions are around 0 degrees in the center of mass frame, which correspond to the 180 degrees in the laboratory frame. Due to the kinematics, the energies of the recoil proton are as low as a few MeV, which is comparable to the multiple scattering and energy spread due to the scattering angle. And thus, the complicated detector system is needed [3]. Furthermore, when the level densities are dense, the respective excited states cannot be resolved.

Alternatively, we proposed measurement of isobaric analog resonances. Owing to the isospin symmetry of nuclear force, the neutron wave functions of parent nucleus ^{Z}A are identical with proton wave functions appeared in the high excitation energies in the daughter nucleus ^{Z+1}A, called “isobaric analog states”. The analog states can be accessed by the proton elastic scattering [4]. When we measure the excitation function of differential cross sections at a given angle, the cross section where the excitation energy corresponds to the analog state will be enhanced as a resonance. By analyzing the shape of the excitation function, we can determine the wave function. In the case of the inverse kinematics reaction, measurement of the excitation function at 180 degrees in the cm frame, which corresponds to 0 degrees in the laboratory frame, is useful. Due to the kinematics, the energies of recoil protons increase to 4 times larger than the reaction energies in the cm frame. Accordingly, the energy difference between the excitation energies will be enhanced to be 4 times larger than that. This feature is very useful for the experiment.

[1] High Energy Accelerator Research Organization (KEK)
[2] Ibaraki University
[3] Japan Atomic Energy Agency (JAEA)
[4] University of Tsukuba

As the first test of measuring the isobaric analog states in medium nuclei using the inverse kinematics proton elastic scattering, we searched for the isobaric analog states of ^{69}Zn with ^{68}Zn beam with a proton target. The analog states were well studied in the normal kinamatic condition [5].

The $^{68}Zn^{13+}$ beam of 5.5 MeV/nucleon was provided by utilizing the Tandem accelerator and super-conducting linac at Japan Atomic Energy Agency. The beam intensity was decreased to several pA, about 10^6 pps, by using the slits of the beam line. A 2.4 mg/cm^2 CH_2 foil was installed as a proton target. The beam energy changed from 5.5 MeV/u to 3.5 MeV/u. Accordingly, the energies of recoiled protons ranged from 22 MeV to 14 MeV. The resonance width was expected as small as 100 keV. And thus, we have to measure the recoil proton with the uncertainty of 100 keV. To achieve the high energy resolution, we attempted to measure the time of flight (TOF) of recoiled protons with a high time resolution. The start timing signal was obtained by detecting the ^{68}Zn beam event-by-event with multi-channel plate (MCP), which was located upstream of the target. The MCP has a small window of 7 mm x 7 mm which the beam passes through, enabling a time resolution of around 200 ps (FWHM). Two layers of plastic scintillators were placed at 5.5 m downstream of the target. Their thicknesses were 2.5 mm and 10 mm, respectively. The scintillators were installed in the vacuum chamber, and both sides of the scintillator were attached to photo-multiplier tubes placed outside the chamber. Particles were identified by measuring the dE-E correlation of the scintilltators. In front of the scinillatorts, we placed 12 mg/cm^2 thick Al sheet to stop the beam.

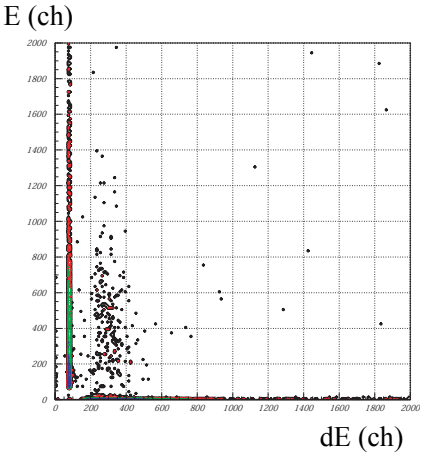

Fig.1 dE-E correlation of plastic scintillators.

A locus in the dE-E correlation was clearly observed as presented in Fig.1. Although we selected the locus, we couldn't find significant relations between the total E and the time of flight of proton. We observed unknown scattered background all over the time range. They may be related to the neutrons produced by the fusion reaction of ^{12}C included in the CH_2 foil with the ^{68}Zn beam. We have changed the experimental setup to measure the isobaric analog states in the second experiment which have recently performed in April 2009.

References

[1] J.M. Blatt and V. F. Weisskopf, *Theoretical Nuclear Physics*, (Wiley, NewYork 1952).
[2] H. Savajols et al., Nucl. Inst. Meth. B 266 (2008) 4583.
[3] A. Bohr and B. R. Mottelson, *Nuclear Structure*, (W.A. Benjamin, New York, 1969).
[4] W.S. Steiner et al., Phys. Rev. C4 (1971) 1684.

3.2 Barrier distribution of quasi-elastic backscattering in heavy systems

S. Mitsuoka[1], H. Ikezoe[1], K. Nishio[1], Y.X. Watanabe[2], S.C. Jeong[2],
Y. Hirayama[2], N. Imai[2], H. Ishiyama[2] and H. Miyatake[2]

By means of the measurements of quasi-elastic (QE) cross sections at backward scattering angles, the Coulomb barrier distributions have been experimentally obtained [1] and theoretically studied [2,3] in ^{48}Ti, ^{54}Cr, ^{56}Fe, ^{64}Ni and ^{70}Zn + ^{208}Pb relating to the cold fusion reactions for the production of super-heavy elements Z = 104, 106, 108, 110 and 112, respectively. The centroid of the barrier distributions showed deviation from the several predicted barrier heights by about 3-10 MeV toward the low energy side. It was reported that such deviation is very small in a similar work on the QE barrier distribution in the heavier system of ^{86}Kr + ^{208}Pb producing Z = 118 [4]. They measured the QE cross sections at various detector angles down to 125° in steps of 5° at five beam energies by using the cyclotron. Recently we have measured it in the same reaction at the backward angles of 172° and 164° with changing the beam energies in steps of 1.5 MeV using the JAEA tandem-booster accelerator.

Fig. 1 shows the typical energy spectra at 172° in ^{86}Kr + ^{208}Pb. As the incident energy increases, the single peak corresponding to the elastic scattering develops a low energy tail including both inelastic scattering and transfer components, and finally another component corresponding to deep-inelastic collisions (DIC) becomes dominant. It was founded that these spectra were well reproduced by the sum of the solid and the dashed curves, respectively, calculated by using a reaction simulation code LINDA [5] for the low energy component and a semiclassical code GRAZING [3] incorporating both transfer and inelastic excitations of collective surface vibrations. We obtained the QE yield as a sum of elastic, inelastic scattering and transfer by carefully excluding the DIC yield. At $E_{c.m.}$ = 292.6 MeV, for example, the QE yield is evaluated to be about half of the whole yield, while in Ref. [4] the whole of the spectrum at the same reaction energy was assumed to be QE. Detailed analysis for the QE cross sections is in progress.

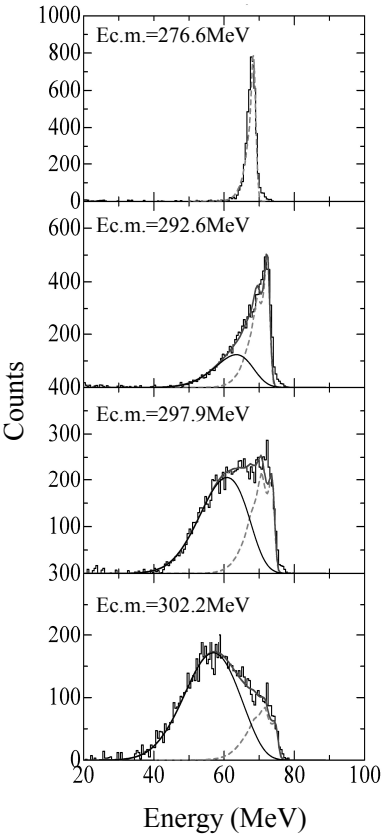

Fig. 1 Energy spectra measured at 172° in ^{86}Kr+^{208}Pb. The solid and the dashed curves are the calculated results by the codes LINDA [4] and GRAZING [3], respectively.

References

[1] S. Mitsuoka el al., Phys. Rev. Lett. **99** (2007) 182701.
[2] Z. Muhammad el al., Phys. Rev. C **77** (2008) 034604.
[3] G. Pollarolo, Phys. Rev. Lett, **100** (2008) 252701.
[4] S.S. Ntshangase et al., Phys. Lett. B **651** (2007) 27-32.
[5] E. Duek et al., Comput. Phys. Commun. **34** (1985) 125.

[1] Japan Atomic Energy Agency (JAEA)
[2] High Energy Accelerator Research Organization (KEK)

3.3 Effects of nuclear orientation on fission fragment mass distributions in the reaction of $^{30}Si + ^{238}U$

K. Nishio[1], H. Ikezoe[1], S. Mitsuoka[1], I. Nishinaka[1], Y.X Watanabe[2],
Y. Nagame[1], T. Ohtsuki[3] and K. Hirose[3]

Super-heavy elements have been successfully produced using two types of fusion reactions. One is the reactions based on lead or bismuth targets [1,2]. The other is the reactions based on actinide targets, where by using projectile ^{48}Ca elements up to atomic number 118 except 117 have been produced [3]. The striking feature in the actinide based reactions [3] is that the cross-sections do not drop with atomic number as in the case of cold-fusion reactions, but keep pico-barn values even in the production of the heaviest elements. A possible explanation for keeping the large cross-section would be associated with the static deformation of the target nuclei. In the case for light projectile ^{16}O, the measured evaporation residue (ER) cross-sections suggest that fusion occurs for every colliding angle and is independent of the nuclear orientation [4]. In the reaction using heavier projectiles $^{30}Si + ^{238}U$ [5], we have measured the ER cross-sections as shown in Fig.1. By comparing the experimental data with the statistical model calculation, we have concluded in 2006 that competition between fusion and quasi-fission was suggested at the sub-barrier energy, whereas no significant fusion hindrance was found at the equatorial collisions. The reaction $^{30}Si + ^{238}U$ would give us an opportunity to observe quasi-fission and fusion-fission and investigate the energy dependence of the yields. We have measured the fission fragment mass distributions in this reaction to see how the quasi-fission appears in the mass distributions.

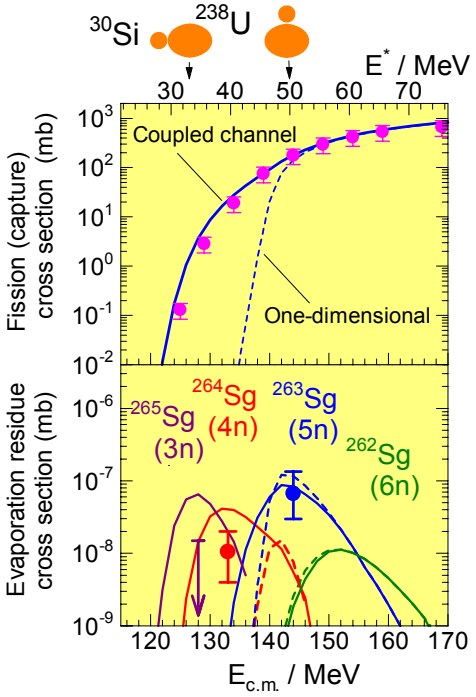

Fig. 1 (Top) Measured fission cross-sections as function of center-of-mass energies ($E_{c.m.}$) measreud at the JAEA tandem accelerator. The solid curve is the coupled channel calculation pass through the Coulomb barrier. Dashed curve is the one-dimensional barrier penetration model. The excitation energies (E^*) are indicated. (Bottom) Evaporation residue cross-sections, compared with the statistical model calculation. For the details, see Ref.[5].

The experiment was carried out by using ^{30}Si beams supplied by the JAEA tandem accelerator. Two fission fragments were detected in coincidence with position-sensitive multi-wire proportional counters. Fission events after full momentum transfer of the projectile to the system are separated from fissions following nucleon transfer reactions, by measuring the emission angles and the out-of-plane angles. In this experiment, we also obtained the fission cross-sections, as shown in the upper panel of Fig.1.

[1] Japan Atomic Energy Agency (JAEA)
[2] High Energy Accelerator Research Organization (KEK)
[3] Tohoku University

Figure 2 shows the dependence of the mass distributions for ^{30}Si + ^{238}U reaction on the center-of-mass energy ($E_{c.m.}$). At the higher energy region than the Bass barrier of $E_{c.m.}$= 139.7 MeV, the spectra show a symmetric shape around mass A = 134. Below the bass barrier, the spectrum shows the asymmetric component with A_H = 178 and A_L = 90.

We can compare the measured mass distributions at $E_{c.m.}$= 144.0 MeV with the ER cross-section for ^{263}Sg (5n). The agreement with the ER cross-section with the calculation indicates that fusion is the major process after the system overcomes the Coulomb barrier. The corresponding mass distribution has symmetric shape, so that the compound nucleus fission dominates. The lower value in the cross-section for ^{264}Sg (4n) than the HIVAP calculation suggests that competition between fusion and quasi-fission occurs. The corresponding mass distribution in Fig.2 at $E_{c.m.}$= 134.0 MeV has asymmetric fission components, indicating that the asymmetric fission is associated with quasi-fission. At the deep sub-barrier energy of $E_{c.m.}$=128.0–129.0 MeV, enhanced quasi-fission yields are predicted from the upper limit in the ER cross-section and the enhanced asymmetric fission yields in the mass distribution. The variation of the mass distribution with bombarding energy results from the orientation effects of the deformed target nucleus ^{238}U on the reaction.

Strong variation of the fragment mass distribution with energy was observed in the reaction ^{36}S+ ^{238}U. The system has dominant quasi-fission in the sub-barrier region, forming the asymmetric mass distribution [6]. The heavier projectile on ^{238}U target results in enhanced quasi-fission probability in the sub-barrier region.

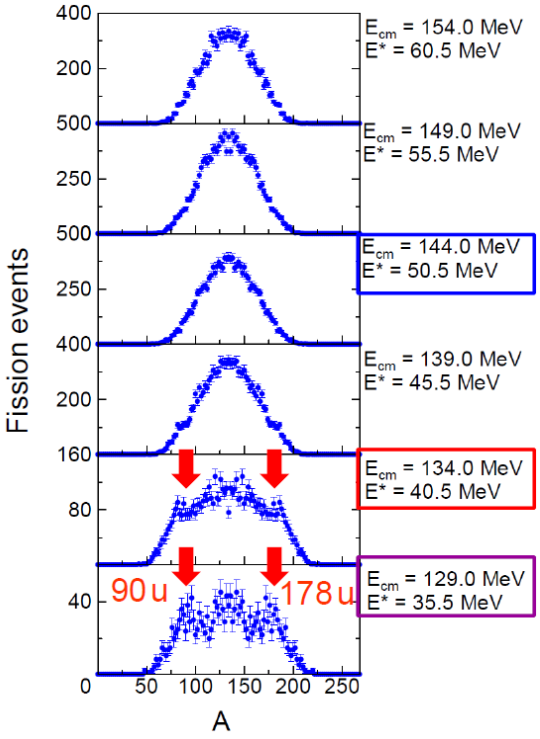

Fig. 2 Fission fragment mass distributions for ^{30}Si + ^{238}U measured at the JAEA tandem accelerator. Bombarding energies and the excitation energies are shown. The arrows show the location of the asymmetric fission components. The spectra marked by the boxes are taken at the energy where ER measurement were carried out.

References

[1] S. Hofmann and G. Münzenberg, Rev. Mod. Phys. **72**, 733 (2000).
[2] K. Morita *et al.*, J. Phys. Soc. Jpn. **73**, 1738 (2004).
[3] Yu.Ts. Oganessian, J. Phys. G, **34**, R165 (2007).
[4] K. Nishio *et al.*, Phys. Rev. Lett. 93 (2004) 162701.
[5] K. Nishio *et al.*, Eur. Phys. J. A29 (2006) 281-287.
[6] K. Nishio *et al.*, Phys. Rev. C. 77 (2008) 064607(1-5).

3.4 Sub-barrier fusion hindrance in $^{19}F + ^{209}Bi$ reaction

I. Nishinaka[1], Y. Kasamatsu[2], M. Tanikawa[3] S. Goto[4] and M. Asai[1]

Unexpected steep falloff of fusion cross sections has recently been observed in heavy-ion fusion reactions at deep sub-barrier energies [1]. Such unexpected steep falloff of fusion cross sections, so-called sub-barrier fusion hindrance, was studied experimentally and theoretically [2-3]. However, the mechanism of sub-barrier fusion hindrance is still an open question. Sub-barrier fusion hindrance has been studied mainly in medium-heavy mass systems because improvements of instruments to detect fusion residues, for example, the Fragment Mass Analyzer [4], makes it possible to determine the fusion-evaporation cross sections in sub-milli-barn level precisely. In contrast, only a limited number of studies was carried out in heavy-mass systems in which fused nuclei decay mainly not by neutron evaporation (fusion-evaporation reactions) but by fission (fusion-fission reactions) [3]. In this work, fusion-fission cross sections for $^{19}F + ^{209}Bi$ at sub-barrier energies were determined by a radiochemical method in order to study sub-barrier fusion hindrance in heavy-mass systems.

The targets of ^{209}Bi with thickness of 0.15-0.22 mg/cm^2 were irradiated with 83-135 MeV ^{19}F ions using the 20 MV tandem accelerator at JAEA-Tokai. Figure 1 schematically shows two types of irradiation setups that were installed in a Faraday cup. Fission fragments were collected in the backing and the catcher foil of 5.4 mg/cm^2 aluminum. The irradiation setup (b) was mainly used to measure the cross sections of some high-yield fission products at the energies $E_{lab} \geqq 91$ MeV by γ-ray spectrometry without chemical procedures. Both the setups (a) and (b) were used to measure the production cross sections of ^{99}Mo at $E_{lab} \leqq 91$ MeV by radiochemical separations. After irradiation, the target, the backing and the catcher foil were dissolved in 6M HCl solution. The radiochemical separations of molybdenum (VI) from fission product mixtures were carried out by using ion-exchange techniques. Precipitation of Mo with α-benzoin-oxime was applied to the preparation of samples for γ-ray spectrometry. Chemical yields of 49-80% were determined by neutron activation analysis. The neutron activations of the samples and standards were performed with neutron flux of 5 x 10^{13} n/cm^2/s for duration of 30 s by using the JRR-3 "PN-1" and "PN-2" equipments at JAEA-Tokai. The cross section of fission products, σ, was calculated by the following equation,

$$\sigma = \frac{C_\gamma}{\varepsilon_c \, \varepsilon_\gamma I_\gamma N \phi (1 - e^{-\lambda T})} ,$$

where C_γ is the counting rate of the photo-peak area at the end of irradiation, ε_c the chemical yield, ε_γ the photo-peak detection efficiency, I_γ the emission probability of the γ-ray, N the number of target atoms, ϕ the beam flux, λ the decay constant, and T the irradiation time. The corrections for the growth and decay of parent-daughter nuclides in the β-decay chain were applied to the 140 keV photo-peak of ^{99}Mo-Tc.

[1] Japan Atomic Energy Agency (JAEA)
[2] The Institute of Physical and Chemical Research (RIKEN)
[3] University of Tokyo
[4] Niigata University

Fig. 2 shows the cross sections of ^{99}Mo as a function of incident beam energy. The solid circles and gray squares indicate the present results obtained by using the respective irradiation setup (a) and (b) in Fig. 1. Energy loss in the catcher foil (5.4 mg/cm^2 aluminum) put on the upstream of beam was calculated to be approximately 24 MeV for E_{lab} = 85 and 87 MeV [5]. The systematic errors of the energy loss calculation probably result in the small shifts of the data (gray squares) to low energy compared with the data shown by solid circles. Fission cross sections were obtained by using the fractional yield of ^{99}Mo to the total fission yield (4.1% / 200%) which was deduced from the mass yield curves at the energies $E_{lab} \geqq 91$ MeV because the mass yield curves were insensitive to the beam energies. The uncertainty of the fractional yield was estimated to be approximately 12%. It should be noted that excitation function of fusion-fission reaction was determined down to nearly two orders of magnitude smaller than the data (open circles) measured by silicon surface barrier detectors [6]. Experimental data deviate from the calculation by a one-dimensional barrier penetration model [7] (solid curve) at $E_{lab} < 86$ MeV. The energy at the point of steep falloff is in good agreement with the energy V_{KNS} = 86.8 MeV at the touching point of the projectile and the target nucleus for ^{19}F + ^{209}Bi that was estimated with Krappe-Nix-Sierk potential [2].

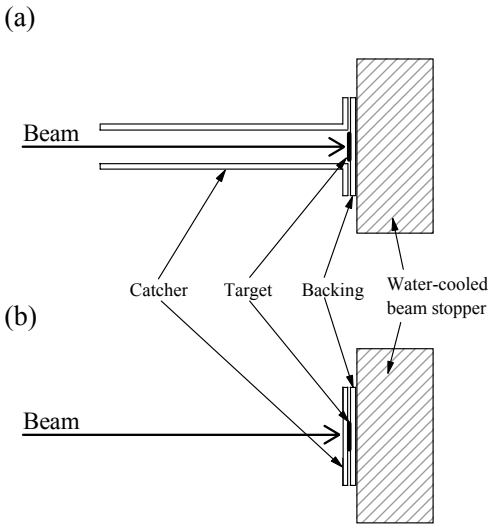

Fig. 1 Irradiation setups.

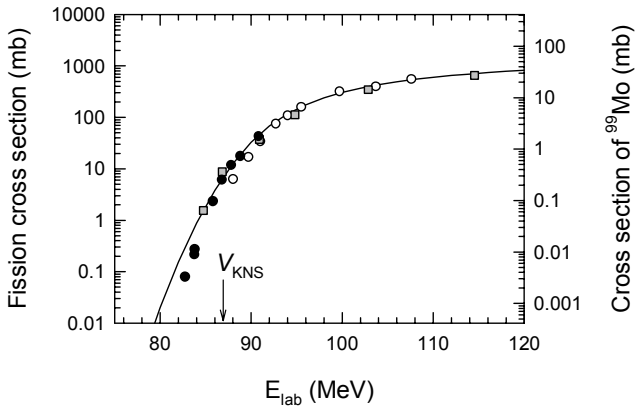

Fig. 2 Fission cross section for ^{19}F + ^{209}Bi. Solid circles and gray squares indicate present results. Open circles are taken from Ref [6]. Solid curve is calculated by a one-dimensional barrier penetration model [7].

References

[1] C. L. Jiang, et al., Phys. Rev. Lett., 89 (2002) 052701-1-4.
[2] T. Ichikawa et al., Phys. Rev C, 75 (2007) 064612-1-4.
[3] M. Dasgupta et al, Phys. Rev. Lett., 99 (2007) 192701-1-4.
[4] C. N. David and J. D. Larson, Nucl. Instrum. Methods Phys. Res. B 40 (1989) 1224-1228; C. N. David et al., *ibid*. 70 (1992) 358-365.
[5] J. F. Ziegler et al., The Stopping and Range of Ions in Solids, Pergamon Press, New York, (1985).
[6] A. M. Samant et al., Eur. Phys. J, A7 (2000) 59-64.
[7] B. B. Back et al., Phys. Rev. C 32 (1985) 195-213.

3.5 Test of time reversal symmetry using polarized nuclei

J. Murata[1], T. Akiyama[1], M. Hata[1], Y. Hirayama[2], Y. Ikeda[1], T. Ishii[4], D. Kameda[3], H. Kawamura[1], S. Mitsuoka[4], H. Miyatake[2], D. Nagae[4], K. Ninomiya[1], M. Nitta[1], E. Seitaibashi[1] and T. Toyoda[1]

In this project, time reversal symmetry is going to be tested using polarized ^{8}Li nuclei produced at TRIAC by tilted foil technique. The first test experiment RNB07K04 is performed in April 2008 [1] with unpolarized ^{8}Li beam. This report describes the second and final experiment RNB08K04. The goal of this project is to examine an existence of transverse polarization of electrons emitted from the polarized ^{8}Li nuclei in beta decay, utilizing analyzing power of Mott scattering. For non-zero value of the transverse electron polarization indicates violation of the time reversal symmetry, which almost holds in the standard model, it can be said that we are aiming to test the standard model in a highest precision in a nuclear system.

We have developed an electron polarimeter using a drift chamber, and have performed a test experiment using ^{8}Li nuclei at TRIAC in April 2008, confirming its high enough performance as a polarimeter. However, it is getting clear that only less than 1% of the recorded events satisfies real V-track filters in the offline analysis in this experiment. It means that the triggered events are dominated by background events, such as Coulomb multiple scattering and X-ray radiation, etc. In order to improve the rejection factor of the triggering system, we have developed a new FPGA based intelligent triggering system. In addition to the previous triggering logic, which composed of a coincidence between incident plastic counter and one of the stopping counters, at least two anode hits per single sense plane are requested for every six sense planes of the drift chamber in the new triggering system (DC trigger). After installing the DC trigger, the second experiment RNB08K04 is performed from September 1st to 5th, 2008 using 178keV/u ^{8}Li beam at around 100kpps intensities.

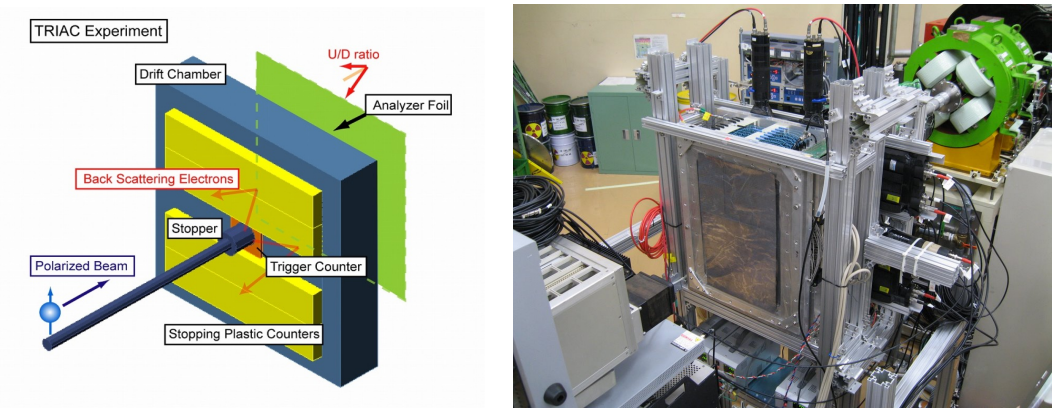

Fig. 1 Experimental setup of the RNB08K04. Electrons scattered at backward angles from the analyzer foil form “V-track”s, which is detected by the planer drift chamber.

[1] Department of Physics, Rikkyo University
[2] High Energy Accelerator Research Organization (KEK)
[3] Nishina Center for Accelerator Based Science, RIKEN
[4] Japan Atomic Energy Agency (JAEA)

The purpose of the experiment is:

1. To test the feasibility of the drift chamber based transverse polarization detectors, aiming to utilize it on the next project being planned to be performed at TRIUMF.
2. To perform a physics data taking, aiming to provide the first experimental test of the time reversal symmetry in nuclear beta decay, without suffering from the dominant scattering background by utilizing a event by event V-track reconstruction technique.

As a result, we have successfully recorded about 1M V-track events from polarized ^{8}Li nuclei in this measurement. Thanks to the DC trigger, purity of the real V-tracks in the recorded gains more than 10 times, and the computer live time is almost 100% in the measurement. In order to cancel geometrical asymmetries etc, the spin direction of incident ^{8}Li beam is flipped every 5 minutes by rotating the tilted foil angles. Totally 17G ^{8}Li ions are implanted on the annealed platinum stopper, which sandwiched by spin holding permanent magnets. About 1.6G plastic triggers are generated at around 12kHz, and finally 13M DC triggered events are recorded at only around 0.1kHz. After the offline data analysis, about 1M V-track events are successfully reconstructed.

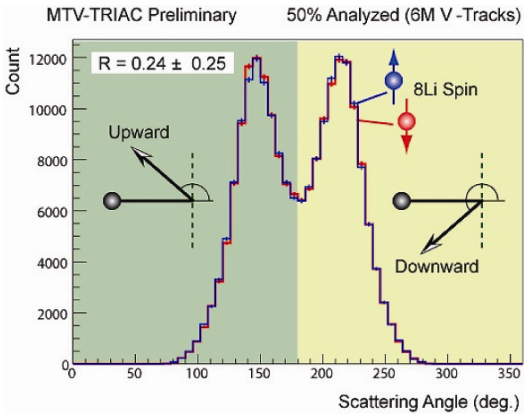

Fig. 2 Scattering angular distribution of the V-track events.

Mott scattering angular distribution is obtained as shown in Figure 2, for both spin-up and -down settings. If time reversal symmetry is broken, the two distributions do not show same shapes. Obtained results from the preliminary analysis is consistent with zero. However, a slight systematic tendency of having non-zero effect is observed in some aspects.

In summary, we have successfully performed a test of time reversal symmetry using polarized ^{8}Li nuclei at TRIAC, as the first measurement using event by event V-track reconstruction without suffering from the dominant backgrounds. The present experiment shows the enough performance as electron transverse polarimeter, which is going to be used at TRIUMF.

References

[1] J. Murata *et al*., JAEA-Tokai Tandem Annual Report 2007 (2008) 58-59

This is a blank page.

CHAPTER 4

Nuclear Chemistry

This is a blank page.

4.1 Anion-exchange experiment of Db with 0.31 M HF/0.10 M HNO_3 solution

Y. Kasamatsu[1,2], A. Toyoshima[1], M. Asai[1], K. Tsukada[1], Z. Li[1], Y. Ishii[1], T.K. Sato[1], I. Nishinaka[1], T. Kikuchi[1], H. Haba[2], Y. Kudou[2], N. Sato[2], Y. Oura[3], K. Akiyama[3], K. Ooe[4], H. Fujisawa[4], A. Shinohara[5], S. Goto[5], H. Kudo[5], M. Araki[6], M. Nishikawa[6], A. Yokoyama[6] and Y. Nagame[1]

Chemical experiments of element 105 (Db), the group-5 element in the 7th period, have been performed by comparative studies with its homologues Nb and Ta and the pseudo homologue Pa [1]. Only few clear results have been, however, obtained and little is known about the chemical properties of Db. For a deeper understanding of the properties of Db, more detailed chemical investigations are required. In our previous work [2], anion-exchange behavior of Nb, Ta, and Pa in HF/HNO_3 solution was systematically investigated by a batch method, and significantly different behavior among these elements was observed. It is very interesting to explore how Db behaves in the anion-exchange chromatography. Based on the results of online anion-exchange experiments with Nb and Ta [3], we conducted the first anion-exchange experiment of Db in 0.89 M HF/0.30 M HNO_3 solution [4]. Unfortunately, the obtained distribution coefficient, K_d, was an upper limit due to the small α events of Db. In the present experiment, the anion-exchange behavior of Db in 0.31 M HF/0.10 M HNO_3 was studied by using a newly developed rapid ion-exchange and α-spectroscopy apparatus "AIDA-II" [5].

Dubnium-262 was produced in the $^{248}Cm(^{19}F, 5n)$ reaction. Reaction products were continuously transported by a He/KF gas-jet system to the collection site of AIDA-II in the chemistry laboratory. The products collected for 83 s were dissolved in 300 μL of 0.31 M HF/0.10 M HNO_3 solution ($[F^-]$ = 0.0030 M) and were fed onto the column (ϕ1.0 mm × 3.5 mm) filled with the anion-exchange resin MCl GEL CA08Y at a flow rate of 1.2 mL/min. The eluate was collected on a 15 mm × 300 mm tantalum sheet which was continuously moving toward an α-particle detection chamber at 20 mm/s (fraction 1). The sample on the sheet was automatically evaporated to dryness with a halogen heat lamp and was subjected to an α-particle measurement in the chamber equipped with an array of 12 silicon PIN photodiode detectors [5]. The remaining Db on the resin was stripped with 290 μL of 0.015 M HF/6.0 M HNO_3. The effluent was collected on another sheet and was subjected to the α-particle measurement in the same way (fraction 2). This anion-exchange cycle was repeated 1222 times.

A total of 26 α counts were detected in the energy region of interest for the decay of 34-s ^{262}Db and its daughter 3.9-s ^{258}Lr. By correcting for background α counts, the number of α counts ascribed to the decay of the nuclides was evaluated as 9.7 for fraction 1 and 7.6 for fraction 2. The percent adsorption (%*ads*) of

[1] Japan Atomic Energy Agency (JAEA)
[2] The Institute of Physical and Chemical Research (RIKEN)
[3] Tokyo Metropolitan University
[4] Niigata University
[5] Osaka University
[6] Kanazawa University

56^{+16}_{-13}% was obtained according to an equation of $\%ads = 100 \times A_2 / (A_1 + A_2)$, where A_1 and A_2 are radioactivities in the fractions 1 and 2, respectively. The K_d value of Db was evaluated from the *%ads* value with the relationship between the *%ads* values and the K_d values of Nb and Ta [3] and is plotted in Fig. 1 together with the upper limit in 0.89 M HF/0.30 M HNO_3 obtained previously [4]. It is found that the adsorption of Db on the resin in the solution with $[F^-]$ of 0.0030 M is considerably weaker than that of the closest homologue Ta in the periodic table and is similar to that of the lighter homologue Nb and the pseudo homologue Pa.

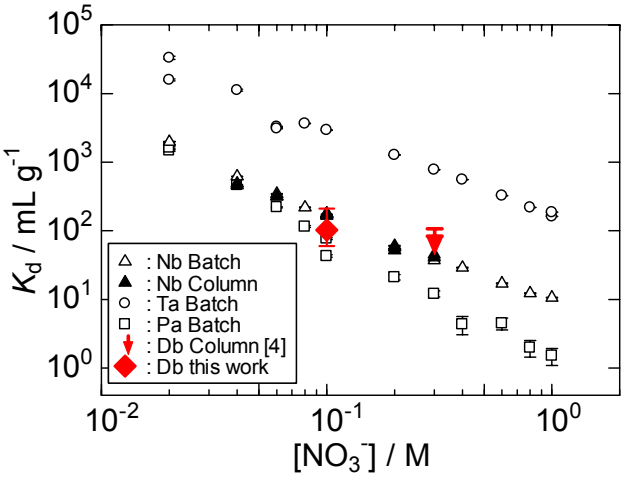

Fig. 1 K_d values of Nb, Ta, Pa, and Db as a function of $[NO_3^-]$ at constant $[F^-]$ of 0.0030 M.

References

[1] J. V. Kratz, The Chemistry of Superheavy Elements, Kluwer Academic Publishers, Dordrecht (2003) 175-191.

[2] Y. Kasamatsu *et al.*, J. Radioanal. Nucl. Chem. 279 (2009) 361-367.

[3] Y. Kasamatsu *et al.*, JAEA-Review 2007-046 (2008) 65-66.

[4] Y. Kasamatsu *et al.*, JAEA-Review 2008-054 (2008) 65-66.

[5] K. Tsukada *et al.*, JAEA-Review 2008-054 (2008) 67-68.

4.2 Development of on-line isothermal gas chromatographic apparatus for ^{265}Sg

T.K. Sato[1], K. Tsukada[1], M. Asai[1], A. Toyoshima[1], Y. Kasamatsu[1], Y. Ishii[1], Z. Li[1], T. Kikuchi[1,2] and Y. Nagame[1]

To investigate chemical properties of the transactinide element seaborgium (Sg, Z=106), we have developed an on-line isothermal gas chromatographic apparatus. The on-line experiments with the group-5 elements using the short lived ^{104}Mo and ^{173}W as the homologues of Sg were conducted. The nuclide ^{173}W was produced in the ^{nat}Tb(^{19}F, xn) reaction at the JAEA tandem accelerator facility and ^{104}Mo was provided from ^{252}Cf spontaneous fission source.

A schematic diagram of the developed apparatus is shown in Fig. 1. The apparatus consists of a target chamber, a unit of chemical reaction, an isothermal column made of quartz, and a gas-jet chamber. Nuclear reaction products recoiling out of the target were transported from the target chamber to the reaction unit continuously with carrier gas. He and Ar gas was used as carrier gas for W and Mo, respectively. In the chemical reaction unit, the reaction products were stopped on a quartz wool where the reactive gas was introduced. Air saturated with $SOCl_2$ vapor at room temperature was used as the reactive gas. Volatile

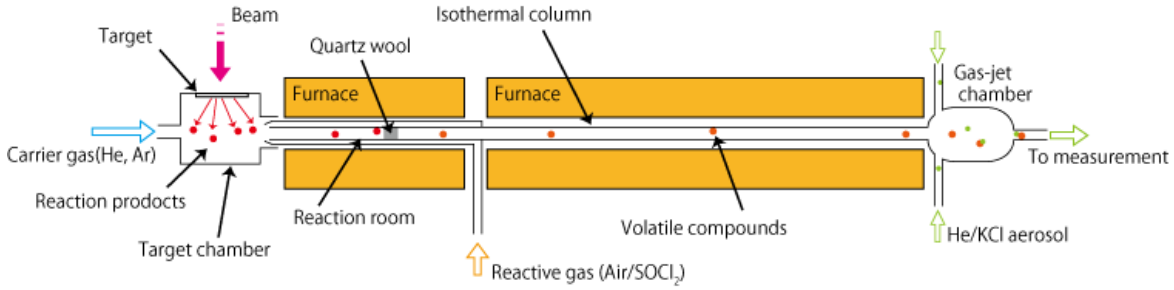

Fig.1 Schematic diagram of the on-line isothermal gas chromatographic apparatus combined with the target chamber.

species produced in the reaction unit were then transported along the isothermal column by the carrier gas flow. Volatile compounds leaving the column were attached to KCl aerosol particles in the gas-jet chamber for transport to a detection system. The radioactivity-laden-aerosol was deposited on a glass filter at the collection site of the detection system. An HP-Ge detector was used to measure the γ-rays of each nuclide.

In order to obtain optimum condition for production of volatile compounds in the online experiments, the chemical yields were measured as functions of the flow rate of the He carrier gas, the flow rate of the reactive gas, and the temperature of the reaction unit. The optimum condition was as follows: 0.75l/min of He carrier gas flow rate, 200ml/min of the reactive gas flow rate and reaction room temperature of 600°C.

[1] Japan Atomic Energy Agency (JAEA)
[2] Ibaraki University

At the above conditions, we measured the relative chemical yields of volatile compounds of ^{173}W and ^{104}Mo as a function of the isothermal temperature (Fig.2). The average yield of Mo remained constant down to 200°C, rapidly dropped below 150°C to about 10 percent at 50°C while that of W remains constant down to 300°C and rapidly dropped to around 0 percent at 200°C. The behavior of Mo and Ta were the same as that obtained in [1].

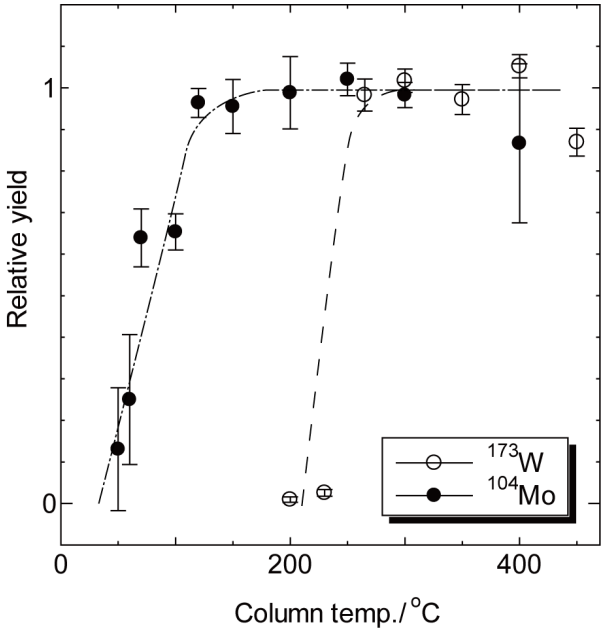

Fig.2 Measured relative yields of volatile species produced under chlorinating conditions with ^{104}Mo and ^{173}W as a function of the isothermal temperature.

References

[1] M. Gärtner et al.,Radiochim. Acta, 78 (1997) 59-68.

4.3 Ion-exchange behavior of Zr and Hf as homologues of element 104, Rf, in H_2SO_4 solutions

Z.J. Li[1], A. Toyoshima[1], K. Tsukada[1] and Y. Nagame[1]

We have systematically investigated complex formation of Rf, e.g. chloride, nitrate, and fluoride complexes and found that Rf behaves like the group-4 elements Zr and Hf in HCl and HNO_3, but significantly different from Zr and Hf in HF and in HF/HNO_3 mixed solutions [1-5]. The stability of Rf chloride complexes is larger than that of Zr and Hf complexes [1], while the formation constant of $[RfF_6]^{2-}$ is determined to be at least one order of magnitude smaller than those of $[ZrF_6]^{2-}$ and $[HfF_6]^{2-}$ [4]. The sulfate ion SO_4^{2-} is a strong complexing agent for the group-4 elements. The stability of Zr and Hf complexes formed with the various inorganic ligands decreases in the order of $F^- > SO_4^{2-} >> Cl^- \geq NO_3^-$ [6]. Therefore, it is of a great interest to investigate the properties of Rf sulfate complexes by comparing with those of Zr and Hf sulfate complexes. In the present study, the ion-exchange behavior of Zr and Hf in H_2SO_4 has been studied by a batch method to clarify a predominant chemical species of these elements adsorbed on cation- and anion-exchange resins.

The carrier-free radiotracers ^{88}Zr ($T_{1/2}$ = 83.4 d) and ^{175}Hf ($T_{1/2}$ = 70.0 d) were produced in the ^{89}Y(*p, 2n*) and ^{175}Lu(*p, n*) reactions, respectively, at the JAEA tandem accelerator and were stocked in 0.1 M H_2SO_4. The cation- and anion-exchange resins used were MCI GEL CK08Y and CA08Y. A portion of 5 - 200 mg of the resin and 3 mL of a desired solution containing 50 μL of the radiotracer solution were added into a polypropylene tube and were mixed for 24 h at 25 ± 1 °C. After centrifugation, a 1 mL aliquot was pipetted and subjected to γ-ray measurement with a Ge detector. Reference experiments without the resin were also carried out. The number of the ^{88}Zr and ^{175}Hf atoms in each batch experiment was about 10^9. The distribution coefficient, K_d in units of mL/g, was calculated in terms of $K_d = A_r V_s/(A_s m_r)$, where A_r and A_s are the radioactivities (Bq) in the resin and solution phases, respectively, V_s is the volume of the solution (mL) and m_r is the mass of the dry resin (g).

In Figs. 1(a) and 1(b), the variation of the K_d values of Zr and Hf on the cation- and anion-exchange resins in H_2SO_4 is plotted as a function of $[H^+]_{eq}$ and $[HSO_4^-]_{eq}$, respectively. It can be seen that the ion-exchange behavior of Zr and Hf is basically similar to each other, and that Zr and Hf are adsorbed on the cation-exchanger as well as anion-exchanger. The adsorption sequence on the cation-exchanger is Hf > Zr, while that on the anion-exchanger is Zr > Hf, confirming that Zr has a stronger ability to form sulfate complexes than Hf [6]. In 0.11–0.99 M H_2SO_4 (0.116 M ≤ $[H^+]_{eq}$ ≤ 1.00 M and 0.097 M ≤ $[HSO_4^-]_{eq}$ ≤ 0.980 M), the log K_d values of Zr and Hf on the cation-exchanger linearly decrease with log $[H^+]_{eq}$ with the slopes of -4.1 ± 0.1 and -3.9 ± 0.1, respectively, and those on the anion-exchanger also decrease with log $[HSO_4^-]_{eq}$ with the slopes of -2.0 ± 0.1 and -1.9 ± 0.1, respectively. The slope analysis shows that M^{4+} and $M(SO_4)_3^{2-}$ (M = Zr and Hf) are the predominant cationic and anionic species of Zr and Hf adsorbed on the resins, respectively.

[1] Japan Atomic Energy Agency (JAEA)

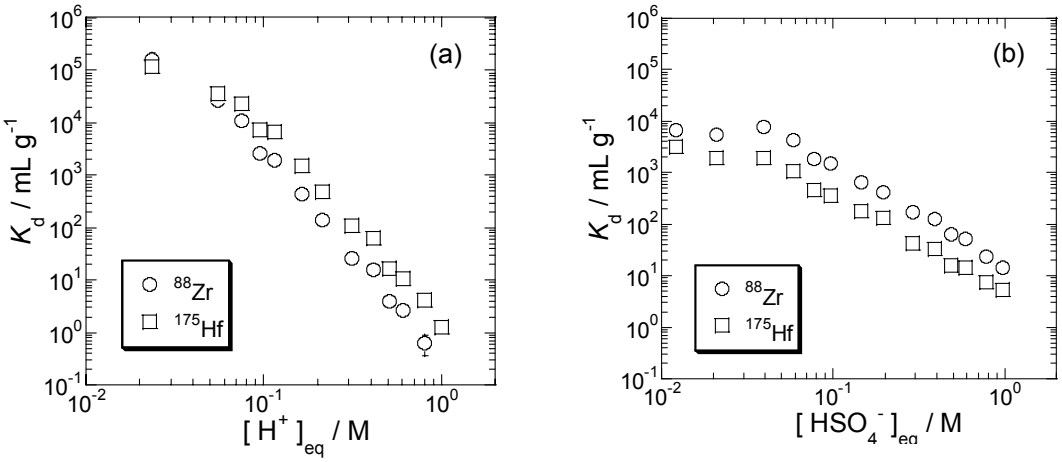

Fig. 1. Variation of the K_ds of ^{88}Zr and ^{175}Hf on (a) the cation-exchanger CK08Y and (b) the anion-exchanger CA08Y as a function of $[H^+]_{eq}$ and $[HSO_4^-]_{eq}$, respectively, in 0.018 - 0.99 M H_2SO_4 solutions.

Theoretical calculation has suggested that the affinity of the SO_4^{2-} ion to the group-4 elements decreases in the sequence of Zr > Hf > Rf [7]. Therefore, the K_d values of Rf on the cation-exchange resin could be larger than those of Zr and Hf, while those on the anion-exchange one are expected to be smaller. Considering the short life of 78s-^{261}Rf and the currently applied AIDA system (an automated ion-exchange separation apparatus coupled with the detection system for alpha-spectroscopy) [1-5] that uses 1.6 mm i.d. × 7.0 mm and 1.0 mm i.d. × 3.0 mm micro-columns, we are able to study Rf behavior under the conditions with the K_d values of 20–500 mL/g. Thus, on-line experiments with ^{261}Rf on the cation-exchange resin in 0.2–0.5 M H_2SO_4 and on the anion-exchange resin in 0.1–0.4 M H_2SO_4 could be performed to analyze the adsorption property of Rf on the resin.

References

[1] H. Haba *et al*., J. Nucl. Radiochem. Sci., 3 (2002), 143-146.
[2] H. Haba *et al*., J. Am. Chem. Soc., 126 (2004), 5219-5224.
[3] A. Toyoshima *et al*., J. Nucl. Radiochem. Sci., 5 (2004), 45-48.
[4] A. Toyoshima *et al*., Radiochim. Acta, 96 (2008), 125-134 .
[5] Y. Ishii *et al*., Chem. Lett., 37 (2008), 288-289.
[6] D.I. Ryabchikov *et al*., J. Inorg. Nucl. Chem., 26 (1964), 965-980.
[7] V. Pershina *et al*., Radiochim. Acta, 94 (2006), 407-414.

4.4 Production of Nb and Ta tracers for chemistry of Db

S. Goto[1], T. Kawasaki[2], T. Hasegawa[2], Y. Shigeno[2], H. Kudo[2], K. Tsukada[3], M. Asai[3], A. Toyoshima[3] and Y. Nagame[3]

Since a transactinide element has a very short life and its production cross-section is very small, only a very little quantity — usually one atom — is handled for a chemistry experiment at a time. To investigate the chemical property of such transactinide element, it is necessary that many repetition experiments in terms of a rapid chemistry method are performed until sufficient statistics are obtained. In other words, it takes very long time to even one experimental condition. Thus, the off-line experiment using a light homologue will be valid for an efficient on-line experiment. The aim of this work is to produce the non-carrier tracer for carrying out the off-line chemical experiments.

For the chemistry experiments of Db, the radioactive isotopes ^{95g}Nb ($T_{1/2}$ = 35 d) and ^{179}Ta ($T_{1/2}$ = 665 d) were selected as a tracer in consideration of whether measuring their gamma-ray (or x-ray) is possible and whether the half life is long enough. The tracers were produced using the ^{96}Zr(p, $2n$)^{95g}Nb, ^{179}Hf(p, n)^{179}Ta and ^{180}Hf(p, $2n$)^{179}Ta reactions with the JAEA tandem accelerator. The ^{nat}Zr foils (13 mg cm^{-2} × 4) and the Hf foils (33 mg cm^{-2} × 4) covered with aluminum foils were stacked and placed at the end of the R2 beam line. The two Zr foils were put on the beam upstream to make the proton energy the optimal to the intended nuclear reactions. The proton beam energies on the Zr and Hf target were about 14 MeV and 11 MeV, respectively, according to the energy loss calculation. The irradiation time was 17 hours, and the average beam current was about 1.7 μA. The irradiated targets were brought to Niigata University after cooling down the activity of the by-products such as ^{90g}Nb ($T_{1/2}$ = 14.6 h), ^{92m}Nb ($T_{1/2}$ = 10.15 d), and ^{96}Nb ($T_{1/2}$ = 23.4 h). The activities of ^{95g}Nb and ^{179}Ta were 1 MBq and 530 kBq, respectively, after 3 weeks from the end of bombardment. Those were enough to perform the experiment for a few months.

Each tracer nuclide was separated from the target material using an anion-exchange method. The target foils were dissolved in 1 mL concentrated HF solution. After evaporation to dryness, the residue was dissolved 1 mL 8 M HCl-2 M HF solution. The solution was introduced to the anion-exchange resin (Dowex 1x8 200–400 mesh, 8 mm i.d. × 60 mm). The bulk of Zr and Hf was eluted in the 8 M HCl-2 M HF solution. Then, 2 M HNO_3-0.1 M HF solution was fed onto the column to elute the niobium tracer. The tantalum tracer was finally eluted in 2 M HNO_3 solution. Each tracer fraction was dried and was dissolved in conc. HF as stock solution. Using the prepared tracers, solvent extraction behavior of 5th-group elements with Aliquat 336 (methyl-tri-octyl ammonium chloride) from hydrofluoric and hydrochloric acid solution has been researched at Niigata University.

[1] Center for Instrumental Analysis, Niigata University
[2] Faculty of Science, Niigata University
[3] Advanced Science Research Center, JAEA

4.5 Synthesis of water-soluble encapsulated-radioisotope fullerenes

K. Sueki[1], K. Akiyama[2], K. Tsukada[3], M. Asai[3], A. Toyoshima[3] and Y. Nagame[3]

Water-soluble fullerene derivatives have been investigated to date mostly within the framework of biological and medical applications. We investigate to trace the synthesis process of water-soluble encapsulated-radioisotope fullerenes using the recoil of nuclear reaction.

In order to produce $^{75}Se@C_{60}$[1] about 60 mg C_{60} fullerenes powder was mixed homogeneously with about 60 mg of As_2O_3 and used as the target material. Proton irradiation with beam energy of 13 MeV was performed at the TANDEM. Radioisotopes of ^{75}Se can be produced by $^{75}As(p,n)^{75}Se$ reaction. The beam intensity was typically 1 μA and irradiation time was about 2 h. The irradiated fullerene samples were dissolved in CS_2 after it was filtrated to remove insoluble materials through a membrance filter (pore size = 0.2 μm). The separation of the $^{75}Se@C_{60}$ from the solved sample was achieved by two steps HPLC which are the HPLC processes on 5PBB and Buckyprep columns.
Toluene solutions of isolated $^{75}Se@C_{60}$ with C_{60} were vigorously vibrated with saturation KOH aq containing few drops of TBAH (10 % in water) as catalyst at room temperature. The sharking times were 5 - 480 minutes. The reaction mixture was filtrated by 0.2 μm PTFE filter. The precipitate was rinsed with methanol to ensure the removal of the catalyst and KOH. The rinsed precipitate was dissolved in 3 mL distilled water for 7 hours. The resultant brown solution was the passed down a Sephadex G25 size-exclusion gel chromatography column using distilled water as the eluent. All products of reaction process were traced 264.7 keV γ-emission of ^{75}Se by an HPGe detector.

We obtained which the activity ratios of ^{75}Se in three phases (Organic phase, KOH aq. phase, and precipitate) as function of sharking time as shown in Fig.1, and which the fraction yields ($^{75}Se@C_{60}$ fraction in 21 - 60 drops and small molecule fraction in 61 – 100 drops) of ^{75}Se in dissolved precipitate through a Sephadex G25 as function time of sharking time as shown in Fig. 2. The sharking time was changed the distributions of the activity to a KOH aq. phase and precipitate. As sharking time is long, the activity exists in the KOH phase, and the fraction yields of $^{75}Se@C_{60}$ increased. These results suggest the chemical behavior corresponded to the $^{153}Sm@C_{82}$ data[2].

[1] University of Tsukuba
[2] Tokyo Metropolitan University
[3] Japan Atomic Energy Agency

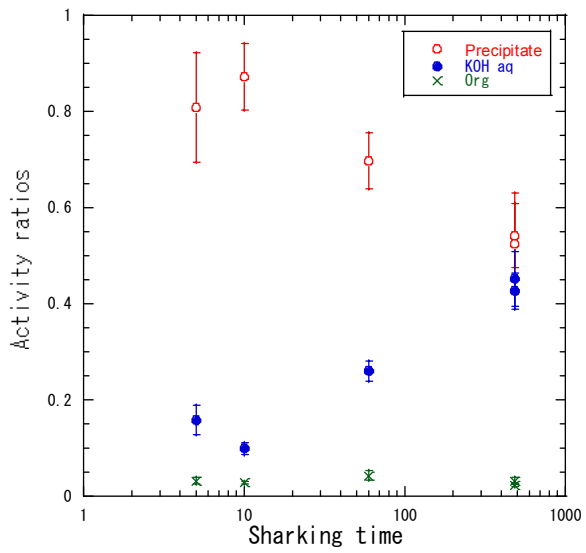

Fig. 1 Tthe activity ratios of ^{75}Se in three phases as a function of sharking time.

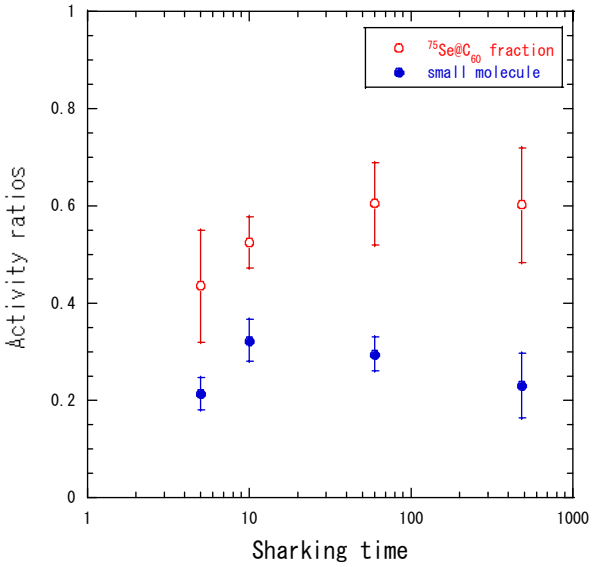

Fig. 2 The fraction yields of ^{75}Se in dissolved precipitate through a Sephadex G25 as a function of sharking time.

References

[1] K. Sueki et al., JAEA-Tokai TANDEM Annu. Rep. 2006, JAEA-Review 2007-046(2008)68-69

[2] K. Sueki and Y. Iwai, J. Radianal. Nucl. Chem. 272 (2007) 505-509.

This is a blank page.

CHAPTER 5

Nuclear Theory

This is a blank page.

5.1 Non-monotonic evolution of the shell gap beyond N=28 caused by the interplay between central and tensor forces

Y. Utsuno[1], T. Otsuka[2], B.A. Brown[3], M. Honma[4] and T. Mizusaki[5]

Evolution of the shell structure far off the stability line has recently been a major topic in the study of nuclear structure. It has a direct impact on the property of nuclei: nuclear stability, level density, shape, etc. Thus, understanding how the shell structure behaves in unknown regions is also important from the viewpoint of application of nuclear physics such as atomic energy and nuclear astronomy. The potential model such as the Woods-Saxon potential has been successful [1] in describing the evolution of the shell structure mainly near the stability line, giving a mild change of the shell structure. On the other hand, very sharp shell evolution has been known in very neutron-rich regions recently. The disappearance of the N=20 magic number and appearance of a new N=16 magic number is a good example.

To understand the situation, we proposed the shell evolution due to the property of effective interaction [2]. The monopole interaction, a mean attraction or repulsion between designated two orbits, differs from one another, causing the sensitivity of the shell gap to the location of the Fermi surface. In particular, it was pointed out that the tensor force is responsible for spin direction [3].

Based on the idea above, we constructed a new shell-model interaction for the full sd-pf shell space. The cross-shell interaction, connecting two nucleons in sd and pf shells, is the newly developed part. The tensor force is the $\pi+\rho$ meson exchange potential, which works well with a mean-field calculation [3]. The central force of the present interaction is determined so as to fit the central part of the GXPF1 interaction [4] by adjusting the strength of a Gaussian force. Without any direct fitting to experiment, the present interaction has been very successful in describing the evolution of shell structure from N=20 to 28 including the sharp lowering of the $1/2^+$ in K isotopes. This is accounted for by the monopole interaction between $0d_{3/2}$ and $0f_{7/2}$ much stronger than that of $1s_{1/2}$ and $0f_{7/2}$ both in the tensor part and in the central part.

The present interaction predicts an interesting evolution of the shell gap beyond N=28. Here, since the Fermi surface rises to $1p_{3/2}$, the monopole interactions of interest are that of $0d_{3/2}$ and $1p_{3/2}$ and that of $1s_{1/2}$ and $1p_{3/2}$. The tensor force plays a minor role because it is small for low-l orbit. Thus, the evolution of the $1/2^+$ beyond N=28 must be dominated by the central force. The monopole interaction by the central force is most attractive between orbits with the same node, thus more favoring attraction between $1s_{1/2}$ and $1p_{3/2}$. As a result, it is predicted that the $1/2^+$ of K isotopes turns up beyond N=28 as shown in Fig. 1. This non-monotonic behavior of the shell gap cannot be given by the potential picture.

[1] Japan Atomic Energy Agency (JAEA)
[2] University of Tokyo
[3]Michigan State University
[4] University of Aizu
[5] Senshu University

Unfortunately, the spins and parities of K isotopes beyond N=28 have not been measured yet. In Fig. 2, the energy levels of ^{48}K, only the energy level available beyond N=28, are compared between an experiment (performed by T. Ishii et al. with the JAEA Tandem) [5] and the present calculation. The observed four levels appear to correspond to 2^-, 2^-, 3^-, and 5^+ from the lowest. Since the γ ray from the 728 keV state (see Fig. 2) to the ground state was not observed, 1^- is more likely to be the ground state from the γ ray experiment. On the other hand, from a β decay experiment 2^- is more likely. This contradiction can be resolved if the M1 decay from the 3^- to the 2^- ground state is strongly hindered. It comes true if the former is the pure $\pi(0d_{3/2})^{-1}\nu(1p_{3/2})^1$ and the latter is $\pi(1s_{1/2})^{-1}\nu(1p_{3/2})^1$. Although the actual calculation gives a B(M1; 3^- to 2^-) which is not sufficiently small to account for the experiment, this direction seems to be promising to explain the confusing situation.

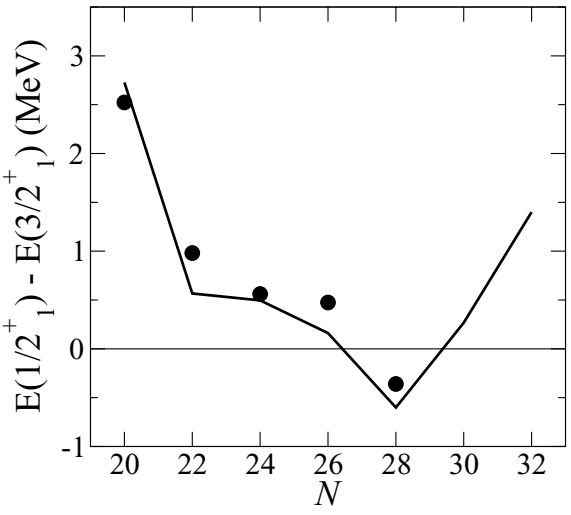

Fig. 1 Evolution of the $1/2^+_1$ state of K isotopes as a function of the neutron number. The circles are experimental data, and the line shows the shell-model result.

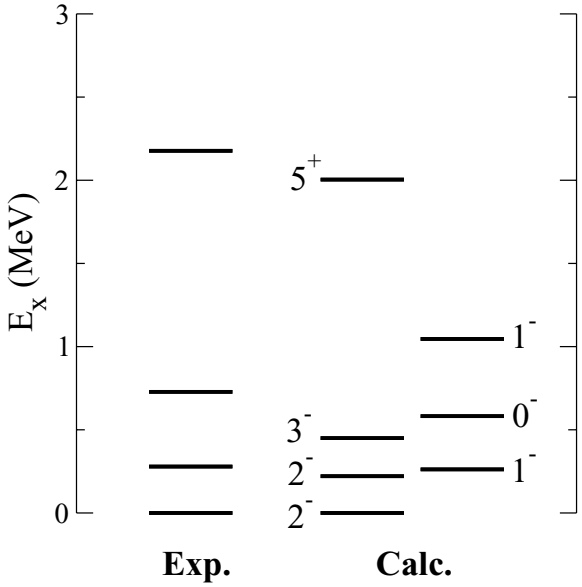

Fig. 2 Comparison of energy levels between experiment (Exp.) and the present calculation (Calc.) for ^{48}K.

References

[1] A. Bohr and B.R. Mottelson, Nuclear Structure, vol. 1, Benjamin, New York (1969).

[2] T. Otsuka et al., Phys. Rev. Lett., 87 (2001) 082502-1-4.

[3] T. Otsuka et al., Phys. Rev. Lett., 95 (2005) 232502-1-4.

[4] M. Honma et al., Phys. Rev. C, 69 (2004) 034335-1-34.

[5] T.W. Burrows (ed.), Nuclear Data Sheets, 107 (2006) 1747-1922.

5.2 Single-particle levels of spherical nuclei in the superheavy nuclear mass region

H. Koura[1]

A nucleus is a composite system consisting of protons and neutrons, and approximately 3000 nuclides have been identified [1]. However, the existence of much more nuclides is postulated theoretically [2]. How far the area of nuclei extends is an essential and important question in nuclear physics. On theoretical determination of the area, estimation of doubly-magic shell gap of superheavy nuclei is one of the most important key points.

We have developed a spherical single-particle potential applicable to a global nuclear mass region [3]. This is a modified Woods-Saxon-like potential with five parameters expressed as a function of proton number Z and neutron number N. This potential has two additional parameters compared to the Woods-Saxon potential, which makes a dip near the surface of a nucleus and broadens the potential shape outside the surface. Obtained single-particle levels give good agreement with the experimental data of doubly-magic or magic-submagic nuclei in the wide nuclear mass region ranging from ^{4}He, ^{8}He, ^{16}O to ^{132}Sn and ^{208}Pb. This single-particle potential also provides nuclear ground-state shell energies in the KTUY mass model, which gives a RMS deviation of 680 keV from experimental masses and those of approximately 300 keV from one- or two-neutron separation energies [3]. By using this single-particle potential, we estimate the single-particle levels of unknown spherical superheavy nuclei.

Fig. 1 and 2 show the single-particle levels of spherical nuclei in the superheavy nuclear mass region. All the shape of the nuclei are almost spherical by a prediction from the KTUY ground-state calculation [4]. In the neutron single-particle levels in Fig. 1, considerably large gaps of N=126 ($^{208}Pb_{126}$, known), 164 ($^{256}U_{164}$), 184 ($^{298}114_{184}$) , 228 ($^{354}126_{228}$), and 308 ($^{472}164_{308}$) are shown as the Fermi levels. These four nuclei except $^{256}U_{164}$ are estimated to be located on the beta-stability of the KTUY mass calculation [5]. Regarding the neutron case in fig. 2, the gaps of Z=82 ($^{208}Pb_{126}$, known), 92 ($^{256}U_{164}$), 114 ($^{298}114_{184}$) and 164 ($^{472}164_{308}$) are also shown, but the neighboring levels generally disperse and consequently the Fermi gaps themselves are not so notable. In the case of $^{354}126_{228}$, The Z=126 gap almost disappears.

References

[1] T. Horiguchi, T. Tachibana, H. Koura and J. Katakura, Chart of the Nulcides 2004, Japanese Nuclear Data Committee and Nuclear Data Canter, Japan Atomic Energy Rsearch Institute (2005).
[2] H. Koura, T. Tachibana, BUTSURI (the bulletin of the Physical Society of Japan), 60 (2005) 717-724.
[3] H. Koura and M. Yamada, Nucl. Phys., A671 (2000) 96-118.
[4] H. Koura, T. Tachibana, M. Uno and M. Yamada, Prog. Theor. Phys., 113 (2005) 305-325.
[5] H. Koura, T. Tachibana, BUTSURI (the bulletin of the Physical Society of Japan), 60 (2005) 717-724.

[1] Japan Atomic Energy Agency (JAEA)

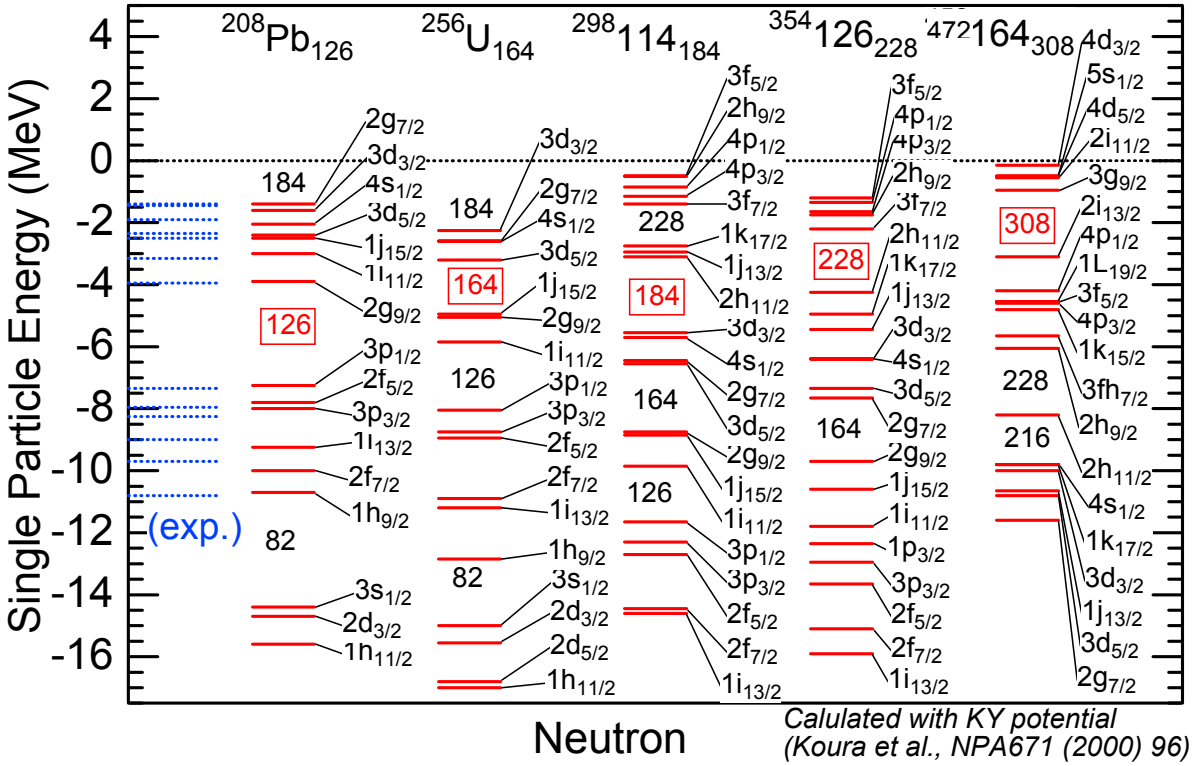

Figure 1: Neutron single-particle levels for spherical superheavy nuclei

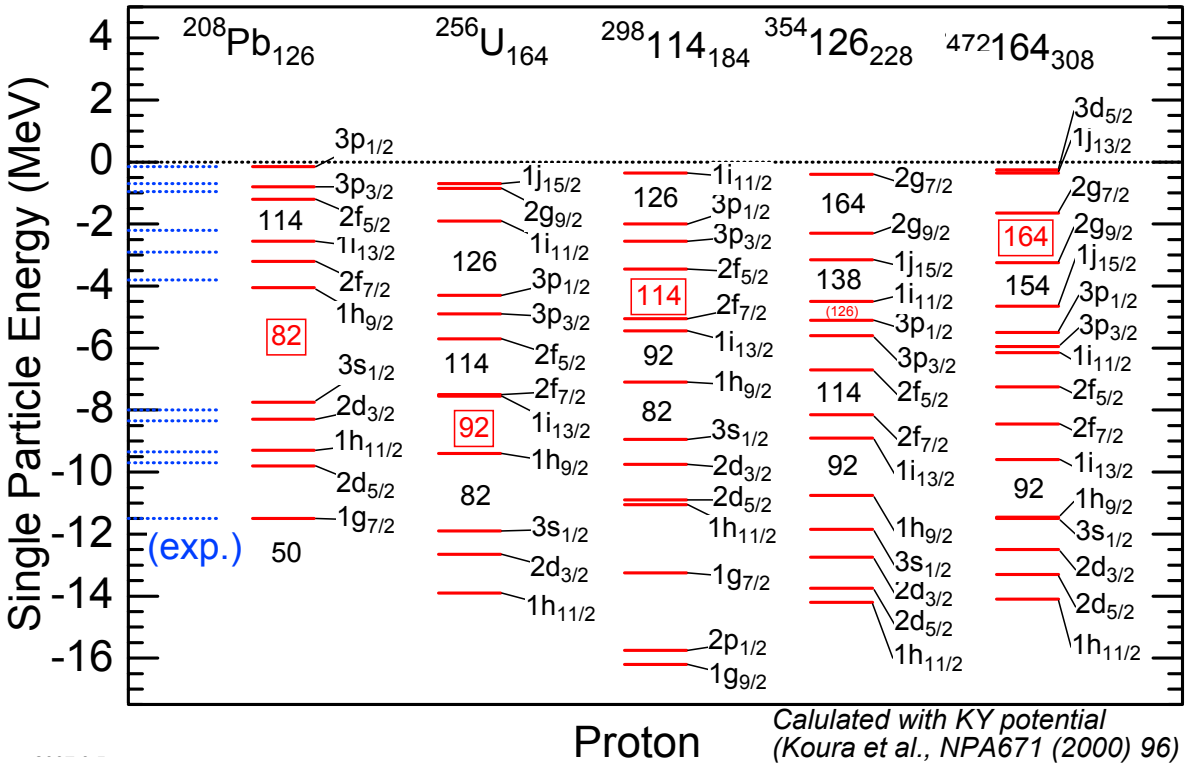

Figure 2: Proton single-particle levels for spherical superheavy nuclei

5.3 New formulation of incomplete and complete fusion cross sections with the CDCC method

S. Hashimoto[1], K. Ogata[2], S. Chiba[1,3] and M. Yahiro[2]

As a high intensity neutron source, inclusive (d,n) reactions on ^{6,7}Li targets will be used in the International Fusion Materials Irradiation Facility (IFMIF) [1]. Ye et al. [2] analyzed experimental data of the reactions at energies below 50 MeV, and found that elastic breakup processes are not enough to reproduce the data and the dominant contribution is the incomplete fusion process, where only a proton in the incident deuteron is fused into the target and the other projectile fragment (neutron) is emitted. The result is very interesting, and motivated us to construct a new method to evaluate the incomplete fusion cross section.

Since imaginary parts of p-Li and n-Li optical potentials W_c (c=p and n) describe absorption (fusion) of the particle c, the total fusion cross section is given as

$$\sigma_{tot.fu.} \propto \int dr_p dr_n \Psi^*(r_p, r_n)(W_p(r_p) + W_n(r_n))\Psi(r_p, r_n), \quad (1)$$

where Ψ is the wave function in the framework of the three-body system, and is the sum of the incomplete fusion and the complete fusion, in which both p and n are fused into the target. Using an absorption radius r_c^{ab}, which is an effective range of W_c, the integration intervals in Eq. (1) can be divided into four regions shown in Fig. 1. In the left-lower region, conditions $r_p < r_p^{ab}$ and $r_n < r_n^{ab}$ are satisfied, that is, p and n are absorbed, and therefore the complete fusion cross section is evaluated by the integration over the region. In the same way, the incomplete fusion cross sections in (d,n) and (d,p) are calculated by the integration over the right-lower and left-upper regions, respectively.

We proposed the above new method to evaluate the complete and incomplete fusion cross sections, and performed a calculation with Ψ derived by using the continuum-discretized coupled-channel method (CDCC) [3] using CDCC codes [4]. In the CDCC calculation, parameterized optical potentials of Ref. [5] are used. The absorption radii r_c^{ab}=4.0 fm are adopted satisfying the condition $W_c(r_c^{ab}) = W_c(0.0\text{ fm})/10$. In Fig. 2, calculated cross sections of each fusion in the deuteron induced reaction on ^{7}Li at incident energies below 50 MeV are shown. The solid line represents the complete fusion, and the dotted and dot-dashed lines represent the incomplete fusions in (d,n) and (d,p), respectively. The elastic breakup cross section obtained with the usual CDCC calculation is also shown by the dashed line. One sees from Fig. 2 that the contribution of the (d,n) incomplete fusion is larger than that of the elastic breakup in the energy region considered. Therefore, the incomplete fusion in (d,n) can be expected to play a major role in analyzing the inclusive (d,n) cross section. Of course, the elastic breakup process is not negligible, and actually the experimental data of the double-differential cross section of inclusive (d,n) reaction on ^{7}Li at 40 MeV are reproduced well by the sum of the two contributions calculated with the Glauber model [6]. The complete

[1] Japan Atomic Energy Agency (JAEA)
[2] Kyushu University
[3] National Astronomical Observatory of Japan

fusion cross section has the major contribution in the deuteron induced reaction, and the energy dependence is the same as that of the (d,n) incomplete fusion. Although the contribution of incomplete fusion in (d,p) is large at high energies, the cross section decreases at low energies. The difference of the energy dependence between the three fusion reactions is attributed to the p-Li and n-Li optical potentials.

We applied the new method to the analysis of the deuteron induced reaction on the ^{7}Li target. In the calculation, the effect of the deuteron breakup was taken into account explicitly by using the CDCC wave function. We found that the complete fusion and the incomplete fusions are dominant processes except the (d,p) incomplete fusion at low energies, and the energy dependence of each fusion cross section is related with that of the optical potential between the fragment and the target. Comparing the (d,n) and (d,p) incomplete fusion cross sections of the new method with those of Glauber model [6], we find a good agreement. The elastic breakup cross section at low energies is larger than that at high energies. Therefore, the contribution might become significant at a few MeV, e.g., around the Coulomb barrier. In order to investigate the reaction mechanism in detail, the development of the formulation is necessary to calculate the angular differential cross section or the energy spectrum of the reaction.

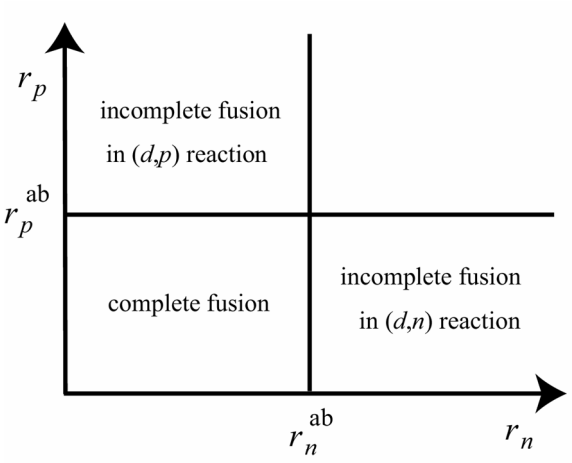

Fig. 1 Schematic illustration of divided integration intervals corresponding to each fusion reaction shown in each region.

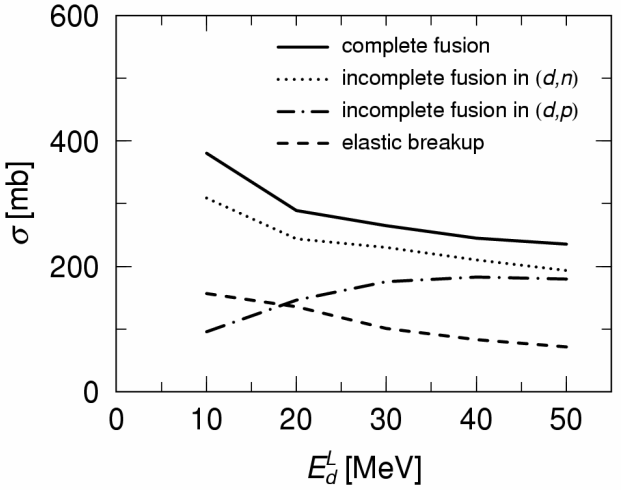

Fig. 2 Complete and incomplete fusion cross sections of d on ^{7}Li as a function of incident energy E_d^L calculated with the new method.

References

[1] H. Matsui, in Proceedings of the 23rd Symposium on Fusion Technology, Venice, Italy, 20-24 Sept. (2004).

[2] T. Ye, Y. Watanabe, and K. Ogata, in Proceedings of the 2008 Symposium on Nuclear Data, Tokai, Japan, 20-21 Nov. (2008), in press.

[3] M. Kamimura et al., Prog. Theor. Phys. Suppl. No. 89 (1986) 1.

[4] Y. Iseri et al., Bull. Res. Comput. Syst. Comput. Commun. Cent. Kyushu Univ. Vol. 5, No. 3, (2006) 117-134 (CDCDEU); Vol. 1, No. 1, (2007) 16-28 (HICADEU).

[5] T. Ye et al., Phys. Rev. C78 (2008) 024611.

[6] T. Ye, Y. Watanabe, and K. Ogata, Phys. Rev. C80 (2009) 014604.

5. 4 Equation of state of low-density nuclear matter at finite temperature

T. Maruyama[1], S. Chiba[1] and T. Tatsumi[2]

The equation of state (EOS) of nuclear matter is an important quantity for astronuclear physics. It affects the static properties of neutron stars and the dynamics of supernova explosions. For cold neutron stars, matter concerned is in beta-equilibrium and the density ranges from ~ρ_0 to several times ρ_0, where ρ_0 denotes the normal nuclear density ~0.16 fm^{-3}. For supernova matter, the temperature can be up to several tens MeV and the beta-equilibrium is not achieved. In other words the relevant condition for supernova matter has much larger variety than neutron star matter. Therefore it is rather difficult to present a theoretical EOS in a systematical way. In this report we show our attempt to calculate the EOS (density dependence of the pressure or energy) of nuclear matter at finite temperature T>0.

We employ a relativistic mean-field (RMF) plus the Thomas-Fermi model for nuclear matter, which can reproduces the saturation property of nuclear matter and properties of nuclei at T=0 [1]. The basic idea of the RMF is that the nuclear interaction is provided by the coupling of baryons with mesons σ,ω,ρ which obey the Kline-Gordon type equation of motion. To study matter at finite temperature, we leave equation of motion for mesons as in the case of T=0. Only the momentum distribution of Fermions are modified to

$$f(p;\mu,T)=\left[1+\exp\left(\left(\sqrt{p^2+m^2}-\mu\right)\Big/T\right)\right]^{-1}. \tag{1}$$

One should note that this distribution function affects the density and the scalar density of Fermions for a given chemical potential μ as follows:

$$\rho=2\int_0^\infty \frac{d^3p}{(2\pi\hbar)^3} f(p;\mu,T), \qquad \rho^s=2\int_0^\infty \frac{d^3p}{(2\pi\hbar)^3}\frac{m_N}{\sqrt{p^2+{m_N}^2}} f(p;\mu,T), \tag{2}$$

First, let us show in Fig. 1 the pressure of uniform symmetric nuclear matter. Different gray scales indicate different temperatures. The total pressure including baryonic and electronic contributions is always positive and monotonically increases as the baryon density ρ_B increases. The baryon partial pressure, on the other hand, has generally two turning points, and between those points the gradient of P_B versus ρ_B becomes negative, where uniform matter becomes unstable and non-uniform "pasta" structures [1,2,3] are expected to appear.

To calculate structure and property of non-uniform matter, we divide the whole space into equivalent cells with a geometrical symmetry, i.e. the Wigner-Seitz cells. In this approximation, we solve density profile of baryons, electrons and mesons in the Wigner-Seitz cell with an optimized size and employ the geometrical dimension of the cell which gives the minimum value of the free energy density. Fig. 2 shows typical

[1] Japan Atomic Energy Agency (JAEA)
[2] Kyoto University

density profiles of symmetric nuclear matter at temperatures T=10 MeV and T=0. First we note that pasta structures appear also in the finite-temperature case. But above about T=15 MeV, matter becomes uniform at any density. Second, baryon density in the dilute phase is positive with finite temperature, while at T=0 the dilute phase consists of only electron. Third the density profiles in both dense and dilute phases are flat. This causes a less screening of the Coulomb interaction. The surface between two phases is more vague for T=10 MeV. This causes weaker surface tension. Both the less screening and the weaker surface tension make the size of nuclear pasta smaller [1]. One can see clearly the difference of structure size in Fig. 2.

Figure 3 shows the baryon partial pressure P_B of symmetric nuclear matter versus baryon density ρ_B. In contrast with Fig. 1, pasta structures are considered in this case. One can see that pasta structures appear in the density region where $dP_B/d\rho_B$ or P_B of uniform matter are negative. For example, ρ_B <0.115 fm^{-3} for T=0 and 0.03 fm^{-3}<ρ_B <0.068 fm^{-3} for T=12 MeV.

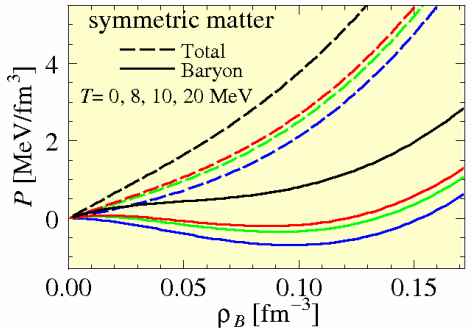

Fig. 1 Pressure versus baryon density. The temperatures from the bottom are T=0, 8, 10 and 20 MeV. The dashed curves indicate total pressure and the solid curves baryon partial pressure.

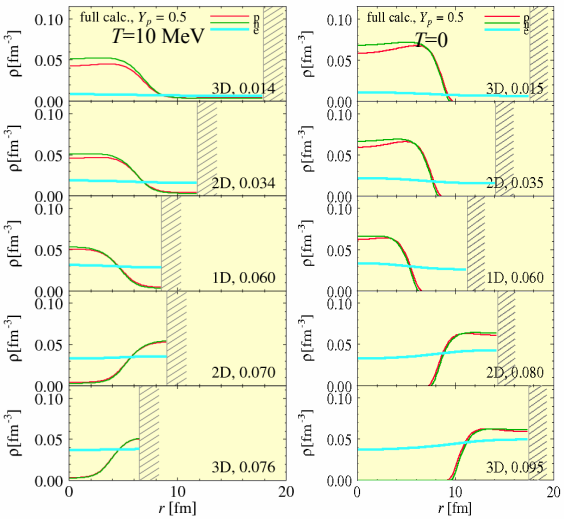

Fig. 2 Density profiles of symmetric nuclear matter in Wigner-Seitz cells at temperature T=10 MeV (left) and T=0 (right).

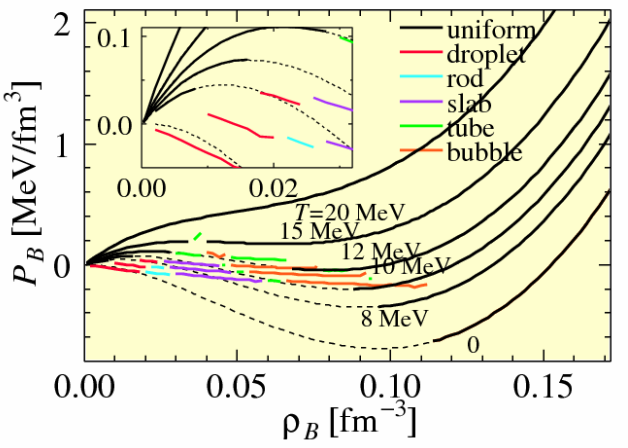

Fig. 3 Equation of state (pressure versus baryon density) of symmetric nuclear matter at several temperatures.

References

[1] T. Maruyama *et al*, Phys. Rev., C73 (2006) 035802; T. Maruyama *et al*., Recent Res. Devel. Phys., 7 (2006) 1.

[2] D. G. Ravenhall, C. J. Pethick and J. R. Wilson, Phys. Rev. Lett. 50 (1983) 2066.

[3] M. Hashimoto, H. Seki and M. Yamada, Prog. Theor. Phys. 71 (1984) 320.

CHAPTER 6

Atomic Physics and Solid State Physics

This is a blank page.

6.1 Coster-Kronig electrons from N^{q+} Rydberg states produced in high-energy collisions with He

K. Kawatsura[1,2], K. Takahiro[2], M. Sataka[3], M. Imai[4], H. Sugai[3],
K. Kawaguchi[2], H. Shibata[4] and K. Komaki[5]

High-Rydberg states in low-energy highly charged ions are produced by electron capture processes, especially double electron capture (DEC). Most of the studies on DEC process have been made on He-like ions such as C^{4+} and O^{6+} [1,2] and N^{5+} [3]. Those from dielectronic recombination (DR) processes have been measured with modest resolution for Li-like ions such as C^{3+}, F^{6+}, Ne^{7+} and Ar^{15+}. Coster-Kronig (C-K) electrons from $1s^22pnl$ states were observed from DEC and DR processes. For high-energy collisions with He, highly excited states are formed mainly by single-electron excitation of metastable $1s^22s2p$ for Be-like ions such as N^{5+}, O^{4+} and S^{12+} [4-6]. We have found with high-resolution measurements that $1s^22pnl$ states with relatively lower angular momenta are produced, while high angular momenta are produced in DEC and DR processes. Recently, the DR spectra for Li-like and Be-like N^{q+} (q=3,4) ions have been measured with high resolution at heavy-ion storage-ring [7,8]. In the present study, to compare with the DR data [7,8] and previous results obtained from 32 MeV O^{q+} + He [4,9], we have measured Coster-Kronig electrons ejected at zero-degrees in 21 MeV $N^{2+, 3+}$ + He and 14 MeV N^+ + He collisions with high resolution and systematically investigated high-Rydberg states of Be-like to B-like and C-like N ions, where the highly excited states are formed by electron excitation/ionization.

The experiments were performed at the tandem accelerator facility at the Japan Atomic Energy Agency (JAEA) of Tokai. The Coster-Kronig electrons ejected at zero-degree in the beam direction were measured using a tandem-type 45° parallel plate electron spectrometer. The primary N^{q+} ion beams were produced by using ECRTIS (Super-Nanogan) installed at the high-energy terminal of the tandem accelerator, and then accelerated up to 14 MeV for N^+ and 21 MeV for N^{2+} and N^{3+} ions. The projectile N^{q+} ions penetrated the He gas target under single collision conditions. The beam currents were 0.3~10 nA and were collected in the Faraday cup placed right after the spectrometer. All spectra were normalized to the same gas-cell target pressure and ion charge.

We have measured for the first time C-K electrons ejected from high-Rydberg states produced in high-energy collisions of N^{q+} (q=1-3) with He. Energy spectra of electrons ejected at zero degrees from moving projectiles in collisions of 14-21 MeV N^{q+} (q=1-3) + He are shown in Figs. 1-3. The representative peaks are assigned to a series of $1s^22p(^2P)nl$ -$1s^22s(^2S)\varepsilon l$' (n=5-9) for N^{3+}, $1s^22s2p(^3P)nl$ -$1s^22s^2(^1S)\varepsilon l$' (n=4-9) for N^{2+}, and $1s^22s2p^2(^4P)nl$ -$1s^22s^22p(^2P)\varepsilon l$' (n=3-8) for N^{2+} ions, respectively.

[1] Theoretical Radiation Research Laboratory
[2] Kyoto Institute of Technology
[3] Japan Atomic Energy Agency (JAEA)
[4] Kyoto University
[5] National Center for University Entrance Examinations

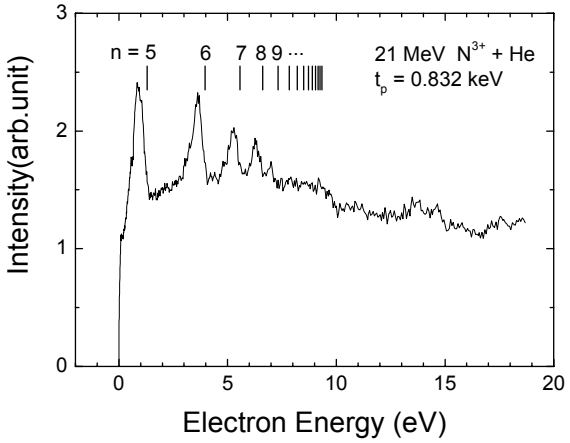

Fig. 1 High-resolution Coster-Kronig electron spectrum ejected at 0^o from the moving projectile in collisions of 21 MeV N^{3+} + He. Energy scale refers to the projectile rest frame.

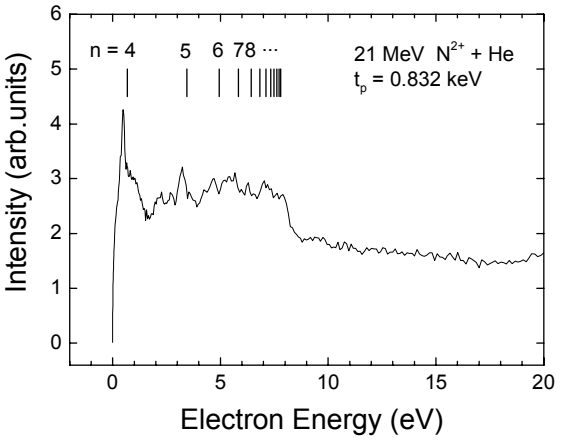

Fig. 2 High-resolution Coster-Kronig electron spectrum ejected at 0^o from the moving projectile in collisions of 21 MeV N^{2+} + He. Energy scale refers to the projectile rest frame.

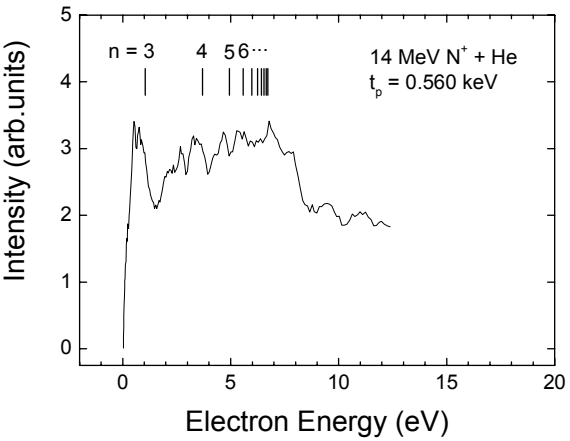

Fig. 3 High-resolution Coster-Kronig electron spectrum ejected at 0^o from the moving projectile in collisions of 14 MeV N^+ + He. Energy scale refers to the projectile rest frame.

References

[1] N. Stolterfoht et al., Phys. Rev. Lett., 57 (1986) 74-77.

[2] F.W. Meyer et al., Phys. Rev. Lett., 60 (1988) 1821-1824.

[3] M. Mack and A. Niehaus, Nucl. Instrum. Methods Phys. Res., B23 (1987) 116-119.

[4] K. Kawatsura et al., Nucl. Instrum. Methods Phys. Res., B205 (2003) 528-532.

[5] M. Sataka et al., Phys. Rev., A65 (2002) 052704 (1-11).

[6] K. Kawatsura et al., Nucl. Instrum. Methods Phys. Res., B267 (2009) 901-904.

[7] P. Glans et al., Phys. Rev., A64 (2001) 043609 (1-11).

[8] M. Fogle et al., Astronom. Astrophys., 442 (2005) 757-766.

[9] K. Kawatsura et al., Nucl. Instrum. Methods Phys. Res., B245 (2006) 44-46.

6.2 Charge state distribution of sulfur ions after penetration of C-foil targets (VI)

M. Imai[1], M. Sataka[2], H. Sugai[2], K. Kawatsura[3,4], K. Takahiro[3],
K. Komaki[5], K. Nishio[2] and H. Shibata[1]

Charge state is one of the most important aspects to study ion-solid interactions. Various processes, such as electron capture, ionization and excitation of projectile and/or target electrons, and the consequent phenomena like energy deposition into the target, i.e. stopping of projectile, are closely related with the projectile charge state and its evolution in the target. Equilibrium charge state distributions of various projectiles after passing gaseous or solid target have been extensively investigated and compiled [1], although the charge state distribution somewhat changes upon exiting the target foil. As has been presented in the previous annual reports [2], we measured the exit charge state distributions for penetrations of S^{6+} – S^{14+} ions through C-foil targets of 0.9 – 10 μg/cm^2 in thickness and performed calculations by ETACHA code [3] to succeed in reproducing the experimental results, although ETACHA has been designed for higher energy region (>10MeV/u) [4]. We have also started another simulation for S^{q+} ion fractions, in which the electron transfer cross sections $\sigma_{qq'}$ are calculated with codes applicable to the present collision energy [5]. In this report, results of our extensive measurements on higher charge state projectiles (S^{15+} and S^{16+}) at 2.0 MeV/u are presented.

The present experiments were performed at the LIR1–3 beam line of the 20UR Tandem Accelerator Facility. A beam of 2.0 MeV/u (64 MeV) S^{7+} ions was provided from the tandem accelerator within 0.1% of energy accuracy, using a calibrated energy analyzing magnet. A post-stripper C-foil of ~20 μg/cm^2 in thickness was placed after the energy analyzing magnet to produce higher charge state projectile ions. The energy losses at the post-stripper foil were estimated to be at most 0.7% by our separate measurement of cusp electron energies with zero-degree electron spectroscopy [6]. The primary S^{7+} or post-stripped S^{q+} (q = 15, 16) ion beam was directed by a switching magnet to a self-support carbon target foil of 0.9, 1.1, 1.5, 2.0, 3.0, 4.7, 6.9, 10, 54, 98, 150 or 200 μg/cm^2 in thickness. The charge state distributions after foil penetration were measured using the heavy ion magnetic spectrometer ENMA and a position-sensitive gas chamber detector. The vacuum condition inside the spectrometer was maintained below 10^{-6} Pa to eliminate the background charge exchange collisions with residual gas, which was confirmed by measurements without target foil.

Measured charge state fractions for 2.0 MeV/u S^{15+} and S^{16+} ion incidences are shown in Fig. 1. The statistical errors are less than 1% for almost all the points. Typical total error values are estimated as 20% for the smallest fractions around 1.0×10^{-5} and less than 0.5% for the largest fractions around 0.3.

[1] Kyoto University
[2] Japan Atomic Energy Agency (JAEA)
[3] Kyoto Institute of Technology
[4] Theoretical Radiation Research Laboratory
[5] National Center for University Entrance Examinations

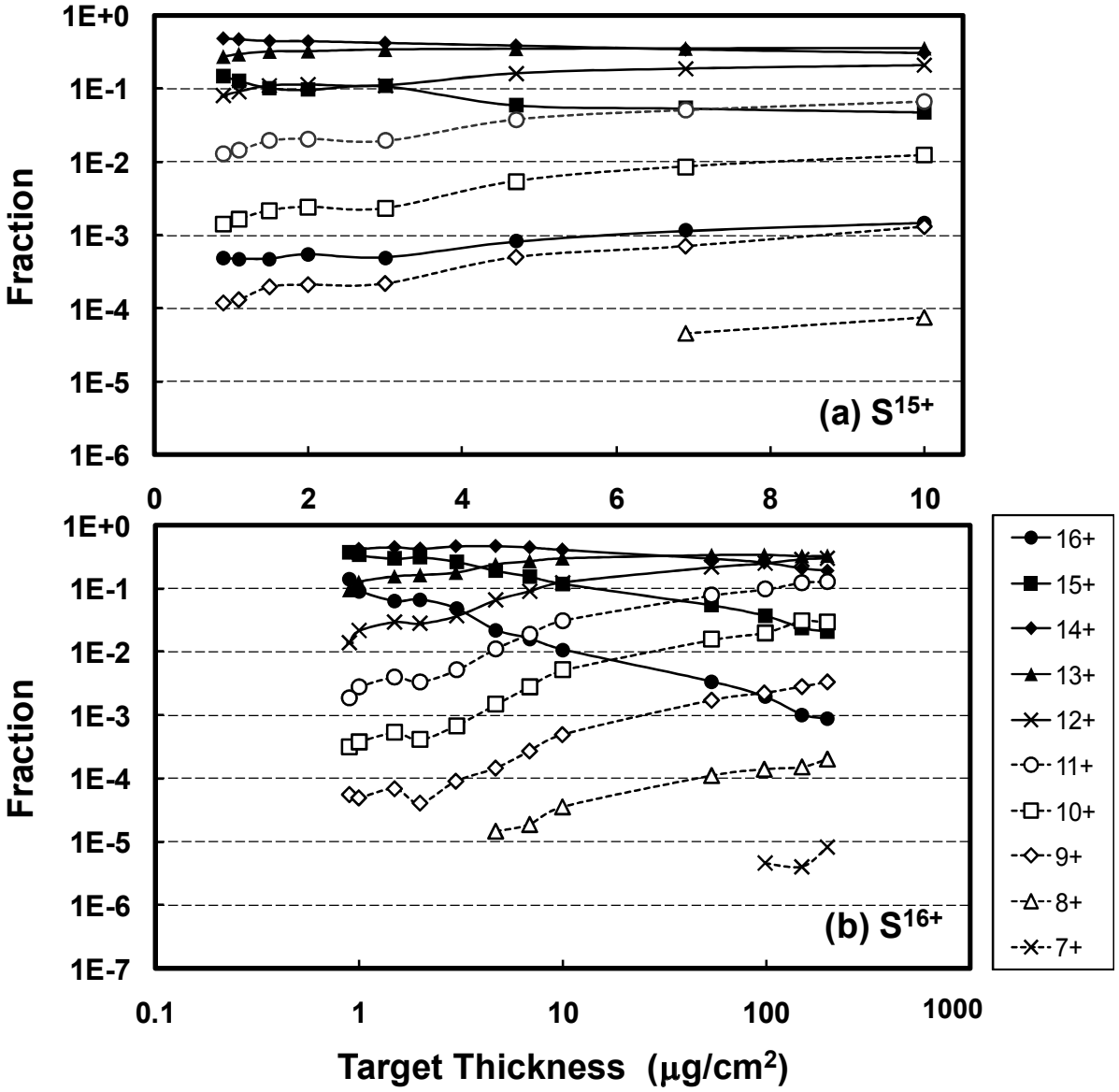

Fig. 1 Charge state evolution for 2.0 MeV/u (a) S^{15+} and (b) S^{16+} projectiles penetrated through C-foil targets of 0.9, 1.1, 1.5, 2.0, 3.0, 4.7, 6.9, 10, 54, 98, 150 and 200 μg/cm^2 in thickness.

References

[1] A. B. Wittkower and H. D. Betz, At. Data Nucl. Data Tables 5 (1973) 113–166; K. Shima *et al*., *ibid*. 51 (1992) 173–241; K. Shima *et al*., Nucl. Instrum. Methods Phys. Res., B33 (1988) 212–215.

[2] M. Imai *et al*., JAEA-Review 2007-046 (2008) 87–88; 2008-054 (2008) 89–90.

[3] J. P. Rozet *et al*., J. Phys. B22 (1989) 33–48; Nucl. Instrum. Methods Phys. Res., B107 (1996) 67–70.

[4] M. Imai *et al*., Nucl. Instrum. Methods Phys. Res., B230 (2005) 63–67.

[5] M. Imai *et al*., Nucl. Instrum. Methods Phys. Res., B256 (2007) 11–15.

[6] M. Sataka *et al*., Phys. Rev. A65 (2002) 052704 (11 pp.); M. Imai *et al*., Nucl. Instrum. Methods Phys. Res., B67 (1992) 142–145.

6.3 Diffusion of ^{8}Li short-lived radiotracer in NaTl-type intermetallic compound LiAl

H. Sugai[1], M. Sataka[1], S. Okayasu[1], S. Ichikawa[1], K. Nishio[1], S. Mitsuoka[1], T. Nakanoya[1],
S.C. Jeong,[2] I. Katayama[2], H. Kawakami[2], Y.X. Watanabe[2], H. Ishiyama[2],
N. Imai[2], Y. Hirayama[2], H. Miyatake[2], T. Hashimoto[3] and M. Yahagi[3]

Non-destructive and on-line Li diffusion experiments in Li-ionic conductors are conducted using a short-lived α-emitting radiotracer of ^{8}Li. Lithium-8 decays through β-emission to ^{8}Be with a half lifetime of 0.84 s, which immediately breaks up into two α-particles with energies broadly distributed around 1.6 MeV with a full width at half maximum (FWHM) of 0.6 MeV. The radiotracer of ^{8}Li produced as an energetic and pulsed ion beam from TRIAC (Tokai Radioactive Ion Accelerator Complex) is implanted into a structural defect mediated Li-ionic conductor LiAl. The experimental time spectra of the yields of α-particles are compared with simulated results and Li diffusion coefficients in LiAl are extracted with an accuracy less than a few percentage [1]. The diffusion coefficients obtained for well characterized LiAl crystals [2] with Li content of 48.5 at.% are presented and discussed in terms of the interaction between Li-ions and the structural defects in the specimen.

The crystal structure of LiAl in β-phase is NaTl-type (Zintl phase) [2], which is composed of two interpenetrating diamond sublattices such that each atom has eight nearest neighbors: four like and four unlike atoms. The characteristic defect structure of the compound consists of two types of defects at room temperature, i.e. vacancies in the Li sublattice (V_{Li}) and Li antistructure atoms in the Al sublattice (Li_{Al}). The concentrations of point defects, [V_{Li}] and [Li_{Al}], strongly depend on Li content; with increasing the Li content from 48 to 56 at.%, [V_{Li}] decreases from 3.5 to 0.2 at.%, while [Li_{Al}] increases from 0 to 5.4 at.%. The Li vacancy, V_{Li} is the dominant defect for the Li-deficient region, though Li_{Al} is dominant for the Li-rich region. The coexistent V_{Li} with Li_{Al} is expected to form V_{Li}-Li_{Al} complex defects as reported for the defect structure [2], which would play an important role in reducing the strain energy caused by the point defects in the real crystal. Especially, almost the same amount of V_{Li} as Li_{Al} is realized around the Li content of 51 at.%. As mentioned above, we can control the Li-vacancy concentration which is a dominant path for the Li diffusion in LiAl [2,4] with changing the Li content. Thus LiAl provides a useful and suitable field to study the Li diffusion mechanism in Li-ionic conductors, which are key materials for Li-ion batteries.

As shown in Fig. 1, the electrical resistivity of LiAl deceases monotonically with decreasing the temperature from 297.5 K to 10 K except around 100 K. The sudden decrease in resistivity around 100 K suggested the ordering of vacancies [3]. On the basis of the features of resistivities [2, 3], the Li content of 48.5 at.% and the vacancy content of 3.1 at.% were determined. Figure 2 shows the temperature (T) dependence of Li diffusion coefficients for the specimen. The Li diffusion coefficient decreases linearly

[1] Japan Atomic Energy Agency (JAEA)
[2] Institute of Particle and Nuclear Studies, KEK
[3] Aomori University

with increasing $1/T$. The activation energy is 0.155 ± 0.016 eV, which is derived from an Arrhenius relation between diffusion coefficients and $1/T$. On the other hand, the activation energies for LiAl of 48.3 at.% and 49.4 at.% Li by means of the NMR study [4] over a temperature range of 297 K to 370 K are 0.128 ± 0.003 and 0.121 ± 0.002 eV, respectively. There is no structural change like a vacancy-ordering in LiAl at the temperatures below 700 K except around 100 K [5], thus we supposed the Arrhenius relation in the temperature range of 297 K to 573 K in which we derived the diffusion coefficients. In order to make clear the above discrepancy in activation energy, we need the further systematic study on the correlation between the Li content and the temperature dependence of Li diffusion coefficient.

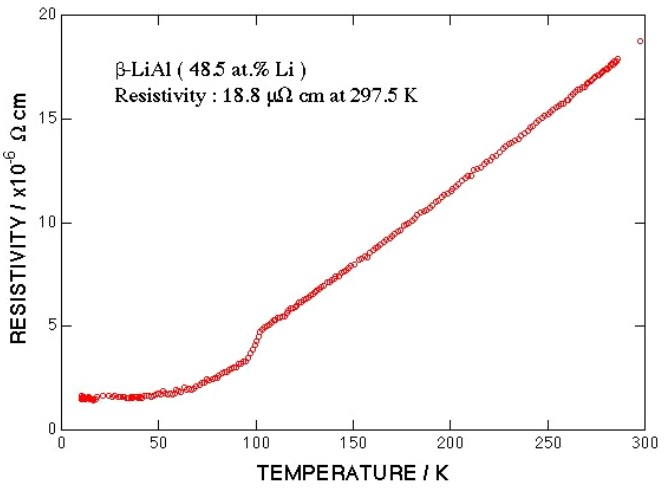

Fig. 1 Temperature dependence of electrical resistivity for LiAl of 48.5 at.% Li.

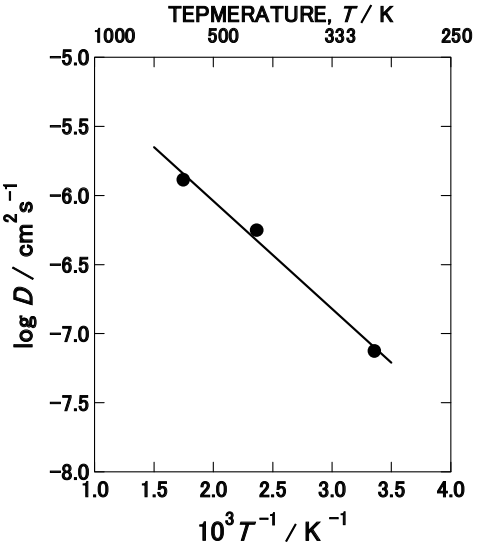

Fig. 2 Temperature dependence of the diffusion coefficients for LiAl of 48.5 at.% Li at 298 K, 423 K and 573 K.

References

[1] S.C.Jeong et al., J. Phase Equilib. diff. 26 (2005) 472-476; Nucl. Instrum. and Methods Phys. Res., B 230 (2005) 596-600; Jpn. J. Appl. Phys., 47 (2008) 6413-6415.

[2] H. Sugai et al.,Phys. Rev. B 52 (1995) 4050-4059.

[3] K. Kuriyama et al.,Phys. Rev. B 52 (1995) 3020-3022.

[4] J.C. Tarczon et al., Mater. Sci. and Eng., A 101 (1988) 99-108.

[5] H. Sugai, Solid State Ionics 177 (2007) 3507-3512.

6.4 Atomic and electronic structure modifications of copper nitride films by ion impact and phase separation

N. Matsunami[1], M. Sataka[2], H. Sugai[2], S. Okayasu[2], H. Kakiuchida[3] and M. Tazawa[3]

We have studied atomic- and electronic-structure modifications of Cu_3N films under high-energy ion impact. The films are known to thermally decompose at 250-470 ºC and X-ray diffraction (XRD) peak of metallic Cu appears [1]. There is, however, no report on ion irradiation effects on Cu_3N films. It is of interest whether the ion-induced decomposition occurs or not, as well as ion-induced modifications of atomic and electronic structures. The results are compared with those by low-energy ions [2].

Cu_3N films were prepared on R-cut-Al_2O_3 substrates at 250 ºC by using a RF-magnetron-sputter deposition method with Cu target (99.99 % purity) and pure N_2 gas of ~2 Pa. [2]. Films have (100) orientation of cubic structure (Fig. 1). The lattice parameter averaged over 20 unirradiated samples is obtained to be 0.3831 nm (sample variation of 0.4 %). This is larger by 0.4 % than the bulk value of 0.3815 nm [1, 3] and agrees with the value of films [4]. According to Rutherford backscattering spectroscopy (RBS) of 1.8 MeV He, with the stopping powers [5] and the film density of $5.4x10^{22}$ Cu cm^{-3} (6.12 gcm^{-3}), the composition is nearly stoichiometric and the film thickness is ~0.2 and ~0.1 μm for high- and low-energy ion irradiation.

After 100 MeV Xe^{+11} ion impact at $1x10^{14}$ cm^{-2}, Cu_3N XRD peaks disappear and a hump due to Cu XRD appears at the diffraction angle of ~50 º (Fig. 1). A Cu XRD peak more clearly appears for 100 keV Ne^+ ion impact at ~10^{15} cm^{-2}. These results lead to Cu phase separation by ion impact. Here, the temperature rise is estimated to be ~20 ºC for both 100 MeV Xe ion with ~1 nA and 100 keV Ne with ~1 μA [6] and thus the temperature under the ion impact is much lower than that of the thermal decomposition. The lattice compaction of ~0.5 % and 1.8 % is observed at 10^{12} (100 MeV Xe) and 10^{15} (100 keV Ne) cm^{-2}.

The electrical resistivity measured at room temperature is shown in Fig. 2. For 100 MeV Xe^{+11} ion impact, the resistivity (~10 Ωcm before the ion impact) slightly increases at ~10^{12} cm^{-2} and decreases by more than five order of magnitude at the fluence < 10^{14} cm^{-2}, where no Cu phase separation is observed. For further ion impact (>10^{14} cm^{-2}), XRD shows Cu phase separation and the resistivity further decreases. In the case of 100 keV Ne ion impact, the resistivity decreases by more than four order of magnitude at ~10^{15} cm^{-2} (no Cu phase separation) and for 10^{15} to $5x10^{16}$ cm^{-2} (Cu phase separation appears), the resistivity further decreases by two order of magnitude. According to Hall measurements, the carrier density (~10^{19} cm^{-3} for unirradiated films) increases by ~10^4 after both ion impacts.

Fig. 3 shows optical absorption spectra. The oscillating structure seen in 0.2-0.6 μm is nearly independent of the film thickness and the mean of minimum and maximum absorption coefficients in the region of 0.35-0.5 μm is obtained as $3.7x10^5$ cm^{-1}, after subtracting the film-thickness-independent background absorbance of ~0.2 in 1 - 2.5 μm. It is found that the oscillation is disappearing after the Xe ion impact. A preliminary bandgap of unirradiated film is obtained to be 1.4 eV and reasonably agrees with 1.3 to 1.24 eV for stoichiometric films [7, 8]. The bandgap is reduced to 1.2 eV (inset in Fig. 3) and ~0.5 eV after the Xe ion impact at $1.2x10^{12}$ and $2.2x10^{12}$ cm^{-2}. For the films after Ne ion impact at $3x10^{14}$ cm^{-2}, there seems to be no absorption edge and hence the bandgap does not exist or extremely small.

As described above, reduction of Cu_3N XRD intensity and the electrical resistivity, and modification of optical absorption have been observed at fluence smaller than the Cu phase separation. Also, RBS shows

[1] Division of Energy Science, EcoTopia Science Institute, Nagoya University
[2] Japan Atomic Energy Agency (JAEA)
[3] National Institute of Advanced Industrial Science and Technology (AIST)

that N atoms remain in the film after the ion impact, even though the accuracy (~30 %) is poor. Furthermore, the erosion yield (i.e., decomposition yield, see [9] for details) is obtained as 511 for 99 MeV Xe (equilibrium charge of 25) with the fluence < $2x10^{12}$ cm^{-2}, applying the carbon-foil collector method and 57 from the film thickness decrease for 100 keV Ne ion impact. The decomposition yields are much larger than the sputtering yields based on the elastic collisions, even for low-energy ion (typically ~1). These also suggest that ion-induced decomposition of Cu_3N occurs at the low ion fluence, i.e., N-release and Cu-enrich, though Cu XRD does not appear.

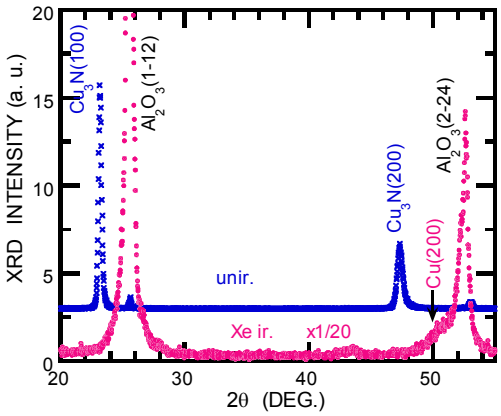

Fig. 1 XRD patterns before and after 100 MeV Xe^{+11} ion impact at $1x10^{14}$ cm^{-2}. The peaks at ~23 and 47 º correspond to Cu_3N (100) and (200) diffraction, those at 26 and 53 º Al_2O_3, that at ~50 º Cu(200). For visible clarity, XRD intensity before the ion impact is sifted by 3 and that after the ion impact is multiplied by 20.

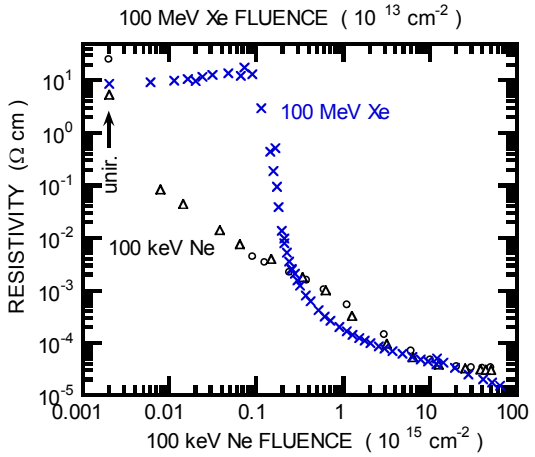

Fig. 2 Electrical resistivity versus 100 MeV Xe^{+11} (x) and 100 keV Ne (o, Δ) ion fluence.

Fig. 3 Optical absorption spectra of Cu_3N films unirradiated and irradiated with 100 MeV Xe^{+11} at $1.2x10^{12}$ cm^{-2}. The inset illustrates square root of absorbance times photon energy vs photon energy for the bandgap determination before (1.4 eV) and after the Xe ion impact (1.2 eV).

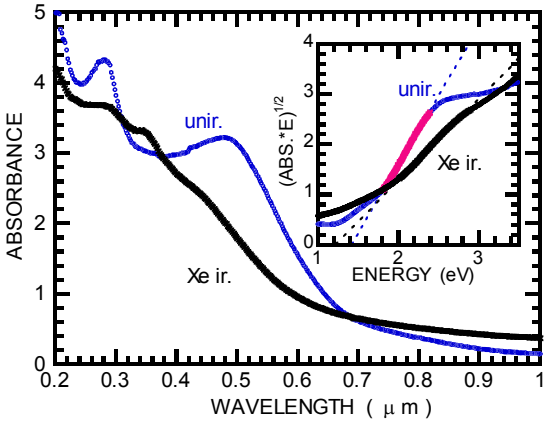

References

[1] J. F. Pierson, Vacuum 66(2002)59.
[2] N. Matsunami, H. Kakiuchida, M. Tazawa, M. Staka, H. Sugai, S. Okayasu, Nucl. Instrum. Meth. B (in print 2009).
[3] JCPDS Card number 21156.
[4] C. G.-Vega, W. Cruz, Appl. Surf. Sci. 252(2006)8001.
[5] J.F. Ziegler, J.P. Biersack and U. Littmark, The Stopping and Range of Ions in Solids, Pergamonn Press, New York (1985).
[6] N. Matsunami, T. Yajima, H. Iwahara, Nucl. Instrum. Meth. B65(1992)278.
[7] S. Ghosh, F. Singh, D. Choudhary, et al. Surf. Coat. Technol. 142-144(2001)1034.
[8] F. Fendrych, L. Soukup, L. Jastrabik, et al. Diamond Rel. Mater. 8(1999)1715.
[9] N. Matsunami, M. Sataka, S. Okayasu, H. Sugai, JAEA-Tokai Tandem Annual Report 2008, JAEA-Review 2009-036(2009)97-98

6.5 Decomposition of copper nitride films by ion impact

N. Matsunami[1], M. Sataka[2], S. Okayasu[2] and H. Sugai[2]

We have studied modifications of copper nitride (Cu_3N) films on R-cut-Al_2O_3 substrates under high-energy ion impact and found decomposition at low ion fluence ($<10^{12}$ cm^{-2}) followed by Cu phase separation, reduction of the electrical resistivity by six order of magnitude and optical absorption modifications such as reduction of the bandgap ([1,2]). We also find a remarkably large decomposition yield of Cu and N atoms by ion impact and this is non-thermal process, since the macroscopic temperature rise under ion impact is much lower than the thermal decomposition temperature of 250-470 ºC [3]. In this section, the decomposition yields are described for various high-energy ions and compared with decomposition by low-energy ions. We discuss contributions of the electronic and nuclear stopping powers to the decomposition yields, difference and similarity between decomposition and sputtering.

In the case of high-energy ion impact, carbon (C)-foil (100 nm) collector method with Rutherford back-scattering spectroscopy (RBS) of 1.8 MeV He^+ ions using the stopping powers [4] was applied to analyze Cu released from Cu_3N films [5]. One sees in Fig. 1 that the amount of Cu in the C-foil is proportional to the ion fluence up to Φ_M (Table 1). From the linear relationship, the release yield of Cu per ion is reduced using the C-foil collection efficiency of Cu (0.3), then the decomposition yield is deduced by multiplying it by 4/3, assuming stoichiometric decomposition. The results are summarized in Table 1. Since ions hit the films after pass through C-foil, the energy loss of ions in the C-foil is subtracted and the equilibrium charge state is assumed for further analysis and discussion. It is noticed that Φ_M is much smaller than the fluence for Cu phase separation. For the fluence > Φ_M, the amount of Cu shows strange behavior, i.e., it is smaller than that expected from the linear relationship mentioned above. It could be due to release of Cu by incident ions and saturation of Cu in the C-foil. It appears that decomposition yields scale with the electronic stopping power S_e as shown in Fig. 2 and is fitted to $(2.6\ S_e)^{1.6}$. These results indicate that the electronic excitations are dominant in the decomposition for high-energy ion impact. It is also noticed that the decomposition yields by high-energy ions are comparable with the electronic sputtering yields of SiO_2, in contrast with the suggested bandgap dependence [5], knowing that the bandgap of Cu_3N (~1.4 eV) is much smaller than that of SiO_2 (8.3 eV). These imply that decomposition mechanism might be different from that of the sputtering due to electronic excitations.

For the low-energy (100 keV Ne^+ and N^+) ion impact, the decomposition yields were directly obtained from the film thickness decrease analyzed by means of RBS, as given in Table 1. The decrease in the film thickness appears to be linear to the fluence up to the fluence comparable with that for Cu phase separation, in contrast with the case of the high-energy ion impacts. The contribution of the electronic excitation is estimated as ~1, using the relation mentioned above and thus the elastic collisions are dominant in the decomposition yields by low-energy ions. However, they do not simply scale with the nuclear stopping powers. Furthermore, the decomposition yields by low-energy ions are much larger than the usual sputtering yields of ceramics by 100 keV Ne, e.g., 1.57 (Cu_2O [5]), 0.4 (Si_3N_4 [6]) and 0.37 (AlN [7]), unless the surface binding energy of Cu_3N is smaller by an order of magnitude than that of these ceramics (several eV). This is another reason that the release of Cu_3N by ion impact is called decomposition in order to distinguish the sputtering based on the elastic collision cascades.

In many cases, the incident charge of high-energy ions differs from the equilibrium charge. It is of interest whether square of charge dependence via electronic stopping holds or not for the electronic excitation effects. According to preliminary results, the decomposition yield under 90 MeV Ni^{+10} (non-equilibrium

[1] Division of Energy Science, EcoTopia Science Institute, Nagoya University
[2] Japan Atomic Energy Agency (JAEA)

charge) ion impact is obtained as ~1/3 of that under 89 MeV Ni ion impact with the equilibrium charge. This ratio is larger than 1/8 estimated from the square of charge dependence of S_e and $S_e^{1.6}$ described above ($(19/10)^{2x1.6}$ =7.8). Depth dependence of charge, effective length attaining equilibrium charge and their effects on decomposition as well as decomposition mechanism is under investigation.

Table 1 Equilibrium charge Q_e, electronic (S_e) and nuclear (S_n) stopping powers in Cu_3N (keV/nm), projected range, R_p (μm) [4], film thickness d (μm), decomposition yield Y_D. Φ_M and Φ_{PS} (10^{14} cm^{-2}) are the maximum fluence for decomposition yield measurements and the fluence of Cu phase separation. The values in the parentheses are S_e and S_n averaged over the film thickness for low-energy ions.

Ions	Q_e	S_e	S_n	R_p	d	Y_D	Φ_M	Φ_{PS}
198 MeV Xe	30	26.13	0.116	11	~0.2	978	0.01	
99 MeV Xe	25	21.67	0.204	7.0	~0.2	511	0.02	1
89 MeV Ni	19	14.53	0.0321	9.6	~0.2	342	0.02	
60 MeV Ar	13	8.621	0.0142	9.2	~0.2	142	0.02	
100 keV Ne		0.289(0.296)	0.236(0.366)	0.12	0.1	57		10
100 keV N		0.363(0.378)	0.106(0.171)	0.15	0.1	12		40

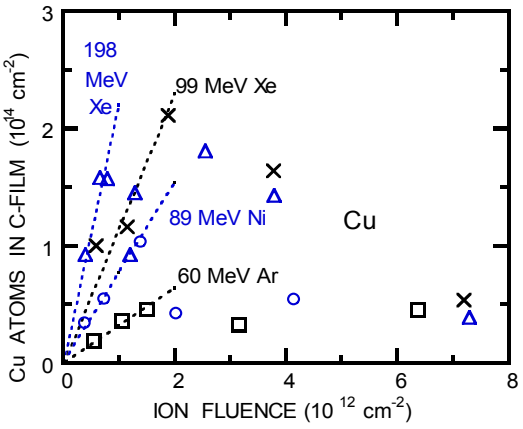

Fig. 1 Cu in carbon-foil collector vs ion fluence for 198 MeV Xe (Δ), 99 MeV Xe (x), 89 MeV Ni (o) and 60 MeV Ar (□) ion impacts on Cu_3N films.

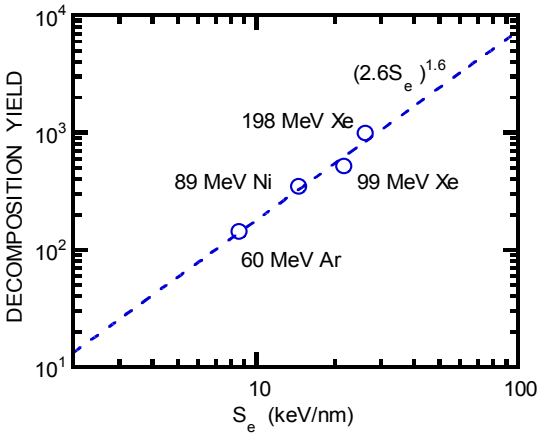

Fig. 2 Decomposition yields of Cu_3N films per ion by high-energy ion impact vs electronic stopping power S_e (keV/nm).

References

[1] N. Matsunami, H. Kakiuchida, M. Tazawa, M. Staka, H. Sugai, S. Okayasu, Nucl. Instrum. Meth. B (in print 2009).
[2] N. Matsunami, M. Sataka, H. Sugai, S. Okayasu et. al., JAEA-Tokai TANDEM Annual Report 2008, JAEA-Review 2009-036(2009)95-96
[3] J. F. Pierson, Vacuum 66(2002)59.
[4] J.F. Ziegler, J.P. Biersack and U. Littmark, The Stopping and Range of Ions in Solids, Pergamonn Press, New York (1985).
[5] N. Matsunami, M. Sataka, S. Okayasu, N. Ishikawa, M. Tazawa, H. Kakiuchida, Nucl. Instrum. Meth. B266(2008)2986.
[6] N. Matsunami, M. Sataka, S. Okayasu, M. Tazawa, Nucl. Instrm. Meth. B256(2007)333.
[7] N. Matsunami, T. Shimura, M. Tazawa, et. al., Nucl. Instrum. Meth. B257(2007)433.

CHAPTER 7

Radiation Effects in Materials

This is a blank page.

7.1 Modification of magnetic properties of FeRh bulk alloys by energetic heavy ion irradiation

S. Kosugi[1], Nao. Fujita[1], N. Ishikawa[2], Y.Saito[2], T. Matsui[1] and A. Iwase[1]

In our previous reports, we have shown that irradiation with several ions with the energies of 100-200MeV induces the ferromagnetic state in Fe-50at.%Rh alloy at low temperatures[1,2]. In this report, we show that the low temperature ferromagnetic state in Fe-50at.%Rh bulk alloy is induced by the energy deposition through the elastic collisions, and that the energetic ion irradiation is a useful tool for the modification of magnetic properties of Fe-50at.%Rh alloy.

Specimens of Fe-50at.%Rh with the dimension of 5x5x0.2 mm^3 were irradiated at room temperature with 60MeV Xe ions and 200MeV Xe ions by using a tandem accelerator at JAEA-Tokai. For 10 MeV I ion irradiation, a tandem accelerator at JAEA-Takasaki was also used. Before and after the irradiation, the magnetization of the specimens was measured as a function of external magnetic field. The scanning range of the applied magnetic field was from -6000 to 6000Oe and the measurement temperature was 20K.

Fig.1 shows the magnetic moment-magnetic filed curves for FeRh specimens irradiated with 60 MeV Xe ions and 200 MeV Xe ions. The magnetic moment tends to increase with increasing the ion-fluence, however, it decreases after the irradiation to the fluence of $1x10^{14}/cm^2$ for 200MeV Xe ion irradiation. Fig.2 shows the depth distributions of the nuclear stopping power, Sn, for 200MeV Xe ions and 10MeV I ions for Fe-50at.%Rh alloy. The depth dependence of Sn for 10 MeV I ion irradiation is about the same as that for 200MeV Xe irradiation around the ion range. Then, we can remove the irradiation effect around the 200MeV Xe ion range by subtracting the value of the magnetic moment for 10MeV I ion irradiation from that for 200MeV Xe ion irradiation. From the value of magnetic moment obtained by this process and the volume of the corresponding region, the average value of <Ms> for the region except around the ion range (hatched region in Fig. 2) , has been deduced. The same process has also been applied for the combination of the results for 60MeV Xe irradiation and 10MeV I irradiation.

In Fig.3, the values of <Ms> are plotted against the total energy deposited by the elastic collision process. The values of <Ms> can be well correlated with the energy density deposited through elastic collisions. On the other hand, we cannot find any correlations between the change in magnetization and the electronic energy loss (Se)[4].The present result indicates that we can modify the low temperature magnetic property of FeRh alloy quantitatively by controlling the energy elastically deposited by energetic ions. Concerning the details of the present result, see Ref. [4].

[1] Osaka Prefecture University
[2] Japan Atomic Energy Agency (JAEA)

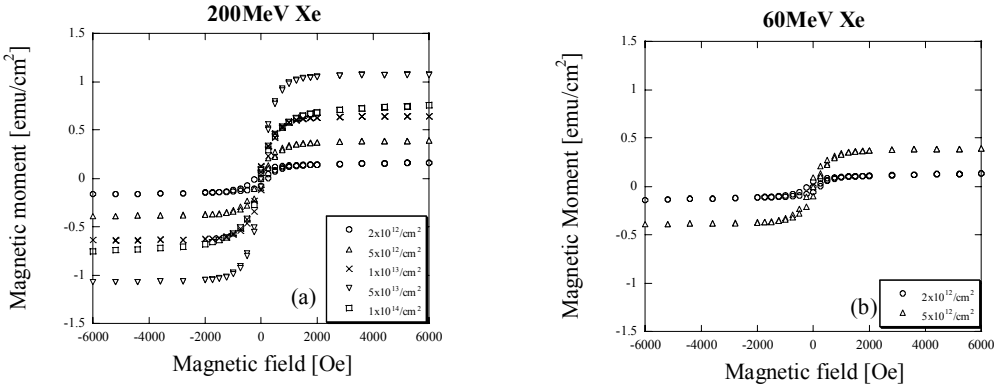

Fig.1 Irradiation induced magnetic moment at 20K as a function of applied magnetic field for: (a) Fe-50at.%Rh irradiated with 200MeV Xe to the ion-fluence of $2x10^{12}$, $5x10^{12}$, $1x10^{13}$, $5x10^{13}$ and $1x10^{14}$/cm^2. (b) Fe-50at.%Rh irradiated with 60MeV I to the ion-fluence of $2x10^{12}$ and $5x10^{12}$/cm^2.

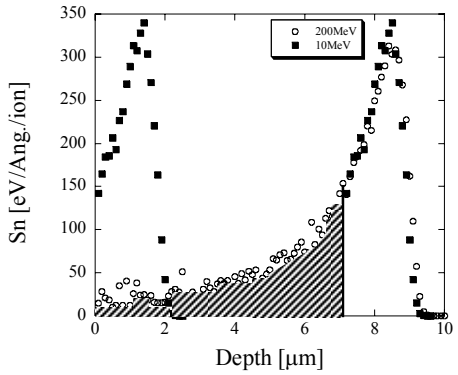

Fig.2 Depth distribution of nuclear stopping power, Sn, for 200MeV Xe, and 10MeV I irradiation for Fe-Rh alloy. The profile of Sn for 10MeV I ions, which are shifted the region around the range of 200MeV Xe ion is also shown.

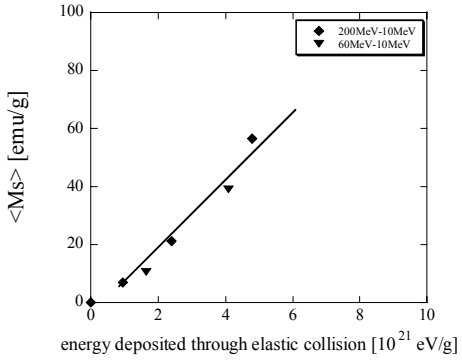

Fig.3 Average values of saturation magnetization, <Ms>, for the region expect around the ion range, as a function of energy deposited through elastic collision

References

[1] M.Fukuzumi et al, Nucl. Instr. And Meth.B230, (2005) 269-273.
[2] M.Fukuzumi et al, Nucl. Instr. And Meth. B245, (2006) 161-165.
[3] Y.Zushi et al, Nucl. Instr. And Meth, B256, (2006) 434-437.
[4] S. Kosugi et al., Nucl. Instr. Meth. B267,(2009) 1612-1615.

7.2 Effects of swift heavy ion irradiation on the structure of Er-doped CeO_2

B.Zhu[1], K.Yasunaga[2], N.Ishikawa[3], H.Ohno[1] and A.Iwase[1]

In order to control the initial reactivity of UO_2 fuel in light-water reactors (LWR), it is useful to dope some elements called burnable poison, which have a high neutron absorption cross section, into UO_2 fuel. Gadolinium trioxide, Gd_2O_3, has already been used as the burnable poison in actual nuclear fuel, and erbium trioxide, Er_2O_3, has also been proposed as another burnable poison. During a long-term reactor operation, nuclear fuel is subjected to the irradiation with high energy (around 100 MeV) fission products (FPs). Therefore, it is important for the nuclear reactor safety to study the effects of high energy FPs on UO_2 fuel doped with burnable poison.

To simulate the effects of high energy FPs irradiation on nuclear fuel UO_2 doped with burnable poison,Er-doped CeO_2 were irradiated at room temperature with 200MeV Xe^{14+} ions at the tandem accelerator of JAEA-Tokai. As the lattice structure of CeO_2 is the same as that of UO_2 and the melting point, and the oxygen mobility of CeO_2 are quite similar to those of UO_2, CeO_2 can be used as a simulation material of UO_2. Specimens used in this study were Er doped CeO_2 bulk pellets which were prepared by sintering the mixture of CeO_2 and Er_2O_3 powders at 1500^{o}C. The changes in lattice parameter by the Er-doping and the irradiation were measured by using X-ray diffraction (XRD) method.

Fig.1 shows the change in XRD spectrum around (004) peaks of 1mol % Er doped CeO2 for various ion-fluences. All peaks are shifted to a lower angle by the irradiation, which means that the lattice parameter increases with increasing the ion-fluence. Another irradiation effect can be observed as a broadening of peaks after the irradiation. Fig. 2 shows the lattice parameter as a function of ion-fluence for 1, 10, 15 and 20 mol % Er doped CeO2 pellets. The increase in lattice parameter is nearly proportional to the ion-fluence. Fig. 3 shows the change in lattice parameter per unit ion fluence (change rate of lattice parameter) as a function of Er concentration. Except for 20 mol % doped CeO_2, the change rate of lattice parameter increases with increasing Er concentration. The full width half maximum (FWHM) of the XRD peaks also increases with increasing Er concentration. The present experimental result implies that the effect of swift heavy ion irradiation on the lattice structure of CeO2 becomes more remarkable with increasing the amount of Er_2O_3 in CeO_2..

[1]Osaka Prefecture University

[2]Kyushu University

[3]Japan Atomic Energy Agency

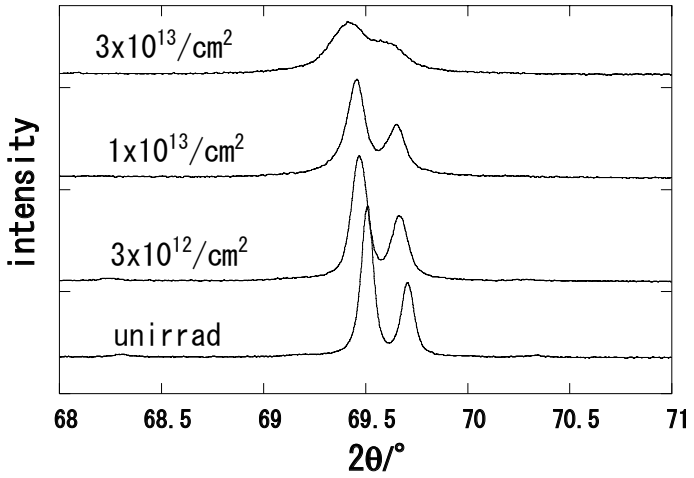

Fig. 1 XRD spectra around (004) peaks of Er-doped CeO_2 for various ion-fluences

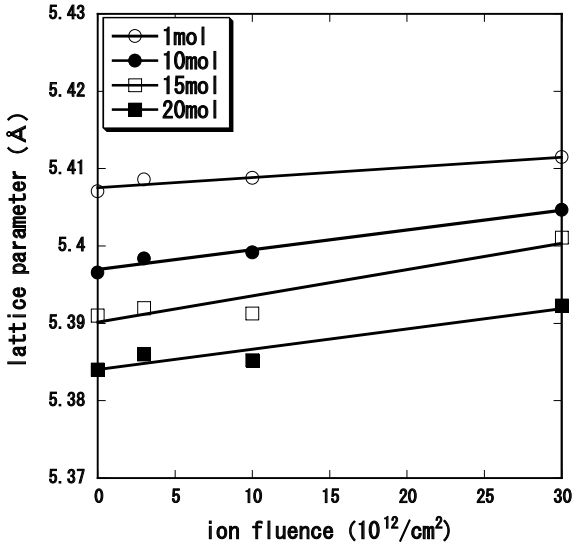

Fig. 2 Lattice parameter as a function of ion-fluence for 1, 10, 15 and 20 mol % Er doped CeO_2 pellets

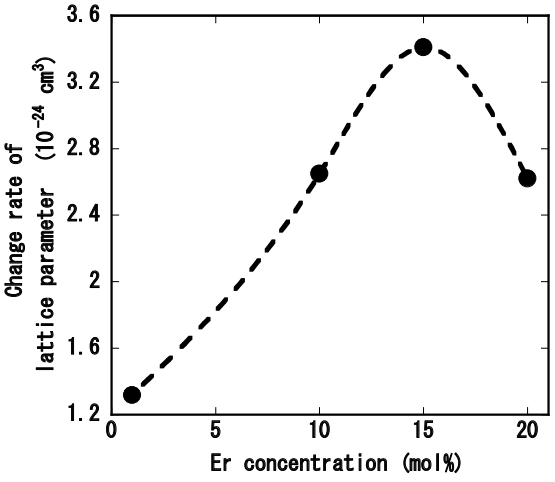

Fig. 3 Change in lattice parameter per unit ion-fluence (change rate of lattice parameter) as a function of Er concentration

7.3 Study on semiconductor device process by high energy ion implantation

H. Sakane[1], T. Ohmori[2] and H. Uno[1]

High-Voltage superjunction devices firstly realized by Infineon's CoolMOS technology, are a novel class of power devices which break the physical limit of silicon with respect to the area-specific turn-on-resistance value[1]. A feature of superjunction devices are deep pillar-like p-n junctions. On a commercial scale the vertical stack is presently fabricated with a high effort by repeated cycles of n-type epi-layer growth, masked boron implantation at common energies and subsequent diffusion. There are numerous suggestions for alternative technologies, most of them involving a deep trench structure [2,3]. In this work, we tired to confirm that p-type layers in n-type layer are built up using the high energy boron ion implantations.

Samples used in this study were prepared from phosphorus-doped, n-type silicon crystals which has a high resistively. A shape of samples were $12\times12mm^2$ and 500μm thickness. Samples were irradiated with 16 MeV Boron using a 20 MV tandem accelerator at JAEA-Tokai, at room temperature. Boron fluences were set to 1×10^{12} and $1\times10^{13}/cm^2$. By using Al foil absorber for energy attenuation the depth of implantation layer was controlled. After implantation, the radiation level drops significantly, but due to the generation of radioactive isotopes a certain radiation levels is still present for some time. Annealing was performed in the temperature of 1100℃ in nitrogen ambient.

Figure 1 shows the depth distribution of the carrier concentration for implanted and unirradiated sample, measured with spreading resistance profiling. It was shown that compare of a 4-fold boron implantation with energies between 4 and 16 MeV. Except for the peak at 5 μm, the peak positions correspond very well with the projected ranges of the respective implantation energy. The average carrier concentration was about $1\times10^{13}cm^3$. It is not known why carrier concentration around 5um is lower than other region.
Figure 2 shows an as-implanted boron profile measured by SEM. Three distinct boron bubbles can be discerned. Circled shadow area are consisted with missing parts around 5mm depth in Figure 1.

We have confirmed that it is possible to produce p-type layer by boron implantation with energies up to 16 MeV.

[1] S.H.I. Examination & Inspection, LTD.
[2] Sanken Electoric Co., LTD.

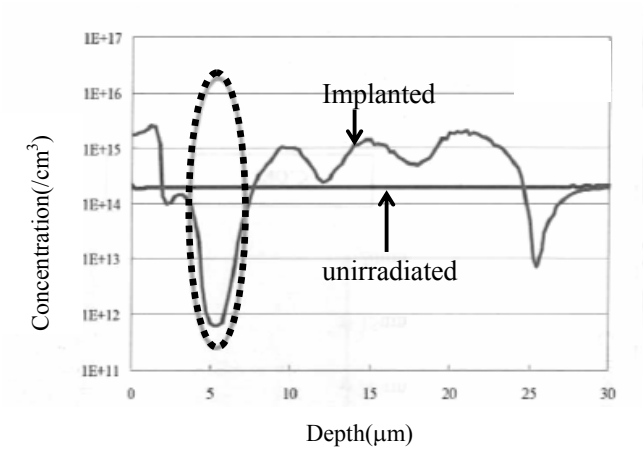

Fig.1 Spreading resistance measurements of identically prepared non-structured wafer for three-fold boron implantation.

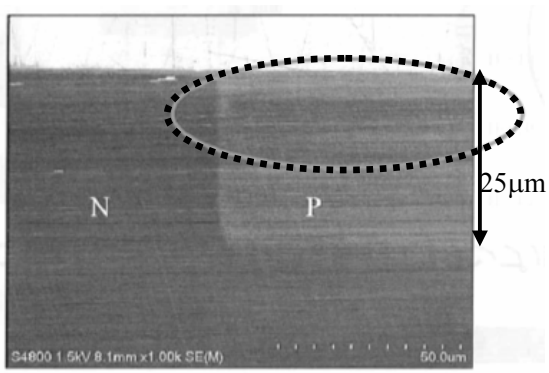

Fig.2 SEM image of decorated boron column in n-type silicon.

References

[1] G. Deboy, L. Lorenz, M. Marz, Elektronik., (1998) 42-43.

[2] T.Minato, T. Nitta, A. Uenisi, M. Yano, M. Harada, S .Hine, Proc. ISPSD 2000, Toulouse, France (2000) 73-76.

[3] M. Rub, D. Ahlers, J. Baumgartl, G. Deboy, W. Friza, O, Haberlein, I. Steingke, Proc. ISPSD2003, Cambrige, UK (2003) 203-206.

7.4 Morphological and compositional change in FePt nanogranular thin films irradiated with swift heavy ions

M. Shirai[1], K. Tsumori[1], K. Yasuda[1], S. Matsumura[1] and N. Ishikawa[2]

Nanogranular films attract a great attention as various functional new materials. For example, FePt nanogranular thin films, in which FePt nanoparticles are embedded in amorphous matrix are one of the promising candidates for future ultrahigh density magnetic recording media. It is essential to control the size, shape and dispersion of nanoparticles to improve their properties for the specific applications. Ion irradiation is a well-defined technique to deposit a high density of energy into a desired local region of materials and has been utilized as a tool controlling the structure of materials in a nanometer scale [1,2]. In the present study, we have examined change in the morphology and composition of FePt nanoparticles in the nanogranular thin films irradiated with swift heavy ions by transmission electron microscopy (TEM), including electron tomography.

FePt nanogranular thin films were produced by ion beam sputtering. FePt nanoparticles were dispersed in amorphous Al_2O_3 matrix with 20 nm in thickness. Swift heavy ions of 210 MeV Xe were irradiated at the Tandem Accelerator Facility of JAEA-Tokai at an ambient temperature to fluence ranging from 5.0×10^{17} to 1×10^{19} ions/m^2. Radiation-induced nanostructural changes were examined by TEM. Electron tomography technique was utilized to characterize their three dimensional (3D) morphology of nanoparticles. The change in the morphology was evaluated quantitatively, by measuring the length of coordinates of nanoparticles from the reconstructed 3D images. Local compositions were also investigated by energy dispersive X-ray spectroscopy (EDX) with scanning transmission electron microscopy (STEM).

Fine FePt nanoparticles were homogeneously dispersed in the films before ion irradiation. Swift heavy ion irradiation induced drastical change in the size and shape of FePt nanoparticles. Figure 1 shows 3D reconstructed images of the nanogranular thin film irradiated with 210 MeV Xe ions up to 5×10^{18} ions/m^2. Well-coarsened FePt balls have been formed near the irradiated surface, and other particles in the film interior have been deformed into rods, which longitudinal direction is along the ion trajectory. Figure 2 shows the plot α, which is defined as an angle between the longitudinal axis and the foil normal, as a function of the aspect ratio. The aspect ratio was evaluated from 3D reconstructed images, by assuming the nanoparticle shape to be ellipsoid. It is seen that data points are widely dispersed before irradiation, suggesting no specific preferential orientation. With progress of irradiation, the domain converges to the left side and extends to the upper part in Fig. 2. It clearly shows that the irradiation with 210 MeV Xe ions deforms particles into rod shape, elongating along the ion beam direction. The composition of FePt particles did not change up to a fluence of 5×10^{18} ions/m^2. However, the particles became inhomogeneous in composition after prolonged irradiation of 1.0×10^{19} ions/m^2. Fig. 3 shows a STEM dark-field image of

[1] Department of Applied Quantum Physics and Nuclear engineering, Kyushu University
[2] Tokai Research Center, Japan Atomic Energy Agency

the specimen irradiated to 1.0×10^{19} ions/m^2 and the corresponding characteristic X-ray mapping images of Fe, Pt, Al and O. Fe-rich domains look a slightly larger than Pt-rich ones. Point X-ray analysis shows that the center part of the particles was enriched with Pt with a ration of Fe:Pt~1:3. It is suggested that Fe atoms are slightly redistributed to the periphery part at a high fluence of 1.0×10^{19} ions/m^2. Doughnut-like contrast gets pronounced for the lager ball particles in the maps of Al as well as of O, as shown in Fig. 3(d) and (f). The Al-O phase is likely to cover the prominent metal particles existing on the surface.

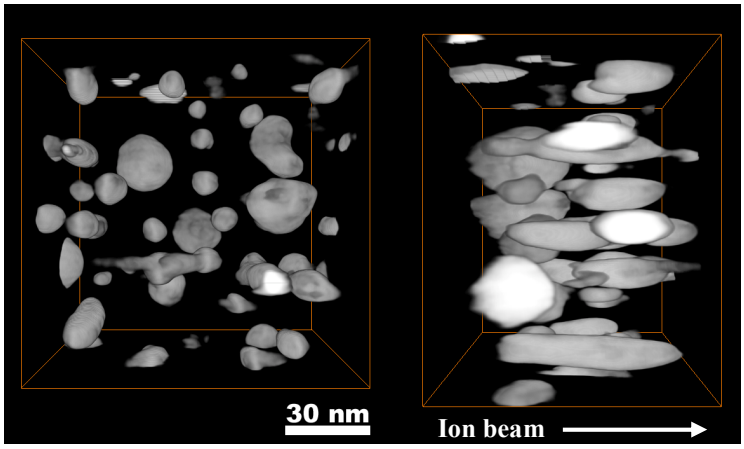

Fig.1 Three dimensional reconstruction image of a film irradiated with 210 MeV Xe ions to 5×10^{18} ions/m^2 at ambient temperature.

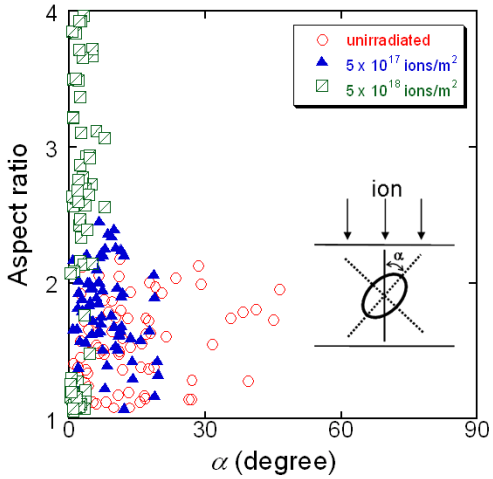

Fig.2 Map showing relationship between α and aspect ratio of individual particles.

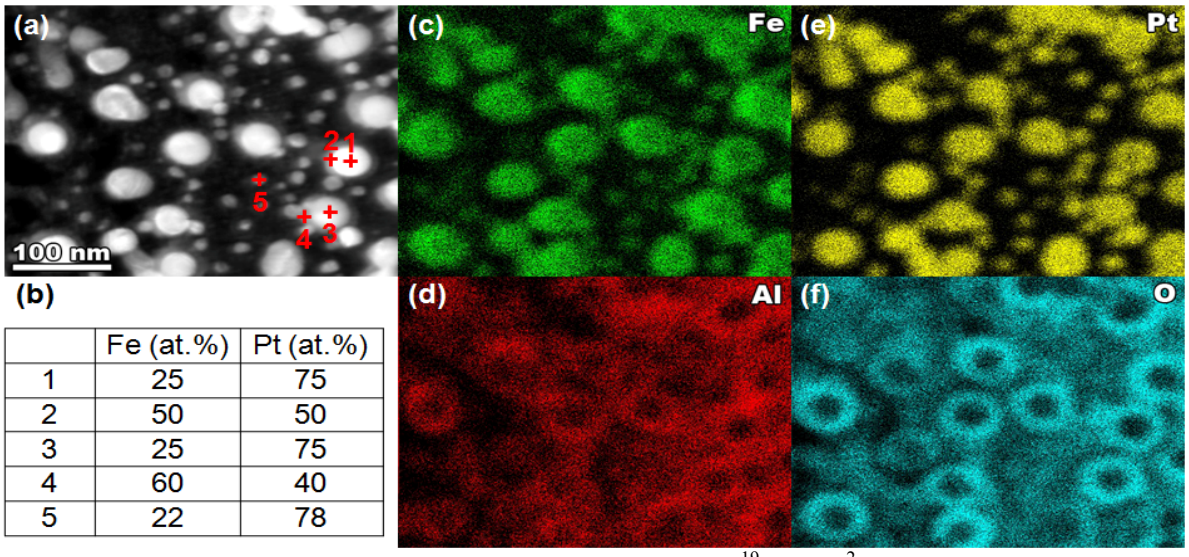

(b)

	Fe (at.%)	Pt (at.%)
1	25	75
2	50	50
3	25	75
4	60	40
5	22	78

Fig.3 STEM dark filed image of irradiated specimen to 1×10^{19} ions/m^2 (a), chemical compositions measured by EDX at positions shown in (a) (b), and elemental mapping images for Fe (c), Pt (e), Al (d) and O (f).

References

[1] M. Shirai, T. Horiuchi, A. Horiguchi, S. Matsumura, K. Yasuda, M. Watanabe and T. Masumoto, Mater. Trans. 47 (2006) 52

[2] M. Shirai, K. Tsumori, M. Kutsuwada, K. Yasuda, and S. Matsumura, Nucl. Instr. and Meth. B 267 (2009) 1787.

7.5 Transport properties of (β-$FeSi_2$) thin films

S. Okayasu[1] and M. Sasase[2]

Iron disilicide (β-$FeSi_2$) is one of the candidates of compound semiconductor, which contains harmless elements to the human bodies and the environment [1]. Another attractive feature of β-$FeSi_2$ is transformation to the metal phase α-$FeSi_2$ when heated above 1246 K. Since the bulk α-$FeSi_2$ has electric resistivity as low as 2.5 x 10^{-4} Ω cm, one may consider if a small part of β-$FeSi_2$ can be transformed into α-$FeSi_2$ selectively, it can be used as the electrode of a β-$FeSi_2$ based device.

When high-energy heavy ions are irradiated into the material, most of their energies are dissipated through an electronic excitation [2]. This leads to strong localization of the dissipated energy along the projectile path. The density of energy deposition is high enough, compared with bond or displacement energy of the target materials, so that nanostructural changes take place such as amorphization and phase transition etc. We attempted to perform phase transition from β-$FeSi_2$ into other phase by the high-energy heavy ion irradiation.

The specimens used in this study were β-$FeSi_2$ films fabricated with the ion beam sputter deposition method by depositing Fe on Si(100) substrates with the thickness 500 nm at a certain temperature [3]. The specimens were irradiated by 200 MeV Ni^{12+} ions at room temperature with a fluence of 1.0 x 10^{13} ions/cm^2 using the tandem accelerator at Japan Atomic Energy Agency (JAEA). The formation of the columnar defects along the ion paths is reported in our previous study, otherwise the transformation of the α-$FeSi_2$ phase has not confirmed yet. In this study, we report the transport properties such as resistivity, Hall coefficient and mobility. The Ni-irradiated sample was become somewhat radioactive due to the nuclear transformation, thus the transport property measurements have not been accomplished yet. Therefore we report only the properties of the specimen before the irradiation. The comparison of the properties will be reported elsewhere in the future.

All of the transport properties were measured by a conventional four-wired method using a commercial superconducting magnet system (PPMS, Quantum Design). To avoid the influence of the additional electromotive forces at the contact points, low frequency alternating currents (30 Hz) were used. Typical I-V characteristics at different temperatures in the applied external field 1 Tesla are shown in Fig. 1. Temperature dependences of resistivities at certain current are shown in Fig. 2. The I-V curves change their properties in different temperature ranges. In the temperature range between 180 K and 300 K, the I-V characteristics are ohmic and the resistivities show metallic properties. In the temperature range between 90 K and 180 K, the I-V curves show nonlinear behaviors and the saturation of voltage can be observed above 1mA. The temperature dependences of resistivity show semiconducting properties. The qualitative change

[1] Japan Atomic Energy Agency (JAEA)
[2] The Wakasa-wan Energy Research Center (WERC)

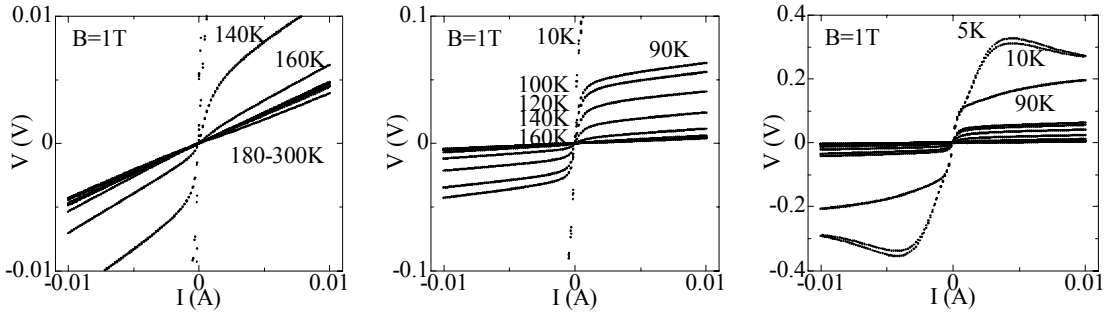

Fig.1 I-V characteristics of unirradiated β-$FeSi_2$ thin films at different temperatures in B= 1 Tesla.

of the transport properties suggests that a change of the transport mechanism occurs around 180 K. Below 90 K, the I-V properties below 2mA are similar to those of the case between 90 K and 180 K, however, decreases of voltage are observed with increase of current above 2mA. The resistivities below 90K show the power law dependence with temperature.

Temperature dependences of Hall coefficients at B= 1 Tesla with different currents are shown in Fig. 3. No current dependence is observed above 220 K. On the other hand, a strong current dependence is observed between 160 K and 220 K. A sharp drop of the Hall coefficient occurs around 160 K suggesting the existence of some phase transition. At lower temperature below 90 K, the Hall coefficient becomes negative suggesting the change of charge carriers. All of our data are only preliminary ones. We will intend to measure the transport properties of Ni-irradiated β-$FeSi_2$, and to compare them to these data.

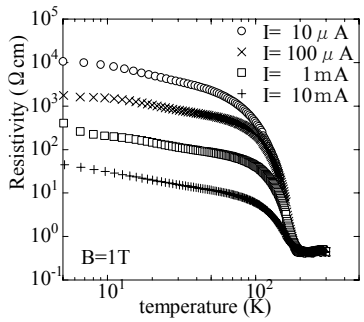

Fig.2 Temperature dependences of resistivities with different currents.

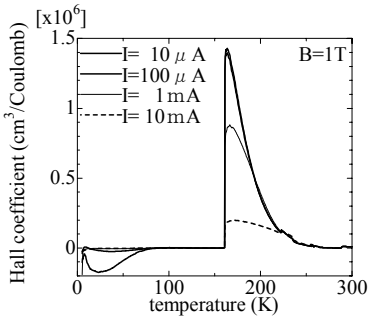

Fig.3 Temperature dependences of Hall coefficient at B = 1 Tesla.

Although the phase transition of β-$FeSi_2$ to α phase is not confirmed yet, our results showed the structural change by high energy heavy ion irradiation. We will intend to observe the microstructure of defects and phase transitions in the irradiated films precisely by using both high resolution TEM and micro-diffraction.

References

[1] K. Yamaguchi and K. Mizushima, Phys. Rev. Lett., **25**(2001)6006.

[2] Calculation using the SRIM code. http://www.srim.org/SRIM/SRIMLEGL.htm

[3] M. Sasase, T. Nakanoya, H. Yamamoto and K. Hojou, Thin Solid Films, **401**(2001)73.

7.6 Irradiation effect on Ag-zeolite

S. Okayasu[1] and Y. Sasaki[2]

Zeolite, a sort of alminosillicate constructed with degenerated SiO_4 and AlO_4 tetrahedrons sharing oxygen atoms with their neighbors, has a cage structure including large porous inside. Alkali or alkaline earth cations (usually Na^+) of the same amount of Al^{3+} ions are absorbed in the cage structure to compensate the charge imbalance. The molecular formula of zeolite can be expressed as

$$(M^{I},M^{II}{}_{1/2})_m(Al_mSi_nO_{2(m+n)})\cdot xH_2O \quad : n \geqq m \qquad (1),$$

where M^{I} and M^{II} are univalent and divalent cations included inside the cage. A crystal structure of a LTA-zeolite classified into type-A (a ratio of Si/Al =1) is shown in Fig.1. The alkali or alkaline earth cations inside the cage structure are easily replaced other cations Ag^+, Mn^{2+}, etc. We synthesized Ag-zeolite samples for irradiation study.

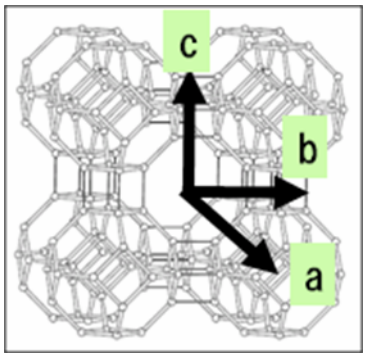

Fig.1 A crystal structure of LTA zeoilte. The diameter of the central cavity is 4.1 Å.

In our previous study [1], we found separation and clustering of Ag atom after 200keV electron irradiation on Ag-LTA zeolite samples. A possible scenario is follow. A four-coordinated Al atom in the zeolite structure can change to a six-coordinated by destruction due to the electron irradiation. A bound Ag ion around Al atom in the cage is neutralized during this process and the free Ag atoms gathered. A similar clustering process can be occurred for heavy ion irradiation. If so, the clustered Ag atoms can form a line along the trajectory of the incident ions. The typical diameters of the ion tracks are several nanometers. Therefore, nanoscopic metal structures may be formed in the zeolite.

A synthesized Ag-zeolite sample was irradiated with 200MeV Au ions in the Tandem accelerator in JAEA at room temperature. We prepared the sample for the cross sectional observation of Transmission Electron Microscope (TEM).

[1] Japan Atomic Energy Agency (JAEA)
[2] Japan Fine Ceramics Center (JFCC)

Reference

[1] Y. Sasaki, T. Suzuki, Materials Transaction, 50, 1050-1053(2009)

7.7 Study of electronic excitation effects on the microstructural evolution in UO_2

T. Sonoda[1], N. Ishikawa[2], M. Sataka[2], K. Yasunaga[3], M. Kinoshita[1] and A. Iwase[4]

One of the topics for progressing high burnup extension of light water reactor (LWR) fuels is the clarification of formation and growth mechanism of a crystallographic re-structuring in the periphery region of high burnup fuel pellets, as named “rim structure” [1]. This structure is characterized by the existence of highly dense small sub-grains whose size is approximately 200 nm, and the accumulation of small pores with average size around 1 μm. The key factor of the formation mechanism of the rim structure should be a high density electronic excitation effects on the accumulation process of radiation damages in LWR fuels [2-4]. In order to clarify the character and the accumulation effects of ion tracks that are formed by highly dense electronic excitation, high energy Xe and Zr ions irradiation examinations on UO_2 have been done at JAEA-Tandem accelerator facility. Microstructure evolutions in the irradiated samples are observed in a FE-SEM (JSM-6340F) and a FE-TEM (HF-3000) at CRIEPI. This study was financially supported by the Budget for Nuclear Research of the Ministry of Education, Culture, Sports, Science and Technology, based on the screening and counseling by the Atomic Energy Commission.

Figure 1 (a) and (b) shows the TEM image of UO_2 and CeO_2 under irradiation with 210 MeV Xe ions at room temperature, respectively. The circle images in this picture correspond to the cross-section images of ion tracks, and the mean diameter of ion tracks was measured around 4.9 nm and 9.3 nm, respectively. Figure 2 indicates the square of mean diameter of ion tracks in UO_2 and CeO_2 as a function of electronic stopping power (S_e). This figure indicates that the square of diameter of ion tracks tend to be proportional to S_e, and suggests that the sensitivity of high density electronic excitation of UO_2 is much less than that of CeO_2.

In order to understand the accumulation effects of ion tracks in UO_2, 210 MeV Xe ions irradiation up to a fluence of 1.5×10^{16} ions/cm^2 were done. Figure 3 shows the typical SEM image of irradiated surface and cross-sectional TEM images in UO_2 under irradiation with 210 MeV Xe at 300 °C to a fluence of (a) un-irradiated, (b) 5×10^{14} ions/cm^2, and (c) 1.5×10^{16} ions/cm^2, respectively. In figure 3 (a), the shape of fabricated pore is polygon and there are very few dislocations. In figure 3 (b), the fabricated pores are deformed elliptically whose major axis is parallel to irradiation direction, and the deformation zone was estimated around 6 μm depth. Moreover, the formation and accumulation of dislocations are observed. In figure 3 (c), some of sub-divided grains whose size is around 1 μm are observed near the irradiation surface, and the dislocations seem to diffuse in the direction of irradiation. These drastic changes of surface morphology and inner structure in UO_2 suggest that the overlapping of ion tracks will cause the point defects and dislocations, enhance the diffusion of point defects and dislocations, and form the sub-grains at

[1] Central Research Institute of Electric Power Industry (CRIEPI)
[2] Japan Atomic Energy Agency (JAEA)
[3] Kyushu University
[4] Osaka Prefecture University

relatively low temperature.

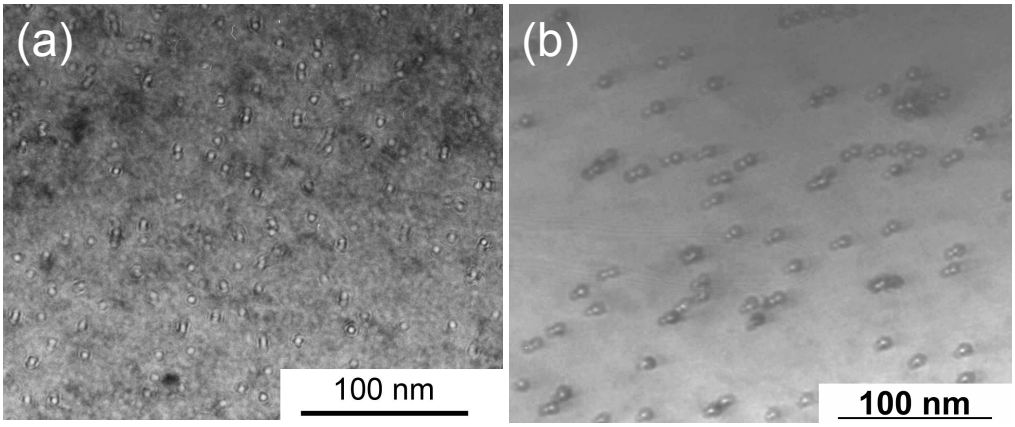

Fig. 1 TEM image of (a) UO_2 and (b) CeO_2 under irradiation with 210 MeV Xe ions to a fluence of (a) 5 x 10^{11} ions/cm^2 and (b) 1 x 10^{11} ions/cm^2 at room temperature. The mean diameter of ion tracks is around (a) 4.9 nm and (b) 9.3 nm, respectively.

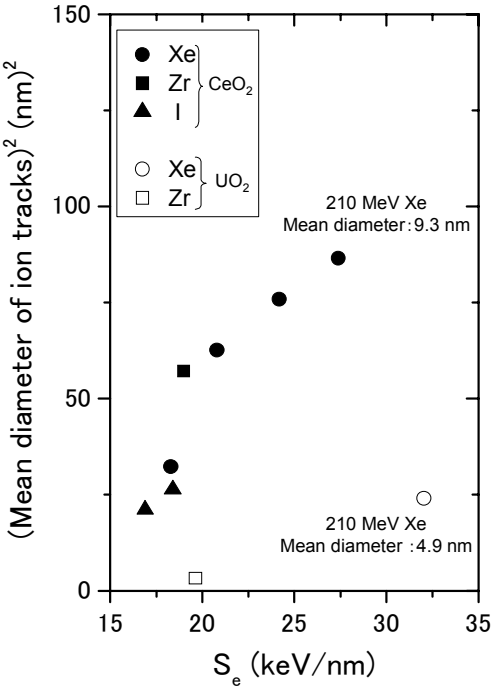

Fig. 2 The square of the mean diameter of ion tracks in UO_2 and CeO_2 at room temperature as a function of electronic stopping power (S_e).

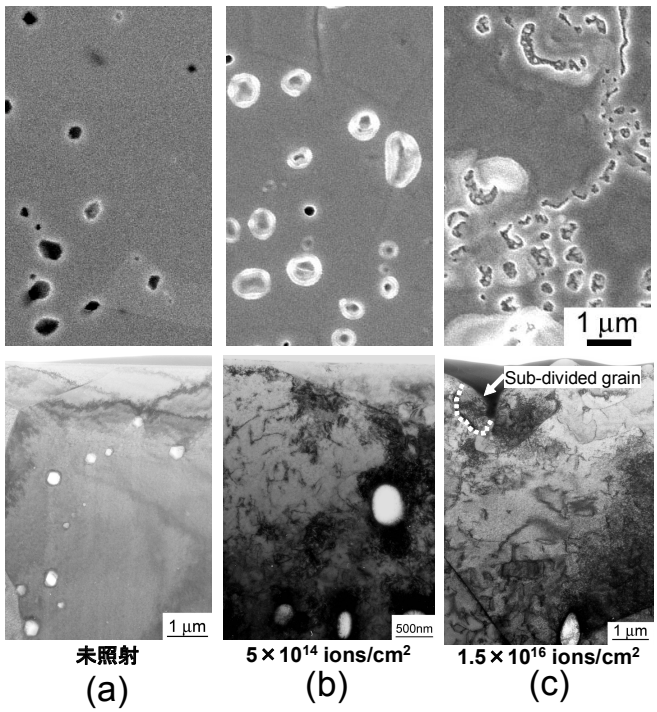

Fig. 3 SEM images (upper row) of irradiated surface and cross-sectional TEM images (lower row) in UO_2 under irradiation with 210 MeV Xe^{+14} to a fluence of (a) unirradiated, (b) 5 x 10^{14} ions/cm^2, and (c) 1.5 x 10^{16} ions/cm^2 at 300°C.

References

[1] J.O. Barner *et al*., HBEP-61, 1990, Battelle Pacific Northwest Laboratories.

[2] T. Sonoda *et al*., Nucl. Instrum. Methods Phys. Res., B191 (2002) 622-628.

[3] T. Sonoda *et al*., Nucl. Instrum. Methods Phys. Res., B250 (2006) 254-258.

[4] T. Sonoda *et al*., Nucl. Instrum. Methods Phys. Res., B266 (2008) 2882-2886.

7.8 Microstructure observations and distribution of chemical compositions of metal precipitates in Zircaloy-2 - Distribution of Si in Zircaloy-2 –

T. Sonoda[1], N. Ishikawa[2] and M. Sataka[2]

In order to progress high burnup extension of light water reactor (LWR) fuels, the improvement of anti-corrosion and hydrogen resistance of nuclear fuel claddings (Zirconium alloy; Zircaloy-2 for boiling water reactor) is indispensable. In previous researches, it becomes clear that the degradation of anti-corrosion and hydrogen resistance is concerned with the composition and size of metal precipitates in zirconium alloy, and the precipitates are deformed under irradiation with high energy neutron in a reactor. Moreover, it was also reported that the density of silicon, that is one of low density impurities in cladding, influence the anti-corrosion and hydrogen resistance of fuel claddings [1]. In order to clarify the mechanism of corrosion and hydrogen pickup in Zircaloy and the correlation between the degradation of fuel cladding and the deformation of metal precipitates in claddings, microstructure observations and ion irradiation examinations have been done. In this report, microstructure and atom distribution of alloy elements and impurity (Fe, Ni, Cr, and Si) in Zircaloy-2 have been clarified by means of a transmission electron microscope (JEM-2100 with EDS system) at CRIEPI. Secondly, 100 MeV Zr ion and 210 MeV Xe irradiation examinations have been treated at JAEA-Tandem accelerator facility.

Figure 1 indicates the typical TEM image of Zircaloy-2. This sample was fabricated by use of focused ion beam method (FIB), and this figure confirms that some of metal precipitates are existed in Zircaloy-2. Figure 2 shows the high magnification TEM image of one precipitate that was indicated as white allows in figure 1, and results of the atom mapping of Cr, Fe, and Ni in this precipitate by means of EDS system. This figure shows that this precipitate was constructed by overlapping of metal precipitates of (Fe, Cr) and (Fe, Ni). In order to confirm the structure of these metal precipitates and the distribution of Si, five spot analysis of EDS was treated whose analysis points are indicated in figure 2 BF. Figure 3 indicates the spectrum data of EDS at position ① in figure 2 BF, and Table 1 indicates the EDS results at four spots in the complex precipitate. This table confirmed that the structure of metal precipitates of (Fe, Ni) base is Zr_2(Fe, Ni).In case of metal precipitates of (Fe, Cr) base, 3D atom probe measurements have confirmed that the structure is Zr(Fe, $Cr)_2$[2]. The EDS result at position ③ will be summarized of the overlapping of two type of metal precipitates, Zr_2(Fe, Ni) and Zr(Fe, $Cr)_2$. Moreover, it becomes clear that Si tend to be accumulated in Zr_2(Fe, Ni) whose concentration is around 1.6 -1.9 at%. These results suggest that Si tends to be in metal precipitates, especially in Zr_2(Fe, Ni). In order to confirm the distribution of Si, systematic analysis of the EDS data of many precipitates and application of advanced microstructure observation method, 3D atom probe method, will be treated in near future.

In order to clarify the deformation of metal precipitates in claddings under irradiation, 100 MeV Zr ion and

[1] Central Research Institute of Electric Power Industry (CRIEPI)
[2] Japan Atomic Energy Agency (JAEA)

210 MeV Xe irradiation examinations have been done. Unfortunately, some of the irradiated specimen was heated up over 400 °C and it become impossible to get ideal specimen for research. The reason of this heat up will be beam heating because of high ion flux and trouble of specimen holder. We will retry the irradiation examinations near future.

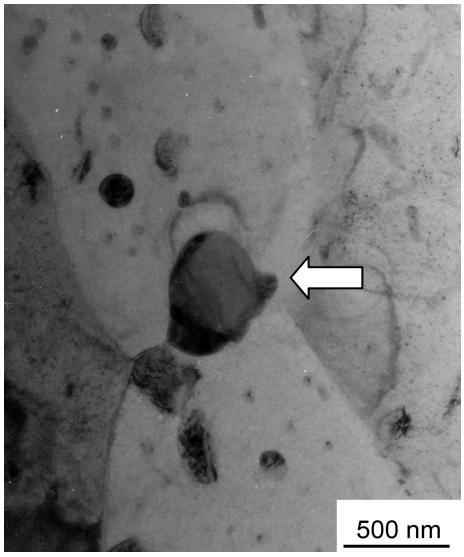

Fig.1 TEM image of Zircaloy-2. Some of metal precipitates are observed.

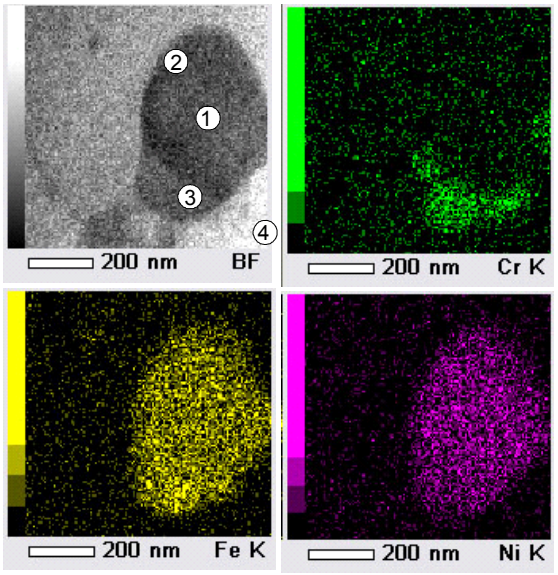

Fig.2 High magnification TEM image of one precipitate in Fig. 1, and the atom mapping of Cr, Fe and Ni in the precipitate.

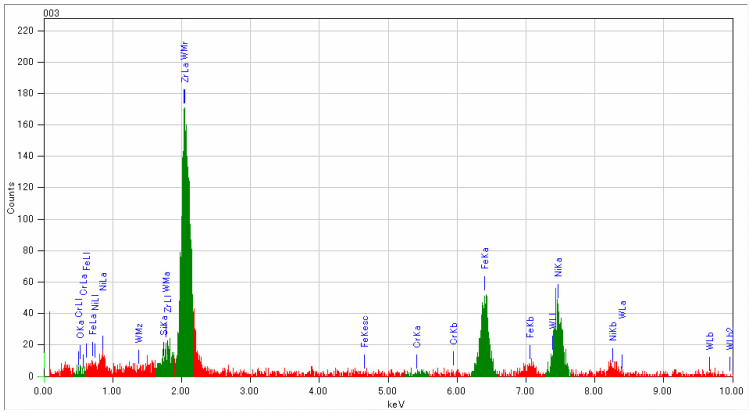

Fig.3 Spectrum data of EDS at white circle in figure 2 BF.

Table 1 EDS results at five spots in the complex precipitate in figure 2 BF.

	Zr (at%)	Fe (at%)	Cr (at%)	Ni (at%)	Si (at%)
①	60.6	18.4	--	18.2	1.9
②	72.5	14.2	--	11.7	1.6
③	58.2	21.1	12.3	12.9	--
④	100	--	--	--	--

References

[1] H. Sell, S. Trapp-Pritsching and F. Garzarolli, ASTM STP 1467(2005) pp404-417.

[2] T. Sonoda et.al, 2009 Spring Meeting of the Atomic Energy Society of Japan, Tokyo Inst. of Tech., (March. 23, 2009).

7.9 Study on irradiation behavior of reactor pressure vessel steels by using high-energy heavy-ion irradiation

Y. Chimi[1], T. Tobita[1], N. Ishikawa[1] and A. Iwase[2]

In order to understand the mechanism of irradiation embrittlement in reactor pressure vessel (RPV) steels of light water reactors, it is important to clarify the contribution of well-controlled irradiation parameters to the property change of RPV steels. In the present report, we have performed ion irradiation in RPV steels, and studied the irradiation response by means of electrical resistivity and hardness measurements.

Specimens were made of two kinds of RPV steels, JRQ and steel A, which were prepared as ASTM A533B class-1 plates. The chemical composition of the materials is shown in Table 1, in which Cu concentration is comparable to old commercial RPV steels constructed at 1970's or before. Irradiation was performed with 100-MeV ^{56}Fe ions at 563 K using a 20-MV Tandem accelerator at JAEA-Tokai. For electrical resistivity measurements, the specimens of thin JRQ films of ~30 μm in thickness were used. The electrical resistivity were measured at liquid-N_2 temperature (~77.3 K) with interrupting the irradiation and cooling the specimens several times. The specimens for hardness measurements were mechanically and electrolytically polished steel-A plates of ~1 mm in thickness, and measured at room temperature in the irradiated and un-irradiated (masked) regions after irradiation. Figure 1 shows the damage profile in case of iron target calculated by the SRIM code [1] with displacement threshold energy of E_d = 40 eV. The projected range of the ion is ~8 μm, which is much smaller than the specimen thickness. Therefore, the property change due to irradiation occurs only near the surface region of the specimen. For hardness measurements, ultra micro hardness testing was carried out with the Vickers indenter tip and indentation depth of 1.5 μm.

The electrical resistivity change, Δρ, for JRQ is shown in Fig. 2 as a function of ion dose, which is defined as the peak of the damage profile at the depth of ~7.8 μm (Fig. 1). The specimen denoted by "un-irradiated" was not irradiated, but experienced almost the same temperature history as the "irradiated" specimen. Therefore, the data for "un-irradiated" specimen indicate only the thermal aging behavior during irradiation. As shown in Fig. 2, the electrical resistivity decreases with ion dose, which is similar to the case of Fe-Cu model alloys, implying that irradiation-induced clustering of Cu and other solute atoms occurs [2]. Figure 3 shows the ion-dose dependence of hardness change, ΔHv, for steel A. The value of ΔHv increases with the ion dose, being concerned with the resistivity change for JRQ, which has similar Cu concentration. In order to clarify the cause of the change in electrical resistivity and hardness by the ion irradiation, it is necessary to evaluate the contribution of the microstructure evolution in detail.

[1] Japan Atomic Energy Agency (JAEA)
[2] Osaka Prefecture University

Table 1. Chemical composition of materials (in wt.%)

Materials	Si	P	S	Cu	Ni	Fe
JRQ	0.25	0.017	0.004	0.14	0.84	Balance
Steel A	0.3	0.015	0.01	0.16	0.68	Balance

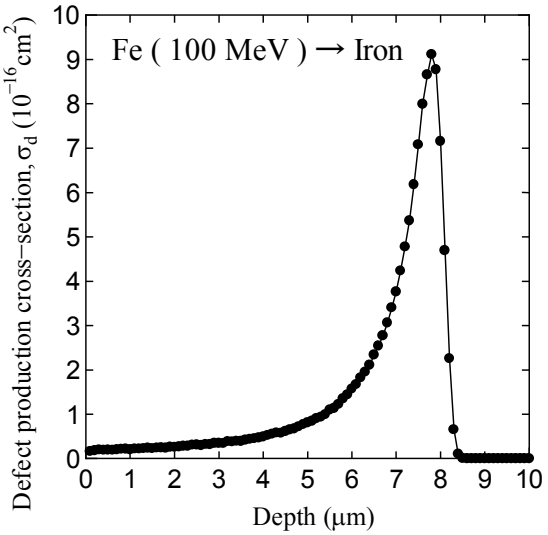

Fig. 1 Damage profile in iron irradiated with 100-MeV Fe ions calculated by the SRIM code.

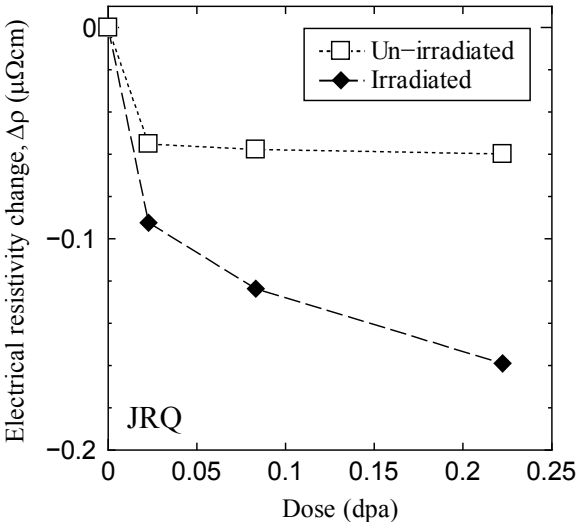

Fig. 2 Electrical resistivity change, Δρ, as a function of ion dose. Data for "un-irradiated" specimen indicate only the thermal aging behavior during irradiation.

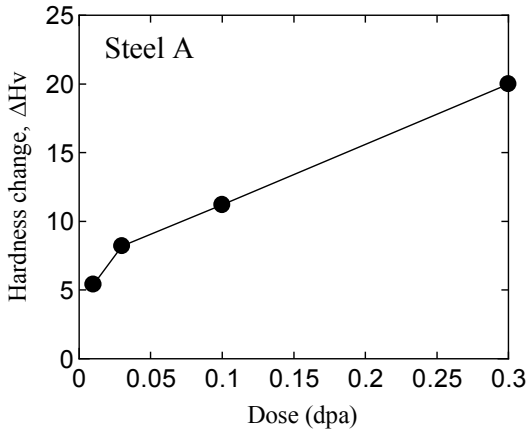

Fig. 3 Dose dependence of hardness change, ΔHv, for steel A.

References

[1] J.F. Ziegler, Nucl. Instrum. Methods Phys. Res., B219-220 (2004) 1027-1036.

[2] S. Ishino et al., J. Nucl. Mater., 323 (2003) 354-359.

7.10 Damage recovery of radiation damage in CeO_2 created by electronic energy deposition

N. Ishikawa[1]

Radiation damage in nuclear fuel of fast breeder reactor can be classified into various types in term of its defect structure, such as 1) point-like defects created by relatively low energy particle irradiation, 2) continuous damage region (ion-track) created by high energy particle irradiation, and 3) strain fields created by accumulation of fission gas. In this study, in order to simulate irradiation damage by high energy fission fragments in MOX (mixed oxide) fuel, oxide ceramic material (CeO_2) with fluorite crystallographic structure is irradiated with high energy particles using tandem accelerator at Tokai Research and Development Center, Japan Atomic Energy Agency (JAEA-Tokai). The characterization of radiation damage is done by X-ray diffraction method, by which quantitative characterization of radiation damage is possible.

Thin films of CeO_2 were prepared on single crystal sapphire substrates by sputtering methods. The film thickness was about 300 nm. The films were irradiated at room temperature with 120MeV Xe from the tandem accelerator at JAEA-Tokai. The objective of the irradiation with 120MeV Xe particles is to simulate radiation damage behavior due to high energy fission fragments. After the irradiation, X-ray diffraction (XRD) patterns were measured at elevated temperature up to 1000^{o}C, in order to investigate damage recovery due to thermal energy. A sharp XRD peak corresponding to (002) reflection is observed before irradiation. In this study irradiation-induced change of the (002) peak intensity is analyzed.

Figure 1 shows (002) diffraction peak observed at elevated temperature from 35°C to 1000°C for CeO_2 irradiated with 120MeV Xe at room temperature. The peak shifts to lower angle side by increasing temperature, indicating that lattice is thermally expanded at high temperature. The peak intensity is almost temperature-independent at relatively lower temperature up to 700°C, indicating that the irradiation-induced defects do not recover in such low temperature range. The temperature dependence of the peak intensity is demonstrated in Fig.2. At low fluence of 6.7×10^{11} ions/cm^2, the peak intensity decreases as increasing temperature from 800°C to 1000°C, indicating that the irradiation-induced defects begin to move at such high temperature. At high fluence of 2.7×10^{12}, 1.3×10^{13} and 1.3×10^{14} ions/cm^2, the peak intensity increases as increasing temperature from 800°C to 1000°C, indicating that the irradiation-induced defects begin to annihilate at such high temperature. Therefore, 800°C can be defined as threshold temperature where the irradiation-induced defects begin to recover. This means that thermal energy corresponding to 700°C is not sufficient to annihilate the damage, while thermal energy corresponding to 800°C is the threshold energy to annihilate damage created by 120MeV Xe irradiation.

Part of the present study is the result of “Research of highly accurate evaluation of radiation damage in

[1] Japan Atomic Energy Agency (JAEA)

advanced nuclear reactor fuel ceramics" entrusted to "Japan Atomic Energy Agency" by the Ministry of Education, Culture, Sports, Science and Technology of Japan (MEXT).

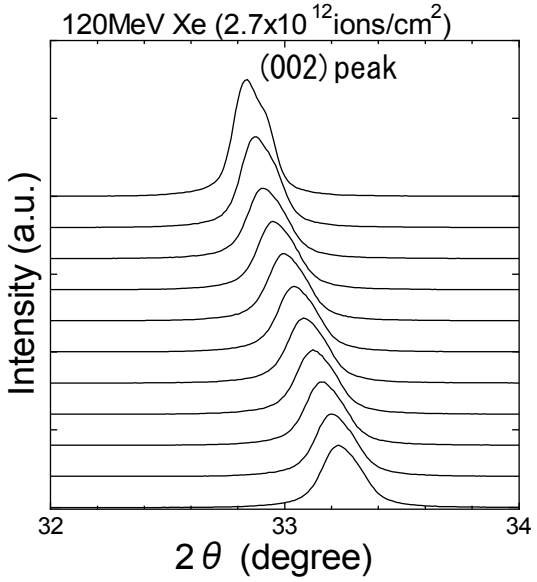

Fig. 1 X-ray diffraction patterns measured at elevated temperature (35°C - 1000°C) for CeO_2 irradiated at room temperature with 120MeV Xe up to $2.7x10^{12}$ ions/cm^2. The measurement temperature is, from up to bottom, 1000°C, 900°C, 800°C, 700°C, 600°C, 500°C, 400°C, 300°C, 200°C, 100°C and 35°C.

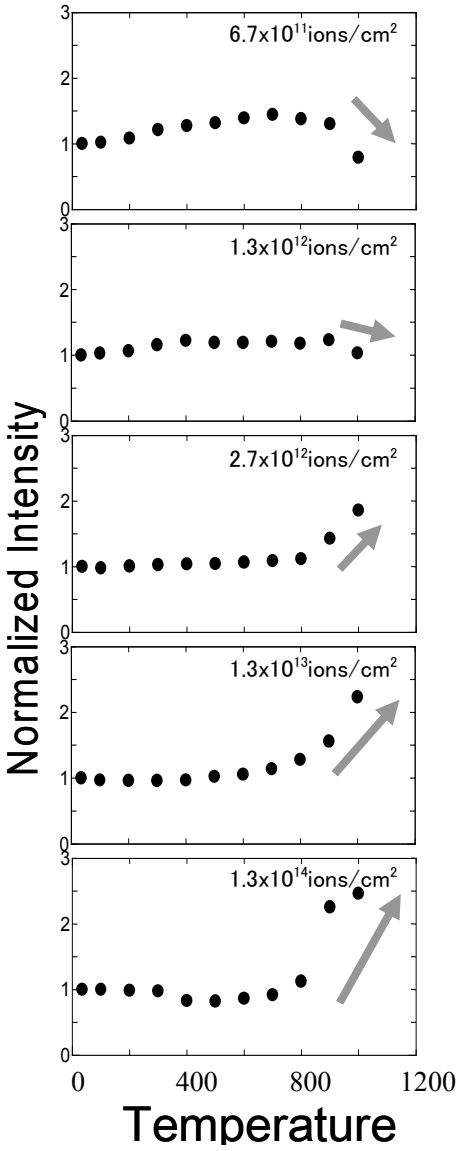

Fig. 2 Measurement temperature dependence of (002) peak intensity normalized by that measured at 35°C for CeO_2 irradiated with 120MeV Xe. The fluence is indicated in each figures.

7.11 Study of spatial distribution of chemical damages by ion beams using dynamic nuclear polarization

T. Kumada[1], Y. Noda[1], K. Ohara[2] and N. Ishikawa[1]

High energy ion beams have been focused on many industrial applications, such as medical treatment of brain cancer. When high-energy ion beams are irradiated into materials, subsequent ionizations and reactions due to secondary electrons take place along the track of the ion beams. It is important to determine the distribution of activated species to study radiation damage of materials by high-energy ion beams, and evaluate difference in quality factor between low linear-energy-transfer (LET) beams such as γ-rays and electron beams, and high LET ones.

Purpose of this study is to determine the spatial distribution of free radicals produced by the ionization of reactions using techniques of dynamic nuclear polarization (DNP) and small-angle neutron scattering (SANS). SANS is used for investigations of structure of various substances, with spatial sensitivity of about 1 - 300 nm. The concentration of free radicals produced by the radiolysis is $\leq 10^{19}$ spins/cm^3 enough for the determination of the spatial distribution of radicals by SANS.

DNP is the technique which transfers spin polarization from electrons to nuclei, thereby aligning the nuclear spins to the extent that electron spins are aligned. About 1000 protons near one electron spin can be polarized by DNP. Scattering length of a proton for a polarized neutron strongly depends on its spin state. The polarized protons around the free radicals are expected to generate strong scattering of polarized neutron beams, whose profile reflects distribution of the free radicals. Thus, we polarized the protons near the free radicals by DNP, and measured SANS profile of the dynamically polarized samples.

Low-density polyethylene (PE) sheets with the size of 20 mm x 20 mm x 0.5 mm were attached on a cold head of a cryostat, and irradiated with C^{6+} (100 MeV) ion beams at 77 K to the total dose of 10^9 – 10^{13} ions / cm^2. Fig. 1 shows the concentrations of the alkyl free radicals measured by an electron spin resonance (ESR) spectrometer. Total amounts of 10^{16} to 10^{19} spins / cm^3 radicals were found to be produced.

Fig. 2 shows a comparison between the enhancement of polarization of the dynamically polarized PE sheets irradiated with the electron beams (EB) and that of the ion beams. The enhancement of ~ 100 was obtained for the EB-irradiated PE, but only 3 was obtained for the ion-beam irradiated PE.

[1] Japan Atomic Energy Agency (JAEA)
[2] Ibaraki University

Since this DNP process is related to three-spin (electron-electron-nucleus) process that mutually flips the coupled three spins under the energy conservation of the Zeeman interactions, the DNP efficiency strongly depends on concentration of electron spins. It is empirically known that the maximum proton polarization is obtained in samples containing free radicals at ~ 10^{19} spins / cm^3. The polarization at the higher concentration of the free radicals is very poor due to fast nuclear spin relaxation by the aid of the free radicals, whereas DNP efficiency is very poor at the lower concentration. The alkyl free radicals were homogeneously produced in the EB-irradiated PE sample. The concentration of free radicals can be optimized by controlling the dose of the EB-irradiation. On the other hand, the alkyl free radicals are localized along the track of ion beams in the ion-beam-irradiated PE. The local concentration of the free radicals along the track is too high for DNP, whereas no radical is generated on the other regions. The number of tracks increases with increasing the dose of the ion-beams, but both the local concentrations of the free radicals along the tracks and that of the other regions are independent of the dose. We hope that the DNP technique can be established to evaluate the quality factor of radiation.

We are planning to carry out a DNP-SANS measurement of the ion-beam irradiated PE samples in near future.

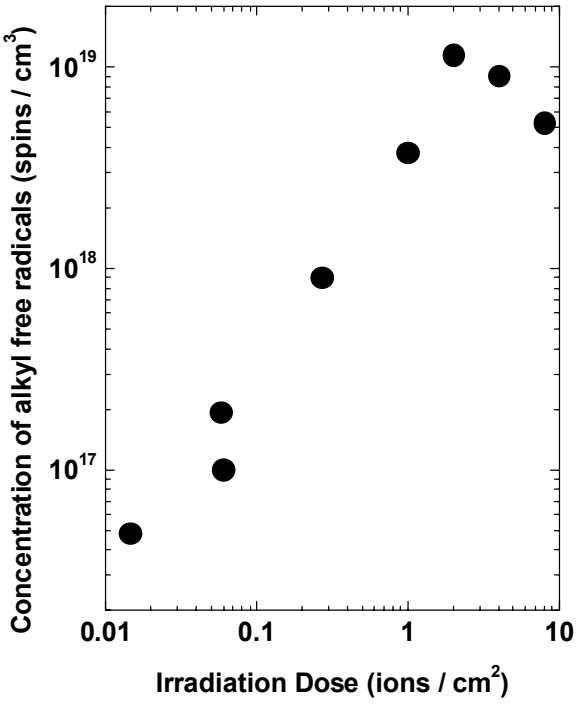

Fig. 1 Concentration of alkyl free radicals in ion-beam irradiated PE.

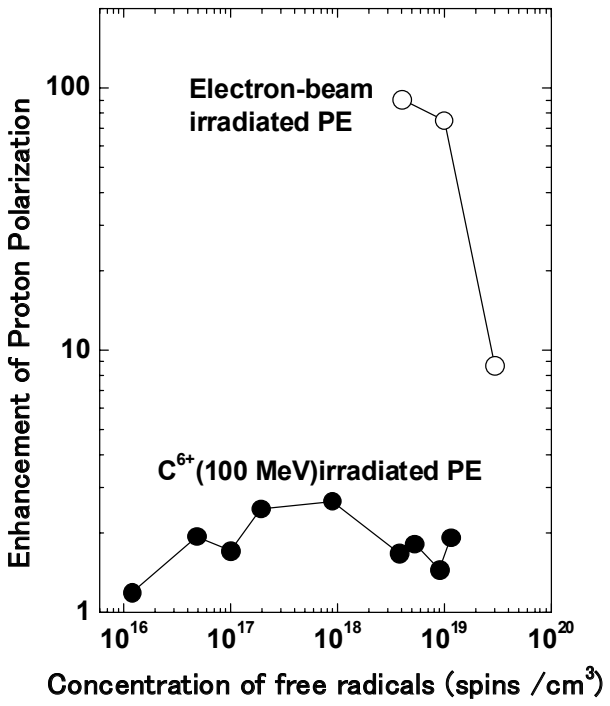

Fig. 2 Enhancement of proton polarization for EB and ion-beam irradiated PE.

CHAPTER 8

Publication in Journal and Proceedings, and Contribution to Scientific Meetings

This is a blank page.

8.1 Accelerator Operation and Development

Journal/Proceedings

T. Ishii, M. Matsuda, H. Kabumoto and A. Osa
*Recent activities in tandem, booster and TRIAC at Toka*i
Proceedings of the 6th Japan-Italy Symposium on Heavy-Ion Physics, Tokai, Japan (Nov. 11-15, 2008)
AIP Conference Proceedings, 1120 (2009) 235-240

A. Osa, M. Matsuda, T. K. Sato and S. Ichikawa
Release and efficiencies of radioactive ion beams from the JAEA-ISOL target/ion source systems
Proceedings of the 15th International Conference on Electromagnetic Isotope Separators and Techniques Related to their Applications (EMIS2007), Deauville, France (June 24-29, 2007).
Nucl. Instrum. Methods Phys. Res., B266 (2008) 4373.

A. Osa, S. Ichikawa, M. Matsuda, T. K. Sato and S.C. Jeong
Ion source development for the on-line isotope separator at JAEA
Proceedings of the 15th International Conference on Electromagnetic Isotope Separators and Techniques Related to their Applications (EMIS2007), Deauville, France (June 24-29, 2007).
Nucl. Instrum. Methods Phys. Res., B266 (2008) 4394.

M. Matsuda, M. Sataka, Y. Tsukihashi, S. Hanashima, S. Abe, A. Osa, N. Ishizaki, T. Nakanoya, H. Kabumoto, M. Nakamura, K. Kutsukake, Y. Otokawa and T. Asozu
Present Status of JAEA-Tokai Tandem Accelerator
Proc. of the 21th Meeting for Tandem Accelerators and their Associated Technologies, Takasaki, JAEA-Takasaki (July. 31- Oct. 1, 2008) , JAEA-Conf 2008-012 (2009)39-43.

S.C. Jeong, N. Imai, M. Oyaizu, S. Arai, Y. Fuchi, Y. Hirayama, H. Ishiyama, H. Miyatake, M. Okada, M.H. Tanaka, Y.X. Watanabe, S. Ichikawa, A. Osa, T.K. Sato, and H. Kabumoto
KEKCB-18GHz ECR charge breeder at TRIAC
Nucl. Instrum. Methods Phys. Res., B257 (2007) 397.

N. Imai, S.C. Jeong, M. Oyaizu, S. Arai, Y. Fuchi, Y. Hirayama, H. Ishiyama, H. Miyatake, M.H. Tanaka, M. Okada, Y.X. Watanabe, S. Ichikawa, H. Kabumoto, A. Osa, Y. Otokawa, and T.K. Sato
KEKCB electron cyclotron resonance charge breeder at TRIAC
Rev. Sci. Inst. 79 (2008) 02A906.

S.C. Jeong, I. Katayama, H. Kawakami, Y. Watanabe, H. Ishiyama, N. Imai, Y. Hirayama, H. Miyatake, M. Sataka, H. Sugai, S. Okayasu, S.-I. Ichikawa, K. Nishio, S. Mitsuoka, Y. Nakanoya, T. Hashimoto, T. Hashimoto, and M. Yahagi

On-line diffusion tracing in Li ionic conductors by the short-lived radioactive beam of ^{8}Li
Jpn. J. Appl. Phys., Part 1 47 (2008)6413.

N. Ishizaki, M. Matsuda, S. Hanashima, M. Nakamura, K. Kutsukake, Y. Otokawa, and T. Asozu
Improvement of transmission of ion beams and replacement of charge analysis electromagnet coil at the tandem accelerator
JAEA-Technology 2008-055

M. Nakamura, M.Matsuda, T. Nakanoya, H. Kabumoto, K. Kutsukake, Y. Otokawa, T. Asozu, T. Ishii, M, Asai, and T. Okura
Identification procedure of natural radon (^{222}Rn) using electrostatic collection method
JAEA-Technology 2008-052

Meetings

T. Ishii
Recent Activities in Tandem, Booster and TRIAC at Tokai
6th Japan-Italy Symposium on Heavy-Ion Physics, Tokai, Japan (Nov. 11-15, 2008).

H, Miyatake
TRIAC - Progress in collaboration -
Biennial meeting of the JAEA-Tokai Tandem Accelerator, on the occasion of attaining a-hundred-thousand hours of accelerator operation for experiments, Tokai, Japan (Jan. 6-7, 2009)

S. Hanashima
Measurement of impedance of bending magnet-2
21th Meeting on Tandem Accelerators and their Associated Technologies, Takasaki, Japan (July. 31- Oct. 1, 2008).

S. Hanashima
Control System of the JAEA-Tokai tandem accelerator
Biennial meeting of the JAEA-Tokai Tandem Accelerator, on the occasion of attaining a-hundred-thousand hours of accelerator operation for experiments, Tokai, Japan (Jan. 6-7, 2009)

M. Matsuda, M. Sataka, Y. Tsukihashi, S. Hanashima, S. Abe, A. Osa, N. Ishizaki, T. Nakanoya, H. Kabumoto, M. Nakamura, K. Kutsukake, Y. Otokawa and T. Asozu
Present status of JAEA-Tokai tandem accelerator
21th Meeting on Tandem Accelerators and their Associated Technologies, Takasaki, Japan (July. 31- Oct. 1, 2008).

M. Matsuda, T. Asozu, T. Nakanoya, K. Kutsukake, S. Hanashima and S. Takeuchi
Highly charged ion injector in the terminal of tandem accelerator
14th International Conference on the Physics of Highly Charged Ions (HCI2008), Chofu, Japan (Sep. 1, 2008).

M. Matsuda
Beam intensity increase with improving the ion injector in the high-voltage terminal(oral)
Highly charged ion injector in the terminal of tandem accelerator(poster)
Biennial meeting of the JAEA-Tokai Tandem Accelerator, on the occasion of attaining a-hundred-thousand hours of accelerator operation for experiments, Tokai, Japan (Jan. 6-7, 2009)

S. Takeuchi
Review of accelerator improvements during past thirty years for the JAEA-Tokai tandem accelerator
Biennial meeting of the JAEA-Tokai Tandem Accelerator, on the occasion of attaining a-hundred-thousand hours of accelerator operation for experiments, Tokai, Japan (Jan. 6-7, 2009)

H. Kabumoto, S. Takeuchi, N. Ishizaki, M. Matsuda, Y. Otokawa, T. Yoshida, T. Ishiguro and K. Yamaguchi
Development of low beta superconducting twin quarter wave resonator
Biennial meeting of the JAEA-Tokai Tandem Accelerator, on the occasion of attaining a-hundred-thousand hours of accelerator operation for experiments, Tokai, Japan (Jan. 6-7, 2009)

M. Oyaizu, S.C. Jeong, N. Imai, Y. Fuchi, Y. Hirayama, H. Ishiyama, H. Miyatake, M. Okada, Y.X. Watanabe, S. Ichikawa, H. Kabumoto, M. Matsuda, A. Osa, and Y. Otokawa
Present status of Charge Breeding in KEKCB at TRIAC
6th Japan-Italy symposium on Heavy-ion physics, Tokai, Japan (Nov. 11, 2008).

M. Oyaizu, S.C. Jeong, N. Imai, Y. Fuchi, Y. Hirayama, H. Ishiyama, H. Miyatake, M. Okada, Y.X. Watanabe, S. Ichikawa, H. Kabumoto, M. Matsuda, A. Osa, and Y. Otokawa
Current status of KEKCB at TRIAC
18th International Workshop on ECR Ion Source, Chicago, USA (Sep. 15, 2008).

A. Osa
Development of ion sources for JAEA-ISOL
Biennial meeting of the JAEA-Tokai Tandem Accelerator, on the occasion of attaining a-hundred-thousand hours of accelerator operation for experiments, Tokai, Japan (Jan. 6-7, 2009)

T. Nakanoya
Generation of metalic ion beams from ECR ions sources and its application to the tandem accelerator

Biennial meeting of the JAEA-Tokai Tandem Accelerator, on the occasion of attaining a-hundred-thousand hours of accelerator operation for experiments, Tokai, Japan (Jan. 6-7, 2009)

M. Nakamura
Present status of the interlock system for the tandem accelerator facility
Biennial meeting of the JAEA-Tokai Tandem Accelerator, on the occasion of attaining a-hundred-thousand hours of accelerator operation for experiments, Tokai, Japan (Jan. 6-7, 2009)

K. Kutsukake
Screening of relays to use in high-pressure SF_6 gas
Biennial meeting of the JAEA-Tokai Tandem Accelerator, on the occasion of attaining a-hundred-thousand hours of accelerator operation for experiments, Tokai, Japan (Jan. 6-7, 2009)

K. Otokawa
Present status of JAEA-ISOL and acceleration of radioactive beams
Biennial meeting of the JAEA-Tokai Tandem Accelerator, on the occasion of attaining a-hundred-thousand hours of accelerator operation for experiments, Tokai, Japan (Jan. 6-7, 2009)

T. Asozu
Existing-device alignment and installation plan of beam profile monitors in the high-voltage-terminal
Biennial meeting of the JAEA-Tokai Tandem Accelerator, on the occasion of attaining a-hundred-thousand hours of accelerator operation for experiments, Tokai, Japan (Jan. 6-7, 2009)

8.2 Nuclear Structure

Journal/Proceedings

T. Shizuma, T. Ishii, H. Makii, T. Hayakawa, and M. Matsuda
A 3-quasiparticle isomer in neutron-rich ^{183}Ta
Eur. Phys. J. A 39, (2009) 263.

Y. Liu, X.H. Zhou, Y.H. Zhang, Y. Zheng, M.L. Liu, Y.X. Guo, M. Oshima, Y. Toh, M. Koizumi, A. Osa, Y. Hatsukawa, and Y. Sun
Prolate and Oblate Shape Coexistence in ^{188}Pt
Chin .Phys. Lett., 25, 1633 (2008)

T. Shizuma, T. Ishii, H. Makii, T. Hayakawa, M. Matsuda, S. Shigematsu, E. Ideguchi, Y. Zheng, M .Liu, T .Morikawa, and M.Oi
One-quasiparticle bands in neutron-rich ^{187}W
Phys.Rev. C 77, 047303 (2008)

S. Ota, S. Shimoura, H. Iwasaki, M. Kurokawa, S. Michimasa, N. Aoi, H. Baba, K .Demichi, Z. Elekes, T. Fukuchi, T. Gomi, S. Kanno, S. Kubono, K. Kurita, H. Hasegawa, E. Ideguchi, N. Iwasa, Y.U. Matsuyama, K.L. Yurkewicz, T. Minemura, T. Motobayashi, T. Murakami, M. Notani, A. Odahara, A. Saito, H. Sakurai, E. Takeshita, S. Takeuchi, M. Tamaki, T. Teranishi, Y. Yanagisawa, K. Yamada, and M. Ishihara
Low-lying proton intruder state in ^{13}B
Phys.Lett. B 666, 311 (2008)

N. Aoi, H. Suzuki, E. Takeshita, S. Takeuchi, S. Ota, H. Baba, S. Bishop, T .Fukui, Y. Hashimoto, H.J. Ong, E. Ideguchi, K. Ieki, N .Imai, H. Iwasaki, S. Kanno, Y. Kondo, T. Kubo, K. Kurita, K. Kusaka, T.Minemura, T. Motobayashi, T. Nakabayashi, T. Nakamura, T. Nakao, M. Niikura, T. Okumura, T.K. Ohnishi, H. Sakurai, S. Shimoura, R. Sugo, D. Suzuki, M.K. Suzuki, M. Tamaki, K. Tanaka, Y. Togano, and K. Yamada
Shape transition observed in neutron-rich pf-shell isotopes studied via proton inelastic scattering
Nucl.Phys. A805, 400c (2008)

N. Aoi, E. Takeshita, H. Suzuki, S. Takeuchi, S. Ota, H. Baba, S. Bishop, T. Fukui, Y. Hashimoto, H.J. Ong, E. Ideguchi, K. Ieki, N. Imai, M. Ishihara, H. Iwasaki, S. Kanno, Y. Kondo, T. Kubo, K. Kurita, K. Kusaka, T. Minemura, T. Motobayashi, T. Nakabayashi, T. Nakamura, T. Nakao, M. Niikura, T. Okumura, T.K. Ohnishi, H. Sakurai, S. Shimoura, R. Sugo, D. Suzuki, M.K. Suzuki, M. Tamaki, K. Tanaka, Y. Togano, and K. Yamada
Development of Large Deformation in ^{62}Cr
Phys.Rev.Lett. 102, 012502 (2009)

Y. Toh, M. Oshima, M. Koizumi, A. Osa, A. Kimura, M. Sugawara, and J. Goto
Octupole collectivity in ^{94}Zr
The Thirteenth International Symposium on Capture Gamma-Ray Spectroscopy and Related Topics, Cologne,Germany (Aug. 25-29, 2008).
AIP Conference Proceedings, 1090 (2009) 189-193.

H. Iimura and F. Buchinger
Charge radii in macroscopic-microscopic mass models of reflection asymmetry
Phys. Rev., C78 (2008) 067301.

T. Ishii, H. Makii, M. Asai, K. Tsukada, A. Toyoshima, M. Matsuda, A. Makishima, S. Shigematsu, T. Shizuma, H. Toume, I. Hossain, T. Kohno and M. Ogawa
Observation of high-j quasiparticle states in 249Cm by in-beamγ-ray spectroscopy using heavy-ion transfer reactions
Phys. Rev, C78 (2008) 054309(1-11).

T. Ishii, H. Makii, M. Asai, H. Koura, S. Shigematsu, K. Tsukada, A. Toyoshima, M. Matsuda, A. Makishima, T. Shizuma, J. Kaneko, H. Toume, I. Hossain, S. Ichikawa, T. Kohno, and M. Ogawa
In-beam γ-ray spectroscopy of neutron-rich nuclei in the uranium region through the heavy-ion transfer reaction
Proc. Int. Nuclear Physics Conference (INPC 2007), (Tokyo 2007) Vol. 2, pp. 257-259.

Meetings

J.J. Carroll
Studies of nuclear structure related to an induced depletion of isomers
Ulaanbaatar Conference on Nuclear Physics and Applications, Ulaanbaatar, Mongolia (Sep. 8, 2008).

J.J. Carroll
Search for induced depletion of nuclear isomers
39th Winter Colloquium on the Physics of Quantum Electronics, Snowbird, USA (Jan. 4, 2009)

M. Koizumi, Y. Toh, M. Oshima, A. Kimura, Y. Hatsukawa, H. Harada, F. Kitatani, S. Nakamura, K. Furutaka, M. Sugawara, and T. Morikawa
Study of low-lying nuclear structure of ^{102}Ru
Annual meeting of The Physical Society of Japan, Tokyo, Japan (Mar. 28, 2009).

M. Asai
Gamma-ray spectroscopy of heavy-actinide and transactinide nuclei: toward more neutron-rich and

heavier nuclei
CNS-RIKEN Joint International Symposium on Frontier Gamma-ray Spectroscopy and Perspectives for Nuclear Structure Studies (Gamma08), Wako, Japan (Apr. 5, 2008).

M. Asai, K. Tsukada, M. Sakama, Y. Ishii, A. Toyoshima, T. Ishii, I. Nishinaka, Y. Nagame, Y. Kasamatsu, H. Haba, Y. Kojima, M. Shibata, H. Hayashi and K. Sueki
Gamma-ray spectroscopy of the heaviest nuclei at JAEA tandem accelerator
6th Japan-Italy Symposium on Heavy-ion Physics ―ASR2008: Perspective in Nuclear Physics―, Tokai, Japan (Nov. 12, 2008).

M. Asai
α-γ spectroscopy of superheavy nuclei
Fall meeting of The Physical Society of Japan, Yamagata, Japan (Sep. 22, 2008).

M. Asai, H. Hayashi, A. Osa, T. K. Sato, Y. Otokawa, D. Nagae, K. Tsukada, Y. Miyashita, H. Ouchi, S. Izumi and T. Shinozuka
Lifetime measurements for long-lived isomers in ^{162,165}Gd using a total absorption detector
Annual meeting of The Physical Society of Japan, Tokyo, Japan (Mar. 28, 2009).

E. Ideguchi, S. Ota, T. Morikawa, T. Shizuma, M. Oshima, M. Koizumi, Y. Toh, Y. Hatsukawa, A. Kimura, K. Furutaka, S. Nakamura, F. Kitatani, H. Harada, M. Sugawara, Y. Watanabe, Y. Hirayama and H. Miyatake
Study of high-spin states in ^{40}Ar
Annual meeting of The Physical Society of Japan (Mar. 28, 2009).

E. Ideguchi
Collective band structure in ^{40}Ar
3rd LACM-EFES-JUSTIPEN workshop, Oak Ridge National Laboratory, USA (Feb. 23, 2009).

E. Ideguchi
Study of high-spin states in A～30 region
Biennial meeting of the JAEA-Tokai Tandem Accelerator, on the occasion of attaining a-hundred-thousand hours of accelerator operation for experiments, Tokai, Japan (Jan. 6-7, 2009)

H. Schuessler, F. Buchinger, T. Cocolios, J.E. Crawford, S. Gulick, H. Iimura, J.K.P. Lee, C.D.P. Levy, M. Pearson, V. Lioubimov, F. Zhu, J. Rikovska, S.D. Rosner, R. Thompson and R. Wyss
Nuclear moments of the radioactive isotope ^{131}La determined by collinear fast-beam laser spectroscopy
5th International Conference on Exotic Nuclei and Atomic Masses ENAM '08, Ryn, Poland (Sep. 11, 2008).

H. Iimura and F. Buchinger
Charge radii in modern macroscopic-microscopic mass models
5th International Conference on Exotic Nuclei and Atomic Masses ENAM '08, Ryn, Poland (Sep. 11, 2008).

H. Iimura and F. Buchinger
Nuclear charge radii calculated with Finite Range Droplet Model
Annual meeting of The Physical Society of Japan, Tokyo, Japan (Mar. 29, 2009).

R. Takahashi, T. Ishii, D. Nagae, M. Asai, H. Makii, K. Tsukada, A. Toyoshima, Y. Ishii, M. Matsuda, T. Shizuma, A. Makishima, T. Kohno and M. Ogawa
In-beam γ-ray spectroscopy of ^{248,250,252}Cf using neutron-transfer reactions
Annual meeting of The Physical Society of Japan, Tokyo, Japan (Mar. 28, 2009).

T. Ishii
Development of in-beam γ-ray spectroscopy in combination with charged-particle detection
Biennial meeting of the JAEA-Tokai Tandem Accelerator, on the occasion of attaining a-hundred-thousand hours of accelerator operation for experiments, Tokai, Japan (Jan. 6-7, 2009)

8.3 Nuclear Reaction

Journal/Proceedings

S. Mitsuoka, H. Ikezoe, K. Nishio, Y. Watanabe, and S.C. Jeong
Barrier distribution of quasi-elastic backward scattering of ^{48}Ti, ^{54}Cr, ^{56}Fe, ^{64}Ni, ^{70}Zn and ^{86}Kr on ^{208}Pb
AIP Conf. Proc. 1098, 122 - 127 (2009).

S. Mitsuoka, H. Ikezoe, K. Nishio, Y. Watanabe, S.C. Jeong, H. Ishiyama, Y. Hirayama, N. Imai, and H. Miyatake
Barrier distribution of quasi-elastic backward scattering
AIP Conf. Proc. 1120, 15 – 20 (2009).

K. Nishio, H. Ikezoe, S. Mitsuoka, I. Nishinaka, Y. Nagame, Y. Watanabe, T. Ohtsuki, K. Hirose, and S.Hofmann
Effects of nuclear orientation on the mass distribution of fission fragments in the reaction of $^{36}S + ^{238}U$
Phys. Rev. C, 77, 064607(1-5) (2008).

J. Khuyagbaatar, S. Hofmann, F.P. Hessberger, D. Ackermann, H.G. Burkhard, S. Heinz, B. Kindler, I. Kojouharov, B. Lommel, R. Mann, J. Maurer, K. Nishio, and Yu. Novikov
Spontaneous fission of neutron-deficient fermium isotopes and the new nucleus ^{241}Fm
Eur. Phys. J. A, 37, 177-183 (2008).

S. Heinz, V. Comas, F.P. Hessberger, S. Hofmann, D. Ackermann, H.G. Burkhard, Z. Gan, J. Heredia, J. Khuyagbaatar, B. Kindler, B. Lommel, R. Mann, J. Maurer, K. Nishio, and B. Sulignano
Di-nuclear systems studied with the velocity filter SHIP
Eur. Phys. J. A, 38, 227-232 (2008).

J. Dvorak, W. Bruchle, M. Chelnokov, Ch. E. Dullmann, Z. Dvorakova, K. Eberhardt, E. Jager, R. Krucken, A. Kuznetsov, Y. Nagame, F. Nebel, K. Nishio, R. Perego, Z. Qin, M. Schadel, B. Schausten, E. Schimpf, R. Schuber, A. Semchenkov, P. Thorle, A. Turler, M. Wegrzecki, B. Wierczinski, A. Yakushev, and A. Yeremin
Observation of the 3n evaporation channel in the complete hot-fusion reaction $^{26}Mg + ^{248}Cm$ leading to the new superheavy nuclide ^{271}Hs
Phys. Rev. Lett., 100, 132503 (2008).

S. Antalic, F.P. Hessberger, S. Hofmann, D. Ackermann, S. Heinz, B. Kindler, I. Kojouharov, P. Kuusiniemi, M. Leino, B. Lommel, R. Mann, K. Nishio, B. Sulignano, B. Sulignano, and M. Venhart
Decay studies of neutron deficient lawrencium isotopes
Eur. Phys. J. A, 38, 219-226 (2008).

K. Nishio, S. Hofmann, H. Ikezoe, F.P. Hessberger, D. Ackermann, S. Antalic, V. Comas, Z. Gan, S. Heinz, J. Heredia, J. Khuyagbaatar, B. Kindler, I. Kojouharov, P. Kuusiniemi, B. Lommel, R. Mann, M. Mazzocco, S. Mitsuoka, Y. Nagame, T. Ohtsuki, A.G. Popeko, S. Saro, H.J. Shoett, B. Sulignano, A. Svirikhin, K. Tsukada, and A.V. Yeremin
Orientation effects of deformed ^{238}U target nuclei on the fusion probability for heavy element synthesis
Proc. Int. Nuclear Physics Conference (INPC 2007), Vol. 2, pp. 516-518.

K. Nishio, H. Ikezoe, S. Mitsuoka, I. Nishinaka, Y. Nagame, Y. Watabnabe, T. Ohtsuki, K. Hirose, and S. Hofmann
Effects of nuclear orientation on fission fragment mass distributions in the reaction of $^{34,36}S + ^{238}U$
New Aspects of Heavy Ion Collisions Near the Coulomb barrier, "FUSION08", Chicago, USA,
AIP Conf. Proc. 1098, p.289-294.

K. Nishio, H. Ikezoe, S. Mitsuoka, I. Nishinaka, Y. Watanabe, Y. Nagame, T. Ohtsuki, K. Hirose, and S. Hofmann
Effects of nuclear orientation on fusion and fission process in heavy ion reactions
Proceedings of the 6th Japan-Italy Symposium on Heavy-Ion Physics,
AIP Conf. Proc. 1120, p.275-279.

I. Nishinaka, M. Tanikawa, S. Goto, K. Nishio, M. Asai, K. Tsukada, Y. Nagame, and H. Kudo
Excitation energy dependence of fragment mass and total kinetic energy distributions in proton-induced fission of uranium isotopes
The 23rd International Nuclear Physics Conference (INPC2007), Tokyo, Japan (Jun. 3-8, 2007)
Proceedings of the 23rd International Nuclear Physics Conference (INPC2007), 2 (2008) 434-436.

I. Nishinaka, M. Tanikawa, S. Goto, K. Nishio, M. Asai, S. Ichikawa, K. Tsukada, A. Toyoshima, H. Haba, K. Akiyama, A. Yokoyama, Y. Nagame, and H. Kudo
Excitation energy dependence of fragment mass and total kinetic energy distributions in proton-induced fission of light actinides
The 4th International Conference on Fission and Properties of Neutron-Rich Nuclei, Sanibel, USA (Nov. 11-17, 2008)
Proceedings of 4th International Conference on Fission and Properties of Neutron-Rich Nuclei, (2008) 206-211.

Meetings

S. Mitsuoka, H. Ikezoe, K. Nishio, Y. Watanabe, and S.C. Jeong
Barrier distribution of quasi-elastic backward scattering of ^{48}Ti, ^{54}Cr, ^{56}Fe, ^{64}Ni, ^{70}Zn and ^{86}Kr on ^{208}Pb

International Conference on New Aspects of heavy Ion Collisions Near the Coulomb Barrier, FUSION08, Chicago, USA, Sep. 22-26, 2008.

S. Mitsuoka, H. Ikezoe, K. Nishio, Y. Watanabe, S.C. Jeong, H. Ishiyama, Y. Hirayama, N. Imai, and H. Miyatake
Barrier distribution of quasi-elastic backward scattering
6th Japan-Italy symposium on Heavy-Ion Physics, ASR2008, Tokai, Japan, Nov. 11-15, 2008.

K. Nishio, H. Ikezoe, S. Mitsuoka, I. Nishinaka, Y. Watanabe, Y. Nagame, T. Ohtsuki, K. Hirose, and S. Hofmann
Effects of nuclear deformation of ^{238}U on the fission fragment mass distribution in the reaction of ^{30}Si + ^{238}U
Annual meeting of The Physical Society of Japan, Tokyo (March.27-30, 2009)

K. Nishio
Effects of nuclear orientation on fusion and fission process for reactions using actinide nuclei
Biennial meeting of the JAEA-Tokai Tandem Accelerator, on the occasion of attaining a-hundred-thousand hours of accelerator operation for experiments, Tokai, Japan (Jan. 6-7, 2009)

K. Nishio
Fusion and fission process for the reactions involving actinide target nuclei
Molecular structure and low energy nuclear reactions, Kyoto University, July.2 – 4, 2008

I. Nishinaka, M. Tanikawa, Y. Nagame, and H. Nakahara
Nuclear-charge polarization at scission in proton-induced fission of light actinides
International Conference on New Aspects of Heavy Ion Collisions near the Coulomb Barrier (Fusion08), Chicago, (Sep. 26, 2008).

H. Kawamura
The first T-Violation Experiment at KEK-TRIAC
Spin Praha 2008, Prague, Czech (July 20-26, 2008).

8.4 Nuclear Chemistry

Journal/Proceedings

A. Toyoshima, H. Haba, K. Tsukada, M. Asai, K. Akiyama, S. Goto, W.Sato, Y. Ishii, I. Nishinaka, T. K. Sato, Y. Nagame, Y. Tani, H. Hasegawa, K. Matsuo, D. Saika, Y. Kitamoto, A. Shinohara, M. Ito, J. Saito, H. Kudo, A. Yokoyama, M. Sakama, K. Sueki, Y. Oura, H. Nakahara, M. Schädel, W. Brüchle, and J. V. Kratz
Hexafluoro complex of rutherfordium in mixed HF/HNO_3 solutions
Radiochim. Acta 96 (2008) 125-134.

A. Toyoshima, Y. Kasamatsu, Y. Kitatsuji, K. Tsukada, H. Haba, A. Shinohara, and Y. Nagame
Development of an electrochemistry apparatus for the heaviest elements
Radiochim. Acta 96 (2008) 323-326.

Y. Kasamatsu, A. Toyoshima, H. Haba, H. Toume, K. Tsukada, K. Akiyama, T. Yoshimura, and Y. Nagame
Adsorption of Nb, Ta and Pa on anion-exchanger in HF and HF/HNO_3 solution – Model experiments for the chemical study of Db -
J. Radioanal. Nucl. Chem. 279 (2009) 371-376.

K. Tsukada, H. Haba, M. Asai, A. Toyoshima, K. Akiyama, Y. Kasamatsu, I. Nishinaka, S. Ichikawa, K. Yasuda, Y. Miyamoto, K. Hashimoto, Y. Nagame, S. Goto, H. Kudo, W. Sato, A. Shinohara, Y. Oura, K. Sueki, H. Kikunaga, N. Kinoshita, A. Yokoyama, M. Schädel, W. Brüchle, and J. V. Kratz
Adsorption of Db and its homologues Nb and Ta, and the pseudo-homologue Pa on anion-exchange resin in HF solution
Radiochim. Acta 97 (2009) 83-89.

Meetings

Y. Kasamatsu, A. Toyoshima, K. Tsukada, M. Asai, Y. Ishii, I. Nishinaka, T.K. Sato, Z. Li, T. Kikuchi, Y. Nagame, S. Goto, H. Haba, and K. Akiyama
Anion-exchange experiments of nuclear reaction products transported by He/KCl and He/KF gas-jet systems
Annual Meeting of the Japan Society of Nuclear and Radiochemical Sciences – The 52th Symposium on Radiochemistry, Hiroshima, Japan (Sep. 25, 2008).

Z. Li., A. Toyoshima, Y. Kasamatsu, M. Asai, K. Tsukada, Y. Nagame, and H. Haba
Ion-exchange behavior of Zr and Hf as homologues of Rf in sulfuric acid solution
52th Symposium on Radiochemistry, Hiroshima, Japan (Sep. 25-27, 2008).

Y. Nagame, A. Toyoshima, Y. Ishii, Y. Kasamatsu, H. Toume, M. Asai, and K. Tsukada
Chemical characterization of the transactinide elements Rf and Db at JAEA
ACS National Meeting, New Orleans, LA, USA, April 6-10, 2008.

A. Toyoshima, Y. Kasamatsu, K. Tsukada, Y. Kitatsuji, H. Haba, Y. Ishii, H. Toume, M. Asai, K. Akiyama, K. Ooe, W. Sato, A. Shinohara, and Y. Nagame
Characterization of Heavy Actinides with Electrochemistry
ACS National Meeting, New Orleans, LA, USA, April 6-10, 2008.

A. Toyoshima, Y. Kasamatsu, K. Tsukada, A. Kitatsuji, H. Haba, M. Aasi, Y. Ishii, H. Toume, K. Akiyama, K. Ooe, W. Sato, A. Shinohara, and Y. Nagame
Electrochemical Oxidation of Element 102, Nobelium
2nd International Nuclear Chemistry Congress, Cancún, Mexico, April 13-18, 2008.

Y. Nagame, K. Akiyama, M. Asai, S. Goto, H. Haba, Y. Ishii, Y. Kasamatsu, I. Nishinaka, T. K. Sato, H. Tome, A. Toyoshima, and K. Tsukada
Fluoro complex formation of Rf and Db
7th International Conference on Nuclear and Radiochemistry, Budapest, Hungary, August 24-29, 2008.

Y. Nagame
Chemical characterization of the heaviest elements at JAEA
American Chemical Society Meeting, Salt Lake City, USA, March 22, 2009.

Y. Nagame, M. Asai, Y. Kasamatsu, T. K. Sato, A. Toyoshima, and K. Tsukada
Rapid chemical separation apparatus for atom-at-a-time chemistry of the heaviest elements
American Chemical Society Meeting, Salt Lake City, USA, March 22, 2009.

Y. Kasamatsu, A. Toyoshima, K. Tsukada, M. Asai, Y. Ishii, I. Nishinaka, T. K. Sato, Z. Li, T. Kikuchi, Y. Nagame, S. Goto, H. Haba, and K. Akiyama
Anion-exchange experiments of nuclear reaction products transported by He/KCl and He/KF gas-jet systems
52nd Symposium on Radiochemistry, Hiroshima, Japan (Sept. 25-27, 2008).

Z. Li, A. Toyoshima, Y. Kasamatsu, M. Asai, K. Tsukada, Y. Nagame, and H. Haba
Ion-exchange behavior of Zr and Hf as homologues of Rf in sulfuric acid solution
52nd Symposium on Radiochemistry, Hiroshima, Japan (Sept. 25-27, 2008).

K. Tsukada, Y. Kasamatsu, M. Asai, A. Toyoshima, Y. Ishii, and Y. Nagame
New apparatus for aqueous chemistry of the heaviest elements
52nd Symposium on Radiochemistry, Hiroshima, Japan (Sept. 25-27, 2008).

A. Toyoshima, Y. Kasamatsu, K. Tsukada, Y. Kitatsuji, Y. Ishii, H. Toume, M. Asai, Y. Nagame, H. Haba, K. Akiyama, K. Ooe, W. Sato, and A. Shinohara
Oxidation of nobelium by an electrochemical approach
52nd Symposium on Radiochemistry, Hiroshima, Japan (Sept. 25-27, 2008).

A. Toyoshima
Chemical studies of rutherfordium and nobelium on an atom-at-a-time scale
52nd Symposium on Radiochemistry, Hiroshima, Japan (Sept. 25-27, 2008).

K. Tsukada, Y. Kasamatsu, M. Asai, A. Toyoshima, Y. Ishii, Z. Li, T. K. Sato, I. Nishinaka, Y. Nagame, T. Kikuchi, S. Goto, T. Hasegawa, H. Kudo, H. Fujisawa, K. Ooe, W. Yahagi, W. Sato, A. Shinohara, T. Nanri, M. Araki, A. Yokoyama, F. Fan, Y. Kudou, and Y. Oura
Anion-exchange behavior of element-105 (Db) in HF/HNO_3 solutions using a newly developed on-line experimental system
Spring meeting of The Chemical Society of Japan, Hunabashi, Chiba (Mar. 29, 2009).

T. K. Sato, M. Asai, K. Tsukada, A. Toyoshima, Y. Kasamatsu, Z. Li, Y. Ishii, H. Haba, S. Goto, H. Kudo, and Y. Nagame
Development of an on-line isothermal gas chromatographic apparatus for gas chemistry of Sg (Z = 106)
Spring meeting of The Chemical Society of Japan, Hunabashi, Chiba (Mar. 29, 2009).

8.5 Nuclear Theory

Journal/Proceedings

V. Tripathi, S.L. Tabor, P. Bender, C.R. Hoffman, S. Lee, K. Pepper, M. Perry, P.F. Mantica, J.M. Cook, J. Pereira, J.S. Pinter, J.B. Stoker, D. Weisshaar, Y. Utsuno, and T. Otsuka
Excited intruder states in ^{32}Mg
Phys.Rev. C, 77 (2008) 034310-1-8.

K. Minamisono, P.F. Mantica, H.L. Crawford, J.S. Pinter, J. B. Stoker, Y. Utsuno, and R.R. Weerasiri,
Quadrupole moment of ^{37}K
Phys. Lett. B, 662 (2008) 389-394.

S. Ettenauer, H. Zwahlen, P. Adrich, D. Bazin, C.M. Campbell, J.M. Cook, A.D. Davies, D.-C. Dinca, A. Gade, T. Glasmacher, J.-L. Lecouey, W.F. Mueller, T. Otsuka, R.R. Reynolds, L.A. Riley, J.R. Terry, Y. Utsuno, and K. Yoneda
Intermediate-energy Coulomb excitation of ^{30}Na,
Phys. Rev. C, 78 (2008) 017302-1-4.

T. Otsuka, T. Suzuki, and Y. Utsuno
Exotic Nuclei and Yukawa's Forces
Nucl. Phys. A ,805 (2008) 127c-136c.

L.A. Riley, P. Adrich, T.R Baugher, D. Bazin, B.A. Brown, J.M. Cook, P.D. Cottle, C.A. Diget, A. Gade, D.A. Garland, T. Glasmacher, K.E. Hosier, K.W. Kemper, T. Otsuka, W.D.M. Rae, A. Ratkiewicz, K.P. Siwek, J.A. Tostevin, Y. Utsuno, and D. Weisshaar
$d_{5/2}$ proton hole strength in neutron-rich ^{43}P: Shell structure and nuclear shapes near N = 28
Phys. Rev. C, 78 (2008) 011303(R)-1-5.

V. Tripathi, S.L. Tabor, P.F. Mantica, Y. Utsuno, P. Bender, J. Cook, C.R. Hoffman, S. Lee, T. Otsuka, J. Pereira, M. Perry, K. Pepper, J.S. Pinter, J. Stoker, A. Volya, and D. Weisshaar
Intruder Configurations in the A=33 Isobars: ^{33}Mg and ^{33}Al
Phys. Rev. Lett., 101 (2008) 142504-1-4.

M. Wiedeking, E. Rodriguez-Vieitez, P. Fallon, M.P. Carpenter, R.M. Clark, D. Cline, M. Cromaz, M. Descovich, R.V.F. Janssens, I.-Y. Lee, M.-A. Deleplanque, A.O. Macchiavelli, F.S. Stephens, R. Teng, X. Wang, D. Ward, C.Y. Wu, S. Zhu, T. Otsuka, Y. Utsuno, and A. Volya
Intruder excitations in ^{35}P
Phys. Rev. C, 78 (2008) 037302-1-4.

D. Kaji, K. Morimoto, N. Sato, T. Ichikawa, E. Ideguchi, K. Ozeki, H. Haba, H. Koura, Y. Kudou, A. Ozawa, T. Sumita, T. Yamaguchi, A. Yoneda, A. Yoshida, and K. Morita
Production of a New Hassium Isotope ^{263}Hs
J. Phys. Soc. Jpn., 78 (2009) 03500

T. Maruyama, S. Chiba, H.-J. Schulze and T. Tatsumi
Properties of hyperon-quark mixed phase in compact stars
J. Phys. G 35, (2008) 104076

T. Muto, T. Maruyama and T. Tatsumi
Structure of multi-antikaonic nuclei in the relativistic mean-field model
Mod. Phys. Lett. A 23 (2008) 2536

T. Maruyama, S. Chiba and T. Tatsumi
Non-uniform structure of matter and the equation of state
Int. J. Mod. Phys. E 17 (2008) 1774

T. Maruyama, S. Chiba and T. Tatsumi
Equation of state of nuclear matter in the first order phase transition
AIP Conf. Proc. 1120 (2009) 129

N. Yasutake, T. Maruyama, T. Tatsumi, K. Kiuchi and K. Kotake
General relativistic compact stars with exotic matter
AIP Conf. Proc. 1120 (2009) 146

T. Muto, T. Maruyama and T. Tatsumi
Structure of Multi-Antikaonic Nuclei
AIP Conf. Proc. 1120 (2009) 270

Meetings

Y. Utsuno, B.A. Brown, T. Otsuka, M. Honma, and T. Mizusaki
Single-particle structure of exotic nuclei in the sd-pf shell by a new shell-model interaction
Nuclear Structure 2008 Conference, East Lansing, USA (Jun. 5, 2008).

Y. Utsuno, T. Otsuka, B. A. Brown, M. Honma, and T. Mizusaki
Deep proton hole states of ^{48}Ca studied by (e,e'p) and its implications on the tensor shell evolution
Joint Meeting of Hokudai-TORIJIN-JUSTIPEN-EFES Workshop "Perspectives in Resonances and Continua Nuclei" and "JUSTIPEN-EFES-Hokudai-UNEDF" meeting, Onuma, Japan (July 22, 2008).

Y. Utsuno, T. Otsuka, B. A. Brown, M. Honma, and T. Mizusaki
Spectroscopic factor of unstable nuclei around N=28 and shell evolution
Fall meeting of The Physical Society of Japan, Yamagata, Japan (Sep. 20, 2008).

Y. Utsuno, T. Otsuka, B. A. Brown, M. Honma, and T. Mizusaki,
Shell evolution in the sd-pf shell studied by the shell model
6th Japan-Italy Symposium on Heavy Ion Physics, Tokai, Japan (Nov. 12, 2008).

Y. Utsuno
Toward understanding the whole nuclear chart by the shell model
RIBF users meeting 2008, Wako, Japan (Nov. 22, 2008).

Y. Utsuno, T. Otsuka, B. A. Brown, M. Honma, and T. Mizusaki,
Description of shell evolution in unstable nuclei by the shell model
5th workshop on “Spectroscopy by Stopped and Slow RI Beam”, Toyonaka, Japan (Dec. 24, 2008).

Y. Utsuno, T. Otsuka, B. A. Brown, M. Honma, and T. Mizusaki,
Shell and nuclear structure of unstable nuclei beyond N=28
Annual meeting of The Physical Society of Japan, Tokyo, Japan (Mar. 27, 2009).

H. Koura
Phenomenological mass formulas and local fits
Mass Olympics, Trento, Italy (May 26-30, 2008)

O. V. Bespalova, I. N. Boboshin, V. V. Varlamov, T. A. Ermakova, B. S. Ishkhanov, S. Y. Komarov, H. Koura, E. A. Romanovskii and T. I. Spasskaya
Single-particle energies of 1f and 2p proton states in ^{58,60,62,64}Ni
Meeting on Nuclear Spectroscopy and Nuclear Structure (NUCLEUS-2008)
"Fundamental Problems of Nuclear Physics, Nuclear Methods in Nanotechnology, Medicine and Atomic Power Engineering," Moscow, Russia (Jun. 23-27, 2008)

H. Koura
Systematical Study of spherical single-particle levels for superheavy nuclei
Fall meeting of The Physical Society of Japan, Yamagata, Japan (Sep. 20-23, 2008)

H. Koura
Nuclear mass formulae and the r-process nucleosynthesis
New Era of Nuclear Physics in the Cosmos -the r-process nucleosynthesis, Wako, Japan (Sep. 25-26, 2008)

H. Koura, T. Tachibana and S. Chiba
Global properties of nuclear decay modes2008
Symposium on Nuclear Data, Tokai, Japan, (Nov. 20-21, 2008)

T. Tachibana, H. Koura and S. Chiba
Calculation of beta-delayed fission and neutron emission probabilities with the use of gross theory and KTUY mass formula
Symposium on Nuclear Data, Tokai, Japan, (Nov. 20-21, 2008)

H. Koura, T. Tachibana and S. Chiba
Global properties of nuclear masses and decay modes
Fifth International Conference on Exotic Nuclei and Atomic Masses (ENAM '08), Ryn, Poland, (Sep. 7-13, 2008)

T. Tachibana, H. Koura and S. Chiba
Systematical calculation of beta-delayed fission and neutron emission probabilities for super-heavy and neutron-rich nuclei relevant to the r-process nucleosynthesis
Fifth International Conference on Exotic Nuclei and Atomic Masses (ENAM '08), Ryn, Poland, (Sep. 7-13, 2008)

M.S. Smith, E.J. Lingerfelt, K.Bucker, C.D. Nesaraja, H. Koura, and F. Kondev
Visualization, Analysis, and Management of Nuclear Mass information at nucearmasses.org
Fifth International Conference on Exotic Nuclei and Atomic Masses (ENAM '08), Ryn, Poland, (Sep. 7-13, 2008)

K. Oyamatsu, K. Iida and H. Koura
Nuclear Liquid-drop model revisited
Annual meeting of The Physical Society of Japan, Ikebukuro, Japan (Mar. 27-30, 2009)

S. Hashimoto, K. Ogata, S. Chiba and M. Yahiro
Analysis of deuteron induced incomplete fusion reaction with Continuum-Discretized Coupled-Channels method
Fall meeting of The Physical Society of Japan, Yamagata, Japan (Sep. 28^{th} , 2008)

S. Hashimoto, K. Ogata, S. Chiba and M. Yahiro
Analysis of deuteron induced incomplete fusion reaction with Continuum-Discretized Coupled-Channels method
Spring meeting of the Atomic Energy Society of Japan, Tokyo, Japan (Mar. 23^{rd} , 2009)

S. Hashimoto, K. Ogata, S. Chiba and M. Yahiro
Analysis of deuteron induced incomplete fusion reaction with Continuum-Discretized Coupled-Channels method
Annual meeting of The Physical Society of Japan, Tokyo, Japan (Mar. 28th , 2009)

T. Maruyama, T. Maruyama, S.Chiba and T.Tatsumi
Structure and properties of nuclear matter at finite temperature studied by a relativistic mean field model
High-density nuclear matter and compact star phenomena, Kyoto, 5/30-31

T. Maruyama, H.-J. Schulze, S. Chiba and T. Tatsumi
Hyperon-quark mixed phase
High-density nuclear matter and compact star phenomena, Kyoto, 5/30-31

T. Maruyama, T. Maruyama, S. Chiba and T. Tatsumi
Structure and properties of nuclear matter at finite temperature studied by a relativistic mean field model
Fall meating of The Physical Society of Japan, Yamagata, 20-23 Sep

T. Maruyama, T. Muto and T. Tatsumi
Multi antikaonic states in nuclei
KEK meeting “Physics of J-PARC: New aspects of hadron and nuclei”, Tsukuba, 7-9 Aug

T. Maruyama, S. Chiba, H.-J. Schulze and T. Tatsumi
Hyperon Suppression in Hadron-Quark Mixed Phase
International Conference on Strangeness in Quark Matter, Beijing, 6-10 Oct. 2008,

T. Maruyama, S. Chiba and T. Tatsumi
Structured mixed phase and the equation of state
Nuclear Physics Meeting on “Clustering in Dilute Nuclear Matter”, Kizugawa, 18 Oct. 2008,

T. Maruyama, S. Chiba and T. Tatsumi
Equation of state of nuclear matter
6th Japan-Italy Symposium on Heavy Ion Physics, Tokai, 11-15 Nov. 2008,

T. Muto, T. Maruyama, and T. Tatsumi
Structure of multi-antikaonic nuclei
6th Japan-Italy Symposium on Heavy Ion Physics, Tokai, 11-15 Nov. 2008

N. Yasutake, T. Maruyama, T. Tatsumi, K. Kiuchi, and K. Kotakea
General relativistic compact stars with exotic matter; Effects of rotation and strong magnetic field
6th Japan-Italy Symposium on Heavy Ion Physics, Tokai, 11-15 Nov. 2008

T. Maruyama, T. Muto and T. Tatsumi
Multi-antikaonic nuclei studied with relativistic mean field model
KEK theory group seminar, Tsukuba, 1 Dec

T. Maruyama, S. Chiba and T. Tatsumi
Equation of state of nuclear matter at the first order phase transition
RIKEN mini workshop on heavy-ion collisions and the equation of state, Wako, 16-17 Dec

N. Yasutake, T. Maruyama, and T. Tatsumi
Finite size effects on quark-hadron phase transition and structurs of compact stars
National Astronomy Observatory meeting “Future of theoretical astronomy”, Mitaka, 15-17 Dec

T. Maruyama, S. Chiba and T. Tatsumi
Properties of non-uniform nuclear matter at finite temperature
Int. school and workshop on the crust of compact stars and beyond, Coimbra, 5-13 Feb. 2009

T. Maruyama, S. Chiba and T. Tatsumi
Mixed phase and the equation of state at the first-order phase transition of nuclear matter
Numazu workshop 2009, Numazu, 16-18 Mar

N. Yasutake, T. Maruyama, T. Tatsumi, K. Kiuchi and K .Kotake
Equation of state of quark-hadron mixed phase with pasta structures and neutron stars with strong magnetic field
Annual meeting of The Physical Society of Japan, Tokyo, 27-30 Mar

T. Muto, T. Maruyama and T. Tatsumi
Effects of K-K interaction on multi-kaonic nuclei
Annual meeting of The Physical Society of Japan, Tokyo, 27-30 Mar

8.6 Atomic Physics and Solid State Physics

Journal/Proceedings

S. Kawatsura, K. Takahiro, M. Sataka, M. Imai, H. Sugai, K. Ozaki, H. Shibata and K. Komaki
Autoionization of N^{q+} (q = 1-3) Rydberg states produced in high-energy collisions with He
Nucl. Instrum. Methods Phys. Res., B267 (2009) 901-904.

S.C. Jeong, I. Katayama, H. Kawakami, Y. Watanabe, H. Ishiyama, N. Imai, Y. Hirayama, H. Miyatake, M. Sataka, H. Sugai, S. Okayasu, S. Ichikawa, K. Nishio, S. Mitsuoka, T. Nakanoya, Takashi Hashimoto, Takanori Hashimoto and M. Yahagi
On-line diffusion tracing in Li ionic conductors by the short-lived radioactive beam of ^{8}Li
Jpn. J. Appl. Phys., **47** (2008) 6413-6415.

S.C. Jeong, I. Katayama, H. Kawakami, Y. Watanabe, H. Ishiyama, N. Imai, Y. Hirayama, H. Miyatake, M. Sataka, H. Sugai, S. Okayasu, S. Ichikawa, K. Nishio, S. Mitsuoka, T. Nakanoya, Takashi Hashimoto, Takanori Hashimoto and M. Yahagi
Abnormal Li diffusion in β-LiGa by the formation of defect complex
Jpn. J. Appl. Phys., **47** (2008) 6413-6415.

Meetings

S. Kawatsura, K. Takahiro, M. Sataka, M. Imai, H. Sugai, K. Ozaki, H. Shibata and K. Komaki
Autoionization of N^{q+} (q = 1-3) Rydberg states produced in high-energy collisions with He
Seventh International Symposium on Swift Heavy Ions in Matter, Lyon, France (June 4, 2008).

S. Kawatsura, K. Takahiro, M. Sataka, M. Imai, H. Sugai, K. Ozaki, K. Kawaguchi, H. Shibata and K. Komaki
Coster-Kronig electron from N^{q+} (q = 1-3) Rydberg states produced in high-energy collisions with He
14th International Conference on the Physics of Highly Charged Ions, Chofu, Japan (September 2, 2008).

S. Kawatsura, K. Takahiro, M. Sataka, M. Imai, H. Sugai, K. Ozaki, K. Kawaguchi, H. Shibata and K. Komaki
Coster-Kronig electron from O^{q+} (q = 1-4) Rydberg states produced in high-energy collisions with He
14th International Conference on the Physics of Highly Charged Ions, Chofu, Japan (September 2, 2008).

M. Imai, M. Sataka, K. Kawatsura, K. Takahiro, K. Komaki, H. Shibata, H. Sugai, and K. Nishio
Equilibrium and non-equilibrium charge-state distributions of 2 MeV/u sulfur ions passing through carbon foils

Int. Natl' Conf . on Atomic Collision in Solids(ICACS2008)
Hans Merensky, South Africa (August, 2008)

M. Imai, M. Sataka, K. Kawatsura, K. Takahiro, K. Komaki, H. Shibata, H. Sugai, and K. Nishio
Charge-state evolution of fully stripped Sulfur ions passing through carbon foil at 2.0MeV/u
Int. Natl' Symp. on Swift Heavy Ions in Matter (SHIM2008)
Lyon, France (June, 2008)

H. Sugai
Diffusion experiments in Li ionic conductors using the short-lived radioactive beam of ^{8}Li
Biennial meeting of the JAEA-Tokai Tandem Accelerator, on the occasion of attaining a-hundred-thousand hours of accelerator operation for experiments, Tokai, Japan (Jan. 6-7, 2009)

N. Matsunami, H. Kakiuchida, M. Tazawa, M. Sataka, H. Sugai, and S. Okayasu
Electronic and atomic structure modifications of copper-nitride films by ion impact and phase separation
Int. Conf. Atomic Collisions in Solids, 2008, August, South Africa.

N. Matsunami, H. Kakiuchida, M. Tazawa, M. Sataka, H. Sugai, and S. Okayasu,
Ion irradiation effects on Cu_3N films and phase separation
Fall meeting of The Physical Society of Japan, Sapporo, Japan (Sep. 20, 2008).

8.7 Radiation Effects in Materials

Journal/Proceedings

S. Kosugi, Nao Fujita, Y. Zushi, T. Matsui, N. Ishikawa, Y. Saito, and A. Iwase
Modification of magnetic properties of FeRh intermetallic compounds by energetic ion beam bombardment
Nucl. Instr. Meth. Phys. Res. B267(2009)1612-1615.

H. Ohno, A. Iwase, D. Matsumura, Y. Nishihata, J. Mizuki, N. Ishikawa, Y. Baba, N. Hirao, T. Sonoda, and M. Kinoshita
Study on effects of swift heavy ion irradiation in cerium dioxide using synchrotron radiation X-ray absorption spectroscopy,
Nucl. Instr. Meth. Phys. Res. B266(2008) 3013-3017.

H. Ohno, D. Matsumura, Y. Nishihata, J. Mizuki, N. Ishikawa, T. Sonoda, M. Kinoshita, and A. Iwase
Study on Effects of Heavy Ion Irradiation on CeO_2 by Using Synchrotron Radiation X-Ray Absorption Spectroscopy-as a Simulation Study for Radiation Damage in High-Burnup Light Water Reactor Fuels-,
Mater. Res. Soc. Symp. Proc., 1043-T09-02(2008)

M. Shirai, K. Tsumori, M. Kutsuwada, K. Yasuda, and S. Matsumura
Morphological change in FePt nanogranular thin films induced by swift heavy ion irradiation
Nucl. Instr. and Meth. B 267 (2009) 1787.

M. Shirai, K. Tsumori, K. Yasuda and S. Matsumura
Electron tomography observation of FePt nanogranlar thin films irradiated with 210 MeV Xe ions
Materia Japan 47 (2008) 639. (in Japanese)

M. Sasase, K. Shimura, K. Yamaguchi, H. Yamamoto, S. Shamoto and K. Hojou
Sputter etching effect of the substrate on the microstructure of β-$FeSi_2$ thin film prepared by ion beam sputter deposition method
Nucl. Instrum. Methods Phys. Res., B257 (2007) 186.

T. Sonoda, M. Kinoshita, N. Ishikawa, M. Sataka, Y. Chimi, N. Okubo, and A. Iwase
Clarification of the properties and accumulation effects of ion tracks in CeO_2
Nucl. Instr. Meth. B **266** (2008) 2882-2886.

N. Ishikawa, Y. Chimi, O. Michikami, Y. Ohta, K. Ohhara, M. Lang and R. Neumann
Study of structural change in CeO_2 irradiated with high-energy ions by means of X-ray diffraction measurement
Nuclear Instr. and Meth. B 266 (2008) 3033.

K. Ohhara, N. Ishikawa, S. Sakai, Y. Matsumoto, O. Michikami and Y. Ohta
Oxygen defects created in CeO_2 irradiated with 200MeV Au ions
Nuclear Instr. and Meth. B 267 (2009) 973.

Meetings

S. Kosugi, Nao. Fujita, T. Matsui, N. Ishiakwa, Y. Saito, R. Neumenn, and A. Iwase
Low temperature ferromagnetism induced by high energy ion irradiation in FeRh bulk alloy
Annual meeting of The Physical Society of Japan, Tokyo (Mar. 27, 2009)

Nao. Fujita, S. Kosugi, Y. Zushi, T. Matsui, N. Ishikawa, Y. Saito, and A. Iwase
Heavy ion irradiation effects on the magnetic properties of FeRh thin films(II)
Fall meeting of The Physical Society of Japan, Iwate (Sep. 20, 2008)

S. Kosugi, Nao. Fujita, Y. Zushi, T. Matsui, N. Ishikawa, Y. saito, R. Neumann, and A. Iwase
Energy dependence of the ion irradiation effects on FeRh alloy
Fall meeting of The Physical Society of Japan, Iwate (Sep. 20, 2008)

S. Kosugi, Nao. Fujita, Y. Zushi, T. Matsui , N. Ishikawa, Y. Saito, and A. Iwase
Modification of magnetic properties of FeRh bulk alloys by energetic heavy ion irradiation
International Conference on Ion Beam Modification of Materials(IBMM2008), Germany (Sep.2, 2008)

S. Kosugi, Nao. Fujita, T. Matsui, Y. Saito, N. Ishikawa, and A. Iwase
Low temperature ferromagnetism induced by high energy ion irradiation in FeRh alloy
FORUM21(Jan. 9,2009)

A. Iwase, N. Ishikawa, D. Matsumura, Y. Nishihata, J. Mizuki, Y. Baba, N. Hirao, T. Sonoda, and M. Kinoshita
Study on the behavior of oxygen atoms in swift heavy ion irradiated CeO2 by means of synchrotron radiation X-ray photoelectron spectroscopy,
Fall meeting of the Atomic Energy Society of Japan, Kochi (Sept. 5,2008)

H. Ohno D. Matsumura Y. Nishihata J. Mizuki B. Baba N. Hirao N. Ishikawa and A. Iwase
Modification of Ce valence state and electric conductivity of CeO2 by means of high energy ion irradiation
International Conference on Ion Beam Modification of Materials(IBMM2008), Germany, (Sept 2,2008)

A. Iwase, H. Ohno, D. Matsumura, Y. Nishihata, J. Mizuki, N. Ishikawa, Y. Baba, N. Hirao, T. Sonoda, and M. Kinoshita
Study on the microstructure of swift heavy ion irradiated CeO2 by means of synchrotron radiation X-ray

photoelectron spectroscopy and Ce K-edge EXAFS spectroscopy
Symposium on Swift Heavy ions in Matter(SHIM2008) France (June 4,2008)

M. Shirai, K. Tsumori, M. Kutsuwada, K. Yasuda, and S. Matsumura
Morphological change in FePt nanogranular thin films induced by swift heavy ion irradiation
16th International Conference on Ion Beam Modification of Materials (IBMM 2008), Dresden, Germany (Sep. 3, 2008).

M. Shirai, K. Tsumori, K. Yasuda, and S. Matsumura
Modification of FePt nanoparticles induced by swift heavy ion irradiation
Spring meeting of the Japanese Society of Microscopy, Kyoto, Japan (May. 23, 2008)

K. Tsumori, M. Shirai, K. Yasuda, and S. Matsumura
Swift heavy irradation effect in FePt nanogranular thin films
Fall meeting of the Japan Institute of Metals, Kumamoto, Japan (Sep. 24, 2008)

M. Sasase, K. Shimura, K. Yamaguchi, H. Yamamoto, S. Shamoto and K. Hojou
Sputter etching effect of the substrate on the microstructure of β-$FeSi_2$ thin film prepared by ion beam sputter deposition method
17th International Vacuum Congress (IVC-17), Stockholm, Sweden (July 2-6, 2007).

T. Sonoda, N. Ishikawa, M. Sataka, S. Okubo, K. Yasunaga, K. Yasuda, K. Shiiyama, S. Matsumura, A. Iwase, and M. Kinoshita,
New Cross-Over Project Study (2) Ion irradiation examinations on UO_2 and CeO_2 for clarification of grain sub-division mechanism in high burnup fuels
Fall meeting of the Atomic Energy Society of Japan, Kochi Univ. of Tech. (Sept. 5, 2008)

T. Sonoda
Electronic excitation effects on the microstructural evolution in UO_2 under irradiation with high energy ions
Global COE Workshop on Multi-scale Modeling on Materials Science -- Exploring a New Approach in Nuclear Fuel Technology --, University of Tokyo, (Dec 8, 2008)

T. Sonoda
Radiation effects of high energy fission products in light water reactor fuels
Biennial meeting of the JAEA-Tokai Tandem Accelerator, on the occasion of attaining a-hundred-thousand hours of accelerator operation for experiments, Tokai, Japan (Jan. 6-7, 2009)

T. Sonoda, K. Yasunaga, N. Ishikawa, M. Sataka, Y. Chimi, S. Okubo, A. Iwase, and M. Kinoshita,
Electronic excitation effects on the microstructural evolution in UO_2 and CeO_2 under irradiation with high

energy ions
NXO IWS-5, University of Tokyo, (Feb. 2-3, 2009)
T. Sonoda, K. Nishida, K. Dohi, S. Kitajima, T. Kameyama, K. Ohira and Y. Otsuka
Microstructure observations of nuclear fuel cladding materials with 3D atom probe and TEM
Spring meeting of the Atomic Energy Society of Japan, Tokyo Inst. of Tech. (March. 23, 2009)

N. Ishikawa, K. Ohhara, S. Yamamoto, H. Sugai and T. Sonoda
Microstructure formation in ion-irradiated CeO_2 in high fluence region
Fall meeting of The Physical Society of Japan, Iwate, Japan (Sep. 20, 2008)

N. Ishikawa
Study on ion-track formation behavior
Biennial meeting of the JAEA-Tokai Tandem Accelerator, on the occasion of attaining a-hundred-thousand hours of accelerator operation for experiments, Tokai, Japan (Jan. 6-7, 2009)

N. Ishikawa
Development of accelerator experiment setup for radiation damage studies of nuclear fuels
New Crossover Project Workshop, Tokyo, Japan (Jan. 7, 2009)

K. Ohhara, N. Ishikawa, S. Sakai, Y. Matsumoto, O. Michikami , Y. Ohta and Y. Kimura
Radiation damage in CeO_2 irradiated with high energy ions
Annual meeting of The Physical Society of Japan, Tokyo, Japan (Mar. 28, 2009)

CHAPTER 9

Personnel and Committee

This is a blank page.

9.1 Personnel

Department of Research Reactor and Tandem Accelerator

Kiyonobu	Yamashita	Director
Masao	Sataka	Deputy Director
Yuichi	Terakado	Manager of Administration Section
Suehiro	Takeuchi	

Department of Research Reactor and Tandem Accelerator

Tandem Accelerator Section *(* General Manager)*

Scientific Staff

Tetsuro	Ishii*
Akihiko	Osa
Makoto	Matsuda

Technical Staff

Yoshihiro	Tsukihasi
Susumu	Hanashima
Shin-ichi	Abe
Nobuhiro	Ishizaki
Hidekazu	Tayama
Takamitsu	Nakanoya
Hiroshi	Kabumoto
Masahiko	Nakamura
Ken-ichi	Kutsukake
Yoshinori	Otokawa
Takuhiro	Asozu

Entrusted Operators

Takahiro	Yoshida
Takayuki	Ishiguro
Kazushi	Yamaguchi
Hikaru	Nisugi
Nobuo	Seki
Teruo	Onodera

Entrusted Assistant

Kenjiro	Obara

Department of Radiation Protection

Facility Radiation Control Section I

Kenji	Yamane	(to Sep. 30)
Kunio	Kawarai	(from Oct. 1)

Katsuji	Yasu	
Hayato	Hiraga	
Daisuke	Higashi	
Susumu	Kinase	

Advanced Science Research Center

Yoshihiko	Hatano	Director
Hiroshi	Ikezoe	Deputy Director

Advanced Science Research Center

Research Group for Shell Structure and Reaction Properties of Heavy Nuclei far from Stability *(* Group Leader)*

Hiroari	Miyatake*	
Satoshi	Chiba	
Toshiki	Maruyama	
Shin-ichi	Mitsuoka	
Katsuhisa	Nishio	
Hiroyuki	Koura	
Yutaka	Utsuno	
Ichiro	Nishinaka	
Daisuke	Nagae	(Post Doc.)
Shintaro	Hashimoto	(Post Doc.)
Shin-ichi	Ichikawa	
Ryuta	Takahashi	(Student)

Advanced Science Research Center

Research Group for Nuclear Chemistry of the Heaviest Elements *(* Group Leader)*

Yuichiro	Nagame*	
Kazuaki	Tsukada	
Masato	Asai	
Tetsuya	Sato	
Atsushi	Toyoshima	(Senior Post Doc.)
Yoshitaka	Kasamatsu	(Post Doc.)
Zijie	Li	(Post Doc.)
Takahiro	Kikuchi	(Student)

Advanced Science Research Center

Research Group for Material Design under Extreme Conditions

Satoru	Okayasu
Norito	Ishikawa

Hiroyuki Sugai
Teruo Kato

Advanced Science Research Center

Research Group for Strongly Correlated Supermolecules

Takayuki Kumada
Yohei Noda (Post Doc.)

Nuclear Science and Engineering Directorate

Innovative Nuclear Science Research Group *(* Group Leader)*

Masumi Oshima*
Hideo Harada
Hideki Iimura
Mitsuo Koizumi
Kazuyoshi Furutaka
Fumito Kitatani
Shoji Nakamura
Yosuke Toh
Atsushi Kimura
Kaoru Hara (Post Doc.)
Tadahiro Kin (Post Doc.)

Nuclear Science and Engineering Directorate

Research Group for Irradiation Field Materials *(* Group Leader)*

Shiro Jitsukawa*
Nariaki Okubo
Daijyu Yamaki

Quantum Beam Science Directorate

Laser Accelerator Group

Toshiyuki Shizuma
Takehito Hayakawa

Quantum Beam Science Directorate

Neutron Imaging and Activation Analysis Group

Yuichi Hatsukawa

Nuclear Safety Research Center

Reactor Component Reliability Research Group

Yasuhiro Chimi

Tohru Tobita

High Energy Accelerator Research Organization (KEK)
- Institute of Particle and Nuclear Studies –

Radioactive Nuclear Beams Project Group *(* Group Leader)*

Physics Division IV

Sun-Chan Jeong*
Hiroari Miyatake
Hironobu Ishiyama
Yutaka Watanabe
Nobuaki Imai
Yoshikazu Hirayama
Yoshihide Fuchi
Michihiro Oyaizu
Ichiro Katayama
Hirokane Kawakami

Physics Division I

Shoji Suzuki

High Energy Accelerator Research Organization (KEK)
- Accelerator Laboratory -

Accelerator Division I

Shigeaki Arai
Masashi Okada
Kazuaki Niki

9.2 Research Planning and Assessment Committee

Chairman	Shigeru	Kubono	(Professor, The University of Tokyo)
Vice Chairman	Ken-ichiro	Komaki	(Professor, National Center for University Entrance Examination)
Member	Tadashi	Kambara	(Senior Scientist, RIKEN)
	Kenji	Kimura	(Professor, Kyoto University)
	Noriaki	Matsunami	(Associate Professor, Nagoya University)
	Tetsuo	Noro	(Professor, Kyushu University)
	Tsutomu	Ohtsuki	(Associate Professor, Tohoku University)
	Tadashi	Shimoda	(Professor, Osaka University)
	Koichi	Hagino	(Associate Professor, Tohoku University)
	Motoharu	Mizumoto	(Adjunct Professor, Tokyo Institute of Technology)
	Naotaka	Yoshinaga	(Professor, Saitama University)
	Yuichi	Hatsukawa	(Quantum Beam Science Directorate, JAEA)
	Shiro	Jitsukawa	(Nuclear Science and Engineering Directorate, JAEA)
	Kazumasa	Narumi	(Advanced Science Research Center, JAEA)
	Hiroshi	Ikezoe	(Deputy Director, Advanced Science Research Center, JAEA)
	Masao	Sataka	(Deputy Director, Dep. Research Reactor and Tandem Accelerator, JAEA)
	Suehiro	Takeuchi	(Dep. Research Reactor and Tandem Accelerator, JAEA)
Organizer	Tetsuro	Ishii	(G. Manager, Tandem Accelerator Section, JAEA)
Secretary	Akihiko	Osa	(Tandem Accelerator Section, JAEA)
	Susumu	Hanashima	(Tandem Accelerator Section, JAEA)

This is a blank page.

CHAPTER 10

Cooperative Researches and Common Use in JAEA

This is a blank page.

10.1 Cooperative Research Programs

Title	Contact Person & Organization
1. Process of structural change in light-water reactor fuel with irradiation damage by fission products	Takeshi SONODA Central Research Institute of Electric Power Industry
2. Process of irradiation damage in nuclear reactor materials with Fe base alloys	Akihiro IWASE Osaka Prefecture University
3. Dynamic behavior of heavy ions in material	Kiyoshi KAWATURA Kyoto Institute of Technology
4. Direct observation of vortices trapped in irradiated columnar defects	Masato SASASE The Wakasa-wan Energy Research Center
5. Nano-fabrication of zeolite with high energy ion irradiations	Yukichi SASAKI Japan Fine Ceramics Center
6. Effects on nuclear reactor material by swift heavy ion irradiation	Takeshi SONODA Central Research Institute of Electric Power Industry
7. Study of microscopic property change in oxides by swift heavy ions	Akihiro IWASE Osaka Prefecture University
8. Material modifications by high-energy-heavy ions	Noriaki MATUNAMI Nagoya University
9. Study of highly deformed states and high-spin shell structure in A~30 nuclei	Eiji IDEGUCHI University of Tokyo
10. Coulomb excitation on neutron-rich Xe nuclei of fission products	Sun-Chan JEONG High Energy Accelerator Research Organization
11. Nuclear spectroscopy using lasers for refractory element isotope in Re region	Takayoshi HORIGUCHI Hiroshima International University
12. Aqueous chemistry of super-heavy element Rf and Db	Hisaaki KUDO Niigata University
13. Alpha-gamma spectroscopy for super-heavy nuclei using californium target	Keisuke SUEKI University of Tsukuba
14. In-beam gamma-ray spectroscopy of super-heavy nuclei using californium target	Toshiyuki KOUNO Tokyo Institute of Technology
15. Development of spectrometer for in-beam gamma- ray spectroscopy of super-heavy nuclei	Toshiyuki KOUNO Tokyo Institute of Technology
16. Study of highly deformed states and high-spin shell structure in A~40 nuclei	Eiji IDEGUCHI University of Tokyo

10.1 Cooperative Research Programs (contd.)

Title	Contact Person & Organization
17. Electric quadrupole moment measurements of Sr isotopes by Coulomb excitation	Masahiko SUGAWARA Chiba Institute of Technology
18. Laser Spectroscopy of the Neutron Deficient Isotopes in Tungsten Region	Takayoshi HORIGUCHI Hiroshima International University
19. Aqueous chemistry of super-heavy element Db	Hisaaki KUDO Niigata University
20. Precise measurement of first excited state energy of even-even Actinide nuclei	Keisuke SUEKI University of Tsukuba
21. Study of new fission channels populated by quasi- fission	Tsutomu OHTSUKI Tohoku University
22. Search of highly excited states of 10Be using 8Li+d reaction	Hironobu ISHIYAMA High Energy Accelerator Research Organization
23. Diffusion study in super-ionic conducting materials using the short-lived nuclei	Sun-Chan JEONG High Energy Accelerator Research Organization
24. Development for search of time-reversal symmetry violation using polarized nuclei	Jiro MURATA Rikkyo University
25. Measurement of hyperfine field of 111Cd in the high-oriented pyrolytic graphite	Wataru SATO Osaka University
26. Diffusion coefficient measurements of perovskite-type lithium ion conductive oxides	Sun-Chan JEONG High Energy Accelerator Research Organization
27. Development of accelerator technology for short-lived radioactive nuclear beam	Sun-Chan JEONG High Energy Accelerator Research Organization

10.2 Common Use Programs in JAEA

Title	Contact Person & Organization
1. Measurement of hyperfine field in oxide magnetic material using gamma-ray perturbed angular correlation	Wataru SATO Osaka University
2. Indirect determination of neutron radioactive capture cross section on medium nuclei	Nobuaki IMAI High Energy Accelerator Research Organization
3. Radiation-induced magnetic transition in FeRh alloys	Akihiro IWASE Osaka Prefecture University
4. Aqueous and gas phase chemistry of lighter homologues for chemical study of $_{104}$Rf and $_{105}$Db	Shinichi GOTO Niigata University
5. Synthesis of water-soluble radioisotope-metallofullerenes	Keisuke SUEKI University of Tsukuba
6. Study on electronic structure and processes for highly charged heavy-ions by zero-degree electron spectroscopy	Makoto IMAI Kyoto University
7. Nuclear structure study of ^{108,109}Ag by transfer reactions	Jeff Carroll Youngstown State University
8. Systematic study of signature inversion and shape coexistence in high-spin states of medium-heavy nuclei	Xiao Hong Zhou Institute of Modern Physics Chinese Academy of Science
9. Decay study on fission products of ^{238}U using on-line mass separator	Michihiro SHIBATA Nagoya University
10. Study of element synthesis in the universe via short-lived nuclei	Hironobu ISHIYAMA High Energy Accelerator Research Organization
11. Development of Semiconductor device using high-energy ion implantation	Hitoshi SAKANE S.H.I. Examination & Inspection, LTD.
12. Electronic excitation effects on non-metals by high energy heavy ions	Noriaki MATUNAMI Nagoya University

This is a blank page.

国際単位系（SI）

表１．SI 基本単位

基本量	SI 基本単位	
	名称	記号
長さ	メートル	m
質量	キログラム	kg
時間	秒	s
電流	アンペア	A
熱力学温度	ケルビン	K
物質量	モル	mol
光度	カンデラ	cd

表２．基本単位を用いて表されるSI組立単位の例

組立量	SI 基本単位	
	名称	記号
面積	平方メートル	m^2
体積	立法メートル	m^3
速さ，速度	メートル毎秒	m/s
加速度	メートル毎秒毎秒	m/s^2
波数	毎メートル	m^{-1}
密度，質量密度	キログラム毎立方メートル	kg/m^3
面積密度	キログラム毎平方メートル	kg/m^2
比体積	立方メートル毎キログラム	m^3/kg
電流密度	アンペア毎平方メートル	A/m^2
磁界の強さ	アンペア毎メートル	A/m
量濃度[(a)]，濃度	モル毎立方メートル	mol/m^3
質量濃度	キログラム毎立法メートル	kg/m^3
輝度	カンデラ毎平方メートル	cd/m^2
屈折率[(b)]	（数字の） 1	1
比透磁率[(b)]	（数字の） 1	1

(a) 量濃度（amount concentration）は臨床化学の分野では物質濃度（substance concentration）ともよばれる。
(b) これらは無次元量あるいは次元１をもつ量であるが、そのことを表す単位記号である数字の１は通常は表記しない。

表３．固有の名称と記号で表されるSI組立単位

組立量	SI 組立単位			
	名称	記号	他のSI単位による表し方	SI基本単位による表し方
平面角	ラジアン[(b)]	rad	1[(b)]	m/m
立体角	ステラジアン[(b)]	sr[(c)]	1[(b)]	m^2/m^2
周波数	ヘルツ[(d)]	Hz		s^{-1}
力	ニュートン	N		m kg s^{-2}
圧力，応力	パスカル	Pa	N/m^2	m^{-1} kg s^{-2}
エネルギー，仕事，熱量	ジュール	J	N m	m^2 kg s^{-2}
仕事率，工率，放射束	ワット	W	J/s	m^2 kg s^{-3}
電荷，電気量	クーロン	C		s A
電位差（電圧），起電力	ボルト	V	W/A	m^2 kg s^{-3} A^{-1}
静電容量	ファラド	F	C/V	m^{-2} kg^{-1} s^4 A^2
電気抵抗	オーム	Ω	V/A	m^2 kg s^{-3} A^{-2}
コンダクタンス	ジーメンス	S	A/V	m^{-2} kg^{-1} s^3 A^2
磁束	ウエーバ	Wb	Vs	m^2 kg s^{-2} A^{-1}
磁束密度	テスラ	T	Wb/m^2	kg s^{-2} A^{-1}
インダクタンス	ヘンリー	H	Wb/A	m^2 kg s^{-2} A^{-2}
セルシウス温度	セルシウス度[(e)]	℃		K
光束	ルーメン	lm	cd sr[(c)]	cd
照度	ルクス	lx	lm/m^2	m^{-2} cd
放射性核種の放射能[(f)]	ベクレル[(d)]	Bq		s^{-1}
吸収線量，比エネルギー分与，カーマ	グレイ	Gy	J/kg	m^2 s^{-2}
線量当量，周辺線量当量，方向性線量当量，個人線量当量	シーベルト[(g)]	Sv	J/kg	m^2 s^{-2}
酸素活性	カタール	kat		s^{-1} mol

(a)SI接頭語は固有の名称と記号を持つ組立単位と組み合わせても使用できる。しかし接頭語を付した単位はもはやコヒーレントではない。
(b)ラジアンとステラジアンは数字の１に対する単位の特別な名称で、量についての情報をつたえるために使われる。実際には、使用する時には記号rad及びsrが用いられるが、習慣として組立単位としての記号である数字の１は明示されない。
(c)測光学ではステラジアンという名称と記号srを単位の表し方の中に、そのまま維持している。
(d)ヘルツは周期現象についてのみ、ベクレルは放射性核種の統計的過程についてのみ使用される。
(e)セルシウス度はケルビンの特別な名称で、セルシウス温度を表すために使用される。セルシウス度とケルビンの単位の大きさは同一である。したがって、温度差や温度間隔を表す数値はどちらの単位で表しても同じである。
(f)放射性核種の放射能（activity referred to a radionuclide）は、しばしば誤った用語で"radioactivity"と記される。
(g)単位シーベルト（PV,2002,70,205）についてはCIPM勧告2（CI-2002）を参照。

表４．単位の中に固有の名称と記号を含むSI組立単位の例

組立量	SI 組立単位		
	名称	記号	SI 基本単位による表し方
粘度	パスカル秒	Pa s	m^{-1} kg s^{-1}
力のモーメント	ニュートンメートル	N m	m^2 kg s^{-2}
表面張力	ニュートン毎メートル	N/m	kg s^{-2}
角速度	ラジアン毎秒	rad/s	m m^{-1} s^{-1}=s^{-1}
角加速度	ラジアン毎秒毎秒	rad/s^2	m m^{-1} s^{-2}=s^{-2}
熱流密度，放射照度	ワット毎平方メートル	W/m^2	kg s^{-3}
熱容量，エントロピー	ジュール毎ケルビン	J/K	m^2 kg s^{-2} K^{-1}
比熱容量，比エントロピー	ジュール毎キログラム毎ケルビン	J/(kg K)	m^2 s^{-2} K^{-1}
比エネルギー	ジュール毎キログラム	J/kg	m^2 s^{-2}
熱伝導率	ワット毎メートル毎ケルビン	W/(m K)	m kg s^{-3} K^{-1}
体積エネルギー	ジュール毎立方メートル	J/m^3	m^{-1} kg s^{-2}
電界の強さ	ボルト毎メートル	V/m	m kg s^{-3} A^{-1}
電荷密度	クーロン毎立方メートル	C/m^3	m^{-3} sA
表面電荷	クーロン毎平方メートル	C/m^2	m^{-2} sA
電束密度，電気変位	クーロン毎平方メートル	C/m^2	m^{-2} sA
誘電率	ファラド毎メートル	F/m	m^{-3} kg^{-1} s^4 A^2
透磁率	ヘンリー毎メートル	H/m	m kg s^{-2} A^{-2}
モルエネルギー	ジュール毎モル	J/mol	m^2 kg s^{-2} mol^{-1}
モルエントロピー，モル熱容量	ジュール毎モル毎ケルビン	J/(mol K)	m^2 kg s^{-2} K^{-1} mol^{-1}
照射線量（X線及びγ線）	クーロン毎キログラム	C/kg	kg^{-1} sA
吸収線量率	グレイ毎秒	Gy/s	m^2 s^{-3}
放射強度	ワット毎ステラジアン	W/sr	m^4 m^{-2} kg s^{-3}=m^2 kg s^{-3}
放射輝度	ワット毎平方メートル毎ステラジアン	W/(m^2 sr)	m^2 m^{-2} kg s^{-3}=kg s^{-3}
酵素活性濃度	カタール毎立方メートル	kat/m^3	m^{-3} s^{-1} mol

表５．SI 接頭語

乗数	接頭語	記号	乗数	接頭語	記号
10^{24}	ヨタ	Y	10^{-1}	デシ	d
10^{21}	ゼタ	Z	10^{-2}	センチ	c
10^{18}	エクサ	E	10^{-3}	ミリ	m
10^{15}	ペタ	P	10^{-6}	マイクロ	μ
10^{12}	テラ	T	10^{-9}	ナノ	n
10^{9}	ギガ	G	10^{-12}	ピコ	p
10^{6}	メガ	M	10^{-15}	フェムト	f
10^{3}	キロ	k	10^{-18}	アト	a
10^{2}	ヘクト	h	10^{-21}	ゼプト	z
10^{1}	デカ	da	10^{-24}	ヨクト	y

表６．SIに属さないが、SIと併用される単位

名称	記号	SI 単位による値
分	min	1 min=60s
時	h	1h =60 min=3600 s
日	d	1 d=24 h=86 400 s
度	°	1°=(π/180) rad
分	’	1’=(1/60)°=(π/10800) rad
秒	”	1”=(1/60)’=(π/648000) rad
ヘクタール	ha	$1ha=1hm^2=10^4m^2$
リットル	L，l	$1L=11=1dm^3=10^3cm^3=10^{-3}m^3$
トン	t	$1t=10^3$ kg

表７．SIに属さないが、SIと併用される単位で、SI単位で表される数値が実験的に得られるもの

名称	記号	SI 単位で表される数値
電子ボルト	eV	$1eV=1.602\ 176\ 53(14)\times10^{-19}J$
ダルトン	Da	$1Da=1.660\ 538\ 86(28)\times10^{-27}kg$
統一原子質量単位	u	1u=1 Da
天文単位	ua	$1ua=1.495\ 978\ 706\ 91(6)\times10^{11}m$

表８．SIに属さないが、SIと併用されるその他の単位

名称	記号	SI 単位で表される数値
バール	bar	1 bar=0.1MPa=100kPa=10^5Pa
水銀柱ミリメートル	mmHg	1mmHg=133.322Pa
オングストローム	Å	1 Å=0.1nm=100pm=10^{-10}m
海里	M	1 M=1852m
バーン	b	$1\ b=100fm^2=(10^{-12}cm)2=10^{-28}m^2$
ノット	kn	1 kn=(1852/3600)m/s
ネーパ	Np	SI単位との数値的な関係は、対数量の定義に依存。
ベル	B	
デジベル	dB	

表９．固有の名称をもつCGS組立単位

名称	記号	SI 単位で表される数値
エルグ	erg	$1\ erg=10^{-7}$ J
ダイン	dyn	$1\ dyn=10^{-5}$N
ポアズ	P	$1\ P=1\ dyn\ s\ cm^{-2}=0.1Pa\ s$
ストークス	St	$1\ St=1cm^2\ s^{-1}=10^{-4}m^2\ s^{-1}$
スチルブ	sb	$1\ sb=1cd\ cm^{-2}=10^4cd\ m^{-2}$
フォト	ph	$1\ ph=1cd\ sr\ cm^{-2}\ 10^4lx$
ガル	Gal	$1\ Gal=1cm\ s^{-2}=10^{-2}ms^{-2}$
マクスウェル	Mx	$1\ Mx = 1G\ cm^2=10^{-8}Wb$
ガウス	G	$1\ G=1Mx\ cm^{-2}=10^{-4}T$
エルステッド[(c)]	Oe	1 Oe ≙ $(10^3/4\pi)A\ m^{-1}$

(c) ３元系のCGS単位系とSIでは直接比較できないため、等号「 ≙ 」は対応関係を示すものである。

表10．SIに属さないその他の単位の例

名称	記号	SI 単位で表される数値
キュリー	Ci	$1\ Ci=3.7\times10^{10}Bq$
レントゲン	R	$1\ R=2.58\times10^{-4}C/kg$
ラド	rad	$1\ rad=1cGy=10^{-2}Gy$
レム	rem	$1\ rem=1\ cSv=10^{-2}Sv$
ガンマ	γ	1γ=1 nT=10-9T
フェルミ		1フェルミ=1 fm=10-15m
メートル系カラット		1メートル系カラット = 200 mg = 2×10-4kg
トル	Torr	1 Torr = (101 325/760) Pa
標準大気圧	atm	1 atm = 101 325 Pa
カロリー	cal	1cal=4.1858J（「15℃」カロリー），4.1868J（「IT」カロリー）4.184J（「熱化学」カロリー）
ミクロン	μ	1 μ =1μm=10^{-6}m

（第8版，2006年改訂）

この印刷物は再生紙を使用しています